Nanoscale

REVIEW

View Article Online
View Journal | View Issue

Cite this: *Nanoscale*, 2021, **13**, 7913

Lanthanide doped luminescence nanothermometers in the biological windows: strategies and applications

Albenc Nexha, Joan Josep Carvajal,* Maria Cinta Pujol, Francesc Díaz and Magdalena Aguiló

The development of lanthanide-doped non-contact luminescent nanothermometers with accuracy, efficiency and fast diagnostic tools attributed to their versatility, stability and narrow emission band profiles has spurred the replacement of conventional contact thermal probes. The application of lanthanide-doped materials as temperature nanosensors, excited by ultraviolet, visible or near infrared light, and the generation of emissions lying in the biological window regions, I-BW (650 nm–950 nm), II-BW (1000 nm–1350 nm), III-BW (1400 nm–2000 nm) and IV-BW (centered at 2200 nm), are notably growing due to the advantages they present, including reduced phototoxicity and photobleaching, better image contrast and deeper penetration depths into biological tissues. Here, the different mechanisms used in lanthanide ion-doped nanomaterials to sense temperature in these biological windows for biomedical and other applications are summarized, focusing on factors that affect their thermal sensitivity, and consequently their temperature resolution. Comparing the thermometric performance of these nanomaterials in each biological window, we identified the strategies that allow boosting of their sensing properties.

Received 28th December 2020,
Accepted 21st March 2021

DOI: 10.1039/d0nr09150b

rsc.li/nanoscale

1. Introduction

Several chemical, physical and biological processes are temperature-dependent. Thus, precise and accurate measurement of the temperature is of paramount importance in countless industrial and research applications.[1–7]

Nowadays, temperature sensors account for 80% of the world-wide sensor market and expect to reach a value of $8.8 billion by 2027, according to Grand View Research, Inc.[8] However, most of these temperature sensors are based on contact thermometers, where the thermal reading is achieved by direct physical contact of an invasive probe material with the body in which the temperature should be determined. Contact thermometers require conductive heat transfer and need to reach a thermal equilibrium between the sensor and the object under study. This connection might disturb the measurement of the temperature at the object, leading to an inappropriate determination of the exact temperature in some cases. These measurements are especially affected when dealing with nanoscale dimensions, in which the size of the object under study is smaller than the sensor head of the thermometer.[9–13] In addition, contact thermometers allow the performance of only surface measurements. Modern requirements for temperature readings in areas such as microelectronics, photonics, nanomedicine and diagnosis, and microfluidics, among others, have led to the replacement of contact thermometers and the development of non-contact nanoscale thermometers.[14–16]

Non-contact nanoscale thermometers can provide feedback of the local temperature of a given system with micro and nanoscale spatial resolution.[17] The precise determination of the temperature at the nanoscale has attracted great interest, especially in nanomedicine and diagnosis fields, as many functions of the human body, including cell division, gene expression or enzyme reactions, are temperature-dependent.[18] Diseases such as the cellular pathogenesis of cancer lead to heat generation.[19] In addition, temperature changes can also be induced intentionally to kill locally infected cells.[20] Therefore, achieving precise temperature reading information is crucial to heal infected cells and simultaneously avoid the destruction of surrounding healthy tissues.

High-resolution temperature non-contact measurement techniques operating in the micro/nanoscale are divided into several types using distinct criteria based on their operating principle. These methods provide different advantages and drawbacks;[21] hence a proper selection according to the required spatial, temporal and temperature resolutions is

Universitat Rovira i Virgili, Departament de Química Física i Inorgànica, Física i Cristal·lografia de Materials i Nanomaterials (FiCMA-FiCNA)-EMaS, Campus Sescelades, E-43007 Tarragona, Spain. E-mail: joanjosep.carvajal@urv.cat

essential. Non-contact techniques for the determination of the temperature include infrared thermometry, thermoreflectance, Raman scattering, interferometry, and non-optical and luminescence nanothermometry.[17]

The principle of infrared thermometry is to determine the temperature by the amount of the thermal radiation emitted by the target which is being monitored.[17] Knowing the amount of infrared energy emitted by the object and its emissivity, the target temperature can be determined. This non-contact method is a well-implemented commercial technique and grants a temperature image profile of the surface of the target, achieving spatial, temporal and temperature resolutions of ~10 μm, ~10 μs and ~0.1 K,[17] respectively. However, this technique requires an additional knowledge of the spatial resolution and the emissivity of the target at the micrometer scale.[2] These are serious drawbacks for the application of this technique at the nanoscale because, with the determination of the temperature on the surface and not inside the target, the precise discrimination of the temperature of a living cell, for instance, strongly impacts on the analysis of its pathology and physiology and, in turn, on the optimization of therapeutic processes (*e.g.* in hyperthermal tumor treatments and photodynamic therapy).[22,23]

Thermoreflectance thermometry extracts temperature readings from the dependence of the refractive index of the material on the temperature.[24] This technique offers high temperature (~0.01 K) and temporal resolution (~0.1 μs), and the combination of qualitative and quantitative measurements.[2] Despite this, it requires the calibration of the refractive index of the material of analysis, and its spatial resolution is restricted by the light diffraction limit.[25]

Raman scattering thermometry is based on the dependence of the position of the Raman modes of the material of interest on temperature.[26] Raman thermometry can be applied to liquids and solids, including powders, achieving spatial, temporal and temperature resolutions of ~1 μm, ~10^6 μs and ~0.1 K,[2] respectively. Regardless of these good parameters, it is a time-consuming technique and the number of the materials to which this technique can be applied is very small because the materials need to have a large Raman efficiency if applied as successful temperature probes.[7]

Optical interferometry provides dual information: local temperature and local deformation due to the thermal expansion of the material under analysis.[27] Interferometers depict the differences in optical paths between light beams that bypass the test section and pass directly through it. Although this technique can be integrated in remote detection systems with spatial, temporal and temperature resolutions of ~1 μm, ~0.001 μs and ~10^{-5} K,[2] respectively, drawbacks related to cross talk with other stimuli, such as strain/stress and bending, and low spatial resolution in the transverse direction, limit their application.[2]

Non-optical thermometry methods include several techniques developed for nanoscale thermometric applications such as scanning thermal microscopy,[28] deposition of metallic temperature sensors by nanolithography,[29] carbon nanotube thermometry,[30] and biomaterial thermometry.[31] Scanning thermal microscopy uses a small thermocouple with a junction diameter of the order of 20 to 100 nm, formed at the probe tip of an atomic force microscope, which is scanned over the surface of interest.[32] It can also consist of a combination of a thermocouple and a resistance temperature,[33] providing sub-micrometric spatial resolution.[2] This technique is limited to solid samples and offers slow acquisition times, requiring at the same time fundamental knowledge of the tip–sample heat transfer mechanisms.[2] Nanolithography can be applied to deposit a platinum strip to form a thermal sensor on the surface of the material of interest. However, ensuring the robustness of the sensor and its chemical consistency is an important challenge for this technique.[17] Carbon nanotubes as thermal probes were originally proposed using gallium as the thermometric liquid filling them, and with the support of a scanning electron microscope to observe their meniscus.[30] These nanotubes have been used also to provide good thermal contact between an electron microscope and the sample with nanoscale resolution,[34] but they presents also some limitations, such as the thermal contact resistance formed between the tip and the surface, which can modify the probe response, especially for high thermal conducting samples.[34] Biomaterials, such as living cells, sense temperature by using their components (proteins, nucleic acids and mRNAs).[31] The change of temperature in these components is manifested either by modifying their conformational structure directly or undergoing complex reactions that can be exploited to extract the temperature at the nanoscale level.[35–37] However, the molecular complexity associated with this temperature sensing is not yet fully understood, and the thermal response occurs within the physiological range of temperatures. Furthermore, this technique often induces conformational changes that are subtle and reversible.[31]

Luminescence thermometry (also called thermographic phosphor nanothermometry[1]) refers to the relationship between the temperature and the luminescence properties of the light emitted by the luminophore to achieve temperature sensing.[10] The major boost for luminescence thermometry at the nanoscale is attributed to the high temperature sensitivity and the easy detection setups required for these signals. With the change of temperature, different luminescence characteristics such as the intensity of the emission, spectral position, decay and rise time, and band positions and widths, may all be modified, which gives rise to different luminescence thermometry classes.[10] Luminescence thermometry provides high spatial resolution (<10 μm) in short acquisition times (<10 μs) and high thermal resolution (0.1 K).[2] Additionally, luminescent thermometers can operate even in harsh conditions such as in biological fluids, strong electromagnetic fields, cryogenic temperatures and fast-moving objects, without restricting their resolutions.[10,13,38,39]

1.1. Luminescence nanothermometry

1.1.1. Fundamental principles of luminescence nanothermometry. Luminescence refers to the emission of light from

an excited electronic state of a given substance.[40] This substance (or phosphor) consists of a luminescence entity, molecule or activator ion, embedded in a host (or matrix) material, and sometimes accompanied by a second entity that favors the absorption of light and transfers this energy to the activator, called a sensitizer. Sometimes, this substance may consist of only an activator embedded in a host, without the presence of a sensitizer. The characteristic luminescence properties of a given substance can be obtained by doping the host with relatively small amounts of foreign ions (activator and sensitizer). An activator incorporated into a host lattice gives rise to an emitting center which can be excited to generate luminescence.

A sensitizer incorporated into a host lattice is capable of absorbing more efficiently the energy from the excitation source and transferring it in a very efficient way to a neighbor activator that at the end will generate luminescence.[41] When exposed to a temperature, the characteristics of the luminescence of the phosphor (intensity, spectral position, decay and/or rise time, the band position and width), may change. Exploring the way in which these characteristics change, with the ultimate goal of determining the temperature of the phosphor, gives rise to luminescent thermometry. Fig. 1 depicts a general schematic illustration of the basic mechanisms of luminescence thermometry. For the sake of simplicity, a single center emission phosphor is illustrated, displaying a change in the intensity of the emissions as the temperature increases. This figure illustrates the class of band-shape luminescence thermometry, probably the widest explored class. In the figure we show how the phosphor is excited with an energy source ($h\nu$) from the ground state level (indicated as 0) to an excited state level (indicated as 3), from where, according to the principle of conservation of energy, it will decay back to an intermediate or to the ground state with the emission of light or through the release of energy *via* non-radiative processes.[40,41] The decay could occur directly from the excited state (3) back to the ground state (0) *via* a radiative relaxation process, generating an emission line (labelled as "Emission 1" with intensity I_1) or *via* a non-radiative relaxing process (shown with a golden wavy arrow) through a lower intermediate excited level (either 2 or 1). From here, the second emission line (labelled as "Emission 2" with intensity I_2) can be generated when a second radiative relaxation process occurs to another lower level, or to the ground state.[40] Please note that from the 2 and 1 intermediate excited states, additional emission lines can be generated, but for simplicity reasons, they are not illustrated in Fig. 1.

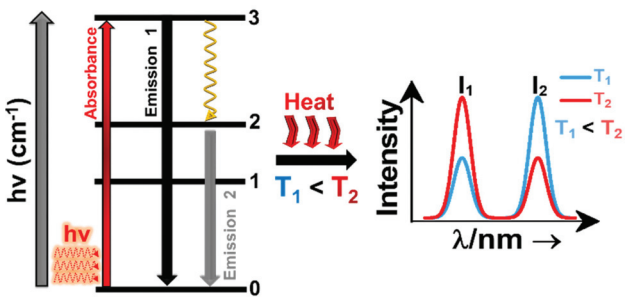

Fig. 1 Basic working principle of luminescence nanothermometry, illustrated *via* the change of the intensity of the emissions with the increase of temperature, as an example.

In order to be used in a luminescent nanothermometer, the generated emissions from the phosphor must fulfill several requirements. These requirements are related to the quality of the emission generated: they should exhibit high quantum yield and should be temperature-dependent.[10] The generated emissions of a phosphor are related to, among other different variables, the composition of the material, the purity level and the local temperature of the system.[1] Thus, the principle of luminescence nanothermometry is to exploit the relationship between the properties of the luminescence emission process and the temperature to achieve temperature sensing by temporal or spectral analysis of the emission.[10] For example, in our simplified single center emission phosphor, upon increasing the temperature from T_1 to T_2 (presented in Fig. 1 by the red curved arrows labelled as "Heat"), this induces changes in the intensity of the emissions. Investigating the variation of the ratio of the intensities of the emissions (I_1 and I_2), the temperature can be determined before calibration of the luminescent thermometer.[10] When the temperature changes are applied, the intensity of the emissions (and other luminescence properties as well) can vary due to the processes of electronic population or depopulation of the energy levels.[1,10]

1.1.2. Classes of luminescence nanothermometry. Temperature can affect the characteristics of the luminescence of the phosphor in different ways. Based on the particular parameter of luminescence whose temperature-dependence is analyzed, different classes of luminescence nanothermometry are developed. Fig. 2 illustrates six parameters that define the luminescence of a given phosphor: band-shape, intensity, bandwidth, spectral shift, lifetime and polarization, and their variation with an increase of temperature.[10] Band-shape nanothermometry refers to the relative intensity between the different spectral lines of the luminescence spectrum (Fig. 2(a)).[10] The changes induced by the temperature in the luminescence intensity are related to the thermal activation of processes of quenching and an increase in the probability of non-radiative mechanisms. This class of luminescence nanothermometry can be used in materials which possess radiative states with an energy gap (hereafter ΔE) of the order of 200 cm^{-1} to 2000 cm^{-1}, *i.e*, the so-called "thermally coupled levels" (hereafter TCLs), and the extraction of thermal knowledge is achieved by the fluorescence intensity ratio (hereafter FIR), based totally on a Boltzmann type-distribution.[42] The main benefit of this class of luminescence nanothermometry is its independency of signal losses and the possible fluctuations in the excitation intensity.[10] TCLs with too small a ΔE (<200 cm^{-1}) will lead to a strong overlap of signals, while too large ΔE values (>2000 cm^{-1}) will result in the weak or null coupling of the electronic levels.[43] Furthermore, the performance of nanothermometers operating by these principles is

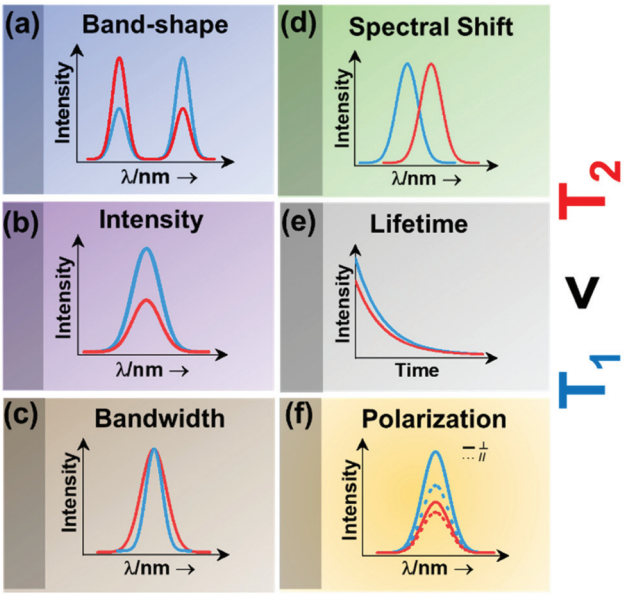

Fig. 2 Classes of luminescence nanothermometry: (a) band-shape, (b) intensity, (c) bandwidth, (d) spectral shift, (e) lifetime and (f) polarization.

restricted by the value of ΔE.[44] In addition, this class of luminescence nanothermometry includes single or dual emitting centers with a change in the intensity of at least two different emission bands in a material, even if they arise from non TCLs, for which different models for FIR have to be proposed,[21] as we will discuss in the following sections.

Intensity luminescence nanothermometry determines temperature through the analysis of the intensity of the luminescence generated by a single emission band (Fig. 2(b)).[10] With the change of temperature, as for the case of the band-shape luminescence nanothermometry class, processes like quenching and the increase in probability of non-radiative mechanisms happening will display a decrease in intensity of the luminescence that can be correlated with the temperature.[45] With the change of temperature, the intensity of the emission spectrum becomes less (or more) intense due to an overall change in the number of emitted photons.[42,46]

Bandwidth luminescence nanothermometry extracts temperature information from the effect that the change of temperature has on the width of the emission lines of the luminescence spectrum (Fig. 2(c)).[10] Generally, with an increase of the temperature, the emission lines become broader because of the thermal vibration of the luminescent center and its neighboring atoms/molecules.[10] The degree of change of the emission line broadening is usually small, and as a result it can only be observed in systems showing inherent narrow emission lines and strongly temperature-dependent transitions.[10]

Spectral shift luminescence nanothermometry is based on the analysis of the spectral positions of the emission lines, which change due to their dependence on temperature. When the temperature increases, the energy value of the emitting level changes, manifested by a shift in the emission wavelength (Fig. 2(d)).[10] This ΔE depends on a large variety of temperature-dependent parameters of the emitting material, including the refractive index and the inter-atomic distances, among others.[10] The shift in the spectral position is usually related to thermally induced strains in the environment of the thermal probes, occurring as a result of electron–phonon interaction.[16]

Lifetime nanothermometry analyzes the temperature dependence of the luminescence lifetime (Fig. 2(e)). Luminescence lifetime studies the time interval in which the emitted intensity decays down to $1/e$ of its maximum value after a pulsed excitation.[10] The experimental lifetime is related to the contribution of the radiative, non-radiative or multiphonon and quenching mechanisms.[47] With the increase of temperature, the lifetime generally shortens due to the increase of the probability of quenching mechanisms happening. The lifetime is also related to the dimension of the material. The lifetime of nanocrystals is shorter when compared with that of macrometric particles. This difference is related to lattice distortion, and a bigger number of surface defects related to the higher surface-to-volume ratio in nanomaterials, which overall leads to an increase of the radiative rates and higher quenching rates.[47]

Polarization luminescence nanothermometry is based on the influence of temperature in the polarization anisotropy parameter, which is the ratio between the luminescence intensities emitted at two orthogonal polarization states (Fig. 2(f)).[10]

In the following sections, we will analyze how these different luminescence nanothermometry classes have been used to determine temperature using lanthanide-doped luminescent nanothermometers operating in the biological windows, with special emphasis on the different strategies developed to improve their performance. For a detailed comprehensive understanding of the six luminescence thermometry classes and the determination of their thermal sensing capacity, the reader is requested to refer to the review of Jaque *et al.*[10] and Brites *et al.*[48]

1.1.3. Materials used to develop luminescent nanothermometers. Different luminescent nanomaterials have been tested for providing a contactless temperature reading through luminescence nanothermometry (Fig. 3). In order to boost their potential nanothermometric applications in different fields, but specially in biomedicine, several factors, including strong luminescence, good photostability, no photobleaching effect, low or barely no toxicity, good dispersibility in biological media and outstanding optical properties that allow for deep tissue light penetration,[49] should be taken into account.

Luminescent materials tested as potential nanothermometers include fluorescent proteins,[50–54] nanogels,[3,55–57] polymers,[58–61] organic–inorganic hybrids,[43,62–64] nanodiamonds,[65–67] metal organic frameworks (MOFs),[39,68–71] organic dyes,[72–76] semiconductor quantum-dots (QDs),[77–81] and lanthanide (Ln^{3+}) doped nanomaterials.[10,21,48,82] Fig. 3 highlights the pros and cons of these materials as potential luminescent nanothermometers.

Fluorescent proteins, either in their simple form or genetically encoded, can be used to measure temperature at the intracellular level.[50–54] These nanothermometers can be

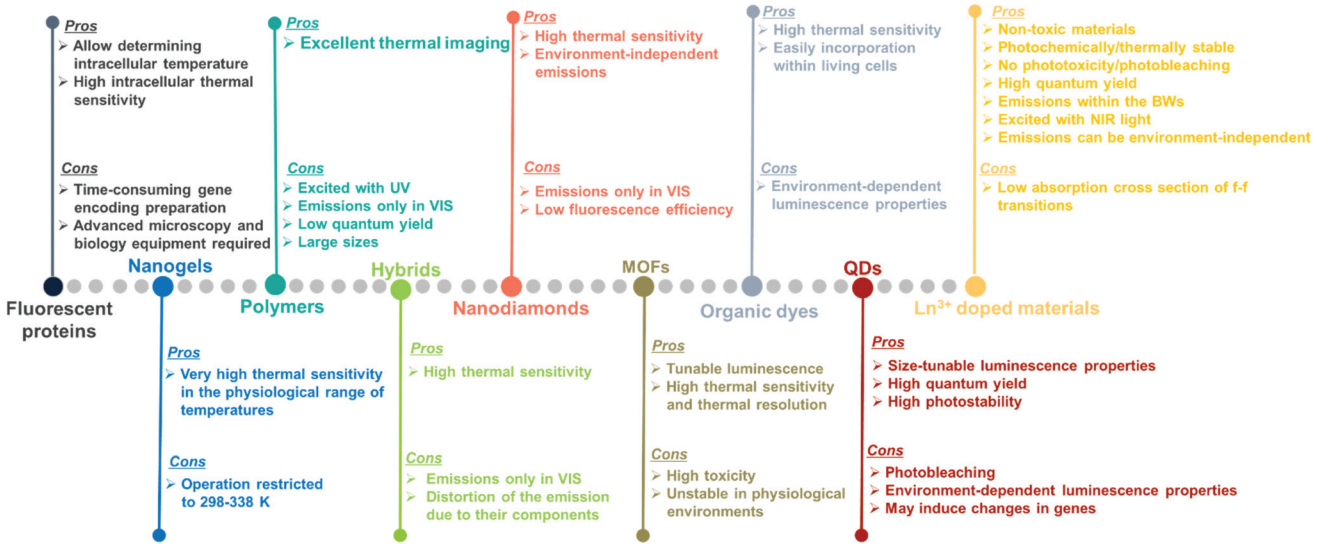

Fig. 3 Pros and cons of different types of material used to develop luminescent thermometers.

applied to obtain thermal images of heated single cells and to study thermogenesis, a fundamental process in cell biology. Regardless of the relatively high intracellular thermal sensitivity achieved with these nanothermometers, drawbacks, including time-consuming gene encoding, the need for specialized microscopy equipment and advanced molecular biology techniques for gene modification,[83,84] have prevented their future applications.

Nanogels portray nanoscale-sized three-dimensional hydrogel materials formed by crosslinked swellable polymer networks with a high capacity to hold water, without actually dissolving into the aqueous medium.[85] Below a particular temperature, normally around 300 K, the structure of the nanogel swells by absorbing water into its interior, which causes a quenching of the fluorescence that is gradually recovered when the temperature increases above this temperature since the nanogel shrinks because of the release of water molecules.[3,55–57] As luminescent nanothermometers, nanogel compounds present an important advantage: the most relevant changes in their fluorescence intensity occur within the physiological range of temperatures. A particular disadvantage is that the emission intensity of the nanogels becomes highly temperature sensitive only in a reduced temperature range (298–338 K).[10]

Polymers stands for large macromolecules composed of repeated structural units, called monomers. The presence of luminescent monomers within the polymers allows their use as luminescent thermometers.[58–61] The luminescence of these compounds is usually found in the visible (VIS) range (500–600 nm) after being excited with ultraviolet (UV) light,[58–61] which can induce phototoxicity if applied to extract thermal information from biological tissues.[86] Despite the good results demonstrated in thermal imaging, these thermometers usually exhibit drawbacks related to their low quantum yield,[87] relatively large sizes, and the dependence of the luminescence not only on temperature, but also on the local concentration of emitting centers.[10]

An organic–inorganic hybrid can be defined as a single particle that combines two different materials belonging to these categories.[88] In the field of luminescence nanothermometry, these materials can be used by exploiting the complementary functionalities of their constituent materials to develop multifunctional platforms, such as temperature sensing and heat generation, for further applications.[62–64,89] Regardless of their good temperature-sensing properties, limitations are also encountered. These limitations are related to nanothermometers being operative only in the VIS region, which represents a low penetration depth in biological tissues and a distortion of the spectra recorded due to the non-negligible absorption of the different components encountered in them.[90]

The application of nanodiamonds as luminescent nanothermometers is attributed to the presence of particular local point defects (nitrogen vacancy centers) in their structure.[91] These nanodiamonds are fluorescent and display a very sensitive temperature transition between two ground quantum spin states.[65–67] The advantages of these nanothermometers rely on their high thermal sensitivity and on the fact that nitrogen vacancy centers are inner defects, hence, in theory, making these thermometers environment-independent.[91] However, when applied to biological tissues, the light generated from these materials might be affected by the biological tissue components. Furthermore, their emissions are often located in the VIS, and the low fluorescence efficiency displayed is a limiting factor especially when acquiring cellular thermal images.[92]

Metal organic frameworks (MOFs) have emerged as an important class of luminescent materials due to their multiple luminescent centers and tunable optical properties.[39,68–71] The tunability of the optical properties of MOFs is related to the fact that the metal nodes, organic linkers, and guest molecules

within porous MOFs all can potentially generate luminescence. Furthermore, the inherent porosity and large surface areas of MOFs offer great opportunities for intermolecular interactions between the frameworks and guest molecules, influencing the coordination environment and the energy transfer processes that can occur among them, thus modulating their luminescence properties.[71] However, it should be admitted that, to use these luminescent thermometers in biological environments, besides high sensitivity and spatial resolution, non-toxicity and stability in the physiological environment are required, which are often lacking in MOF-based thermometers.[71]

Organic dyes are organic compounds with strong luminescence intensity, in general.[10] Despite their high temperature-sensing properties and the ability to be easily incorporated into living cells, the spectral properties of the luminescence band depend on many factors, including temperature, solvent used, concentration, and pH, among others.[10,92] Being specially dependent on the environment in which the organic dye is embedded makes it necessary to recalibrate the thermometers in each particular environment, and thus, the temperature-sensing ability will strongly depend on the medium where the compound is embedded.[92]

Quantum dots (QDs) are highly attractive nanomaterials for application as luminescent nanothermometers, due to their size-tunable spectroscopic properties,[77–81] narrow emissions, high photostability and high quantum yields.[93,94] For years, concerns regarding their phototoxicity and cytotoxicity towards biological matter due to UV light excitation,[86,95] and emission wavelengths limited to the range shorter than 1000 nm, have been resolved by the preparation of core@shell structures.[94,96,97] Despite this, limitations still remain concerning the variation of the luminescence parameters (intensity, lifetime and spectral shift) with the environment, including surfactants and ligands, which leads to a source of error in thermal readings,[98] and their genetically-induced changes.[95,97]

Lanthanide (Ln^{3+}) doped nanomaterials, due to their peculiar electronic configuration, exhibit stable and narrow emissions covering a wide range of the electromagnetic spectrum, upon proper selection of the dopants and the transparency of the host, with high emission quantum yields (>50% in the visible range).[99–102] In addition, these barely non-toxic materials[103] can generate their emission lines upon excitation *via* near infrared (NIR) light, which stands for a low-cost excitation source with no photobleaching, no autofluorescence and no phototoxicity upon biological matter.[21,48] Furthermore, the generation of NIR light and its use instead of VIS or UV light allows for deep-tissue penetration,[86] specifically when the wavelengths of the emissions fall within the so-called biological windows[104,105] (section 1.3). A drawback of these materials relates to the low absorption cross section of the 4f–4f electronic transitions because of their forbidden nature.[106] Different strategies have been implemented to increase the absorption properties of Ln^{3+}-doped materials, including plasmonic enhancement, organic-dye sensitization, and coupling with semiconductors.[107,108] Thus, inspired by these properties of Ln^{3+}-doped luminescent nanomaterials, the rest of this review will be focused on the performance of these nanomaterials to extract information on the local temperature of a given system when the generated emissions fall in the biological window regions. Furthermore, the strategies explored to boost their ability to achieve better thermal readings will be analyzed.

1.2. Performance of a lanthanide-doped luminescent nanothermometer

Regardless of the luminescent nanothermometry class used to extract temperature information, the performance of a lanthanide-doped nanothermometer, as well as that of other thermometers based on other materials, can be evaluated and compared with other nanothermometers, based on their thermal sensitivity, temperature resolution, spatio-temporal resolution, repeatability and reproducibility. Detailed information about all these parameters is summarized elsewhere.[21,48] Thus, here we will emphasize, in general terms, how these parameters can be calculated.

The thermal sensitivity expresses the degree of change of the thermometric parameter (generally denoted by Δ) per degree of temperature. The thermal sensitivity can be expressed as the absolute thermal sensitivity and the relative thermal sensitivity. The absolute thermal sensitivity (S_{abs}) is defined as the rate of change of the thermometric parameter (Δ) with the temperature and is expressed as:[109]

$$S_{abs} = \frac{\partial \Delta}{\partial T} \quad (1)$$

S_{abs} is expressed in units of K^{-1}. This parameter is strictly related to the experimental setup used and the sample characteristics; thus, its use is restricted to comparing only nanothermometers of the same nature and tested under the same conditions.

To compare the thermometric performance of different nanothermometers, independently of their nature or material employed, the relative thermal sensitivity (S_{rel}) can be used. S_{rel} expresses the maximum change in the thermometric parameter (Δ) for each temperature degree and it is defined as:[38,42,110]

$$S_{rel} = \frac{1}{\Delta}\left|\frac{\partial \Delta}{\partial T}\right| \times 100\% \quad (2)$$

S_{rel} is expressed in units of % change per degree of temperature change (% K^{-1}).

The temperature resolution (also defined as temperature sensitivity), δT, represents the smallest temperature change that can be resolved in a given measurement.[38]

Depending on the experimental detection setup used, the acquisition conditions applied, and the signal-to-noise ratio in the experiment, δT might change.[38] δT is measured in kelvin (K) and it is expressed as:[111]

$$\delta T = \frac{1}{S_{rel}}\frac{\delta \Delta}{\Delta} \quad (3)$$

where $\delta\Delta$ is the uncertainty in the determination of Δ that depends on the experimental detection setup used.

Another way of determining δT experimentally is by recording several consecutive emission spectra at a fixed temperature.[21,112] By using the calibration curve of the nanothermometer, the range of variability of the calculated temperature is determined. Results display a gaussian distribution with a mean value and a standard deviation value, corresponding to the average temperature and uncertainty (δT) of the measurement.[21,112]

The spatial resolution represents the minimum distance between points presenting a temperature difference higher than δT, when the temperature is measured at different spatial positions.[21] The spatial resolution (δx) is expressed as:[21]

$$\delta x = \frac{\delta T}{|\vec{\nabla} T|_{\max}} \quad (4)$$

where $|\vec{\nabla} T|_{\max}$ is the maximum temperature gradient in the system.

The temporal resolution of the measurement (δt) is defined as the minimum time interval between measurements presenting a temperature difference higher than δT and is expressed as:[48]

$$t = \frac{\delta T}{\left|\frac{dT}{dt}\right|_{\max}} \quad (5)$$

where $\left|\frac{dT}{dt}\right|_{\max}$ is the maximum temperature change per unit of time.

The repeatability indicates the ability of a nanothermometer to provide the same temperature measurement under the same identical conditions,[113] and is defined as:

$$R = 1 - \frac{\max|\Delta_c - \Delta_i|}{\Delta_c} \quad (6)$$

where Δ_c is the mean thermometric parameter and Δ_i is the value of each measurement of the thermometric parameter.

Finally, the reproducibility refers to the variations of the same measurement in different modified circumstances, including different measurement methods, different equipment in use, different observers, or measurements made over a period of time within the true level of the already measured data.[114]

From these performance parameters, the most reported ones are the thermal sensitivity and the temperature resolution, while the rest are scarcely used to determine the performance of a luminescent thermometer, despite their importance for the use of these thermometers in real applications.

1.3. Biological windows

A good use of luminescent thermometers in biological tissues requires knowledge about several parameters that influence the excitation of the nanothermometers by optical means, and also the detection of the emitted light by the materials. These parameters, including the emission characteristics, the optical path length through biological tissues and the volumetric energy distribution, are linked to the absorption and scattering properties of the biological samples.[115,116] The selection of these parameters should meet the overall goal of achieving a high penetration depth in real biological samples, allowing deeper thermal readings, and favoring the development of an efficient and reliable luminescent material for early detection and diagnosis of diseases. Applying NIR light instead of UV or VIS as the excitation source results in a more efficient and deeper penetration in biological tissues due to the reduced scattering and absorption of light with longer wavelengths.[105] Spectral regions where both tissue absorption and scattering are minimized are known as biological windows (hereafter BWs).[105] The main absorbers of light in biological tissues include water, hemoglobin, melanin and lipids, and their size, composition and morphology are responsible for the scattering of light.[117] Water absorbs in the NIR region at around 980 nm and it is nearly transparent in the visible region.[118] Hemoglobin (oxy-hemoglobin and deoxy-hemoglobin), from its side, is the component responsible for the absorption of visible light by blood. The highest absorbance of hemoglobin is in the visible region and it decreases above 600 nm.[119] The absorbance of melanin is inversely proportional to the increase of the wavelength from the visible to the NIR.[120] Regarding the absorbance of lipids *in vivo*, the data available in the literature are quite scarce; however as reported by Smith *et al.*, the absorption contribution of fat components in biological tissues is less important than that of water and blood.[105] Scatterers of light in biological tissues include cell nuclei, mitochondria, cell membranes and whole cells.[121] Light scattering decreases exponentially as the wavelength increases from the visible to the NIR.[122]

Within these BWs, four distinctive wavelength regions have been established (Fig. 4(a)):

- First biological window (I-BW) (650–950 nm)
- Second biological window (II-BW) (1000–1350 nm)
- Third biological window (III-BW) or short-wavelength infrared (SWIR) window (1400–2000 nm)
- Fourth biological window (IV-BW) (centered at 2200 nm)

The I-BW is limited at short wavelengths by the absorption of light by oxygenated blood and at long wavelengths by the absorption of water due to the second overtone of its stretching band, a combination of symmetric and antisymmetric stretching modes.[123] This biological window encounters limitations attributed to signal interference by biological tissue autofluorescence, which produces background noise, thus limiting the maximum tissue penetration to 1–2 cm.[120] This biological window is also known as the therapeutic window.[124]

The II-BW provides an improved signal-to-noise ratio by a factor over 100-fold by effectively filtering out autoflorescence from biological tissues.[116] The limits of the II-BW lie in the short wavelength by the second overtone of the stretching band of water and at longer wavelengths by the combination of the bending and stretching (symmetric and antisymmetric) modes of water also.[123]

The III-BW or SWIR, despite the limitation from the absorption bands of water (stretching and bending modes),[123] offers improved image contrast and higher penetration depths

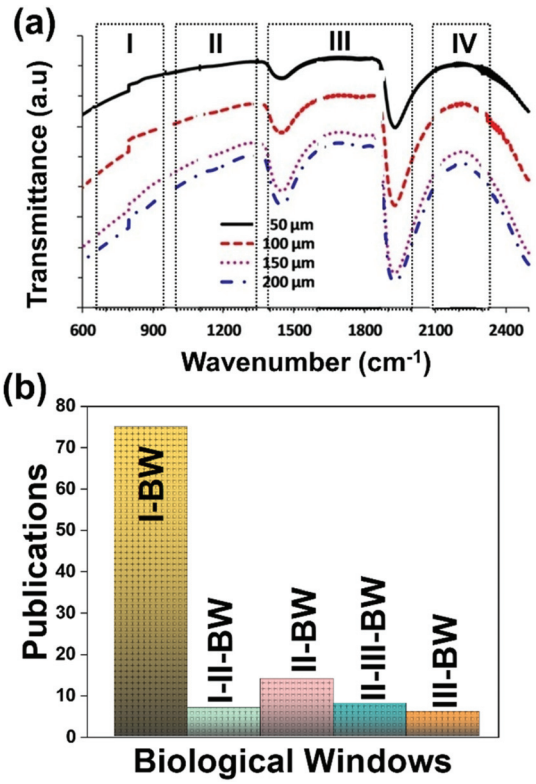

Fig. 4 (a) Transmittance of brain tissue in biological tissues. Adapted with permission from ref. 124, Copyright 2016, Wiley-VCH Verlag GmbH & Co. KGaA. (b) Number of publications of luminescence thermometry in every biological window, including also the thermometers whose performance is evaluated by emissions lying in two different BWs simultaneously.

compared with the other BWs due to the reduction of light scattering.

The IV-BW, centered at 2200 nm, is the least explored one due to the lack of sensitive detectors operating at these wavelengths.[125] The advent of new photodetectors (InSb in single or array photodiodes) and excitation laser sources (supercontinuum lasers operating in the range from 400 nm to 2500 nm) now makes the IV-BW a viable spectral domain.[126] The IV-BW shows similar values of light attenuation for skin and other soft tissues comparable with that of the II-BW, lower than the III-BW but better than the I-BW.[125]

Fig. 4(a) shows the variation of transmittance of rat brain tissue as a function of the thickness of the biological sample, covering all four BWs.[124] The maximum transmittance is located in the III-BW, regardless of the thickness. The transmittances in the II-BW and the IV-BW are close to each other and are much higher than the transmittance in the I-BW, indicating a better potential application for deep imaging.[124] Fig. 4(b) presents the number of publications implementing lanthanide-doped materials as luminescent thermometers operating in the different biological window regions. Apart from the main four BWs, the regions in which the luminescent nanothermometer performance has been evaluated with emissions lying partly in the I- and II-BWs (named as I–II-BW) and II- and III-BWs (named as II–III-BW) are also presented. The biological window with the highest number of publications is the I-BW, whereas the IV-BW represents, up to now, an unexplored region for luminescence thermometry. Recently, however, an increase has been observed in the number of publications regarding the II-BW and III-BW, mainly due to the benefits of better image contrast and higher penetration depths. The following sections have been structured according to the emission lines used for luminescent thermometry lying within any of these BWs, despite the fact that their excitation is provided in a spectral range lying in a different biological window.

Several reviews have been published about luminescence thermometry, and more specifically about the use of Ln^{3+}-doped materials devoted to this practice. Precisely, Brites *et al.*[48] published in 2019 a review on these materials, focused on strategies to enhance the thermometric performance and on cutting-edge applications of Ln^{3+}-doped materials mainly operating in the visible region. The present review unveils key guidelines to promote the application of Ln^{3+}-doped materials only within the BW spectral regions. We stress the mechanisms behind the generation of the emission lines within the BWs, something not analyzed in detail in the review mentioned above, and emphasize the role of the different excitation sources. We point out the different fitting models applied to evaluate the thermometric performance of Ln^{3+}-doped luminescent thermometers. We highlight strategies towards the development of highly sensitive nanothermometers by stating the important role of the morphology of the host in which these Ln^{3+} ions are embedded, such as the shape of core@shell or multishell structures. We define the differences between the thermometric performances based on the combination of emissions arising from the same Ln^{3+} ion, different Ln^{3+} ions or Ln^{3+} ions combined with transition metal ions or quantum dots. Potential applications of these nanothermometers in the biological/biomedical field and possible applications outside of these fields are presented. Finally, we share our opinions on future challenges for luminescence nanothermometry in the BW spectral regions, and possible routes to overcome these.

2. Lanthanide-doped luminescent nanothermometers operating in the I-BW

The I-BW is the most explored biological window in relation to the performance of lanthanide-doped luminescent thermometers up to now. The most encountered lanthanide active ions are Tm^{3+} and Nd^{3+}, mainly due to their emission bands in the 700–800 nm and 800–950 nm regions, respectively (Table 1). This section and the later ones will be arranged as follows: the lanthanide ion with the best thermometric performance (only the maximum value of S_{rel} and the associated

Table 1 Ln^{3+}-doped luminescent thermometers operating in the I-BW. The table includes activators (A) and sensitizers (S). The excitation (λ_{exc}) and emission (λ_{em}) wavelengths are indicated in nanometers (nm), together with the corresponding electronic transition with which the emissions are associated. ΔT stands for the temperature range where the temperature reading was investigated. The thermometric parameter (Δ) indicates the luminescent nanothermometry class used in each case: FIR for band-shape, I for intensity ratio, $\Delta\lambda$ for spectral shift, and Δ for bandwidth thermometry, respectively. VPR stands for valley-to-peak ratio. The maximum relative thermal sensitivity (S_{rel}) is given at the temperature at which this value was obtained. The minimum temperature resolution (δT) is given at the same temperature. We indicate with an asterisk S_{rel} or δT values calculated by us using the parameters published in the corresponding references. The double line separation between rows stands for different types (single or dual emitting centers) of lanthanide-doped nanothermometers, as discussed in the corresponding subsections

A	S	Host	λ_{exc} (nm)	λ_{em} (nm)	Transitions	ΔT (K)	Δ	S_{rel}/T (% K^{-1})/K	δT (K)	Ref.
Tm^{3+}	Tm^{3+}	YAP	1210	705, 800	$^3F_{2,3} \rightarrow {}^3H_6$, $^3H_4 \rightarrow {}^3H_6$	324–424	$FIR_{705/800}$	2.61/324	0.20*	127
Tm^{3+}	Tm^{3+}	$NaNbO_3$	1319	800	$^3H_4 \rightarrow {}^3H_6$	303–453	$FIR_{797/807}$	0.80/303	0.62*	128
Tm^{3+}	Yb^{3+}	Phosphate glass	980	658, 693	$^3F_2 \rightarrow {}^3H_6$, $^1G_4 \rightarrow {}^3H_5$	303–653	I_{693}/I_{658}	3.9/303	0.13*	130
Tm^{3+}	Yb^{3+}	$GdVO_4@SiO_2$	980	700, 800	$^3F_{2,3} \rightarrow {}^3H_6$, $^3H_4 \rightarrow {}^3H_6$	298–333	$FIR_{700/800}$	2/303	0.4	131
Tm^{3+}	Yb^{3+}	$LaPO_4$	975	700, 800	$^3F_{2,3} \rightarrow {}^3H_6$, $^3H_4 \rightarrow {}^3H_6$	293–773	$FIR_{700/800}$	3/293	0.16*	132
Tm^{3+}	Yb^{3+}	S-$LiNbO_3$	980	700, 800	$^3F_{2;3} \rightarrow {}^3H_6$, $^3H_4 \rightarrow {}^3H_6$	323–773	$FIR_{700/800}$	3/323	0.17*	133
Tm^{3+}	Yb^{3+}	$CaWO_4$	980	700, 800	$^3F_{2,3} \rightarrow {}^3H_6$, $^3H_4 \rightarrow {}^3H_6$	303–753	$FIR_{700/800}$	2.79/303	0.17*	134
Tm^{3+}	Yb^{3+}	$NaYF_4@NaYF_4@SiO_2$	980	697, 798	$^3F_{2,3} \rightarrow {}^3H_6$, $^3H_4 \rightarrow {}^3H_6$	298–623	$FIR_{697/798}$	2.58/298	0.18*	135
Tm^{3+}	Yb^{3+}	Bi_2TiO_7	980	700, 797	$^3F_{2,3} \rightarrow {}^3H_6$, $^3H_4 \rightarrow {}^3H_6$	300–505	$FIR_{797/700}$	2.41/300	0.20*	136
Tm^{3+}	Yb^{3+}	$LiY_9(SiO_4)_6O_2$	980	695, 789	$^3F_{2,3} \rightarrow {}^3H_6$, $^3H_4 \rightarrow {}^3H_6$	293–553	$FIR_{797/700}$	2.38/293	0.21*	137
Tm^{3+}	Yb^{3+}	$Ca_2Gd_8(SiO_4)_6O_2$	980	700, 790	$^3F_{2,3} \rightarrow {}^3H_6$, $^3H_4 \rightarrow {}^3H_6$	293–553	$FIR_{700/790}$	2.36/293	0.21*	138
Tm^{3+}	Yb^{3+}	YPO_4	975	700, 800	$^3F_{2,3} \rightarrow {}^3H_6$, $^3H_4 \rightarrow {}^3H_6$	293–773	$FIR_{700/800}$	2.33/293	0.21*	132
Tm^{3+}	Yb^{3+}	YAG	976	683, 782	$^3F_{2,3} \rightarrow {}^3H_6$, $^3H_4 \rightarrow {}^3H_6$	333–733	$FIR_{700/800}$	2.31/333	0.22*	139
Tm^{3+}	Yb^{3+}	$BiPO_4$	980	700, 804	$^3F_{2,3} \rightarrow {}^3H_6$, $^3H_4 \rightarrow {}^3H_6$	313–573	$FIR_{700/804}$	2.14*/425	0.23*	140
Tm^{3+}	Yb^{3+}	$Bi_2SiO_5@SiO_2$	977	650, 700	$^1G_4 \rightarrow {}^3F_4$, $^3F_3 \rightarrow {}^3H_6$	260–400	$FIR_{700/650}$	2.6/260	0.19*	141
Tm^{3+}	Yb^{3+}	$Bi_2SiO_5@SiO_2$	977	700, 800	$^3F_{2,3} \rightarrow {}^3H_6$, $^3H_4 \rightarrow {}^3H_6$	280–800	$FIR_{700/800}$	2.1/280	0.25	141
Tm^{3+}	Yb^{3+}	P-$LiNbO_3$	980	700, 800	$^3F_{2,3} \rightarrow {}^3H_6$, $^3H_4 \rightarrow {}^3H_6$	323–773	$FIR_{700/800}$	2.04/323	0.25*	133
Tm^{3+}	Yb^{3+}	Sr_2GdF_7	980	650, 700	$^1G_4 \rightarrow {}^3F_4$, $^3F_3 \rightarrow {}^3H_6$	293–563	I_{700}/I_{650}	1.97/353	0.25*	142
Tm^{3+}	Yb^{3+}	$KLuF_4$	980	690, 795	$^3F_{2,3} \rightarrow {}^3H_6$, $^3H_4 \rightarrow {}^3H_6$	303–503	$FIR_{690/795}$	1.36*/503	0.37*	143
Tm^{3+}	Yb^{3+}	YOF	980	801, 806	$^3H_4 \rightarrow {}^3H_6$	12–300	$\Delta\nu_{800.9}$	0.84/300	0.60*	144
Tm^{3+}	Yb^{3+}	PbF_2 oxyfluoride glass	976	700, 800	$^3F_{2,3} \rightarrow {}^3H_6$, $^3H_4 \rightarrow {}^3H_6$	288–498	I_{700}/I_{800}	0.78/448	0.64*	145
Tm^{3+}	Yb^{3+}	$NaYbF_4$	980	697, 803	$^3F_{2,3} \rightarrow {}^3H_6$, $^3H_4 \rightarrow {}^3H_6$	298–778	I_{697}/I_{803}	0.49*/458	1.02*	146
Tm^{3+}	Yb^{3+}	$NaGdTiO_4$	980	795, 798	$^3H_4 \rightarrow {}^3H_6$	100–300	$FIR_{795/798}$	0.36/100	1.38*	147
Tm^{3+}	Yb^{3+}	$NaGdTiO_4$	980	798, 807	$^3H_4 \rightarrow {}^3H_6$	100–300	$FIR_{807/798}$	0.22/100	2.27*	147
Tm^{3+}	Yb^{3+}	$NaGdTiO_4$	980	798, 812	$^3H_4 \rightarrow {}^3H_6$	100–300	$FIR_{812/798}$	0.21/100	2.38*	147
Tm^{3+}	Yb^{3+}	$NaYF_4@CaF_2$	980	802, 820	$^3H_4 \rightarrow {}^3H_6$	313–373	$FIR_{802/820}$	0.21/313	2.38*	148
Tm^{3+}, Ho^{3+}	Yb^{3+}	YPO_4	980	668 (Ho^{3+}), 699 (Tm^{3+})	$^5F_5 \rightarrow {}^5I_8$ (Ho^{3+}), $^3F_3 \rightarrow {}^3H_6$ (Tm^{3+})	303–563	I_{668}/I_{699}	2.85/563	0.18*	149
Tm^{3+}, Ho^{3+}	Tm^{3+}	$KLu(WO_4)_2$	808	696 (Tm^{3+}), 755 (Ho^{3+})	$^3F_{2,3} \rightarrow {}^3H_6$ (Tm^{3+}), $^5S_2$,$^5F_4 \rightarrow {}^5I_7$($Ho^{3+}$)	300–333	I_{696}/I_{755}	2.84/303	0.2	150
Tm^{3+}, Ho^{3+}	Yb^{3+}	$Gd_2(WO_4)_3$	980	655 (Ho^{3+}), 700 (Tm^{3+})	$^5F_5 \rightarrow {}^5I_8$ (Ho^{3+}), $^3F_{2,3} \rightarrow {}^3H_6$ (Tm^{3+})	295–595	I_{700}/I_{655}	1.42*/415	0.35*	151
Tm^{3+}, Er^{3+}	Yb^{3+}	$NaLuF_4$	980	660 (Er^{3+}), 695 (Tm^{3+})	$^3F_2 \rightarrow {}^3H_6$ (Tm^{3+}), $^4F_{9/2} \rightarrow {}^4I_{15/2}$ (Er^{3+})	300–600	I_{695}/I_{660}	1.94/300	0.26*	152
Tm^{3+}, Er^{3+}	Yb^{3+}	YF_3:ceramic	980	655 (Er^{3+}), 700 (Tm^{3+})	$^3F_{2,3} \rightarrow {}^3H_6$ (Tm^{3+}), $^4F_{9/2} \rightarrow {}^4I_{15/2}$ (Er^{3+})	298–563	I_{700}/I_{655}	1.89/393	0.27*	153
Tm^{3+}, Er^{3+}	Yb^{3+}	LuF_3	980	656 (Er^{3+}), 701 (Tm^{3+})	$^3F_2 \rightarrow {}^3H_6$ (Tm^{3+}), $^4F_{9/2} \rightarrow {}^4I_{15/2}$ (Er^{3+})	303–543	I_{656}/I_{701}	0.95/363	0.54*	154
Nd^{3+}	Nd^{3+}	YAG	590	730–770, 780–840	$^4F_{7/2} \rightarrow {}^4I_{9/2}$, $^4F_{3/2} \rightarrow {}^4I_{9/2}$	77–850	$FIR_{730-770/780-840}$	2.98/200	0.17*	155
Nd^{3+}	Nd^{3+}	La_2O_2S	532	818, 897	$^4F_{5/2} \rightarrow {}^4I_{9/2}$, $^4F_{3/2} \rightarrow {}^4I_{9/2}$	270–600	$FIR_{818/897}$	1.95/270	0.26*	156
Nd^{3+}	Nd^{3+}	YAP	532	820, 890	$^4F_{5/2} \rightarrow {}^4I_{9/2}$, $^4F_{3/2} \rightarrow {}^4I_{9/2}$	293–611	$FIR_{820/890}$	1.83/293	0.9	157
Nd^{3+}	Nd^{3+}	Gd_2O_3	580	820, 892	$^4F_{5/2} \rightarrow {}^4I_{9/2}$, $^4F_{3/2} \rightarrow {}^4I_{9/2}$	288–323	$FIR_{820/892}$	1.75/288	0.14	158
Nd^{3+}	Nd^{3+}	$LaPO_4$	690	804, 890	$^4F_{5/2} \rightarrow {}^4I_{9/2}$, $^4F_{3/2} \rightarrow {}^4I_{9/2}$	303–773	$FIR_{804/890}$	1.65/303	0.30*	159
Nd^{3+}	Nd^{3+}	Fluorotellurite glass	514	815, 885	$^4F_{5/2} \rightarrow {}^4I_{9/2}$, $^4F_{3/2} \rightarrow {}^4I_{9/2}$	298–600	$FIR_{815/885}$	1.55*/298	0.32*	160
Nd^{3+}	Nd^{3+}	SBN	532	820, 880	$^4F_{5/2} \rightarrow {}^4I_{9/2}$, $^4F_{3/2} \rightarrow {}^4I_{9/2}$	300–700	$FIR_{820/880}$	1.52*/300	0.33*	161

Table 1 *(Contd.)*

A	S	Host	λ_{exc} (nm)	λ_{em} (nm)	Transitions	ΔT (K)	Δ	S_{rel}/T (% K^{-1})/K	δT (K)	Ref.
Nd^{3+}	Nd^{3+}	YAG	590	780–840, 870–920	$^4F_{5/2} \rightarrow {}^4I_{9/2}$, $^4F_{3/2} \rightarrow {}^4I_{9/2}$	77–850	$FIR_{780-840/870-920}$	1.02/200	0.49*	155
Nd^{3+}	Nd^{3+}	$LiLuF_4$	808	862, 866	$^4F_{3/2} \rightarrow {}^4I_{9/2}$	77–575	I_{862}/I_{866}	0.62/77	0.6	162
Nd^{3+}	Nd^{3+}	SrF_2	573	800–950	$^4F_{3/2} \rightarrow {}^4I_{9/2}$	293–328	$FIR_{800-950(2)/(1)}$	0.61/293	2.1	163
Nd^{3+}	Nd^{3+}	$LiLuF_4$@$LiLuF_4$	793	883, 887	$^4F_{3/2} \rightarrow {}^4I_{9/2}$	293–318	I_{887}/I_{883}	0.58/293	3.4	164
Nd^{3+}	Nd^{3+}	$LiLaP_4O_{12}$	808	850–900	$^4F_{3/2} \rightarrow {}^4I_{9/2}$	83–600	$\Delta\lambda_{850-900}$	0.47/323	1.05*	165
Nd^{3+}	Nd^{3+}	$RbLaP_4O_{12}$	808	850–900	$^4F_{3/2} \rightarrow {}^4I_{9/2}$	83–600	$\Delta\lambda_{850-900}$	0.47/323	1.05*	165
Nd^{3+}	Nd^{3+}	$KLaP_4O_{12}$	808	850–900	$^4F_{3/2} \rightarrow {}^4I_{9/2}$	83–600	$\Delta\lambda_{850-900}$	0.47/323	1.05*	165
Nd^{3+}	Nd^{3+}	$NaLaP_4O_{12}$	808	850–900	$^4F_{3/2} \rightarrow {}^4I_{9/2}$	83–600	$\Delta\lambda_{850-900}$	0.42/323	1.2*	165
Nd^{3+}	Nd^{3+}	$LiLaP_4O_{12}$	808	850–900	$^4F_{3/2} \rightarrow {}^4I_{9/2}$	83–600	$\Delta\nu_{850-900}$	0.32/323	1.5*	165
Nd^{3+}	Nd^{3+}	Y_2O_3	808	870, 920	$^4F_{3/2} \rightarrow {}^4I_{9/2}$	298–333	I_{870}/I_{820}	0.31/298	1	166
Nd^{3+}	Nd^{3+}	$RbLaP_4O_{12}$	808	850–900	$^4F_{3/2} \rightarrow {}^4I_{9/2}$	83–600	$\Delta\nu_{850-900}$	0.28/323	1.1*	165
Nd^{3+}	Nd^{3+}	$YNbO_4$	752	880, 890	$^4F_{3/2} \rightarrow {}^4I_{9/2}$	303–473	I_{880}/I_{890}	0.28/303	1.1	167
Nd^{3+}	Nd^{3+}	LaF_3	808	865, 885	$^4F_{3/2} \rightarrow {}^4I_{9/2}$	283–333	I_{865}/I_{885}	0.26/283	1.95*	168
Nd^{3+}	Nd^{3+}	$NaLaP_4O_{12}$	808	850–900	$^4F_{3/2} \rightarrow {}^4I_{9/2}$	83–600	$\Delta\nu_{850-900}$	0.24/323	2.1*	165
Nd^{3+}	Nd^{3+}	$KLaP_4O_{12}$	808	850–900	$^4F_{3/2} \rightarrow {}^4I_{9/2}$	83–600	$\Delta\nu_{850-900}$	0.20/323	2.5*	165
Nd^{3+}	Nd^{3+}	YVO_4	808	879, 887	$^4F_{3/2} \rightarrow {}^4I_{9/2}$	298–333	I_{879}/I_{887}	0.19/298	2.6*	169
Nd^{3+}	Nd^{3+}	$Gd_3Sc_2Al_3O_{12}$	806	936, 946	$^4F_{3/2} \rightarrow {}^4I_{9/2}$	293–323	$FIR_{936/946}$	0.21/293	2.38*	170
Nd^{3+}	Nd^{3+}	YAG	808	938, 945	$^4F_{3/2} \rightarrow {}^4I_{9/2}$	283–343	$FIR_{938/945}$	0.15/283	0.3	171
Nd^{3+}	Nd^{3+}	$BiVO_4$	750	872, 902	$^4F_{3/2} \rightarrow {}^4I_{9/2}$	310–523	$FIR_{872/902}$	0.14/310	3	172
Nd^{3+}	Nd^{3+}	$NaYF_4$	830	863, 870	$^4F_{3/2} \rightarrow {}^4I_{9/2}$	273–423	$FIR_{863/870}$	0.12/273	0.1	173
Nd^{3+}	Nd^{3+}	$KGd(WO_4)_2$	808	883, 895	$^4F_{3/2} \rightarrow {}^4I_{9/2}$	298–333	$FIR_{883/895}$	0.12/298	0.43	174
Nd^{3+}	Nd^{3+}	$NaNdF_4$@$NaYF_4$@$NaYF_4$:Nd	808	857, 863	$^4F_{3/2} \rightarrow {}^4I_{9/2}$	293–333	$FIR_{857/863}$	0.11/293	4.5*	175
Nd^{3+}	Nd^{3+}	$RbLaP_4O_{12}$	808	850–900	$^4F_{3/2} \rightarrow {}^4I_{9/2}$	83–600	$FIR_{880(2)/(1)}$	0.108/323	4.6*	165
Nd^{3+}	Nd^{3+}	$NaLaP_4O_{12}$	808	850–900	$^4F_{3/2} \rightarrow {}^4I_{9/2}$	83–600	$FIR_{880(2)/(1)}$	0.104/323	4.8*	165
Nd^{3+}	Nd^{3+}	$KLaP_4O_{12}$	808	850–900	$^4F_{3/2} \rightarrow {}^4I_{9/2}$	83–600	$FIR_{880(2)/(1)}$	0.097/323	5.1*	165
Nd^{3+}	Yb^{3+}	Oxyfluoride glass	980	750, 863	$^4F_{7/2} \rightarrow {}^4I_{9/2}$ $^4F_{3/2} \rightarrow {}^4I_{9/2}$	303–623	$FIR_{750/863}$	3.27/303	0.15*	176
Nd^{3+}	Yb^{3+}	$SrWO_4$	980	750, 863	,$^4F_{7/2} \rightarrow {}^4I_{9/2}$, $^4F_{3/2} \rightarrow {}^4I_{9/2}$	313–453	$FIR_{750/863}$	3.1/313	0.16*	177
Nd^{3+}	Yb^{3+}	$CaWO_4$	980	755, 872	$^4F_{7/2} \rightarrow {}^4I_{9/2}$, $^4F_{3/2} \rightarrow {}^4I_{9/2}$	303–873	$FIR_{750/863}$	3/303	0.16*	178
Nd^{3+}	Yb^{3+}	$Al_4B_2O_9$	977.7	800, 920	$^4F_{5/2} \rightarrow {}^4I_{9/2}$ (Nd^{3+}), $^2F_{5/2} \rightarrow {}^2F_{7/2}$ (Yb^{3+})	298–333	$FIR_{800/920}$	2.6/298	0.19*	179
Nd^{3+}	Yb^{3+}	$NaYF_4$	980	750, 863	$^4F_{7/2} \rightarrow {}^4I_{9/2}$, $^4F_{3/2} \rightarrow {}^4I_{9/2}$	293–333	$FIR_{750/863}$	2.4/293	0.20*	180
Nd^{3+}	Yb^{3+}	Oxyfluoride glass	980	750, 803	$^4F_{7/2} \rightarrow {}^4I_{9/2}$, $^4F_{5/2} \rightarrow {}^4I_{9/2}$	303–623	$FIR_{750/863}$	2.05/303	0.24*	176
Nd^{3+}	Yb^{3+}	Oxyfluoride glass	980	803, 863	$^4F_{5/2} \rightarrow {}^4I_{9/2}$, $^4F_{3/2} \rightarrow {}^4I_{9/2}$	303–623	$FIR_{750/863}$	1.95/303	0.25*	176
Nd^{3+}	Yb^{3+}	La_2O_3	980	750, 803	$^4F_{7/2} \rightarrow {}^4I_{9/2}$, $^4F_{3/2} \rightarrow {}^4I_{9/2}$	293–1233	$FIR_{750/803}$	1.6/293	0.1	181
Nd^{3+}	Yb^{3+}	$Al_4B_2O_9$	977.7	864, 920	$^4F_{5/2} \rightarrow {}^4I_{9/2}$ (Nd^{3+}), $^2F_{5/2} \rightarrow {}^2F_{7/2}$ (Yb^{3+})	299–333	$FIR_{800/920}$	1.38/299	0.36*	179
Nd^{3+}, Eu^{3+}	Nd^{3+}, Eu^{3+}	Ba_2LaF_7	578.3	699 (Eu^{3+}), 800 (Nd^{3+})	$^5D_0 \rightarrow {}^7F_4$ (Eu^{3+}), $^4F_{3/2} \rightarrow {}^4I_{9/2}$ (Nd^{3+})	290–740	I_{699}/I_{800}	2.2/290	0.22*	182
Nd^{3+}, Eu^{3+}	Nd^{3+}, Eu^{3+}	YVO_4	590	696 (Eu^{3+}), 812 (Nd^{3+})	$^5D_0 \rightarrow {}^7F_4$ (Eu^{3+}), $^4F_{3/2} \rightarrow {}^4I_{9/2}$ (Nd^{3+})	299–466	I_{696}/I_{812}	0.79/299	1.4	183
Nd^{3+}, Ti^{4+}	Nd^{3+}, Ti^{4+}	YAG	260	668 (Ti^{4+}), 870 (Nd^{3+})	$^2T_2 \rightarrow O^{2-}$ (Ti^{4+}), $^4F_{3/2} \rightarrow {}^4I_{9/2}$ (Nd^{3+})	123–773	I_{668}/I_{870}	3.70/473	0.13*	184
Nd^{3+}, Cr^{3+}	Nd^{3+}, Cr^{3+}	YAG	590	690 (Cr^{3+}), 890 (Nd^{3+})	$^4T_1 \rightarrow {}^4A_2$ (Cr^{3+}), $^4F_{3/2} \rightarrow {}^4I_{9/2}$ (Nd^{3+})	77–850	I_{690}/I_{890}	3.49/200	0.14*	155
Nd^{3+}, Mn^{4+}	Nd^{3+}, Mn^{4+}	YAG	355	670 (Mn^{4+}), 880 (Nd^{3+})	$^2E \rightarrow {}^4A_2$ (Mn^{4+}), $^4F_{3/2} \rightarrow {}^4I_{9/2}$ (Nd^{3+})	123–823	I_{670}/I_{880}	0.60/475	0.83*	185
Eu^{3+}	Eu^{3+}	Y_2O_3	590	690–715	$^5D_0 \rightarrow {}^7F_4$ ($^7F_1$,$^7F_0$)	180–280	$FIR_{690-714/690-714}$	1.7/180	0.29*	186
Eu^{3+}	Eu^{3+}	Y_2O_3	611	690–715	$^5D_0 \rightarrow {}^7F_4$ ($^7F_2$,$^7F_0$)	283–333	$FIR_{690-714/690-714}$	1.55/283	0.29*	186
Er^{3+}	Er^{3+}	SBN	532	800, 850	$^2H_{11/2} \rightarrow {}^4I_{13/2}$, $^4S_{3/2} \rightarrow {}^4I_{13/2}$,	300–700	$FIR_{800/850}$	1.39*/300	0.36*	161
Er^{3+}	Er^{3+}	$NaErF_4$@$NaGdF_4$	1530	654, 806	$^4F_{9/2} \rightarrow {}^4I_{15/2}$, $^4I_{9/2} \rightarrow {}^4I_{15/2}$	303–593	I_{806}/I_{654}	0.54/303	0.9*	187

Table 1 *(Contd.)*

A	S	Host	λ_{exc} (nm)	λ_{em} (nm)	Transitions	ΔT (K)	Δ	S_{rel}/T (% K^{-1})/K	δT (K)	Ref.
Er^{3+}	Er^{3+}	$NaErF_4$@Yb:$NaYF_4$@Nd:$NaYbF_4$	800	652, 670	$^4F_{9/2} \rightarrow {}^4I_{15/2}$	305–425	$FIR_{652/670}$	0.22/305	2.2*	188
Er^{3+}	Er^{3+}	Y_2O_3	800	654, 660	$^4F_{9/2} \rightarrow {}^4I_{15/2}$	200–1300	$FIR_{654/660}$	0.15/300	3.3*	189
Er^{3+}, Mn^{4+}	Er^{3+}, Mn^{4+}	YAP	980	660 (Er^{3+}), 714 (Mn^{3+})	$^4I_{9/2} \rightarrow {}^4I_{15/2}$ (Er^{3+}), $^2E \rightarrow {}^4A_2$ (Mn^{4+})	300–550	I_{714}/I_{660}	1.95/530	0.25*	190
Er^{3+}, Ho^{3+}	Yb^{3+}	$NaLuF_4$	975	817 (Er^{3+}), 887 (Ho^{3+})	$^4I_{9/2} \rightarrow {}^4I_{15/2}$ (Er^{3+}), $^5I_6 \rightarrow {}^5I_8$ (Ho^{3+})	293–568	I_{887}/I_{817}	1.73/293	0.29*	191
Er^{3+}	Yb^{3+}	YF_3	980	793, 840	$^2H_{11/2} \rightarrow {}^4I_{15/2}$, $^4S_{3/2} \rightarrow {}^4I_{15/2}$	293–473	$FIR_{793/840}$	0.98/293	0.51*	192
Er^{3+}	Yb^{3+}	ZrO_2	980	660, 682	$^4F_{9/2} \rightarrow {}^4I_{15/2}$	293–573	$VPR_{660/682}$	0.75/293	0.66*	193
Ho^{3+}, Mn^{4+}	Yb^{3+}	YAP	980	660 (Ho^{3+}), 714 (Mn^{3+})	$^5F_5 \rightarrow {}^5I_8$ (Ho^{3+}), $^2E \rightarrow {}^4A_2$ (Mn^{4+})	300–550	I_{714}/I_{660}	1.17/450	0.42*	190
Ho^{3+}	Yb^{3+}	$KLu(WO_4)_2$	980	650, 660,	$^5F_5 \rightarrow {}^5I_8$,	297–673	$FIR_{650/660}$	0.38/297	1	194
Ho^{3+}	Yb^{3+}	$Ba_2In_2O_5$	980	653, 661,	$^5F_5 \rightarrow {}^5I_8$	303–573	$FIR_{653/661}$	0.19*/303	2.5	195

minimum value of δT will be given) will appear first. After this, single- or dual-doped materials and the excitation wavelengths associated with the luminescent thermometers will be presented, providing an overview of how these parameters influence the performance of that specific lanthanide active ion, in order to underline strategies for boosting thermometric performance.

2.1. Thulium-doped luminescent thermometers operating in the I-BW

Thulium (Tm^{3+}) ion exhibits an electronic configuration $1s^2$ $2s^2$ $2p^6$ $3s^2$ $3p^6$ $3d^{10}$ $4s^2$ $4p^6$ $4d^{10}$ $5s^2$ $5p^6$ $4f^{12}$, and up to now, represents one of the most investigated active ions for luminescent nanothermometry in the I-BW due to, among others aspects, its NIR-to-NIR upconversion optical properties. Different Tm^{3+}-doped luminescent nanothermometers have been developed including single Tm^{3+}-doped materials, those using Tm^{3+} as an activator and Yb^{3+} as a sensitizer, and those that use Tm^{3+} together with another Ln^{3+} ion as activators in the presence or absence of Yb^{3+} as a sensitizer.

2.1.1. Single Tm^{3+}-doped luminescent thermometers operating in the I-BW. Single Tm^{3+}-doped luminescent nanothermometers operating in the I-BW without the presence of Yb^{3+} as a sensitizer are scarce. In fact, only two examples can be found in the literature, with orthorhombic yttrium orthoaluminate perovskite ($YAlO_3$, known as YAP)[127] and sodium niobate ($NaNbO_3$)[128] as hosts.

Tm^{3+}:YAP nanothermometers (with a grain size of 35 nm) have been developed based on the temperature dependence of the emission lines located at 705 nm and 800 nm, arising from the $^3F_{2,3}$ and $^3H_4$ TCLs decaying to the $^3H_6$ ground state, after excitation at 1210 nm.[127] These upconversion emissions can be generated either by sequential absorption of two excitation photons by a single Tm^{3+} ion through excited state absorption (ESA) or by the simultaneous absorption of two photons by two nearby Tm^{3+} ions *via* energy transfer upconversion (ETU) processes.[127,129] The process of upconversion refers to a nonlinear optical phenomenon known as anti-Stokes emission in which the sequential absorption of two or more low-energy photons leads to a high-energy luminescence emission.[129] From these two processes, the $^3F_{2,3}$ excited state is populated. From this state, a radiative decay to the ground state will generate the emission line at 705 nm. A non-radiative relaxation from the $^3F_{2,3}$ level to the $^3H_4$ level, followed by a radiative decay to the ground state, generates the second emission line at 800 nm (Fig. 5(a)).[127,129]

For the evaluation of the thermometric performance of the Tm^{3+}:YAP nanothermometers, the FIR between the emission lines at 705 nm and 800 nm was used in the temperature range from 324 K–424 K. The FIR is defined using the emission intensities of the of $|2> \rightarrow |0>$ ($I_{02} \equiv I_2$) and $|1> \rightarrow |0>$ ($I_{01} \equiv I_1$) transitions, where $|0>$, $|1>$, $|2>$ denote the ground state and TCLs 1 and 2,[42,196] respectively, as:

$$\mathrm{FIR} = \frac{I_2}{I_1} = \frac{A_{02} h\nu_{02} N_2}{A_{01} h\nu_{01} N_1} \quad (7)$$

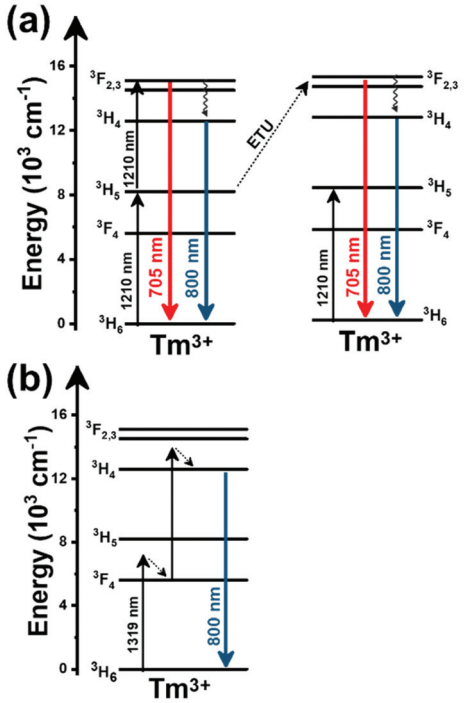

Fig. 5 Mechanisms of generation of the emission lines for single active Tm^{3+}-doped luminescent thermometers: (a) YAP after excitation at 1210 nm and (b) $NaNbO_3$ after excitation at 1319 nm. Please note that despite the fact that other emission lines can be produced, for sake of simplicity, only the emission lines involved in the luminescence thermometer development are considered.

where N_2 and N_1 are the populations of the |2> and |1> levels, ν_{02} and ν_{01} are the frequencies of the |2> → |0> and |1> → |0> transitions, and A_{02} and A_{01} are the total spontaneous emission rates from levels |2> and |1> to level |0>. Since the energy levels 1 and 2 are in thermal equilibrium, the electronic populations can be correlated by the following equation:

$$N_2 = \frac{g_2}{g_1} N_1 \exp\left(-\frac{\Delta E}{k_B T}\right) \quad (8)$$

where g_2 and g_1 are the degeneracies of the two levels, and ΔE is the energy gap between the barycenters of the |2> → |0> and |1> → |0> emission bands.[21,42,196]

Thus, the expression for FIR can be rewritten as:

$$\mathrm{FIR} = \frac{I_2}{I_1} = \frac{g_2 A_{02} h\nu_{02}}{g_1 A_{01} h\nu_{01}} \exp\left(-\frac{\Delta E}{k_B T}\right) = B \exp\left(-\frac{\Delta E}{k_B T}\right) \quad (9)$$

where $B = \frac{g_2 A_{02} h\nu_{02}}{g_1 A_{01} h\nu_{01}}$. By applying the expression for FIR to eqn (2) and (3), the corresponding expressions for S_{rel} and δT can be obtained as follows:[21,42,196]

$$S_{rel} = \left|\frac{\Delta E}{k_B T^2}\right| \times 100\% \quad (10)$$

$$\delta T = \frac{k_B T^2}{\Delta E} \frac{\delta \mathrm{FIR}}{\mathrm{FIR}} \quad (11)$$

Thus, considering the |2> → |0> as the electronic transition generating the emission line at 705 nm and the |1> → |0> as the electronic transition generating the emission line at 800 nm, the maximum S_{rel} of the Tm^{3+}:YAP nanothermometer is 2.64% K^{-1} at 324 K, whereas the δT was not reported by the authors.[127] However, knowing the reported value of ΔE = 1926 cm^{-1},[127] and applying an experimental setup error, which is the most commonly used in the literature,[21] δT can be calculated according to eqn (11), with a minimum value of 0.20 K at 324 K that increases to 0.32 K at 424 K.

Tm^{3+}:$NaNbO_3$ luminescent thermometer, from its side, was based on the change of the FIR of the emission peaks arising from different Stark sub-levels of the $^3H_4 \rightarrow {}^3H_6$ transition with a broad emission band located at ~800 nm, using in particular the emission lines located at 797 nm and 807 nm, after excitation at 1319 nm, in the temperature range 303–453 K.[128] The generation of the 800 nm emission line is assigned to a multiphonon-assisted excitation from the ground state $^3H_6$ to the $^3H_5$ excited level, a rapid relaxation to the $^3F_4$ level, followed by an excited-state absorption to the $^3H_4$ level (Fig. 5(b)).

Instead of using the expression indicated above for FIR, to calculate the thermometric parameter in this case the authors propose to use the following equation:[128]

$$R = A + B \times T \quad (12)$$

where R is the thermometric parameter used in this case (I_{707}/I_{807}), and A and B are parameters determined by the fitting of the experimental data. The authors preferred to use a linear function for this parameter, according to the trend followed by the experimental points obtained in the calibration of the thermometer, without taking into account that the different Stark sub-levels of a particular transition are, of course, under thermal equilibrium, and that the Boltzmann distribution proposed by the FIR model would be more convenient in this case. As a consequence, S_{rel}, with a maximum value of 0.80% K^{-1} at 303 K, had to be calculated using again a different equation:[128]

$$S_{rel} = \frac{B}{A + B \times T} \times 100\% \quad (13)$$

This value is higher than the one that should be obtained when applying strictly the FIR model according to eqn (9) (0.25% K^{-1}), and according to that, the δT calculated according to eqn (11) (0.62 K if the thermal sensitivity given by the authors is used, and 2 K if the thermal sensitivity according to the FIR model is used) is clearly overestimated.

Curiously, the two examples included here are based on upconversion mechanisms with excitation in the II-BW, despite the fact that the exploited emissions are in the I-BW, ensuring that both excitation and emission have a good penetration in the biological tissues. Upconversion nanomaterials offer the possibility of a relatively high thermal sensing in combination with high penetration depths and optical tunability.[130]

In fact, Pereira *et al.*[128] could demonstrate that the penetration of light by exciting at 1319 nm was twice the one that could be obtained when exciting at 800 nm. Nevertheless, the excitation wavelength they used (1319 nm) induced a local heating in the environment where the Tm^{3+}:$NaNbO_3$ nanoparticles were used, of up to 8 K for a pump power of 350 mW, due to the fact that this wavelength is not resonant with any of the electronic levels of Tm^{3+}. So part of the energy of the excitation source was lost in the form of heat, which the nanoparticles dispersed in the surrounding medium.[128]

The only conclusion that can be extracted from these two examples is that to maximize S_{rel}, and consequently minimize the thermal resolution, the best strategy would be to maximize the separation between the emission lines used in the thermometer, but maintaining it below to 2000 cm^{-1} to maintain them inside the defined range of TCLs.[42]

2.1.2. Tm^{3+},Yb^{3+}-codoped luminescent thermometers operating in the I-BW. Lanthanide nanothermometers codoped with Tm^{3+} acting as an activator and Yb^{3+} acting as a sensitizer is, by far, the most explored model for luminescent thermometers operating in the I-BW. Probably this great interest is due to their NIR-to-NIR upconversion, more efficient than that obtained in single Tm^{3+}-doped thermometers.[148] This is a consequence of the bigger absorption cross-section of Yb^{3+} at the pumping wavelength of 980 nm,[196] the lower costs of NIR excitation sources emitting this wavelength,[197] and the generation of emission lines lying in the I-BW. However, it has to be mentioned here the strong heating effect that this pumping wavelength has in biological tissues, due to the efficient absorption of this wavelength by water.[122] This is why several authors considered that this approach should be avoided when performing luminescence thermometry for biomedical applications due to its non-discriminating effect with respect to the heating of biological tissues.

Another characteristic of the Tm^{3+},Yb^{3+}-codoped luminescent thermometers operating in the I-BW is that most of them use the same emission lines to build the luminescent thermometer: the emission at around 700 nm, arising from the $^3F_{2,3} \rightarrow {}^3H_6$ transition, and the emission produced at around 800 nm, arising from the $^3H_4 \rightarrow {}^3H_6$ transition, in both cases of Tm^{3+}, as was shown in the first example of the previous subsection. However, in this case, due to the presence of Yb^{3+}, the excitation and emission mechanism is different. Fig. 6(a) shows the excitation mechanism used to generate these emission lines after excitation at 980 nm. The 980 nm radiation is absorbed by Yb^{3+}, promoting its electrons from the $^2F_{7/2}$ ground state to the $^2F_{5/2}$ excited state. From this excited state of Yb^{3+}, *via* energy transfer (hereafter ET) processes, the excited states of Tm^{3+} are populated. Hence, three ET processes populate the $^1G_4$, $^2F_{2,3}$ and $^3H_5$ levels of Tm^{3+}. From the $^1G_4$ level, electrons relax non-radiatively to the $^3F_{2,3}$ level, from which they fall back to the $^3H_6$ ground state level, generating the 700 nm emission. From the $^3F_{2,3}$ level, a non-radiative relaxation process to the $^3H_4$ level, followed by a radiative decay to the ground state, gives rise to the 800 nm emission.[131] It should be emphasized here that other mechanisms and emission lines might be involved in this process, but we are presenting only the emission lines used to determine the thermometric performance.

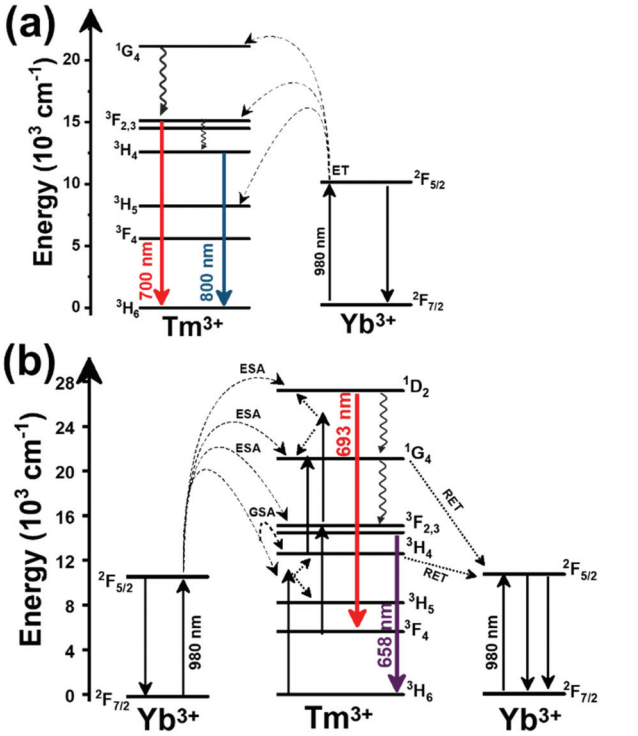

Fig. 6 Mechanisms of generation of the emission lines for: (a) Tm^{3+}, Yb^{3+}:$GdVO_4$@SiO_2 core@shell nanoparticles (as an illustrative example) after excitation at 980 nm, and (b) Tm^{3+},Yb^{3+}-doped phosphate glass material after excitation at 980 nm.

In all these cases, since the $^3F_{2,3}$ and $^3H_4$ energy levels can be considered to be thermally coupled, the FIR model was used as the thermometric parameter. However, despite the big majority of the papers analyzed defining this FIR as the ratio between the intensity of the emission at 800 nm divided by the intensity of the emission at 700 nm, following the recommendation of Wade *et al.* in their seminal publication,[42] we encountered two recent publications (ref. 136 and 137) in which they defined it in the inverse way. Nevertheless, since eqn (10) does not take into account the way in which FIR has been defined, they could be compared with the rest of the luminescent thermometers analyzed in this section. If we analyze the maximum S_{rel} obtained for these kinds of luminescent thermometer, it is encountered in the range between 2–3% K^{-1}, as a result of having a ΔE between the Tm^{3+} $^3F_{2,3}$ and the $^3H_4$ energy levels of around 1785 cm^{-1}. This energy difference can change slightly from host to host, due to their different crystal fields, and this would be reflected in the different S_{rel} values reported by the authors and that are listed in Table 1. This would provide a δT of ~0.2 K, approaching the desired limit of 0.1 K for biomedical purposes.[13] The temperatures at which these values are obtained are in all cases around room temperature, and all of them became worse as the temperature increased (Fig. 7).

In some cases the FIR model was modified, compared with the equation proposed by Wade *et al.*,[42] to account for the sig-

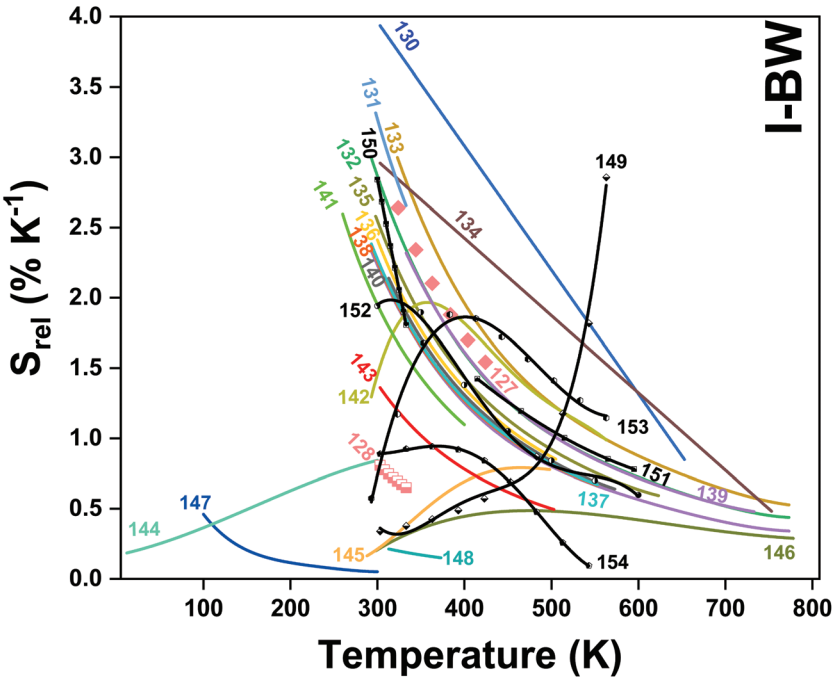

Fig. 7 Temperature dependence of S_{rel} of Tm^{3+}-doped luminescent thermometers, operating in the I-BW. In symbols only, in solid lines and in solid lines with symbols, single Tm^{3+}, Tm^{3+}/Yb^{3+} and Tm^{3+}/Ln^{3+} based thermometers, respectively. The numbers represent the corresponding references for each Tm^{3+}-based thermometer.

nificant overlapping between the two emission bands used in the luminescent thermometer, adding an additional summand to the equation as:

$$\mathrm{FIR} = B\exp\left(-\frac{\Delta E}{k_B T}\right) + D \quad (14)$$

where D is a fitting parameter. Then if S_{rel} is calculated according to eqn (10), the value is not correct. In fact, it is underestimated, since according to eqn (2), the right way to determine S_{rel} should be:

$$S_{rel} = \frac{\mathrm{FIR} - D}{\mathrm{FIR}}\left|\frac{\Delta E}{k_B T^2}\right| \times 100\% \quad (15)$$

It is important also to note here the large variety of materials used to host Tm^{3+} and Yb^{3+} for this kind of thermometer, including vanadates,[131] phosphates,[130,132,140] niobates,[198] tungstates,[134] fluorides,[135,142,143,146,148] oxyfluorides,[144,145] titanates,[136,147] silicates,[137,138,141] and aluminates.[139]

It is worth mentioning here that in some cases the inner active cores have been coated with an inactive shell. This strategy has been used in the case of $GdVO_4$@SiO_2,[131] $NaYF_4$@$NaYF_4$@SiO_2,[135] Bi_2SiO_5@SiO_2,[141] and $NaYF_4$@CaF_2 nanoparticles,[148] using an inert layer constituted by amorphous silica (SiO_2), or cubic CaF_2. The aim of coating the active core with this inert layer was to prevent the thermal degradation of the active core from potential oxidation, and at the same time prevent non-radiative relaxation processes of the active ions encountered on the surface of the nanoparticles by their interactions with the surface-bound ligands in the case of colloidal dispersions.[135] Also, in the case of $NaYF_4$@$NaYF_4$@SiO_2, an inert $NaYF_4$ interlayer was used for further protection of the radiative properties of the active ions.[135] Thus, despite the fact that it seems evident that these core@shell structures help to increase the quantum yield of the luminescent nanoparticles, no conclusion can be extracted about their thermometric performance, since none of the papers published up to now for Tm^{3+},Yb^{3+}-codoped systems operating in the I-BW reported a comparison between the same material coated and not coated with the inert layer. Also, by analyzing the data provided in Table 1 for the phosphates, it seems that when the phosphate material is based on a metal of the lanthanide series (Y or La), the S_{rel} achieved is higher than that obtained for a material based on a post-transition metal. In fact, S_{rel} values obtained for Tm^{3+},Yb^{3+}:$LaPO_4$ (S_{rel} = 3% K^{-1}) and in Tm^{3+},Yb^{3+}:YPO_4 (S_{rel} = 2.33% K^{-1}) nanoparticles[132] are slightly higher than the ones obtained for Tm^{3+},Yb^{3+}:$BiPO_4$ (S_{rel} = 2.14% K^{-1}).[140] However, other factors, such as the structure, can also affect the thermometric performance of these luminescent thermometers, since $LaPO_4$ crystallizes in the monoclinic system, YPO_4 does so in the tetragonal system, and $BiPO_4$ is a hexagonal compound.

From another side, Xing *et al.*[133] studied the effect of using a single crystal or a polycrystal on the temperature-sensing performance of Tm^{3+},Yb^{3+}:$LiNbO_3$ (labelled as S-$LiNbO_3$ and P-$LiNbO_3$, respectively, in Table 1). A higher S_{rel} was obtained for the single crystal (~3% K^{-1} *vs.* ~2% K^{-1} in the polycrystal). The authors assigned these differences in S_{rel} to the effect of

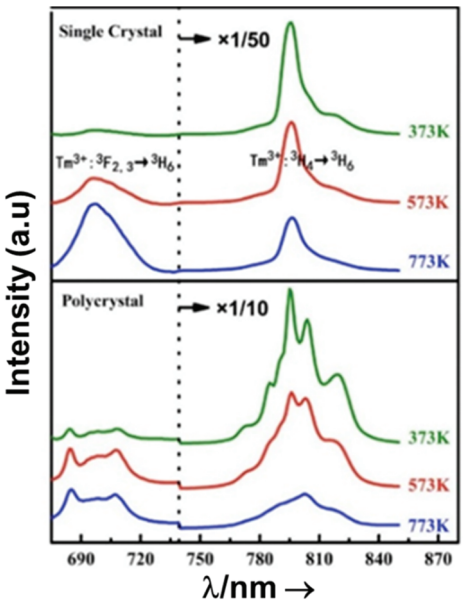

Fig. 8 Emission spectra of Tm^{3+}/Yb^{3+}-codoped $LiNbO_3$ polycrystal and single crystal at different temperatures under 980 nm excitation (1/10 and 1/50 represent the factor of division applied above the marked wavelength to visualize clear the different emission bands). Reprinted with permission from ref. 133. Copyright 2015, Elsevier.

the crystallinity of the material based on the degree of splitting of the upconversion emission spectra. In fact, in Fig. 8 it can be seen that the spectrum recorded for the single crystal is narrower than the spectrum recorded for the polycrystalline material, and that the spectrum of the polycrystalline material has a richer peak structure. However, the intensity of the spectrum for the single crystal is much higher than that of the polycrystalline material (Fig. 8), which could generate also a saturation in the intensity of the spectrum that might affect also the thermometric performance of the luminescent thermometer. In fact, δT and, as a consequence, S_{rel} are greatly affected by the signal-to-noise $\left(\frac{dI}{I}\right)$ ratio of the emission spectra from which temperature is estimated.[21,199] At lower intensity signals, the probability of having a high signal-to-noise ratio increases, hampering obtaining a good thermometric performance of the material.

A small number of examples applied the FIR method to the thermal evolution of the intensities of different emission lines arising from Stark sublevels of the $^3H_4 \rightarrow {}^3H_6$ transition of Tm^{3+}, lying at around 800 nm, to develop thermometers based on Tm^{3+} and Yb^{3+}-codoped materials.[147,148] Since the $^3H_4 \rightarrow {}^3H_6$ transition generates the emission band with the maximum intensity in this region with Tm^{3+}, it is logical to use it to develop luminescent thermometers since the optical sensitivity of the detection system is less strict, allowing the use of cheaper, and even portable detectors. However, as mentioned in the previous section, the fact that ΔE in this cases is small (>300 cm^{-1}) makes the S_{rel} values obtained smaller (in the range 0.20–0.40% K^{-1}) than those obtained using other strategies, which gives δT values ~1 K. Hence, these luminescent thermometers are not competitive enough in front of the other strategies proposed.

A different example, based on the analysis of the intensity of two different emission lines, is that provided by an amorphous Yb^{3+} and Tm^{3+}-codoped phosphate glass,[130] and by Tm^{3+},Yb^{3+}:Sr_2GdF_7 glass ceramics.[142] In both cases, the luminescent thermometer developed was based on the intensity ratio between two emissions arising from two different energy levels of Tm^{3+} ($^1G_4$ and $^3F_{2,3}$) that are not thermally coupled, although the population of the $^3F_{2,3}$ level is potentiated as the temperature increases by the non-radiative relaxations generated from the upper excited levels, including the $^1G_4$ level (Fig. 6(b)). In these cases, the authors used two emission bands located at ~700 nm (generated by the $^1G_4 \rightarrow {}^3H_5$ transition) and ~650 nm (generated by the $^3F_{2,3} \rightarrow {}^3H_6$ transition) after excitation at 980 nm, although these two lines exhibited a very low intensity when compared with the 800 nm emission line used in the previous examples. The mechanism of generation of these emission lines is presented in Fig. 6(b). Under 980 nm excitation, Yb^{3+} is excited from the $^2F_{7/2}$ ground state to the $^2F_{5/2}$ excited state. The energy of this transition can be transferred to Tm^{3+}, which excites its electron from the $^3H_6$ ground state to the $^3H_5$ excited state, which then relaxes rapidly and non-radiatively to the $^3F_4$ level. When the energy of a second photon of 980 nm is transferred from Yb^{3+} to the electrons that are in this excited state, they can promote to the $^3F_{2,3}$ level. From here, the radiative $^3F_{2,3} \rightarrow {}^3H_6$ transition can take place, generating the emission at 650 nm. The second emission is generated when part of the energy of the electrons lying in the $^3F_{2,3}$ is dissipated non-radiatively, populating the lower $^3H_4$ energy level. From here, the transfer of the energy of a third photon of 980 nm from Yb^{3+} boosts these electrons to the $^1D_2$ level that can relax radiatively to the $^3F_4$ level, generating the emission at 700 nm. Despite the fact that the two electronic levels from which these emissions arise are not thermally coupled, the authors fitted their intensity ratio to the FIR model, and from it they extracted a ΔE value (2493 cm^{-1} and 2207 cm^{-1} for the phosphate[130] and ceramic glass[142] respectively) that allowed the calculation of S_{rel} according to eqn (13). Since the energy separation between the electronic levels involved in these emissions is of the order of 6000 cm^{-1}, higher than the upper limit defined for TCLs, the Boltzmann model cannot be used, and instead a phenomenological model fitting the experimental data to a conventional exponential curve should be taken into account. One might think that, according to that, the S_{rel} values they provided (3.94% K^{-1} and 1.97% K^{-1} at 303 K,[130,142] respectively) should not be considered, since they are based on a wrong model. But, surprisingly, by taking the FIR equation they provided as a phenomenological equation, of the form:

$$\Delta = \frac{I_2}{I_1} = C \exp\left(-\frac{D}{T}\right) \quad (16)$$

where C and D are fitting parameters, and calculating S_{rel} using eqn (2), the result is exactly the same, constituting the

strategy that provides the highest S_{rel} among the other ones proposed for the Tm^{3+},Yb^{3+}-codoped systems. However, the low intensity of the emissions used in these luminescent thermometers will hamper their practical use in real biomedical applications.

To end up this subsection, it is worth mentioning a totally different example, based on bandwidth thermometry instead of band-shape thermometry, as are all the luminescent thermometers reported up to now. Lu *et al.* synthesized rhombohedral Tm^{3+},Yb^{3+}:YOF irregular nanoparticles and analyzed their temperature-sensing performance applying the bandwidth luminescence nanothermometry model to the 800 nm emission band of Tm^{3+}, that as we said before is by far the band with the highest emission generated by Tm^{3+} in this region, after exciting the material at 980 nm in the temperature range from 12 to 300 K.[144] The temperature variation of the full width at half maximum (FWHMs) of the emission band was fitted to a simplified exponential equation:[200]

$$\Delta\nu = \Delta\nu_0 + Ae^{R_0T} \quad (17)$$

where $\Delta\nu_0$ represents the initial FWHM, and A and R_0 are empirical constants to be determined from the fitting model. The corresponding S_{rel} was deduced from the following equation:

$$S_{rel} = \frac{1}{\Delta\nu}\left|\frac{\partial\Delta\nu}{\partial T}\right| \times 100\% \quad (18)$$

The maximum S_{rel} obtained was 0.84% K^{-1} at the highest temperature analyzed.[144] Despite the fact that this example, strictly speaking, could not be used for biomedical applications since the temperature range analyzed was located at lower temperatures than those used in biological media, the fact that the maximum S_{rel} value was obtained at 300 K might suggest that it would be also useful in this temperature range. This is why we decided to include this example here.

Thus, the conclusion that can be extracted from the examples included in this subsection is that the most effective strategy to get a high S_{rel} is using the emissions arising from two non-thermally coupled electronic levels that are apart by a distance higher than the upper limit defining the thermally coupled range of energies (2000 cm^{-1}). Other strategies are not as effective as this one to increase S_{rel}. However, the quantum yield of the materials and that of the emissions used has not been taken into account in any of the luminescent thermometers operating in the I-BW reported as lying in the category described here. In fact, the low intensity of the emissions considered at ~650 nm and ~700 nm, or the big difference of intensity existing between the two emissions located at ~700 nm and at ~800 nm, would imply using highly sensitive (and thus bulky and costly) detectors, or that recording one of the signals in the optimum conditions would affect the collection of the other one in terms of signal-to-noise ratio or saturation of the detector. Thus, other strategies that, *a priori*, have a lower S_{rel}, like those involving different Stark sublevels of the $^3H_4 \rightarrow {}^3H_6$ transition of Tm^{3+}, lying at around 800 nm, might be more effective, due to the high intensity of this emission, which is the consequence of the $^3H_4$ level of Tm^{3+} being electronically fed by different radiative and non-radiative mechanisms. Nevertheless, this would lead to δT of around 1 K, one order of magnitude higher than that desired for biomedical applications.

2.1.3. Other Tm^{3+},Ln^{3+}-codoped luminescent thermometers operating in the I-BW. Dual emission center luminescent nanothermometers, *i.e.* those luminescent thermometers in which there are two activators emitting at different wavelengths,[21] operating in the I-BW, have been based on the emissions arising from Tm^{3+} and another Ln^{3+} ion acting as activators, with or without Yb^{3+} acting as a sensitizer. Two groups of luminescent thermometers could be identified in this category: (i) those using Tm^{3+} and Ho^{3+} as activators, with the presence or absence of Yb^{3+} as a sensitizer;[149–151] and (ii) those using Tm^{3+} and Er^{3+} as activators, using always Yb^{3+} as a sensitizer.[152–154]

In the case of Ho^{3+}, an important temperature-dependence of the emissions arising from the electronically linked energy levels of Ho^{3+} and Tm^{3+} has been reported, from which ET and back ET (hereafter BET) processes are possible. Despite the fact that the electronic levels of these different ions are not thermally coupled, a relationship between their intensities as the temperature changes can be established. Two different strategies have been proposed in this case. Savchuk *et al.* doped monoclinic potassium lutetium double tungstate KLu$(WO_4)_2$ nanoparticles with Ho^{3+} and Tm^{3+} and investigated their thermal performance in the physiological range of temperatures (303 K–333 K), after exciting the material at 808 nm.[150] In this case, Tm^{3+} acted both as a sensitizer, by absorbing the energy of the 808 nm laser source and transferring part of the energy to Ho^{3+}, and as an activator, generating different emission lines, among which one located at ~700 nm attributed to the $^3F_{2,3} \rightarrow {}^3H_6$ transition. The laser radiation at 808 nm excites the Tm^{3+} electrons to the $^3H_4$ level, from where they non-radiatively relax to the $^3F_4$ level. The absorption of a second photon at 808 nm promotes the electrons from the $^3F_4$ level to the $^1G_4$ level, from which a non-radiative decay can take place to the $^3F_{2,3}$ level, from which a radiative transition to the ground state can occur, generating the emission at 696 nm. The energy levels of Ho^{3+} can be populated through two different ET mechanisms: one from the Tm^{3+} $^3H_4$ level to the Ho^{3+} $^5I_5$ level, and a second one from the $^3F_4$ level of Tm^{3+} to the $^5I_7$ level of Ho^{3+}, from which also a BET process to Tm^{3+} can take place. Besides the direct ET from Tm^{3+}, the $^5I_7$ level of Ho^{3+} can also be populated by the non-radiative relaxation from its $^5I_5$ energy level. The ET of another photon of 808 nm from Tm^{3+} promotes the electrons lying in the $^5I_7$ level of Ho^{3+} to the higher energy levels $^3K_8$ and $^5F_3$. From these levels, non-radiative decay processes populate the $^5S_2$ and $^5F_4$ levels of Ho^{3+} from which a radiative transition towards the $^5I_7$ level can take place, generating an emission at 755 nm. A non-radiative relaxation from the $^5S_2$ and $^5F_4$ levels to the $^5F_5$ level, followed by a radiative transition to the $^5I_8$ ground state, generated an

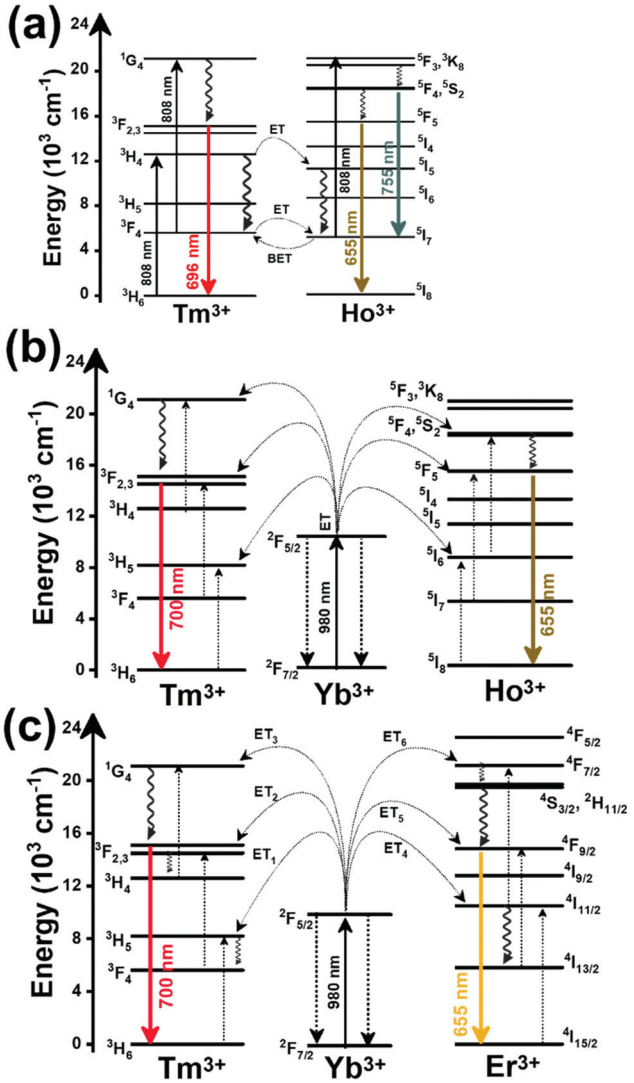

Fig. 9 Mechanisms of generation of the emission lines for: (a) Tm^{3+}, Ho^{3+}-doped $KLu(WO_4)_2$ nanocrystals after excitation at 808 nm, (b) Tm^{3+},Ho^{3+},Yb^{3+}-doped YPO_4 or $Gd_2(WO_4)_3$ nanoparticles after excitation at 980 nm, and (c) Tm^{3+},Er^{3+},Yb^{3+}:YF_3 nanoparticles embedded in a glass ceramic after excitation at 980 nm.

emission at 655 nm.[150] The detailed mechanism for this complex system is depicted in Fig. 9(a).

The temperature-sensing capacity was estimated by the integrated intensity ratio of the $^3F_{2,3} \rightarrow {}^3H_6$ and the $^5S_2$,$^5F_4 \rightarrow {}^5I_7$ transitions of Tm^{3+} and Ho^{3+}, respectively, corresponding to the emission bands located at 696 nm and 755 nm, arising from non-thermally coupled electronic levels (NTCLs).[150] Hence, the thermometric parameter (Δ) in this case was fitted to an empirical exponential growing equation of the type:[150]

$$\Delta = \Delta_0 + B\exp(\alpha T) \quad (19)$$

where Δ_0 and B are constants to be determined from the fitting of the experimental data.

Thus, the corresponding S_{rel} was calculated by:

$$S_{rel} = \frac{B\alpha\exp(\alpha T)}{\Delta_0 + B\exp(\alpha T)} \times 100 \quad (20)$$

The maximum S_{rel} = 2.84% K^{-1} was achieved at 303 K. Savchuk *et al.*, also estimated the δT of this luminescent thermometer using the equation:[150]

$$T = \frac{\delta\Delta}{B\exp(\alpha T)} \quad (21)$$

determining a value of 0.2 K at 303 K.

The second strategy developed in Tm^{3+},Ho^{3+}-codoped systems in the presence of Yb^{3+} as a sensitizer is that demonstrated in Tm^{3+},Ho^{3+},Yb^{3+}:YPO_4 microplates,[149] and in Tm^{3+}, Ho^{3+},Yb^{3+}:$Gd_2(WO_4)_3$ nanocrystals.[151] In these two cases, Yb^{3+} acted as a sensitizer to absorb the energy of the 980 nm excitation source and transferred it to Tm^{3+} and Ho^{3+}, to generate an emission line at ~650–660 nm, corresponding to the Ho^{3+} $^5F_5 \rightarrow {}^5I_8$ transition, and another one at ~700 nm, corresponding to the Tm^{3+} $^3F_{2,3} \rightarrow {}^3H_6$ transition. Yb^{3+} absorbs the 980 nm excitation, exciting its electrons from the $^2F_{7/2}$ ground state to the $^2F_{5/2}$ excited state (Fig. 9(b)). Subsequently, the energy of this sensitizer is transferred to the adjacent activators Ho^{3+} and Tm^{3+}, and the sensitizer is relaxed back to the ground state. Ho^{3+} and Tm^{3+} activators promote their electrons to their excited states (Tm^{3+} to $^3H_5$, $^3F_{2,3}$ and $^1G_4$ levels, and Ho^{3+} to $^5I_6$, $^5F_5$ and $^5S_2$, $^5F_4$ levels). In addition, the excited states involved in the generation of the red emissions ($^3F_{2,3}$ of Tm^{3+} and $^5F_5$ of Ho^{3+}) can be populated by non-radiative processes from the higher energy excited states of the corresponding ions ($^1G_4$ of Tm^{3+} and $^5S_2$, $^5F_4$ of Ho^{3+}).[149,151] From these states, decaying back radiatively to the corresponding ground states ($^3F_{2,3} \rightarrow {}^3H_6$ of Tm^{3+} and $^5F_5 \rightarrow {}^5I_8$ of Ho^{3+}) generated the emissions used for temperature sensing.

Again, these emission bands do not arise from TCLs; hence the thermometric parameter could be deduced from the intensity ratio between these bands by fitting the experimental data to a linear equation,[149] or to a polynomial function:[151]

$$\Delta = X - S \times T \quad (22)$$

$$\Delta = C_1 + B_1T + B_2T^2 + B_3T^3 \quad (23)$$

where X and S, and C_1, B_1, B_2 and B_3 were fitting parameters. From these equations the thermal sensitivities could be calculated, depending on the thermometric equation used, as:

$$S_{rel} = \left|\frac{S}{S - ST}\right| \times 100\% \quad (24)$$

$$S_{rel} = (B_1 + 2B_2T + 3B_3T^2) \times 100\% \quad (25)$$

The maximum S_{rel} = 2.86% K^{-1} at 563 K was obtained for Tm^{3+},Ho^{3+},Yb^{3+}:YPO_4,[149] which allowed the calculation of a δT of 0.2 K. In the case of Tm^{3+},Ho^{3+},Yb^{3+}:$Gd_2(WO_4)_3$, the authors reported a substantially lower S_{rel} of 1.43% K^{-1} at 595 K, due to the different phenomenological model used to fit the experimental data.[149]

When the two emission centers consisted of the combination of Tm^{3+} and Er^{3+}, in the presence of Yb^{3+} as a sensitizer, the same strategy was always used: the temperature reading was achieved by the intensity ratio between the 700 nm emission line of Tm^{3+} attributed to the $^3F_{2,3} \rightarrow {}^3H_6$ transition, and the 655–660 nm emission line of Er^{3+}, arising from the $^4F_{9/2} \rightarrow {}^4I_{15/2}$ transition.[152–154]

The mechanism of the generation of these emission lines is depicted in Fig. 9(c).

In short, Yb^{3+} acts as a sensitizer to absorb the energy of the 980 nm excitation source, and generates three ET processes towards Tm^{3+}, populating its $^3H_5$, $^3F_{2,3}$, and $^1G_4$ states after some non-radiative relaxation processes in some cases (Fig. 9(c)):

- $Yb^{3+}:{}^2F_{5/2} + Tm^{3+}:{}^3H_6 \rightarrow Yb^{3+}:{}^2F_{7/2} + Tm^{3+}:{}^3H_5$ (ET1)
- $Yb^{3+}:{}^2F_{5/2} + Tm^{3+}:{}^3H_4 \rightarrow Yb^{3+}:{}^2F_{7/2} + Tm^{3+}:{}^3F_{2,3}$ (ET2)
- $Yb^{3+}:{}^2F_{5/2} + Tm^{3+}:{}^3H_4 \rightarrow Yb^{3+}:{}^2F_{7/2} + Tm^{3+}:{}^1G_4$ (ET3)

On the other hand, a two-step ET processes from Yb^{3+} to Er^{3+} can also occur:

- $Yb^{3+}:{}^2F_{5/2} + Er^{3+}:{}^4I_{15/2} \rightarrow Yb^{3+}:{}^2F_{7/2} + Er^{3+}:{}^4I_{11/2}$ (ET4)
- $Yb^{3+}:{}^2F_{5/2} + Er^{3+}:{}^4I_{11/2} \rightarrow Yb^{3+}:{}^2F_{7/2} + Er^{3+}:{}^4F_{7/2}$ (ET5)followed by a non-radiative relaxation to populate the Er^{3+} $^2H_{11/2}$, $^4S_{3/2}$ and $^4F_{9/2}$ electronic levels.

In addition, the population of the Er^{3+} $^4F_{9/2}$ state can be achieved through another ET process:

- $Yb^{3+}:{}^2F_{5/2} + Er^{3+}:{}^4I_{13/2} \rightarrow Yb^{3+}:{}^2F_{7/2} + Er^{3+}:{}^4F_{9/2}$ (ET6)

Finally, a last ET process between Er^{3+} and Tm^{3+} can occur, populating the $^3F_{2,3}$ level of Tm^{3+} (not presented in Fig. 9(c) for clarity reasons):

- $Er^{3+}:{}^4F_{9/2} + Tm^{3+}:{}^3H_6 \rightarrow Er^{3+}:{}^4I_{15/2} + Tm^{3+}:{}^3F_{2,3}$ (ET7)

Once the $^3F_{2,3}$ level of Tm^{3+} and the $^4F_{9/2}$ level of Er^{3+} are populated, the emissions at 700 nm and at 666–660 nm are generated arising from the electronic transitions indicated above.

This strategy was used in Tm^{3+},Er^{3+},Yb^{3+}:YF_3 nanoparticles embedded in a glass ceramic,[153] and in Tm^{3+},Er^{3+},Yb^{3+}:LuF_3,[154] and in oleic acid-capped Tm^{3+},Er^{3+},Yb^{3+}:$NaLuF_4$ nanocrystals.[152] It is important to note here that due to the non-resonant energy matching between the $^3F_{2,3}$ level of Tm^{3+} and the $^4F_{9/2}$ level of Er^{3+}, the multiphonon-assisted ET rate (K_{ET}) can be described by the Mott–Seitz model:[201,202]

$$K_{ET} \propto \exp\left(-\frac{\Delta E}{k_B T}\right) \quad (26)$$

indicating the temperature-dependent behavior and the link between the two emissions involved in this thermometer. ΔE here stands for the energy gap between the excited and de-excited states.

In the case of Tm^{3+},Er^{3+},Yb^{3+}:YF_3 nanoparticles embedded in a glass ceramic,[153] the one exhibiting the highest S_{rel} (1.89% K^{-1} at 393 K) among these examples of luminescent thermometers, the authors fitted the experimental data to a FIR model of the form of eqn (14). However, as discussed previously, since the two energy levels from which the emissions considered are not thermally coupled since they do not belong to the same Ln^{3+}, this model should not be used, and instead a phenomenological one should be implemented, exponential in that case. In the two other cases, phenomenological models were implemented, following polynomial equations in both cases, of second order in the case of oleic acid-capped Tm^{3+}, Er^{3+},Yb^{3+}:$NaLuF_4$ nanocrystals with the form:[152]

$$\Delta = C_1 - B_1 T + B_2 T^2 \quad (27)$$

and of third order in the case of Tm^{3+},Er^{3+},Yb^{3+}:LuF_3 mesocrystals with the form:[154]

$$\Delta = C_1 - B_1 T + B_2 T^2 - B_3 T^3 \quad (28)$$

The S_{rel} of these systems were obtained using eqn (2), with values of 0.76% K^{-1} at 500 K,[152] and 0.95% K^{-1} at 363 K,[154] respectively. The differences between S_{rel} obtained can be attributed to the different phenomenological models implemented in each case.

In general, the strategies to develop luminescent nanothermometers analyzed in this section do not provide higher S_{rel} than those highlighted in the previous sections for Tm^{3+}-doped systems, although in some cases they are pretty close. However, they use emission bands with a more similar intensity than those used previously in Tm^{3+},Yb^{3+}codoped systems (Fig. 10), which would facilitate recording the two emission bands with enough guarantees with the available detection systems, facilitating their practical use in biomedical applications with a δT of ~0.2 K, closer to the ones demanded by the scientific community.

Table 1 summarizes all the information regarding Tm^{3+}-doped luminescent nanothermometers, and Fig. 7 depicts the evolution of the S_{rel} of every luminescent thermometer based on Tm^{3+} analyzed in this section operating in the I-BW in the range of temperatures studied. From this figure, it can be seen that in the majority of the cases analyzed, S_{rel} reaches its

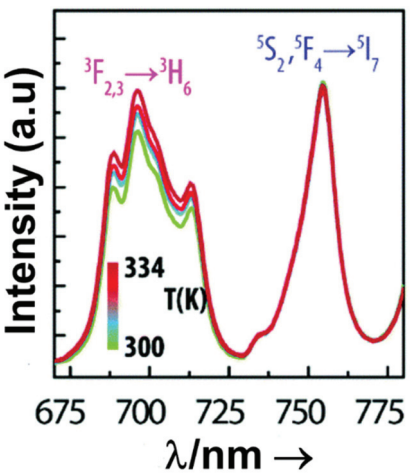

Fig. 10 Temperature dependence of the emission spectra of Ho,Tm:$KLu(WO_4)_2$ nanocrystals, demonstrating the similar intensity between the $^3F_{2,3} \rightarrow {}^3H_6$ of Tm^{3+} and $^5S_2, {}^5F_4 \rightarrow {}^5I_7$ of Ho^{3+}. Reprinted with permission from ref. 150. Copyright 2018, The Royal Society of Chemistry.

maximum value at room temperature, and then it decreases as the temperature increases. However, there are three cases in which S_{rel} increases in the biological range of temperatures, decreasing later, and showing maxima at around 350–400 K. These luminescent thermometers, based on Tm^{3+},Yb^{3+}:Sr_2GdF_7,[142] Tm^{3+},Er^{3+},Yb^{3+}:YF_3 nanoparticles embedded in a glass ceramics,[153] and Tm^{3+},Er^{3+},Yb^{3+}:LuF_3 mesocrystals,[154] would be the best options to perform luminescence thermometry for biological applications in the I-BW, particularly in the two first cases, since their maximum S_{rel} is around 2% K^{-1}, which might allow a δT of ~0.2 K, and the emission bands in which they are based have a similar intensity, simplifying the detection setup.

2.2. Neodymium-doped luminescent thermometers operating in the I-BW

Nd^{3+}-doped luminescent thermometers have attracted significant attention due to their superior luminescent yields in the NIR spectral region.[158,173,203] Nd^{3+} ions can be excited with UV, VIS and NIR light to generate emissions in the I-BW,[204–206] with potential advantages for biomedical applications, including large penetration depths, minimal background interference, and little damage to the targeted samples, especially when excited in the NIR, enhancing their application as luminescent probes for various bioapplications as NIR-to-NIR luminescent nanoprobes.[207,208] Different Nd^{3+}-doped luminescent thermometers operating in the I-BW have been designed based on three different pairs of TCLs that the electronic structure of this ion provides: $^4F_{7/2}$/$^4F_{3/2}$ (TCL 1), $^4F_{7/2}$/$^4F_{5/2}$ (TCL 2) and $^4F_{5/2}$/$^4F_{3/2}$ (TCL 3). In the field of luminescent nanothermometry, Nd^{3+}-doped materials have been frequently used as sensitive thermometers in the physiological range of temperatures. An important number of papers have been also devoted to exploring luminescent thermometers based on the transitions from different Stark sublevels of the $^4F_{3/2}$ excited state to the $^4I_{9/2}$ ground state. Furthermore, other recent references explore the possibilities of developing dual emitting center luminescence thermometers combining Nd^{3+} with other Ln^{3+} ions, such as Eu^{3+}, and transition metals like Ti^{4+}. This section will focus first on the temperature-sensing properties of single-doped Nd^{3+} luminescent thermometers, then on dual emitting center Nd^{3+}/Ln^{3+}-codoped luminescent thermometers, and will conclude with dual emitting center Nd^{3+}/transition metal-codoped luminescent thermometers, all of them operating in the I-BW.

2.2.1. Single Nd^{3+}-doped luminescent thermometers operating in the I-BW. Contrary to single Tm^{3+}-doped thermometers (section 2.1.1), single Nd^{3+}-doped luminescent thermometers operating in the I-BW represent the widest explored class of luminescent thermometers operating in the I-BW due to the temperature dependence of the TCLs of Nd^{3+}, lying in this spectral region. The thermometric performance of these thermometers, in general, is based on the FIR model, as can be seen in Table 1, because ΔE between these electronic levels lies in the range 200–2000 cm^{-1}. In single Nd^{3+}-doped luminescent thermometers operating in this region, the TCL 1, TCL 2 and TCL 3, with theoretical ΔE 1910 cm^{-1}, 1020 cm^{-1} and 960 cm^{-1},[176] respectively, are applied to determine their thermometric performance.

The reported single Nd^{3+}-doped luminescent thermometers operating in the I-BW have been excited with VIS and NIR light sources. In a typical example of exciting the Nd^{3+}-doped particles with green light, the mechanism of the generation of the emission bands (Fig. 11(a)) is as follows: photons of the 580 nm excitation light source are absorbed by Nd^{3+}, promoting its electrons from the $^4I_{9/2}$ ground state to the $^4G_{9/2}$ or $^4G_{7/2}$ excited state, decaying then non-radiatively to the $^4F_{5/2}$ and $^4F_{7/2}$ states. From the $^4F_{5/2}$ state, a radiative relaxation decaying back to the ground state generates an emission lying at 780–840 nm. The second emission band at 870–920 nm is generated after the non-radiative relaxation of the electrons from the $^4F_{5/2}$ state to the $^4F_{3/2}$ level, prior to a radiative relaxation to the ground state.[158] A third emission band at 730–770 nm is generated when electrons relax back to the ground state from the $^4F_{7/2}$ state.

Nd^{3+} ions were embedded in hosts such as La_2O_2S,[156] YAP,[157] Gd_2O_3,[158] $LaPO_4$,[159] fluorotellurite glass,[160] and strontium barium niobate (SBN) glass ceramic,[161] for this class of luminescent thermometers. In general, the performance of these luminescent thermometers was evaluated by analyzing the intensity ratio of the emissions corresponding to the $^4F_{5/2} \rightarrow {}^4I_{9/2}$ and $^4F_{3/2} \rightarrow {}^4I_{9/2}$ transitions (TCL 3). It should be

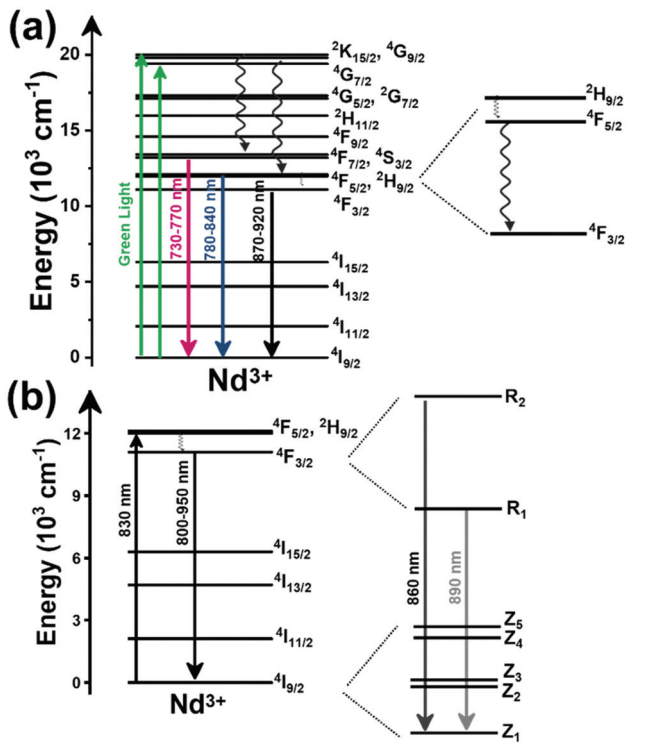

Fig. 11 Mechanisms of generation of the emission bands in single Nd^{3+}-doped nanoparticles after being excited with: (a) a green light source (the magnification detail depicts the thermally coupled $^4F_{5/2}$ and $^4F_{3/2}$ levels), and (b) a near infrared light source.

noted here that for La_2O_2S, the FIR model applied was that of eqn (14), in which a correction term accounting for the overlapping of the emissions was used although the emission bands were largely apart, whereas for the other cases, the classical FIR model, described by eqn (9), was applied. Nd^{3+}-doped hexagonal La_2O_2S particles operated as a luminescent thermometer in the I-BW over the range of temperatures from 270 K to 600 K, exhibiting a maximum S_{rel} of 1.95% K^{-1} at the lowest temperature analyzed, which is a little overestimated with respect to the other luminescent thermometers based on Nd^{3+} due to the fitting model used in its calibration.[156] However, the big size of the particles obtained, and the temperature where this maximum value of S_{rel} was obtained, quite often might limit the potential applications of this thermometer.[13] In fact, for this thermometer, by taking into consideration the value of the experimental ΔE reported (987 cm^{-1}),[156] and the proper FIR equation (eqn (9)), the correct value of the S_{rel} that should be considered would be 1.15% K^{-1} (at 293 K). In the case of the fluorotellurite glass,[160] and the SBN glass ceramic,[161] we calculated the values of the S_{rel} (and δT) by considering the ΔE provided by the authors and the temperature ranges analyzed. From all these results, we can conclude that the maximum S_{rel} of this class of luminescent thermometers would be in the range 1.15–1.83% K^{-1}, in all cases obtained at the lowest temperature analyzed. A higher S_{rel} was reported in Nd^{3+} embedded in YAG, when TCL 2 was taken into account.[155] If we compare the performance of the luminescent thermometers based on TCL 2 and TCL 3, it is clear that the best temperature-sensing properties were achieved for the former one, mainly due to the higher ΔE between the electronic levels.[155] Despite the higher S_{rel} (2.95% K^{-1}) this value was obtained at 200 K, whereas in the physiological range of temperatures, it drops down to 0.3% K^{-1}.[155] The performance of the Nd^{3+}-doped luminescent thermometers based on considering the Stark-sublevels of the $^4F_{3/2} \rightarrow {}^4I_{9/2}$ transition resulted in a lower S_{rel} (0.11–0.62% K^{-1}) which implied a larger δT when determined using eqn (3) (>1 K), independently of the excitation source used. Nevertheless, in some cases in the bibliographic references δT was reported to be smaller, associated with better S_{rel} values reported that are impossible to get according to the E associated with the Stark sublevels involved in the emissions used to build the luminescent thermometer, of the order of 50–270 cm^{-1} depending on the host in which the Nd^{3+} has been embedded. This energy difference, strictly speaking, does not allow for the application of the FIR model to those emission lines arising from energy levels apart by an energy difference below 200 cm^{-1}, so several reports fit the experimental data to an exponential function of the form of that shown in eqn (16), which might also explain why in some cases better S_{rel} values were reported.

Fig. 11(b) shows the mechanism of generation of the emission lines associated with the Stark-sublevels of the $^4F_{3/2} \rightarrow {}^4I_{9/2}$ transition after excitation in the NIR. In this way, the electrons in the Nd^{3+} $^4I_{9/2}$ ground state are excited to the $^4F_{5/2}$, $^2H_{9/2}$ states; then they relax *via* a non-radiative process populating the $^4F_{3/2}$ metastable state. If instead, visible light in the green range is used to excite the sample, the electrons will be excited to the more energetic $^4G_{9/2}$ or $^4G_{7/2}$ excited states, as shown in Fig. 11(a), but from there, they relax non-radiatively to the $^4F_{5/2}$, $^2H_{9/2}$ state, from which the rest of the emission mechanism is the same. The $^4F_{3/2}$ metastable state may be radiatively depopulated, generating emission bands in the I-BW, assigned to the $^4F_{3/2} \rightarrow {}^4I_{9/2}$ transition.[165] Since both levels ($^4F_{3/2}$ and $^4I_{9/2}$) are composed of several Stark sublevels (R_1 and R_2 for $^4F_{3/2}$, and Z_1–Z_5 for $^4I_{9/2}$, as presented in Fig. 11(b)), a plethora of emission bands lying in the 800–950 nm spectral range (Table 1) may be generated, which can be used to define different luminescent thermometers, depending on the host considered. Note that here we focused only on the generation of the emissions lines used to build this class of luminescent thermometers, without taking into account that Nd^{3+} can generate other emission lines in different spectral regions, as we will see in the following sections.

The case of Nd^{3+}:$LiLuF_4$@$LiLuF_4$ should be mentioned here, where instead of the thermalization of the R_2 and R_1 levels, the contributions to peak shift and the width change of the intensity of the emissions were considered to build the luminescent thermometers, leading to higher sensitivity values (if only the thermalization is considered with an ΔE of 55 cm^{-1}, a maximum S_{rel} value of 0.09% K^{-1} would have been achieved).[164]

Despite these limitations in this class of thermometer, Marciniak *et al.* investigated the effect of the Nd^{3+} concentrations and the alkali ion in the host on the thermometric performance of Nd^{3+}-doped monoclinic tetraphosphates of the form $ALaP_4O_{12}$, where A = Li, K, Na and Rb.[165] The authors investigated the thermometric performance of these compounds, *via* three different classes of luminescence nanothermometry technique: band-shape, bandwidth and spectral position.

Regarding the performance of the luminescent thermometer *via* the band-shape thermometry technique, the experimental data were fitted to an exponential function of the form of that shown in eqn (16). The authors observed a tendency of the intensity ratio to increase as the temperature increased for all the investigated hosts. However, at higher temperatures, an inversion of this trend could be observed for the hosts containing Li and Na, due to the drastic lowering of the intensity of one of the emissions with respect to the other, due to the excited state absorption to higher energy levels (Fig. 12(a)). This effect reduces the usable temperature range for these luminescent thermometers. The highest S_{rel} was obtained for the $LiLaP_4O_{12}$ host while the lowest one was obtained for the $KLaP_4O_{12}$ host, while the other two, the $RbLaP_4O_{12}$ and $NaLaP_4O_{12}$ hosts, have similar values (Table 1), following a linear trend with the crystallographic b parameter of the materials, coinciding with the direction along which the $(PO_4)^{3-}$ tetrahedral chains characteristic of these compounds run (Fig. 12(b)).[165] Here, the influence of the symmetric P–O–P vibration mode, that shifts towards lower energies as the mass of the alkali ion in the host increases due to the distance

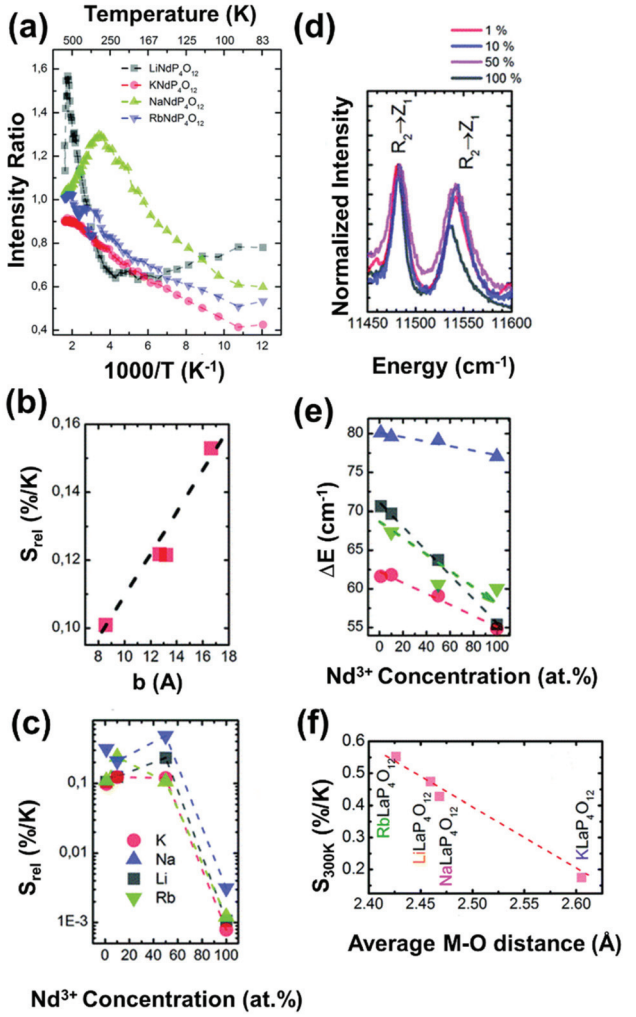

Fig. 12 (a) Effect of the temperature on the intensity ratio of Nd^{3+}-doped $ALaP_4O_{12}$ nanocrystals. (b) Variation of the relative sensitivity as a function of the cell parameter *b* of these compounds. (c) Change in S_{rel} as a function of the dopant concentration. (d) Comparison of the emission band positions for the $R_2 \rightarrow Z_1$ and $R_1 \rightarrow Z_1$ transitions for different concentrations of Nd^{3+} ions in $KLaP_4O_{12}$. (e) Effect of the dopant concentration on the energy separation between the R_1 and R_2 Stark sublevels for AP_4O_{12} nanocrystals. (f) Variation of S_{rel} with the M–O mean distance in Nd^{3+}-doped AP_4O_{12} nanocrystals. Reprinted with permission from ref. 165. Copyright 2016, The Royal Society of Chemistry.

between the alkali ion and the phosphorus ion, seems to play a major role. Also the concentration of Nd^{3+} in the hosts highly influences the S_{rel} value due to the dependence of the energy separation between the two Stark sublevels involved in the generation of the emissions used to build the thermometer (Fig. 12(c)). With the increase of the Nd^{3+} concentration, the position of R_2 and R_1 is shifted (Fig. 12(d)), using the $KLaP_4O_{12}$ host as an example. This tendency, with different rates, can be noticed for each of the other hosts. The decrease of the ΔE value was stronger for $RbLaP_4O_{12}$ (a decrease of 24 cm^{-1}), compared with $LiLaP_4O_{12}$ (15 cm^{-1}), $NaLaP_4O_{12}$ (6 cm^{-1}) and $KLaP_4O_{12}$ (3 cm^{-1}) (Fig. 12(e)). Since S_{rel} for these nanothermometers is ruled by the Boltzmann distribution, it depends on ΔE, and it is clear that a decrease of this parameter will lead to a decrease in the thermal sensitivity.

Concerning spectral position thermometry, with the increase of the temperature a red-shift of the emission lines was observed for all the hosts analyzed, with $RbNdP_4O_{12}$ showing the strongest changes, while $KNdP_4O_{12}$ exhibited the smallest ones. This shift in the position of the emission lines is usually associated with the electron-phonon coupling effect that results from the introduction of random perturbations in the active-ion-surrounding environment by the host vibration modes at higher temperatures that can be thermally occupied, generating stronger electron–host interactions. This results in a decrease of the energy of the emitted phonons and thus a slight shift of the emission band towards higher wavelengths. The spectral change can be described by:[165,209]

$$\Delta\lambda = \Delta\lambda^{S} + \Delta\lambda^{D} + \Delta\lambda^{M} + \Delta\lambda^{R} \quad (29)$$

where $\Delta\lambda^{S}$, $\Delta\lambda^{D}$, $\Delta\lambda^{M}$ and $\Delta\lambda^{R}$ represent the contributions to the spectral shifting of the crystal strain inhomogeneity, the single phonon processes, the multiphonon processes, and the electron–host interaction effect associated with Raman scattering, respectively. However, the three first parameters can be considered to be temperature independent, and thus only the electron–host interaction parameter should be considered as the one which controls the emission line shift as the temperature increases.

According to that, the change in the spectral position can be expressed as:[209,210]

$$\delta\lambda = \delta\lambda_0 + \alpha\left(\frac{T}{\Theta_D}\right)^4 \int_0^{\Theta_D/T} \frac{x^3}{e^x - 1}\mathrm{d}x \quad (30)$$

$$x = \frac{\hbar\Omega}{k_B T}$$

where $\delta\lambda_0$, α, Θ_D and $\hbar\Omega$ and represent the initial line position, the electron–host coupling parameter, the effective Debye temperature, and the phonon energy, respectively. The corresponding S_{rel}, thus, can be calculated from the following equation:

$$S_{rel} = \frac{1}{\lambda_2}\frac{\lambda_2 - \lambda_1}{\Delta T} \times 100\% \quad (31)$$

where λ_2 and λ_1 represent the spectral shifts at temperatures T_2 and T_1 and ΔT is the result of $T_2 - T_1$.

S_{rel} follows a linear inverse trend with the average distance between the metal and the oxygen host (Fig. 12(f)).[165] After these results, the general conclusion that can be drawn is that the materials exhibiting the shortest metal–oxygen distance exhibited the highest thermometric performance. This is because the electron–host coupling parameter is proportional to the average metal–oxygen distance while the electron–phonon interaction strength increases with the covalence of the bond, which increases proportionally to the shortening of the chemical bond length.[209,210] These results indicate that, to further enhance the thermometric performance of lumines-

cent thermometers based on Nd^{3+}, host types with strong electron–host interaction parameters should be selected.

Using bandwidth luminescence nanothermometry, it was observed that the width of the emission band was broadened as the temperature increased, as a consequence of the electron–phonon interaction. To determine the thermometric performance, the bandwidth of the emission band at a particular temperature could be determined according to:[211]

$$\Delta\nu = \nu_0\sqrt{\coth\left(\frac{\hbar\Omega}{2k_BT}\right)} \quad (32)$$

where ν_0 stands for the full width at half-maximum at the initial temperature. The highest S_{rel} (determined using eqn (18)) was seen, yet again, for 1% Nd^{3+}-doped $LiLaP_4O_{12}$ for a value of 0.32% K^{-1}.[165] However, in that case, it was not possible to establish a correlation between the structural parameters of the host and S_{rel} for the case of the bandwidth luminescence nanothermometry.

As a final remark, among the three luminescence nanothermometry classes explored to study the thermometric performance of these compounds, the spectral position luminescence nanothermometry technique displayed the best temperature-sensing properties.[165] Despite this better performance, according to the authors the spectral position is much more difficult to accurately determine and requires high-resolution detection systems, which hampers the implementation of this technique to determine the temperature in real biomedical samples.[165] Thus, please note that Table 1 presents only the nanomaterial with the highest S_{rel} and the corresponding way of evaluating this performance. As can be observed from Table 1, the thermometric performance of this class of materials is still lower compared with other materials operating within this spectral region.

2.2.2. Dual Nd^{3+}/Ln^{3+}-codoped luminescent thermometers operating in the I-BW. Dual Nd^{3+}/Ln^{3+} luminescent thermometers operating in the I-BW are mainly based on the incorporation of Yb^{3+} as a sensitizer due to its large absorption cross section at 980 nm, which would lead to brighter emissions.[196] This feature has led this element to be used together with Nd^{3+} and other Ln^{3+} ions in photon conversion processes involving ET mechanisms. For the case of Nd^{3+}, the application of Yb^{3+} as a sensitizer allows the use of the three TCLs ($^4F_{7/2}$, $^4F_{5/2}$ and $^4F_{3/2}$) for temperature-sensing purposes (Table 1). However, as in the case of Tm^{3+}/Yb^{3+}-codoped luminescent thermometers, the overheating problem due to the strong water absorption band at around 980 nm makes nanothermometers containing Yb^{3+} and pumped at this wavelength non ideal for biomedical applications.[206] The mechanism of the generation of the emissions in Nd^{3+}/Yb^{3+}-codoped thermometers is based on phonon-assisted energy transfer (hereafter PAET) processes.[179,181] In a typical process (Fig. 13(a)), under 980 nm excitation, electrons are excited from the Yb^{3+} $^2F_{7/2}$ ground state to the Yb^{3+} $^2F_{5/2}$ excited level. The transfer of energy from this state to the Nd^{3+} states is achieved through PAET processes. This allows the population of the $^4F_{3/2}$, $^4F_{5/2}$ and $^4F_{7/2}$ states of Nd^{3+} if the maximum phonon energy of the host is the suitable one for covering ΔE

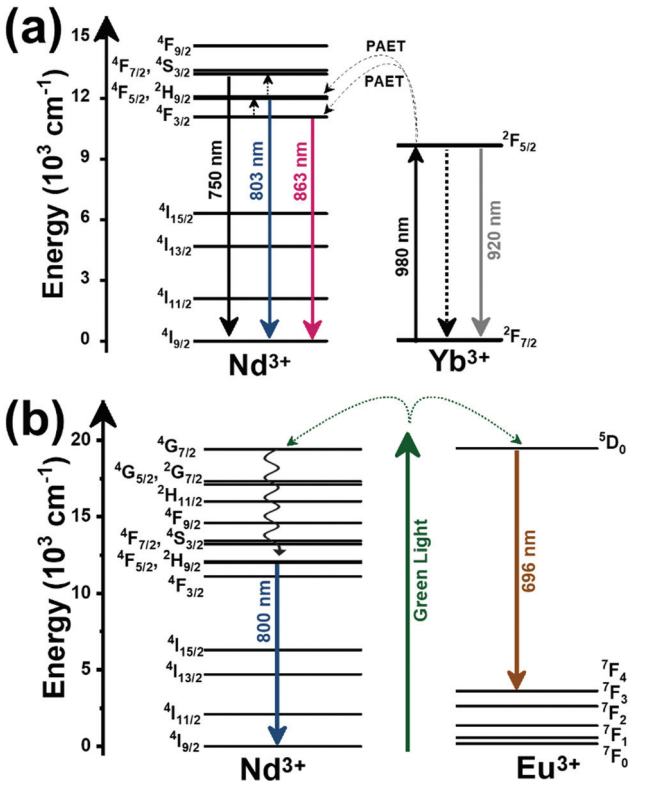

Fig. 13 Mechanisms of generation of the emission bands of nanoparticles codoped with Nd^{3+} and: (a) Yb^{3+} after 980 nm excitation, and (b) Eu^{3+} after excitation in the green range.

between these energy levels, of the order of 1750 cm^{-1}. Also, the PAET process becomes more effective as the temperature increases,[179,181] making these electronic levels thermally coupled. Hence, thermal population of the $^4F_{5/2}$ and $^4F_{7/2}$ levels can be achieved from the lower energy level. From these states, radiative decay to the ground state generates Nd^{3+} emissions in the I-BW window at 863 nm, 803 nm and 750 nm, respectively, as shown in Fig. 13(a). The performance of these Nd^{3+},Yb^{3+}-codoped nanoparticles was evaluated by the typical FIR model. The most used TCLs are the $^4F_{3/2}$ and the $^4F_{7/2}$ levels, which showed higher S_{rel} values than when the emission arising from the $^4F_{5/2}$ level is used (Table 1). A full comparison between the temperature-sensing performance of the three TCLs in Nd^{3+} with emissions in the I-BW is provided by Nd^{3+},Yb^{3+}-codoped oxyfluoride glass.[176] The results show that the thermometric performance follows the order: $^4F_{7/2}/^4F_{3/2} > {}^4F_{7/2}/^4F_{5/2} > {}^4F_{5/2}/^4F_{3/2}$ (Fig. 14(a)), which is in agreement with the experimental ΔE determined between these levels (2076 cm^{-1}, 1300 cm^{-1} and 1216 cm^{-1}, respectively).[176] The S_{rel} values obtained when using the $^4F_{3/2}$ and $^4F_{7/2}$ TCLs allows the calculation of a δT of ~0.15–0.2 K, approaching the desired values for biomedical applications,[13] although this low limit is always attained at the minimum temperature analyzed, normally room temperature.

Another interesting example here is the luminescent thermometer constituted by Nd^{3+},Yb^{3+}-codoped trigonal La_2O_3 microparticles, in which the thermometric performance was

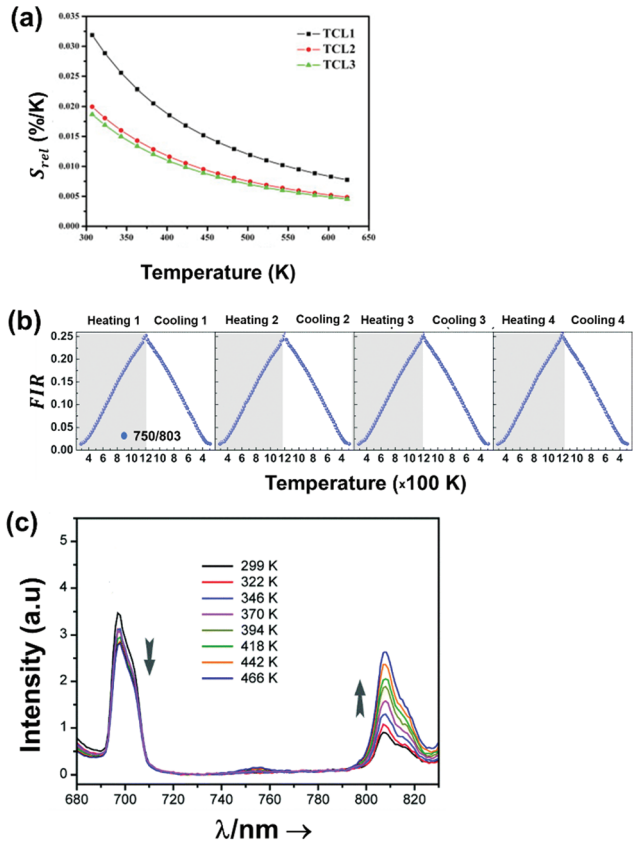

Fig. 14 (a) Evolution of S_{rel} as a function of the three TCLs in Nd^{3+}, Yb^{3+}-codoped oxyfluoride glass: TCL1 = $^4F_{7/2}/^4F_{3/2}$, TCL2 = $^4F_{7/2}/^4F_{5/2}$, and TCL3 = $^4F_{5/2}/^4F_{3/2}$. Reprinted with permission from ref. 176. Copyright 2013, Elsevier. (b) Repeatability of the FIR 750 nm/803 nm over 4 heating and cooling cycles from 293 to 1233 K with a step of 20 K in Nd^{3+},Yb^{3+}-codoped trigonal La_2O_3 microparticles. Adapted with permission from ref. 181. Copyright 2018, The Royal Society of Chemistry. (c) Emission spectra of Eu,Nd:YVO_4 nanoparticles under excitation at 590 nm in the temperature range of 299–466 K. Adapted with permission from ref. 183. Copyright 2020, The Royal Society of Chemistry.

explored in the widest temperature range among this class of thermometers, from room temperature to 1233 K.[181] Here, the repeatability of the measurements was tested *via* four heating and cooling cycles, revealing an excellent performance (Fig. 14(b)). Also, based on these heating and cooling cycles, the authors could calculate the temperature uncertainty as:

$$\mathrm{A}T_{\min} = \frac{\sigma}{S_{\mathrm{rel}}} \quad (33)$$

where σ represents the standard deviation of the intensity ratio ($^4F_{7/2}/^4F_{3/2}$ in this case). The value obtained was 0.1 K in the temperature range below 400 K, whereas it increased for higher temperatures, reaching a maximum of ~3 K at 1230 K.[181]

An interesting choice with these dual emitting center Nd^{3+}, Ln^{3+}-codoped luminescent thermometers operating in the I-BW is the choice of combining the emissions of Nd^{3+} with the emission of Yb^{3+}, which besides acting as a sensitizer can also generate an emission line that can be used to measure the temperature. An example of this kind of thermometer is that of Nd^{3+},Yb^{3+}:$Al_4B_2O_9$ orthorhombic nanoparticles excited at 977.7 nm.[179] The mechanism of the generation of the emissions is exactly the same as that described before in Fig. 13(a), including the emission generated by the $^2F_{5/2} \rightarrow {}^2F_{5/2}$ radiative relaxation in Yb^{3+}. The highest S_{rel} was obtained when calculating the 800 nm *versus* 920 nm intensity ratio of the emissions of Nd^{3+} and Yb^{3+}, respectively (Table 1), as ΔE is larger when compared with the one between the 864 nm and 920 nm emissions.[179] The results obtained from this combination are comparable to that obtained for the TCL 3 when only the Nd^{3+} emissions are used, but are still lower than that of the TCL 1.

Besides Nd^{3+}/Yb^{3+}-codoped luminescent thermometers operating in the I-BW, another choice, rarely reported, is Nd^{3+}/Eu^{3+}-doped materials. These luminescent thermometers are based on the emissions arising from non-thermally coupled levels (hereafter NTCLs) of Eu^{3+} at ~700 nm and Nd^{3+} at ~800 nm.[182,183] The reason why these Nd^{3+}/Eu^{3+} co-doped thermometers were proposed was to overcome the drawback of the limitation in the maximum value of the S_{rel} that can be achieved operating with TCLs.[212] Thus, the strategy of implementing emission lines generated from two different active centers was tested. The mechanism of the generation of these emission lines is depicted in Fig. 13(b). The excited energy states $^5D_0$ of Eu^{3+} and $^4G_{7/2}$ of Nd^{3+} are very close in energy; therefore they can be simultaneously excited at 590 nm. From these excited states, the electrons of Eu^{3+} can fall back to the $^7F_4$ state, generating the emission located at ~700 nm. The electrons of Nd^{3+}, from the $^4G_{7/2}$ level, followed a series of non-radiative relaxations that populate the $^4F_{5/2}$ level (among others). From this level, the radiative relaxation back to the ground state generates the emission at ~800 nm.[182,183] It is worth noticing here again that we only focused on the mechanisms to generate the emissions involved in the luminescent thermometers, independently of the fact that other emission lines can be generated with these ions.

Two examples that apply this combination of Nd^{3+} and Eu^{3+} ions involve YVO_4,[183] and Ba_2LaF_7,[182] as hosts. One of the interesting characteristics of these luminescent thermometers is that the emission that should be expected at around 750 nm for Nd^{3+}, arising from the transition of the $^4F_{7/2}$ level to the ground state, is very weak, compared with that observed in Nd^{3+}/Yb^{3+} luminescent thermometers, so it cannot be used for luminescence thermometry in this case. Another interesting feature of this class of thermometers is that while the emission of Eu^{3+} changes slightly with temperature, the emission of Nd^{3+} is highly dependent on the temperature, and its intensity increases as the temperature increases (Fig. 14(c)). In the case of Ba_2LaF_7, the S_{rel} reported was calculated using eqn (1), corresponding to S_{abs}, so it cannot be compared with that of other luminescent thermometers reported in the literature. From the fitting function a ΔE of 1890.8 cm^{-1} could be extracted,[182] a value that can be used to calculate S_{rel} using eqn (10), obtaining a value of 2.2% K^{-1} and a δT of 0.22 K at the lowest temperature under investigation (290 K).

From Table 1 and Fig. 15(a) and (b), it can be noted that the purpose of these Nd^{3+}/Eu^{3+}-codoped luminescent thermo-

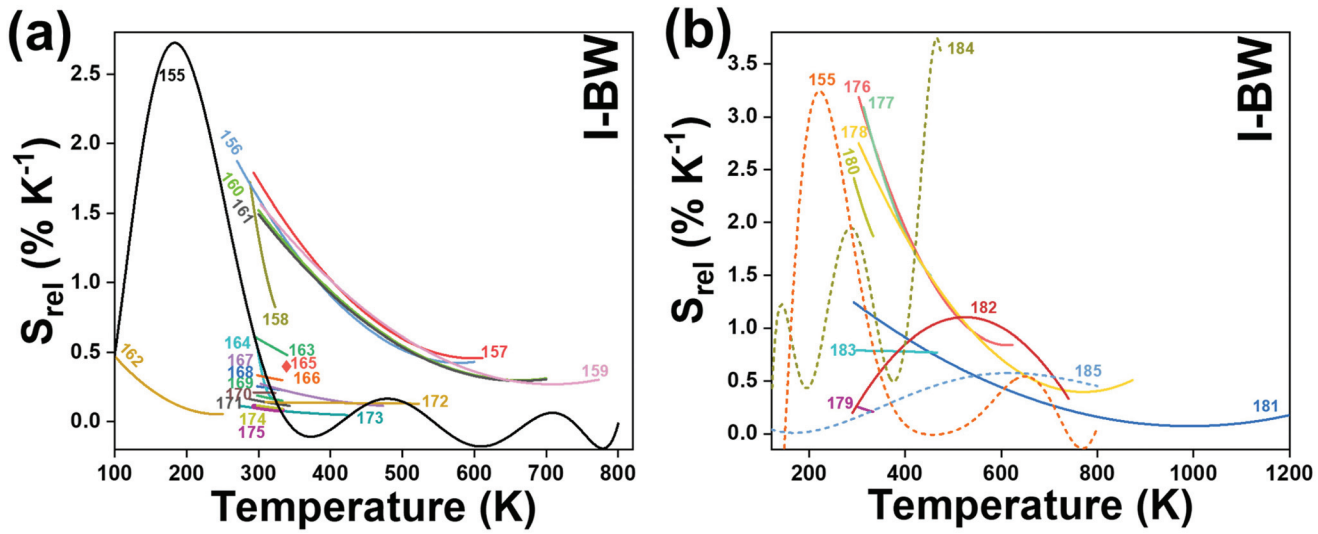

Fig. 15 Temperature dependence of S_{rel} for: (a) single doping and (b) codoping with other lanthanide ions (in solid lines) and transition metal ions (in dashed lines) for Nd^{3+} luminescent thermometers, operating in the I-BW. The numbers represent the corresponding references for each Nd^{3+}-based thermometer.

meters to achieve better thermal sensing properties than that of thermometers based on TCLs is partially achieved. The performance is better when compared with that of the Nd^{3+}/Yb^{3+} luminescent thermometers operating under TCL 3, similar to TCL 2, but still lower than that of TCL 1. However, an important aspect to consider here is that Nd^{3+}/Eu^{3+}-codoped luminescent thermometers are excited in the green region, whereas the ones based on Nd^{3+}/Yb^{3+} are excited in the NIR. Thus, a limitation for this class of luminescent thermometers is the penetration depth that can be achieved with them in biological applications.[86]

2.2.3. Dual Nd^{3+}/transition metal-codoped luminescent thermometers operating in the I-BW. The combination of Ln^{3+} with transition metals in the same host lattice introduces new luminescence properties involving the emissions of both kinds of ion.[213] Mixed Ln^{3+}/transition metal compounds with luminescence properties from both ions have emerged recently with especial interest for luminescence thermometry, attributable to the fact that the luminescence properties of the transition metals are drastically affected by local symmetry changes and the allowed character of the d–d transitions, which renders these ions as competitive thermal probes when compared with the f–f transitions of Ln^{3+}.[155,184,185] Here, the intensity of the emissions arising from the Ln^{3+} change barely with temperature; thus, they can be considered as reference signals.[155,184,185] For the Nd^{3+}-based luminescent thermometers operating in the I-BW, the transition metals involved for thermal sensing purposes include titanium,[184] chromium,[155] and manganese,[185] all embedded in yttrium aluminum garnet (YAG). To generate the emission lines, however, these materials have to be excited with UV (exciting Ti(IV) and Mn(IV)) and VIS (exciting Cr(III)) light (Table 1)), which will hamper their possible biomedical applications. As an illustrative example, Nd^{3+},Cr^{3+}-co-doped YAG was excited at 590 nm and the multiple emissions generated are presented in Fig. 16(a).

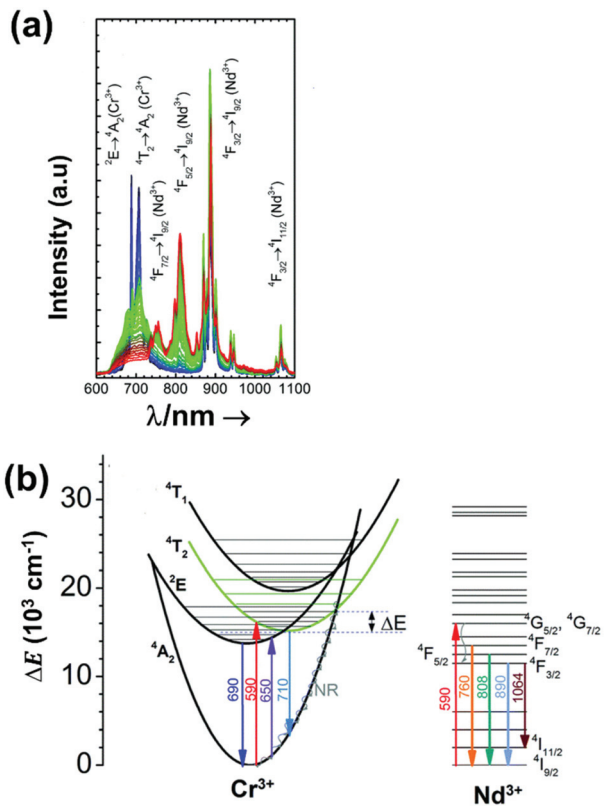

Fig. 16 (a) Emission lines and (b) mechanisms for their generation in Nd^{3+},Cr^{3+}-codoped YAG, after being excited at 590 nm. Reprinted with permission from ref. 155. Copyright 2017, the Owner Societies.

Absorption of light at 590 nm allows for the excitation of electrons of Cr^{3+} from the $^4A_2$ ground state to the $^4T_2$ excited state, which was followed by nonradiative multiphonon relax-

ation processes leading to the population of the ^2E state. Radiative relaxation from these two states led to narrow (690 nm) and broad emission bands (710 nm), assigned to the $^2E \rightarrow {}^4A_2$ and $^4T_2 \rightarrow {}^4A_2$ transitions, respectively.[155] In Fig. 16(b), the displacement of the position of the $^4T_2$ state with respect to that of the $^4A_2$ ground state is due to the distortion introduced by the crystal field, leading to the appearance of a crossing point between these parabolas.[155] Through this crossing point, electrons can be transferred to the ground state *via* nonradiative multiphonon relaxation processes, if the thermal energy provided to the system is sufficiently high.[155] Nd^{3+} emissions are generated after this ion absorbs the energy provided by the excitation source, promoting its electrons to the $^4G_{5/2}$, $^4G_{7/2}$ excited states, followed by a non-radiative relaxation to the $^4F_{3/2}$ state, where either: (i) radiative relaxation to the $^4I_{9/2}$ and $^4I_{11/2}$ states, or (ii) thermalization of the higher energy levels $^4F_{5/2}$ and $^4F_{7/2}$, can occur, giving rise to emission bands in the I-BW and II-BW.[155]

The performance of this luminescent thermometer (and the Nd^{3+}/Ti^{4+} and Nd^{3+}/Mn^{4+} systems as well) was evaluated through the intensity ratio, defined as:[155]

$$\Delta = \frac{I_{0\,\mathrm{Cr}}}{1+\exp\left(\frac{\Delta E_1}{k_B T}\right)} \frac{1}{I_{0\,\mathrm{Nd}} - \left[1+\exp\left(\frac{\hbar\omega}{k_B T}\right)\right]^p - \left(-\exp\left(\frac{\Delta E_2}{k_B T}\right)\right)} \quad (34)$$

The temperature dependence of this intensity ratio involves 3 mechanisms:

(i) the luminescence thermal quenching with a cross-over point, where $I_{0\ \mathrm{Cr}}$ and ΔE_1 represent the initial intensity of the Cr^{3+} emission bands at low temperature, and the energy difference between the bottom of the excited state parabola and the energy of the crossing point of the excited and ground state parabolas (Fig. 16(b)).

(ii) the temperature dependence of the intensity of the emission band arising from the $^4F_{3/2} \rightarrow {}^4I_{9/2}$ transition of Nd^{3+}, where $I_{0\ \mathrm{Nd}}$ is the initial intensity of this transition, whose intensity decreased as the temperature increased due to multiphonon depopulation processes, and where $\hbar\omega$ and p represent the maximum phonon energy of the host material and the number of phonons involved in the process, respectively.

(iii) the thermal depopulation of the $^4F_{3/2}$ state towards the $^4F_{5/2}$ state of Nd^{3+}, lying $\Delta E_2 = 1000\ cm^{-1}$ above the $^4F_{3/2}$ state.

S_{rel} was calculated according to eqn (2). The temperature dependence of S_{rel} for each Nd^{3+}/transition metal luminescent thermometer is presented in Fig. 15(b), whereas their maxima are listed in Table 1. A maximum S_{rel} of 3.49% K^{-1} was achieved for this class of luminescent thermometers, being higher than the one that can be achieved in Nd^{3+}/Yb^{3+} and single-doped Nd^{3+} luminescent thermometers.[155] In fact, this value of sensitivity is approximately 3 times higher than the thermal sensitivity that can be obtained when using the intensity ratio of TCL 2 or TCL 3 in single-doped Nd^{3+} in YAG. The reason behind this improvement in the thermometric performance is the efficiency of the $Cr^{3+} \rightarrow Nd^{3+}$ ET process.[155] This class of luminescent thermometers, constituted by the combination of the emissions arising from Nd^{3+} and a transition metal, definitely exhibit higher temperature-sensing performances, especially in the case of Nd^{3+}/Ti^{4+} and Nd^{3+}/Cr^{3+}. Thus, their potential application as temperature sensors is attractive. Despite this, as can be observed in Fig. 15(b) and in Table 1, the maximum S_{rel} values are either achieved at lower (Nd^{3+}/Cr^{3+}) or higher (Nd^{3+}/Ti^{4+}) temperatures than those similar to those that can be achieved with Nd^{3+}/Yb^{3+} luminescent thermometers (for Nd^{3+}/Ti^{4+} this value is ~3.3% K^{-1},[184] for example). It should be emphasized as well that these systems are quite complex, and detailed studies to understand the effect of the factors that govern the temperature-sensing properties, such as the electron–phonon interaction, the crystal field strength and the physical processes responsible for temperature susceptibility, are highly needed.[184] Last, these materials are excited with UV and VIS light, at wavelengths that might induce autofluorescence, phototoxicity, and limited penetration depths when applied in biological tissues.[86] Thus, novel strategies to excite these materials with NIR light sources are needed.

2.3. Europium-doped luminescent thermometers operating in the I-BW

The application of Eu^{3+}-doped materials as luminescent thermometers operating in the I-BW is based on their emissions located in the deep red region, ~710 nm, assigned to the $^5D_0 \rightarrow {}^7F_4$ transition. These thermometers are rarely reported in the literature (Eu^{3+}:Y_2O_3).[186] However, the most significant aspect of the Eu^{3+}:Y_2O_3 luminescent thermometer it that it offered for the first time the possibility of predicting the calibration curve of the thermometric parameter independently of the medium in which this thermometer operates, allowing the development of a luminescent primary thermometer based on Ln^{3+}-doped materials. Primary thermometers are systems in which the temperature can be determined based on the knowledge of thermodynamic laws and quantities.[214] In general, to extract the thermometric parameter, the calibration process requires an independent measurement of the temperature through a thermocouple or an IR camera. But when this thermometer operates in different media, a new calibration procedure is required. Hence, primary thermometers guarantee a single calibration procedure that is medium-free. The thermometric parameter, Δ, in Eu^{3+}:Y_2O_3 was determined by the ratio between the emission intensity of the its $^5D_0 \rightarrow {}^7F_4$ transition, when the $^5D_0$ state is excited through the $^7F_2$ or the $^7F_0$ state, in the physiological range of temperature, or through the $^7F_1$ and $^7F_0$ states, for lower temperatures (down to 180 K).[186] Considering the physiological range of temperatures as a particular region of interest for biomedical applications, Δ is defined as:

$$\Delta = \frac{I_{23}\ (^7F_2)}{I_{23}\ (^7F_0)} = \frac{p\ (^7F_2)}{p\ (^7F_0)} \frac{W_{31}\ (^7F_2)}{W_{31}\ (^7F_0)} \quad (35)$$

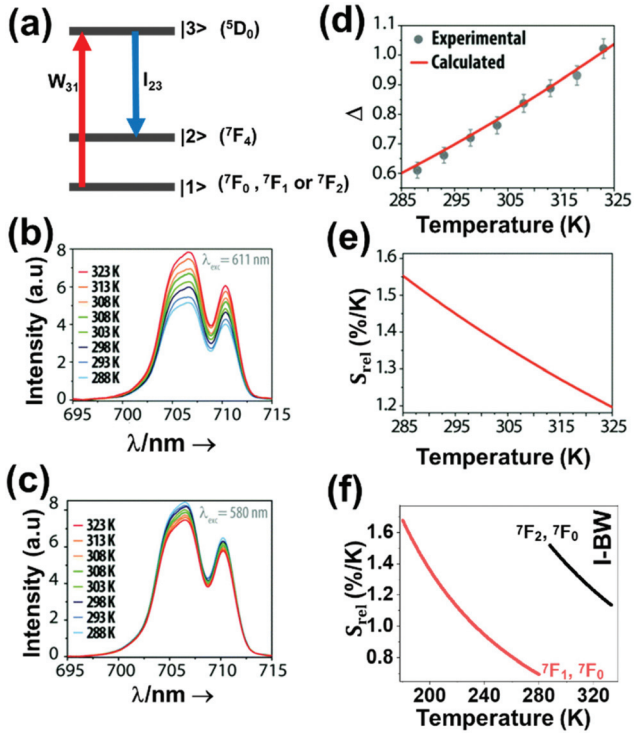

Fig. 17 (a) Energy level diagram used for stimulating the energy levels of Eu^{3+} involved in the luminescent thermometer operation. Deep red emission spectra of Eu^{3+}:Y_2O_3 nanocrystals excited at: (b) 611 nm, and (c) 580 nm. (d) Thermometric parameter calculated in the physiological range of temperatures. Points are the experimental values of the Δ parameter obtained from the spectra in (b) and (c) after being corrected for the respective excitation intensity, whereas the line is the calculated curve obtained from eqn (37), corresponding to the primary thermometer. (e) Relative sensitivity in the physiological range of temperatures. (b)–(e) Reprinted with permission from ref. 186. Copyright 2016, The Royal Society of Chemistry. (f) The variation of S_{rel} of Eu^{3+}-doped nanothermometers operating in the I-BW. The red line is computed using eqn (35) and the black line using eqn (36).

where I_{23} is the intensity of the transition from level 3 ($^5D_0$) to level 2 ($^7F_4$) at the steady state regime (Fig. 17(a)), p stands for the Boltzmann population factor, and W_{31} is the absorption rate from level 1 ($^7F_0$ or $^7F_2$) to level 3 (Fig. 17(a)).

Δ is determined by measuring the integrated areas under the emission curves of the $^5D_0 \rightarrow {}^7F_4$ transition, excited resonantly through the $^7F_2$ and the $^7F_0$ levels, considering that the two different excitations towards the $^5D_0$ level are the same and are dielectric in nature, and that the emitting level ($^5D_0$) and the $^7F_0$ ground state are nondegenerate:[186]

$$\Delta = \frac{S\left({}^5D_0 \rightarrow {}^7F_2\right)}{S\left({}^5D_0 \rightarrow {}^7F_0\right)} \exp\left(-\frac{\Delta E}{k_B T}\right) \quad (36)$$

where, S ($^5D_0 \rightarrow {}^7F_2$) and S ($^5D_0 \rightarrow {}^7F_0$) represent the area under the red emission curves, excited resonantly through the $^7F_2$ and $^7F_0$ levels, respectively; and ΔE stands for the energy difference between the $^7F_2$ and the $^7F_0$ levels. To calculate the thermometric parameter in the physiological range of temperatures, the theoretical expression of this parameter, predicted by considering the absorption rates in eqn (35), is expressed as:[186]

$$\Delta = 51 \exp\left(-\frac{875}{k_B T}\right) \quad (37)$$

where ΔE = 875 cm^{-1} and the pre-exponential factor 51 are determined from the energy difference between the barycenters when excited *via* the $^7F_2$ or $^7F_0$ level, and the ratio between the areas of the emissions rising from these levels, respectively. The experimental values of Δ were extracted from the integrated intensities of the $^5D_0 \rightarrow {}^7F_4$ transition. Two excitation wavelengths were used, 611 nm and 580 nm, to excite the $^5D_0$ level resonantly from the $^7F_0$ and the $^7F_2$ levels, respectively. The red emission observed displayed a different behavior with the increase of the temperature, depending on the excitation wavelength used. When excited at 611 nm, the intensity of the red emission increased due to the increase of the thermal population of the Stark sublevels of the $^7F_2$ state (Fig. 17(b)), whereas when excited at 580 nm, the opposite tendency was detected, due to the thermal depopulation of the $^7F_0$ ground state (Fig. 17(c)).

The experimental values were in excellent agreement with those obtained from the equation defining the primary thermometer (eqn (37)) (Fig. 17(d)), displaying an error of 3%,[186] and demonstrating the successful development of a Ln^{3+}-doped material as a primary luminescent thermometer. In terms of S_{rel}, it is in the order of 1.55% K^{-1} at the physiological range of temperatures (Fig. 17(e)). Higher values of thermal sensitivity (~1.7% K^{-1} at 180 K) were obtained when calculating the thermometric parameter from the red emission excited through the $^7F_1$ and $^7F_0$ levels. Also for this case, the principles of the primary thermometer could be applied, with a maximum error of 2%.[186] In that case, the thermometric parameter was defined as:

$$\Delta = \left[\frac{n^3\left(\frac{n^2+2}{3}\right)}{n^5}\right] \frac{S\left({}^5D_0 \rightarrow {}^7F_1\right)}{S\left({}^5D_0 \rightarrow {}^7F_0\right)} \exp\left(-\frac{\Delta E}{k_B T}\right) \quad (38)$$

where n stands for the refractive index of the host where the Eu^{3+} ions are embedded.

If we compare the performance of this single-doped Eu^{3+} luminescent nanothermometer with the dual emitting center Nd^{3+}/Eu^{3+} ones, based as well in the red emission of Eu^{3+}, the latter exhibit higher S_{rel} in the physiological range of temperatures (Table 1).

2.4. Erbium-doped luminescent thermometers operating in the I-BW

The application of erbium (Er^{3+}) doped materials as luminescent nanothermometers operating in the I-BW is mainly assigned to the presence of the red (~660 nm) and NIR (800 nm and 850 nm) emissions, either in single-doped materials, or in combination with other dopants, including other Ln^{3+} and transition metals.

2.4.1. Single Er^{3+}-doped luminescent thermometers operating in the I-BW. Single Er^{3+}-doped materials used as luminescent nanothermometers operating in the I-BW are based on the emissions located in the red and NIR. Upon excitation in the visible or NIR, these emission lines are generated, governed by the cross relaxation (CR) process ($^4F_{7/2}$, $^4I_{11/2}$) → ($^4F_{9/2}$, $^4F_{9/2}$) (Fig. 18(a)).[187] In short, the electrons of Er^{3+}, *via* absorption of two photons, are excited from the ground state to the $^4I_{11/2}$ level first, and further to the $^4F_{7/2}$ excited level at the end of the process. Also in short, the electrons of Er^{3+}, *via* the absorption of two photons, are excited from the ground state to the $^4I_{9/2}$ level first, and further to the $^4F_{7/2}$ excited level at the end of the process. From this level, successive non-radiative decays lead to the population of the $^4I_{9/2}$ and $^4F_{9/2}$ levels. From these levels, when relaxing back to the $^4I_{15/2}$ ground state, emissions lying in the red (654 nm) and in the NIR (806 nm) are generated (Fig. 18(a)).[187]

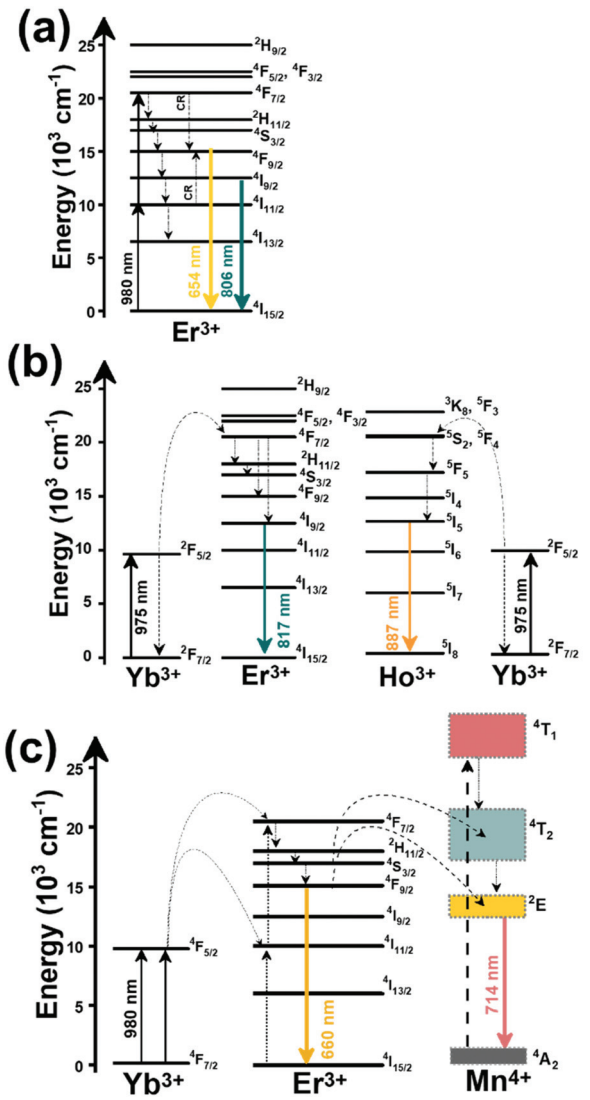

Fig. 18 Mechanisms of generation of the emission lines located in the I-BW of: (a) Er^{3+}, (b) $Er^{3+}/Ho^{3+}/Yb^{3+}$, and (c) $Er^{3+}/Mn^{4+}/Yb^{3+}$ doped materials.

The operation of these luminescent thermometers is based on the temperature dependence of the electronic population of the different Stark sublevels of the $^4F_{9/2}$ level, with emissions located in the red region, the intensity ratio of the emissions at ~800 nm, or the intensity ratio between the red and NIR emissions (Table 1). Among these, the high S_{rel} extracted from the intensity ratio of the NIR emissions represents a promising strategy.

Er^{3+}-doped strontium barium niobate (SBN) glass ceramic was investigated as a luminescent thermometer in a wide range of temperatures (300–700 K), by studying the intensity ratio in the NIR between the 800 nm and 850 nm emissions, attributed to the $^2H_{11/2}$ → $^4I_{13/2}$ and $^4S_{3/2}$ → $^4I_{13/2}$ electronic transitions, respectively.[161] The temperature dependence of this intensity ratio was fitted to the FIR equation (eqn (9)), achieving a maximum S_{rel} and a minimum δT of 1.39% K^{-1} and 0.36 K, respectively, at the lowest temperature investigated. It should be noted here that the authors did not report these two parameters, but they provided an experimental value of ΔE (872.3 cm^{-1}) between the thermally coupled $^2H_{11/2}$ and $^4S_{3/2}$ levels, which allowed us to determine their performance. However, the excitation wavelength (532 nm) used to activate this luminescent thermometer,[161] located in the visible region, may hamper its biological/biomedical applications.

The S_{rel} obtained from the intensity ratio between the red and NIR emissions is higher when compared with that achieved using the emissions of the Stark sublevels of the $^4F_{9/2}$ level. An example of this class of luminescent thermometers is that of Er^{3+} incorporated within active core–inert shell $NaErF_4$@$NaGdF_4$ nanoparticles.[187] The emissions of these nanocrystals, located at 654 nm and 806 nm, are generated from excitation either at 980 or 1530 nm.[187] These two emissions arise from NTCLs, and their performance was extracted by fitting the intensity ratio with a second-order polynomial function, as presented in eqn (27).

When using emissions arising from a different Stark sublevel of the $^4F_{9/2}$ level, red emissions (654 nm and 660 nm) were obtained after excitation at 800 nm. The S_{rel} of this class of luminescent nanothermometers was up to 9 times smaller than that obtained with the two other luminescent thermometer classes described in this subsection (Table 1). The reason for that is the low ΔE between the different Stark sublevels from which the emissions arose.[188,189] Moreover, the overlap of the two emission signals causes a low discriminability between the emission lines, and a large detection deviation.[189] Regardless of the poor performance of this class of luminescent thermometers (Fig. 19), it is worth mentioning here the idea behind heavily concentrated core@shell@shell Tm^{3+}:$NaErF_4$@Yb^{3+}:$NaYF_4$@Nd^{3+}:$NaYbF_4$ nanostructures, in which Tm^{3+}-mediated transient energy trapping coupled to Nd^{3+}/Yb^{3+} cascade-sensitization is used to efficiently trigger a single-band red emission of Er^{3+}, after careful optimization of the doping composition.[188]

2.4.2. Er^{3+}/Yb^{3+}-codoped luminescent thermometers operating in the I-BW. Materials codoped with Er^{3+} as an activator

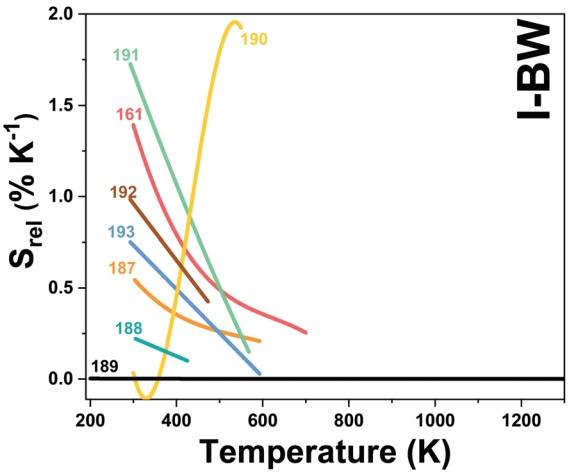

Fig. 19 Temperature dependence of S_{rel} of Er^{3+}-doped luminescent thermometers, operating in the I-BW. The numbers represent the corresponding references for each Er^{3+}-based thermometer.

and Yb^{3+} as a sensitizer are the most explored class of Er^{3+} luminescent thermometers operating in the I-BW. Yb^{3+} ions, due to the efficient absorption at 980 nm, allow the development of NIR-to-NIR based luminescent thermometers, besides improving the signal intensity of Er^{3+} emissions.[191–193] Er^{3+}/Yb^{3+}-codoped materials can be applied as luminescent thermometers based on the emissions of Er^{3+}, or in combination with other emissions arising from other Ln^{3+} or transition metals (Table 1). An effective strategy is the combination of emission arising from Er^{3+} and Ho^{3+} in the NIR region, in the presence of Yb^{3+} as a sensitizer, in hexagonal $NaLuF_4$ microcrystals.[191] The emission bands used to determine the thermometric performance of these particles are located at 887 nm and 817 nm, assigned to the $^5I_6 \rightarrow {}^5I_8$ transition of Ho^{3+} and the $^4S_{3/2} \rightarrow {}^4I_{13/2}$ transition of Er^{3+}, respectively. The mechanism of generation of these emissions is presented in Fig. 18(b). In short, Yb^{3+} absorbs the 975 nm excitation source and transfers the absorbed energy to the emitters Ho^{3+} and Er^{3+}, exciting their excited states *via* ET mechanisms.[191] From these excited states ($^4F_{7/2}$ for Er^{3+} and $^5S_2$, $^5F_4$ for Ho^{3+}), and *via* non-radiative decays, the $^4F_{9/2}$ (Er^{3+}) and $^5I_5$ (Ho^{3+}) electronic levels are populated, and from their radiative decays back to the ground states ($^4I_{15/2}$ (Er^{3+}) and $^5I_8$ (Ho^{3+})), the corresponding 817 nm and 887 nm emission lines are generated. Since these two emission lines arise from different emitting ions, the intensity ratio was fitted to a second-order polynomial function of the form of that in eqn (27). The maximum S_{rel} was ~1.73% K^{-1} at room temperature.[191]

When codoped Er^{3+},Yb^{3+} materials were investigated alone, without the addition of other ions, S_{rel} decreased around 2 times (Table 1). Two typical examples exploring this strategy are Er^{3+},Yb^{3+}: ZrO_2,[193] and Er^{3+},Yb^{3+}:YF_3 nanoparticles.[192] In these cases, the temperature-sensing properties were explored by using the emissions located in the red (Er^{3+},Yb^{3+}:ZrO_2) and NIR (Er^{3+},Yb^{3+}:YF_3) spectral regions, by exciting the particles at 980 nm. Here, it is important to note that the luminescent thermometer based on Er^{3+},Yb^{3+}:ZrO_2 nanoparticles worked under the so-called "valley-to-peak" model (VPR).[193] According to this model, and for emissions that originate from TCLs, if the emission lines are close enough, they will overlap, and as a consequence, a valley will be formed between them.[193,215] As the temperature increases, the linewidth of each emission peak broadens monotonically and the intensity valley formed overlaps also.[215] The VPR model is predicted to be a monotonic function of the temperature and is expressed as:[193,215]

$$\mathrm{VPR} = a(T - T_0) + b \quad (39)$$

where a is the slope of the linear fitting, b is a constant, and T_0 and T represent the initial and final temperatures, respectively. S_{rel}, described as the changing rate of VPR with temperature, is expressed as:[193,215]

$$S_{rel} = \frac{1}{\mathrm{VPR}} \frac{\mathrm{d}\,\mathrm{VPR}}{\mathrm{d}T} \quad (40)$$

The temperature evolution of this S_{rel} is presented in Fig. 19, together with that of the rest of the luminescent thermometers described in this subsection, showing a tendency to decrease as the temperature increases.

Er^{3+},Ho^{3+},Yb^{3+}:$NaLuF_4$ luminescent thermometers exhibit a S_{rel} two times larger (Table 1), so that the combination of the emissions of Er^{3+} and those of other Ln^{3+}, in the presence of Yb^{3+} as a sensitizer, is a promising strategy for luminescence thermometry.

An additional strategy towards better temperature-sensing properties is that of codoping materials with Er^{3+} and transition metals, such as Mn^{4+}. Manganese ions generally display red to NIR luminescence assigned to the spin-forbidden $^2E \rightarrow {}^4A_2$ transition under excitation with UV or blue light, owing to their high effective positive charge and the influence of a strong local crystal-field.[216,217] Upon proper modification of the crystal-field environment, the spectral position of these ions can be tuned from 620 nm to 723 nm.[218,219] Hence, since the luminescence of transition metals is highly influence by the medium in which they are embedded, and often it drastically reduces, this makes them highly desirable in luminescence nanothermometry, in combination with Ln^{3+}, in which the latter acts as a reference probe.[165,184,185,190]

In comparison with the case of materials codoped with Nd^{3+} and transition metal materials, in which the excitation source was UV or VIS light (section 2.2.3), here, the incorporation of Yb^{3+} as a sensitizer has allowed for excitation in the NIR, overcoming the problems related to the phototoxicity and limited penetration depth exhibited by UV and VIS light.

Triply doped Er^{3+},Mn^{4+},Yb^{3+}:YAP nanocrystals were investigated as luminescent temperature sensors operating in the I-BW over the temperature range 300–550 K.[190] They worked with the intensity ratio of the emissions arising from NTCLs located at 714 nm and 660 nm, corresponding to the $^2E \rightarrow {}^4A_2$ and $^4F_{9/2} \rightarrow {}^4I_{15/2}$ electronic transitions of Mn^{4+} and Er^{3+}, respectively. The generation of these emission bands is presented in Fig. 18(c). Yb^{3+} absorbs the energy of the 980 nm

excitation source, and *via* two photon-assisted processes, the excited energy levels ($^4F_{7/2}$ and $^4I_{11/2}$) of Er^{3+} are populated. Through a non-radiative decay process, the $^4F_{9/2}$ state is populated, which when relaxing back to the $^4I_{15/2}$ ground state generates the red emission at 660 nm. Via two ET processes, from the $^4F_{7/2}$ and $^4F_{9/2}$ levels of Er^{3+}, the $^4T_2$ and ^2E levels of Mn^{4+} are populated. The ^2E energy level can relax back to the $^4A_2$ ground state, generating the emission centered at 714 nm.[190]

To calculate the dependence of the intensity ratio with the temperature and the thermometric performance the same model as in the case of materials codoped with Nd^{3+} and transition metals (eqn (34)) was applied. The maximum S_{rel} obtained was 1.95% K^{-1} at 530 K.[190] Despite the relatively high thermal sensitivity reported, this value was obtained at a higher temperature than those used in the physiological range, for which S_{rel} reduces substantially.[190] The overall temperature dependence of S_{rel} of this material is depicted in Fig. 19, together with those of all the other Er^{3+}-doped luminescent thermometers operating in the I-BW.

To conclude with the section of Er^{3+}-doped luminescent thermometers operating in the I-BW, it should be said that the most promising strategy identified for improving their thermometric performance involves dual emitting center nanoparticles, either with other Ln^{3+} or with transition metals. Concerning the use of red or NIR emissions, the better choice is using NIR emissions, not only because of the better performance, but also because deeper penetration depths can be achieved.

2.5. Holmium-doped luminescent thermometers operating in the I-BW

Luminescent temperature sensors based only on holmium (Ho^{3+}) as an activator operating in the I-BW are very rare in the literature. The reason for that is because mainly Ho^{3+} is used together with Tm^{3+} for luminescence thermometry purposes exhibiting high relative thermal sensitivities in the I-BW (section 2.1.3) and in the III-BW (section 6.1).

The examples encountered involving Ho^{3+} as the main emitting ion incorporate Yb^{3+} as a sensitizer to enhance the red emission of Ho^{3+}, lying at around 660 nm and attributed to the $^5F_5 \rightarrow {}^5I_8$ electronic transition of this ion. Monoclinic Ho^{3+},Yb^{3+}:$KLu(WO_4)_2$ nanocrystals,[194] and tetragonal $Ba_2In_2O_5$ particles,[195] have been investigated as luminescent thermometers operating in the I-BW. The red emissions, located at ~650 nm and ~660 nm, were generated after exciting these at 980 nm. By means of ground state absorption (GSA), Yb^{3+} absorbs the radiation from the excitation source, exciting its electrons from the $^2F_{7/2}$ ground state to the $^2F_{5/2}$ excited state. Via two ET processes, the electrons of Ho^{3+} are promoted to the $^5I_6$ and $^5S_2$, $^5F_4$ energy levels. A nonradiative relaxation process from the $^5S_2$, $^5F_4$ energy levels populates the $^5F_5$ level, from which a radiative process generates the red emissions with two main peaks centered at ~650 nm and ~660 nm (Fig. 20(a)). A second path to explain the electronic population of the $^5F_5$ energy level can also be postulated from a non-radiative process after the first ET transfer process from Yb^{3+},

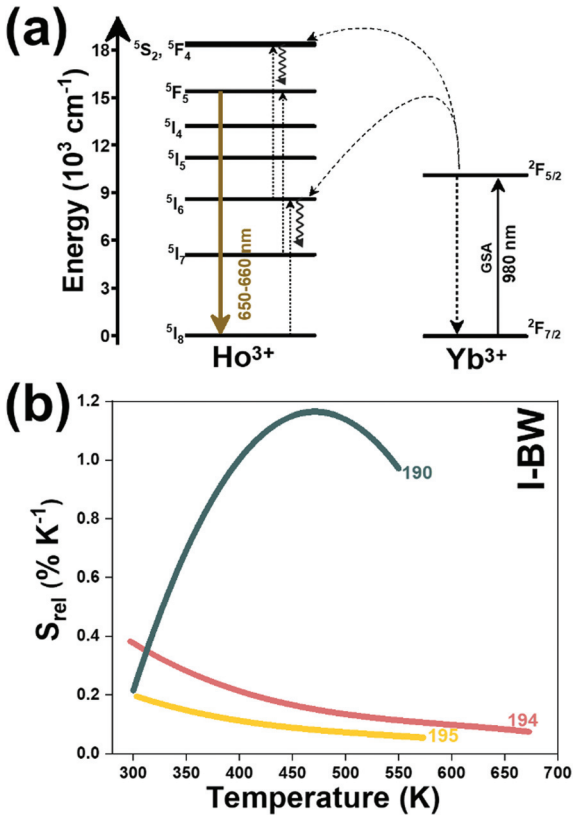

Fig. 20 (a) Mechanism of generation of the emission lines of Ho^{3+}/Yb^{3+}-doped luminescent thermometers. (b) Temperature dependence of S_{rel} of Ho^{3+}-doped luminescent thermometers operating in the I-BW. The numbers represent the references for each Ho^{3+}-based thermometer.

populating the $^5I_7$ energy level of the Ho^{3+} ion. The second ET from Yb^{3+} promotes these electrons directly to the $^5F_5$ energy level of Ho^{3+}.[194] These luminescent thermometers operate with emissions generated by TCLs. Nevertheless, for the case of Ho^{3+},Yb^{3+}:$KLu(WO_4)_2$ nanocrystals, the authors take into consideration the overlapping factor for the emission peaks, such as the case of red emissions of Ho^{3+}.[194] Hence, in that case, eqn (14) was used to fit the experimental data of the thermometric parameter, whereas for the case of Ho^{3+},Yb^{3+}:$Ba_2In_2O_5$ particles, the simple form of the FIR model (eqn (9)) was applied, which may lead to an underestimation of the performance of the luminescent thermometer. In fact, the S_{rel} of Ho^{3+},Yb^{3+}:$KLu(WO_4)_2$ nanoparticles is approximately four times higher than that of Ho^{3+},Yb^{3+}:$Ba_2In_2O_5$ particles (Table 1 and Fig. 20(b)). Nevertheless, the performance of Ho^{3+},Yb^{3+}:$KLu(WO_4)_2$ nanoparticles is lower (~3 times) compared with that of Ho^{3+},Mn^{4+},Yb^{3+}:YAP nanoparticles,[190] (Fig. 20(b)). The red emission of Ho^{3+} was combined with the 714 nm emission arising from Mn^{4+}, generated after NIR excitation ensured by the presence of Yb^{3+}. However, in the physiological range of temperatures, the S_{rel} of this material does not differ much from that of Ho^{3+},Yb^{3+}:$KLu(WO_4)_2$ nanoparticles.

3. Lanthanide-doped luminescent nanothermometers operating in the I- and II-BW simultaneously

The emissions of Ln^{3+} ions, upon proper excitation, could be located in a wide range of the electromagnetic spectrum. Besides lying in each of the four biological window regions, the emissions of Ln^{3+} ions used for thermometry can also be found in two different BWs. Hence, here, we focus our attention on the luminescent thermometers that use emissions which are placed in the I-BW and the II-BW. Although the number of publications that report luminescent thermometers working in this mixed region is reduced, the most representative examples are those of Nd^{3+}-doped materials due to the emissions located at 850 nm and 1050 nm, covering simultaneously the I- and the II-BWs.

3.1. Nd^{3+}-doped luminescent thermometers operating in the I-BW and II-BW region simultaneously

Nd^{3+}-doped materials operating in the I- and II-BWs simultaneously can be classified in single emitting Nd^{3+}-doped luminescent thermometers, dual emitting center luminescent thermometers in combination with other Ln^{3+}, and dual emitting center luminescent thermometers in combination with transition metals. Alkali earth fluorides such as CaF_2,[220] and SrF_2,[163] have been studied as hosts for single emitting Nd^{3+} luminescent thermometers, due to their low phonon energies that reduce the probability of non-radiative relaxing processes happening, favoring in this way the luminescence efficiency.[221] They are also biocompatible, and nanoparticles of these materials with sizes below 10 nm can be produced, which makes them attractive for biomedical applications.[163,220] These water-dispersible nanocrystals were prepared by hydrothermal synthesis,[222] in which Gd^{3+} was introduced to enhance the emissions of Nd^{3+}.[163,220] Upon excitation at 573 nm, these nanocrystals generate emissions at ~850 nm (I-BW) and ~1050 nm (II-BW), attributed to the $^4F_{3/2} \rightarrow {}^4I_{9/2}$ and $^4F_{3/2} \rightarrow {}^4I_{11/2}$ transitions of Nd^{3+}, respectively.[163,220]

Upon excitation at this wavelength, the $^4G_{5/2}$, $^4G_{7/2}$ energy levels of Nd^{3+} are populated. Then, a non-radiative decay process takes place populating the $^4F_{3/2}$ state. From this energy level, a radiative decay to the $^4I_{11/2}$ level generates the emission located in the II-BW (Fig. 21(a)). Concerning the emission in the I-BW, from the lower lying Stark sublevels of the $^4F_{3/2}$ level (R_1 in Fig. 21(a)), a radiative decay to the lower lying Stark sublevel of the $^4I_{9/2}$ ground state (Z_1 in Fig. 21(a)) generates this emission

The thermometric parameter for these luminescent thermometers was a FIR between the 1050 nm and 850 nm emissions in the physiological range of temperatures, using eqn (9). The results, summarized in Table 2, show that the highest S_{rel} was obtained for Nd^{3+}:SrF_2 nanoparticles with a value of 0.50% K^{-1} and δT of 1.2 K at room temperature.[163] The different thermometric performance of SrF_2 and CaF_2 can be due to the lower phonon energy of SrF_2 (366 cm^{-1}) compared with CaF_2 (466 cm^{-1}).[230] Thus, it seems that materials with low phonon energies maximize S_{rel}. Nevertheless, it should be taken into consideration that the excitation wavelength used to activate these luminescent thermometers is not located in the BW spectral regions; instead it is located in the VIS, for which the absorption and scattering in the biological tissues is high, resulting in a limited penetration depth, not allowing for deep-tissue imaging.[86] Hence, this limitation should be surpassed by using other ions that are able to absorb excitation sources located within the BWs spectral regions.

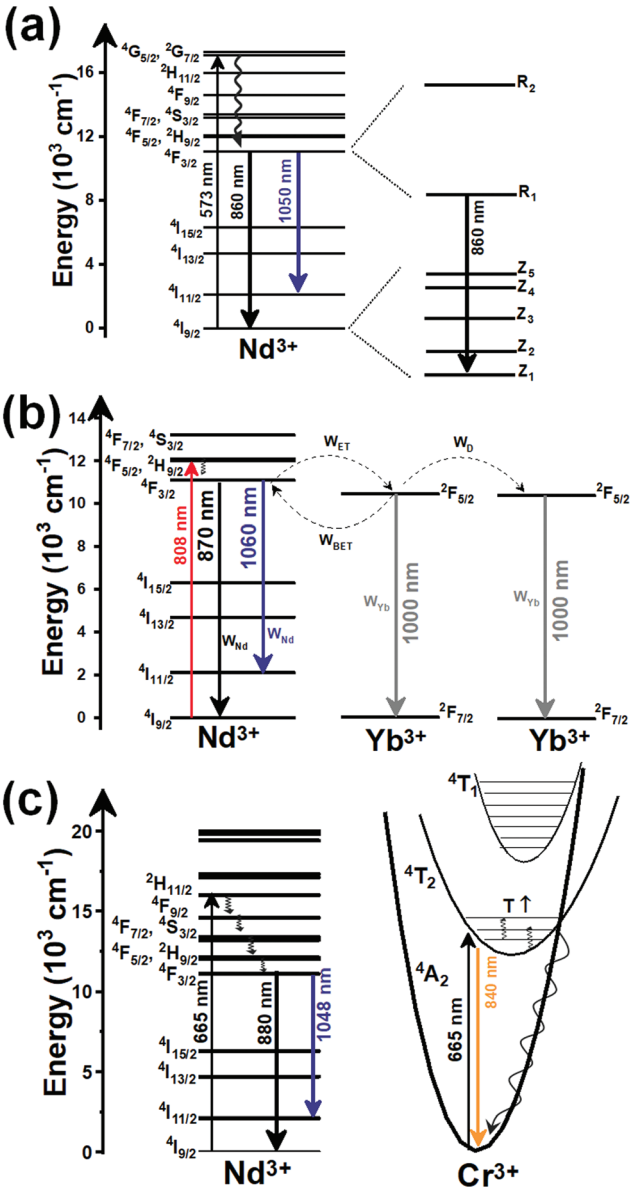

Fig. 21 Mechanisms of generation of the emission lines of: (a) single-doped Nd^{3+} luminescent thermometers excited at 573 nm, (b) dual emitting center Nd^{3+}/Yb^{3+} luminescent thermometers excited at 808 nm, and (c) dual emitting center Nd^{3+}/Cr^{3+} luminescent thermometers excited at 665 nm, operating simultaneously in the I- and II-BWs.

Table 2 Ln^{3+}-doped luminescent thermometers operating in the I and II-BWs. The table includes activators (A) and sensitizers (S). The excitation (λ_{exc}) and emission (λ_{em}) wavelengths are indicated in nanometers (nm), together with the corresponding electronic transition with which the emissions are associated. ΔT stands for the temperature range where the temperature reading was investigated. The thermometric parameter (Δ) indicates the luminescent nanothermometry class used in each case: FIR for band-shape, I for intensity ratio, and τ for lifetime, respectively. The maximum relative thermal sensitivity (S_{rel}) is given at the temperature at which this value was obtained. The minimum temperature resolution (δT) is given at the same temperature. We indicate with an asterisk S_{rel} or δT values calculated by us using the parameters published in the corresponding references. The double line separation between rows stands for different types (single or dual emitting centers) of lanthanide-doped nanothermometers, as discussed in the corresponding subsections

A	S	Host	λ_{exc} (nm)	λ_{em} (nm)	Transitions	ΔT (K)	Δ	S_{rel}/T (% K^{-1})/K	δT (K)	Ref.
Nd^{3+}	Nd^{3+}	Gd^{3+}:SrF_2	573	950, 1150	$^4F_{3/2} \rightarrow {}^4I_{9/2}$, $^4F_{3/2} \rightarrow {}^4I_{11/2}$	293–338	$FIR_{950/1150}$	0.50/293	1.2	163
Nd^{3+}	Nd^{3+}	Gd^{3+}:CaF_2	573	867, 1058	$^4F_{3/2} \rightarrow {}^4I_{9/2}$, $^4F_{3/2} \rightarrow {}^4I_{11/2}$	294–338	$FIR_{1058/867}$	0.12/294	1.85	220
Nd^{3+}, Yb^{3+}	Nd^{3+}	Nd:LaF_3@Yb:LaF_3	790	890 (Nd^{3+}), 1060 (Yb^{3+})	$^2F_{5/2} \rightarrow {}^2F_{7/2}$ (Yb^{3+}), $^4F_{3/2} \rightarrow {}^4I_{13/2}$ (Nd^{3+})	283–323	I_{890}/I_{1060}	0.41/283	1.2*	223
Nd^{3+}, Yb^{3+}	Nd^{3+}	Yb:LaF_3@Nd:LaF_3	790	890 (Nd^{3+}), 1060 (Yb^{3+})	$^2F_{5/2} \rightarrow {}^2F_{7/2}$ (Yb^{3+}), $^4F_{3/2} \rightarrow {}^4I_{13/2}$ (Nd^{3+})	283–323	I_{890}/I_{1060}	0.36/283	1.4*	223
Nd^{3+}, Yb^{3+}	Nd^{3+}	$LiLaP_4O_{12}$	808	870 (Nd^{3+}), 1000 (Yb^{3+})	$^4F_{3/2} \rightarrow {}^4I_{9/2}$, ($Nd^{3+}$), $^2F_{5/2} \rightarrow {}^2F_{7/2}$ (Yb^{3+})	93–663	I_{870}/I_{1000}	0.3/330	1.6*	201
Nd^{3+}, Yb^{3+}	Nd^{3+}	Nd,Yb:LaF_3	790	890 (Nd^{3+}), 1060 (Yb^{3+})	$^2F_{5/2} \rightarrow {}^2F_{7/2}$ (Yb^{3+}), $^4F_{3/2} \rightarrow {}^4I_{13/2}$ (Nd^{3+})	283–323	I_{1300}/I_{1000}	0.1/283	5*	223
Nd^{3+}, Cr^{3+}	Nd^{3+}, Cr^{3+}	$LiLaP_4O_{12}$	665	810 (Cr^{3+}), 1048 (Nd^{3+})	$^4T_2 \rightarrow {}^4A_2$ (Cr^{3+}), $^4F_{3/2} \rightarrow {}^4I_{11/2}$ (Nd^{3+})	293–323	I_{810}/I_{1048}	4.89/323	0.10*	224
Er^{3+}, Yb^{3+}	Yb^{3+}	$NaYF_4$@SiO_2	975	810 (Er^{3+}), 1010 (Yb^{3+})	$^4I_{9/2} \rightarrow {}^4I_{15/2}$ (Er^{3+}), $^2F_{5/2} \rightarrow {}^2F_{7/2}$ (Yb^{3+})	299–337	I_{1010}/I_{810}	1.64/337	0.76	225
Yb^{3+}	Yb^{3+}	$NaGdF_4$	808	1012	$^2F_{5/2} \rightarrow {}^2F_{7/2}$	303–343	τ_{1012}	1.59/343	0.31*	226
Yb^{3+}	Nd^{3+}	$NaYF_4$@Y@CaF_2	800	980	$^2F_{5/2} \rightarrow {}^2F_{7/2}$	283–337	τ_{980}	1.4/283	0.36*	227
Yb^{3+}	Yb^{3+}	$Bi_7F_{11}O_5$	808	1030	$^2F_{5/2} \rightarrow {}^2F_{7/2}$	323–573	τ_{1012}	0.24/323	2.1*	228
Yb^{3+}, Cr^{3+}	Yb^{3+}, Cr^{3+}	$LiLaP_4O_{12}$	665 + 920	820 (Cr^{3+}), 975 (Yb^{3+})	$^4T_2 \rightarrow {}^4A_2$ (Cr^{3+}), $^2F_{5/2} \rightarrow {}^2F_{7/2}$ (Yb^{3+})	100–475	I_{820}/I_{975}	1.2/333	0.42*	229
Yb^{3+}, Cr^{3+}	Yb^{3+}, Cr^{3+}	$LiLaP_4O_{12}$	665	820 (Cr^{3+}), 975 (Yb^{3+})	$^4T_2 \rightarrow {}^4A_2$ (Cr^{3+}), $^2F_{5/2} \rightarrow {}^2F_{7/2}$ (Yb^{3+})	100–475	I_{820}/I_{975}	0.32/333	1.6	229

An interesting alternative, was proposed by Marciniak *et al.* through the preparation of dual emitting center luminescent thermometer-based Nd^{3+},Yb^{3+}:$LiLaP_4O_{12}$ nanoparticles, in which, under 808 nm NIR excitation, Nd^{3+} acts both as a sensitizer and an activator, while Yb^{3+} acts only as an activator.[201] The reason for this selection is because the Nd^{3+} absorption cross section at 800 nm is higher than that of Yb^{3+} at 980 nm, and the water absorption at 800 nm is around 25 times lower than that at 980 nm, overcoming in this way also the overheating problems displayed by the 980 nm excitation.[201] Upon 808 nm excitation, Nd^{3+} absorbs this energy and excites its electrons from the $^4I_{9/2}$ ground state to the $^4F_{5/2}$ excited state. Via a non-radiative process, the $^4F_{3/2}$ state is populated. From this state, two radiative processes towards the $^4I_{9/2}$ and $^4I_{11/2}$ levels generate the Nd^{3+} emissions at 870 nm and 1060 nm, respectively (Fig. 21(b)). From the $^4F_{3/2}$ state of Nd^{3+}, an ET process with W_{ET} probability can populate the $^2F_{5/2}$ state of Yb^{3+}. A radiative decay from this state, back to the $^2F_{7/2}$ ground state, allows for the generation of the 1000 nm emission band of Yb^{3+}.[201] The thermometric parameter of these nanocrystals was defined as the intensity ratio between the emissions at 870 nm (Nd^{3+}) and 1000 nm (Yb^{3+}) as function of the temperature over the range 93–663 K, and as a function of the concentration of Yb^{3+} ions (Fig. 21(a)). The thermometric performance of these nanocrystals is influenced by three processes: (i) with the increase of temperature, the electronic population of the Stark sublevels of the $^2F_{5/2}$ manifold of Yb^{3+} increases gradually, leading to a BET process, with probability W_{BET}, towards the $^4F_{3/2}$ state of Nd^{3+} (Fig. 21(b)); (ii) by increasing the concentration of Yb^{3+}, the average distance between these ions decreases, and consequently, the energy diffusion between Nd^{3+} and Yb^{3+} ions, with probability W_D, and among Yb^{3+} ions (W^{Yb}) increases; and (iii) the energy difference between the $^4F_{3/2}$ state of Nd^{3+} and the $^2F_{5/2}$ level of Yb^{3+}, that controls the ET processes, with probability W_{ET}, is affected by the changes of temperature and the concentration of Yb^{3+}.[201] Hence, the intensity ratio between these two nonresonant energy matching ions, extracted from the phonon-assisted model of ET described by Miyakawa and Dexter,[231] was correlated to these processes by the following equation:[201]

$$\Delta = \frac{W_{BET} - W_D - W^{Yb}}{W_{ET}} \quad (41)$$

From eqn (41) it can be deduced that as the doping concentration of Yb^{3+} increases, the effectiveness of the energy diffusion among the Yb^{3+} network gradually increases, while the impact of the BET process towards Nd^{3+} decreases, leading to changes in Δ. The highest S_{rel} was obtained for the highest concentration of Yb^{3+} (Fig. 22(a)), probably because the decrease in the average distance among the Nd^{3+}–Yb^{3+} ions facilitated energy diffusion.[201] The S_{rel} of these luminescence thermometers is, however, very low, with a maximum of 0.3% K^{-1} in the physiological range of temperatures (the full variation of the S_{rel} in the interval of temperatures analyzed is presented in Fig. 22(b)).

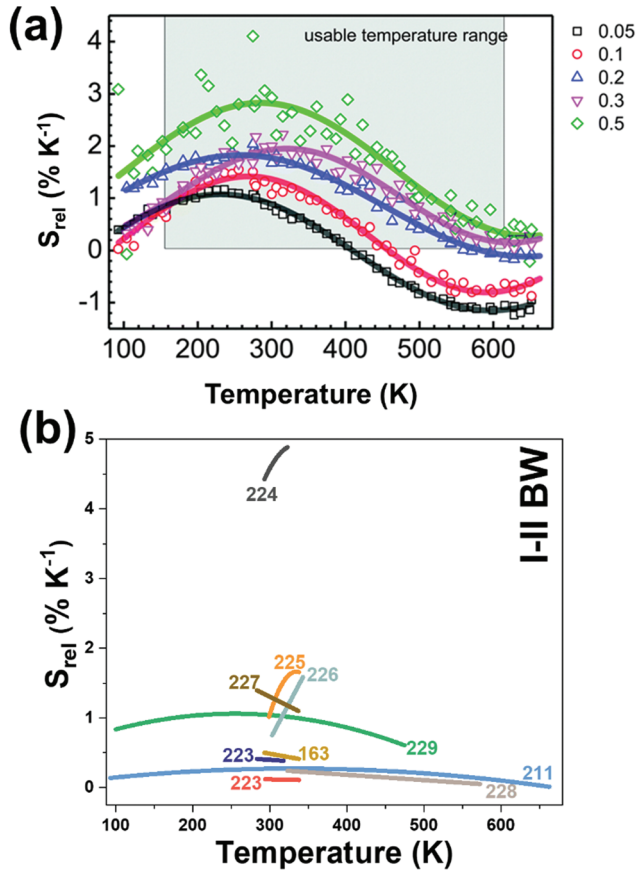

Fig. 22 (a) S_{rel} of Nd^{3+}- and Yb^{3+}-doped $LiLaP_4O_{12}$ as a function of Yb^{3+} concentration. Reprinted with permission from ref. 201. Copyright 2015, the Owner Societies. (b) Temperature dependence of S_{rel} of lanthanide-doped luminescent thermometers operating in the I-BW and II-BWs, simultaneously. The numbers indicate the corresponding references for each thermometer.

The same strategy was followed for the case of two different active core@active shell nanostructures, one having the core doped with Nd^{3+} and the shell with Yb^{3+} (Nd^{3+}:LaF_3@Yb^{3+}:LaF_3), and the other constituted by a Yb^{3+}-doped core and a Nd^{3+}-doped shell (Yb^{3+}:LaF_3@Nd^{3+}:LaF_3).[223] The performance of these two different core@shell structures was also compared with the corresponding nanoparticles containing the two ions in the same layer, revealing a four-fold enhancement of S_{rel}. In addition, the core@shell nanocrystals displayed an enhanced emission intensity, attributed to the reduction of intensity when the doping ions are located in the same layer due to self-quenching effects originating from non-radiative mechanisms such as cross-relaxation, energy migration, and energy-trap processes occurring between the emitting ions and the OH^- radicals present at the surface of the nanoparticles.[223] These types of material, however, are more interesting for the emissions generated by Nd^{3+} in the II-BW (1060 nm and 1350 nm); hence they will be mentioned again in section 4.2.

When combining the emissions arising from Nd^{3+} and those of a transition metal, such as Cr^{3+}, a substantial increase on S_{rel} is observed (Table 2). In that case, the emission of Nd^{3+} located at ~1050 nm in the II-BW was combined with the emission at 810 nm of Cr^{3+} in the I-BW, both ions being embedded in $LiLaP_4O_{12}$.[224] These emission bands were generated after exciting the nanoparticles at 655 nm, in the lower limit of the I-BW that allows the excitation of Cr^{3+} and Nd^{3+} at the same time. To describe the generation of the emission band of Cr^{3+}, a low crystal field assumption for the low-symmetry host used was applied by the authors. Electrons of Cr^{3+} are excited after illumination with the 655 nm light from the $^4A_2$ fundamental state to the $^4T_2$ excited state (Fig. 21(c)).

When relaxing back to the $^4A_2$ state, the broad emission line centered at ~810 nm is generated. When the temperature increases, the electronic population of the higher vibrational levels of the $^4T_2$ state also increases, and the Cr^{3+} emission can be quenched *via* non-radiative processes as soon as the thermally excited electrons reach the crossing point between the $^4T_2$ and $^4A_1$ energy level parabolas (Fig. 21(c)).[232] At the same time, the electrons of Nd^{3+} are pumped from the $^4I_{9/2}$ ground state to the $^2H_{11/2}$ excited state. Then, a non-radiative relaxation to the $^4F_{3/2}$ state happens, from which the 880 nm ($^4F_{3/2} \rightarrow {}^4F_{9/2}$) and the ~1050 nm ($^4F_{3/2} \rightarrow {}^4I_{11/2}$) emissions are produced.[224] The intensity of the emission of Nd^{3+} is barely influenced by temperature, so it can be used as a reference probe. A maximum S_{rel} of 4.89% K^{-1} at 323 K (Fig. 22(b) was obtained in this case.

In Nd^{3+},Cr^{3+}-doped $LiLaP_4O_{12}$ nanoparticles, as the size of the nanocrystals decreases, the intensity of the emissions decreases (~0.81% nm^{-1}, Fig. 23(a)), the emission band position blue-shifts (~0.066 nm grain size^{-1}), the temperature-sensing region narrows (from 300 to 600 K for particles with a size of 240 nm to 300–420 K for particles with a size of 20 nm), S_{rel} increases from 1% K^{-1} to 5% K^{-1} (Fig. 23(b)), and δT drops down to 0.03 K (Fig. 23(c)).[232] The reason for that is that with

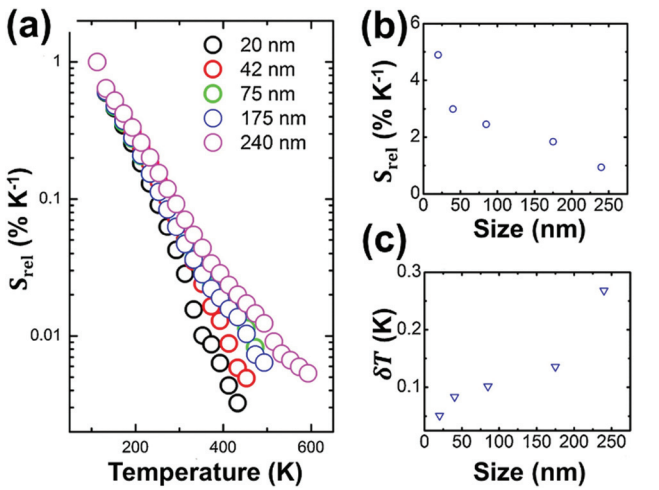

Fig. 23 The effect of the size of Nd^{3+},Cr^{3+}:$LiLaP_4O_{12}$ nanoparticles on: (a) the intensity ratio between the emissions lines of Cr^{3+} and Nd^{3+} at 810 nm and 1048 nm, respectively, (b) S_{rel}, and (c) δT. Reprinted with permission from ref. 232. Copyright 2016, Elsevier.

the decrease of the size of the nanoparticles, non-radiative depopulation processes become more important, being the main processes responsible for the decreasing of the intensity of the emissions. Furthermore, this leads to a faster decrease in the intensity ratio used in the luminescent thermometer, which allows a higher S_{rel} and a lower δT to be obtained.[232]

3.2. Yb^{3+}-doped luminescent thermometers operating in the I- and II-BWs simultaneously

Another example of luminescent thermometers operating simultaneously in the I- and II-BWs is that of Yb^{3+}-doped materials, based on the ~1000 nm emission of this ion, combined with other emissions arising from other Ln^{3+} or transition metal ions.

Only a few publications explored the case of dual emitting center luminescent thermometers consisting of Yb^{3+} with another Ln^{3+} (such as Er^{3+}) or a transition metal ion (such as Cr^{3+}). For the Yb^{3+}/Er^{3+}-coemitting material, the host was an active core of hexagonal $NaYF_4$ nanorods coated with an amorphous silica shell, synthesized by a hydrothermal method.[225] Under excitation at 975 nm, Yb^{3+} acts as a sensitizer, besides the role of activator, absorbing the energy of the excitation source and transferring this energy to Er^{3+} (Fig. 24(a)). By these ET processes, the $^4F_{7/2}$ state of Er^{3+} can be populated, from which a non-radiative decay can take place that populates the $^4F_{9/2}$ and $^4I_{9/2}$ energy levels of Er^{3+}. From there, by relaxing back to the $^4I_{15/2}$ ground state, the red emission at 660 nm and the NIR emission located at 810 nm are generated, respectively.[225] The 1010 nm emission of Yb^{3+} is generated by simply relaxing back the electrons to the $^2F_{7/2}$ ground state from the $^2F_{5/2}$ excited energy level. The thermometric performance of this material was extracted by studying the temperature dependence of the 1010 nm/810 nm and 1010 nm/660 nm intensity ratios, both modelled according to a second-order polynomial fitting equation, as expected for a luminescent thermometer based on NTCLs (eqn (27)). The results reveal that the 1010 nm/810 nm intensity ratio allows a S_{rel} two times higher than the 1010 nm/660 nm intensity ratio to be obtained.[225] The maximum S_{rel} was 1.64% K^{-1} and the minimum δT was 0.76 K, both obtained at 337 K.[225]

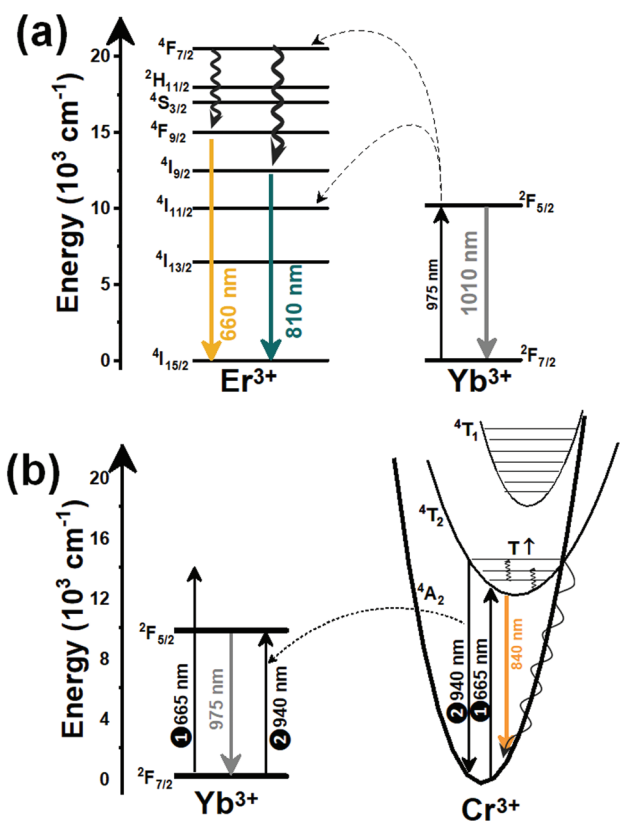

Fig. 24 Mechanisms of generation of the emission lines of dual-doped (a) Er^{3+}/Yb^{3+} and (b) Cr^{3+}/Yb^{3+} materials operating simultaneously in the I- and II-BWs.

In the case of Yb^{3+},Cr^{3+}:$LiLaP_4O_{12}$,[229] the intensity ratio between the emissions of Cr^{3+} located at 840 nm and Yb^{3+} located at 975 nm did not allow the obtaining of results as promising as those obtained for the combination of Nd^{3+}/Cr^{3+}. To generate these emission bands, a first alternative is excitation at 665 nm that allows the excitation of electrons of Cr^{3+} from the $^4A_2$ ground state to the $^4T_2$ excited state. A radiative relaxation from this level led to a broad emission band, centered at ~840 nm, assigned to the $^4T_2 \rightarrow {}^4A_2$ transition, as explained before. Also, after thermalization of the higher energy levels of the $^4T_2$ excited state, an emission at 940 nm can take place, when relaxing back radiatively to the ground state. For the excitation of Yb^{3+}, the authors considered an ET process from Cr^{3+} to Yb^{3+} or a reabsorption process of the 940 nm emission band generated by Cr^{3+}, that allowed excitation of the Yb^{3+} electrons to the $^2F_{5/2}$ level (Fig. 24(b)), from where the radiative relaxation to the ground state generated the emission line at 975 nm used in the luminescent thermometer.

Here, the maximum S_{rel} obtained in the physiological range of temperatures was 0.32% K^{-1}, with a δT of 1.6 K.[229] The authors tried to correlate the differences between the sensitivity of Yb^{3+}/Cr^{3+} and Nd^{3+}/Cr^{3+} luminescent thermometers to the population mechanism of the excited states in these ions. For the Nd^{3+}/Cr^{3+} combination, the 655 nm excitation wavelength was chosen to excite simultaneously both ions.[224] For the Yb^{3+}/Cr^{3+} combination, the simple energy diagram of Yb^{3+} and the lack of high energy levels hampers the simultaneous excitation of both ions, which concurrently reduces the sensitivity of such luminescent thermometers.[229] A possible solution for the dually doped Yb^{3+}/Cr^{3+} materials would be the use of two excitation beams simultaneously, one for Cr^{3+} (at 650 nm) and another one for Yb^{3+} (~940 nm). In terms of thermometric performance, this last approach achieved a three times higher S_{rel} (Fig. 25), with a value of 1.2% K^{-1}.[229] However, this approach is technically rather complex, and exhibits strong sensitivity fluctuations above 320 K (Fig. 25).[229]

Recently, lifetime nanothermometry[226–228] has been applied for materials operating within the I and II BWs simultaneously. Tan *et al.* studied the temperature dependence of the 980 nm emission of Yb^{3+} in a $NaYF_4$@$NaYF_4$:Nd^{3+},

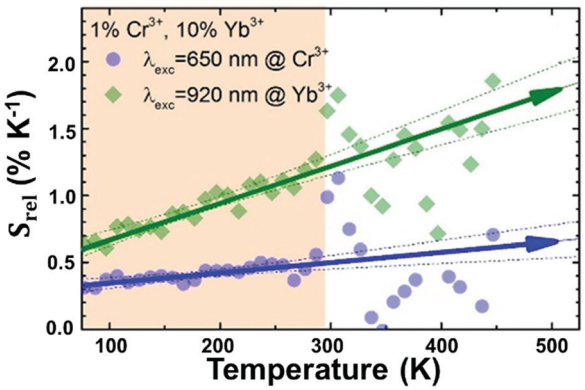

Fig. 25 S_{rel} of codoped Cr^{3+},Yb^{3+}:$LiLaP_4O_{12}$ nanoparticles operating simultaneously in the I- and II-BWs, as a function of the excitation wavelength. Reprinted with permission from ref. 229. Copyright 2016, Elsevier.

Yb^{3+}@CaF_2 core–shell nanostructure with a size of 13.5 nm.[227] This nanostructure does not only minimize the probability of deactivation processes happening, produced by crystal defects and surface quenching centers, but also maximizes the thermal sensitivity of the luminescent nanothermometer. The emission band of Yb^{3+} is generated after exciting the nanoparticles at 800 nm. Nd^{3+} ions absorb this energy to promote their electrons from the $^4I_{9/2}$ ground state to the $^4F_{5/2}$ excited state. From here, a non-radiative relaxation leads to the population of the $^4F_{3/2}$ level. From this level, which is resonant in energy with the $^2F_{5/2}$ level of Yb^{3+}, ET and BET processes occur. ET processes populate the $^2F_{5/2}$ level of Yb^{3+}, from which, upon relaxation back to the $^2F_{7/2}$ ground state, the 980 nm emission band is generated (as has been described in Fig. 21(b)).

The lifetime of this emission was recorded from 283 K to 337 K, after optimizing the concentration of the Ln^{3+} ions in these structures. This temperature dependence was governed by the temperature dependence of the ET and BET rates, the multiphonon process probabilities, and the energy migration that can take place among Yb^{3+} ions. The authors modelled the lifetime according to a polynomial function (as that presented in eqn (23)) and S_{rel} was expressed as follows:[227]

$$S_{rel} = \left|\frac{1}{\tau}\frac{d\tau}{dT}\right| \times 100\% \quad (42)$$

The maximum S_{rel} was obtained at the lowest temperature under investigation with a value of 1.4% K^{-1}.

Similarly, Wang *et al.*[228] and Ji *et al.*[226] studied the temperature dependence of the lifetime of this emission embedded in $Bi_7F_{11}O_5$ and Nd^{3+}:$NaGdF_4$ (see Table 2), respectively. Here the chosen fitting model was an exponential equation (as that presented in eqn (19)). Among these materials, Yb^{3+},Nd^{3+}:$NaGdF_4$ displayed the highest S_{rel} with a value of 1.59% K^{-1} at 343 K. The variation of S_{rel} with temperature is presented in Fig. 22(b). Lifetime nanothermometry, although not too much used within the BW regions, portrays a potential and very powerful route towards biomedical applications of Ln^{3+}-doped luminescent nanothermometers, as it is independent of the optical properties of the medium in which the nanoparticles are embedded.[227] However, this technique requires the use of complex and expensive acquisition systems based on either fast detectors or time-gated detection procedures, which might hamper their implementation at a practical level.

4. Lanthanide-doped luminescent nanothermometers operating in the II-BW

Lanthanide-doped luminescent thermometers operating in the II-BW are based on Yb^{3+} and Nd^{3+}-doped materials. The explanation for this relies on the ability of these two Ln^{3+} ions to absorb the energy of an excitation source located in the I-BW, and generate emissions in the II-BW,[48,90,233] providing deeper penetration depths into biological tissues, while maintaining a high spatial resolution.[86,90,233] The luminescent thermometers based on Yb^{3+} use the emission at ~1000 nm, either in single-doped materials by studying the Stark sublevels of the electronic transition that generate this emission, or combined with other emissions arising from other Ln^{3+}, including Tm^{3+} and Nd^{3+}. Luminescent thermometers based on Nd^{3+}-doped materials used the emissions arising from the Stark sublevels of the 1050 nm and 1330 nm emission bands in single-doped materials, or the combination with emissions from other Ln^{3+} (Ho^{3+}) in codoped materials, or from semiconductor quantum dots in dual emitting materials.

4.1. Yb^{3+}-doped luminescent nanothermometers operating in the II-BW

4.1.1. Single Yb^{3+}-doped luminescent thermometers operating in the II-BW. The number of reports based on single Yb^{3+}-doped materials operating as luminescent thermometers in this spectral region is scarce, and their thermometric performance is relatively poor. For instance, a hybrid compound composed of mesostructured dipyridyl-pyridazine functionalized either with ethenylene bridged mesoporous organosilica (dppz-ePMO) or vinyl silica (vSilica) were both complexed with ytterbium(III) on 2-thenoyltrifluoroacetonate ($Yb(tta)_3$).[234] The different peaks in the manifold corresponding to electronic transitions between the different Stark sublevels of the $^2F_{5/2} \rightarrow {}^2F_{7/2}$ transition of Yb^{3+} in dppz-ePMO@$Yb(tta)_3$ and dppz-vSilica@ $Yb(tta)_3$ particles, located at 990 nm and 1025 nm or 986 nm and 1015 nm, respectively, were used to determine the temperature through the FIR method. These emission lines have been generated in these materials *via* excitation with ultraviolet light. In this way, the $^4f_{13}$ electronic configuration of Yb^{3+} can easily gain one electron to reach the more stabilized $^4f_{14}$ configuration of the full shell, corresponding to Yb^{2+}. This tendency of reduction to Yb^{2+} enables the Yb^{3+} ion in some hosts, such as is the case with these organic complexes, to receive an electron from the host's anion under high-energy

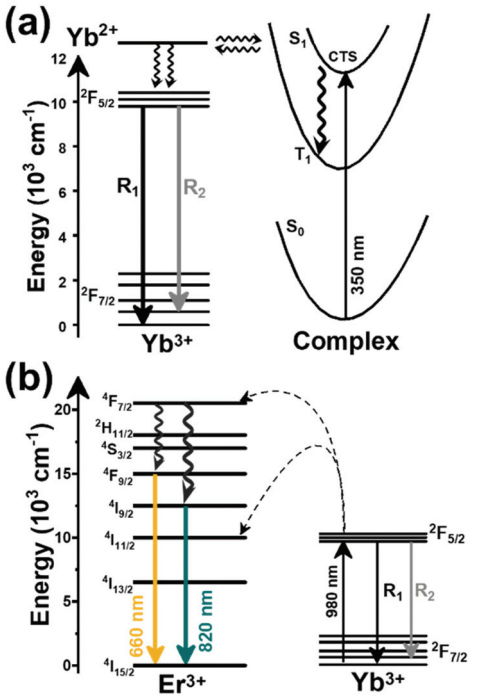

Fig. 26 Mechanisms of generation of Yb^{3+} emissions lines in: (a) organic complexes *via* charge transfer state (CTS) and (b) ZrO_2 codoped with Er^{3+}.

external excitation, such as UV light, forming a charge transfer state (CTS) (Fig. 26(a)). The CTS of Yb^{3+} can transfer the excitation energy to the $^2F_{5/2}$-emitting state *via* a non-radiative relaxation process, generating the emission bands located at around 980–990 nm (labelled as R_1) and 1015–1025 nm (labelled as R_2).

Nevertheless, for these hybrids, besides the low S_{rel} they exhibit (0.13–0.17% K^{-1}) with maximum values at cryogenic temperatures (110 K)[234] (Table 3), they are excited with UV light, hampering significantly their implementation in possible biomedical applications.

Another choice to excite single Yb^{3+}-doped luminescent thermometers operating in the II-BW is using NIR light at 980 nm. This approach has been investigated in ZrO_2 nanocrystals codoped with Er^{3+}, in which the authors investigated the performance of the thermometer in the I-, II- and III-BWs, using the different emissions of Er^{3+} and Yb^{3+}.[193] For the luminescent thermometer operating in the II-BW the linear model of VPR (eqn (39)) was applied between the different peaks in the manifold corresponding to the $^2F_{5/2} \rightarrow {}^2F_{7/2}$ electronic transition of Yb^{3+}, with peaks located at 1023 nm (label R1 of Fig. 26(b)) and 1036 nm (label R2 of Fig. 26(b)).[193] The mechanism for the generation of these emission lines is similar to that reported in Fig. 24(a), in which Yb^{3+} not only acts as a sensitizer, but also as an activator. These nanocrystals exhibited a better S_{rel} with a value of 1.1% K^{-1} at room temperature, making this approach a better strategy towards the development of single Yb^{3+}-doped luminescent thermometers operating in the II-BW. Nevertheless, as pointed out before, the strong water absorption band at around 980 nm makes Yb^{3+}-based luminescent nanothermometers pumped at this wavelength not ideal for biomedical or biological applications, as it might generate strong heating in the biological tissues when excessive pumping power densities are applied, which might damage biological tissues.[206]

4.1.2. Dual-doped Yb^{3+}/Ln^{3+} luminescent thermometers operating in the II-BW. Dual-doped Yb^{3+}/Ln^{3+} luminescent thermometers operating in II-BW are often based on the combination of the 1000 nm emission of Yb^{3+} with either the emission of Tm^{3+} located at 1230 nm or emissions of Nd^{3+} located at 1050 nm and 1300 nm. Here, generally, we underline the differences among incorporating a simple core, a core@shell, or a multishell structure in the nanoparticles used for luminescence nanothermometry (Table 3). In Table 3, as well, it can be observed that Yb^{3+} ions are not performing any more the role of sensitizers, as often reported in the previous sections, but instead they are acting only as activators. This approach uses excitation wavelengths ranging from 690–808 nm, matching the strong absorptions of Tm^{3+} and Nd^{3+} ions,[204,235] and may lead to a promising strategy to ensure biomedical applications, avoiding the heating problems generated by the 980 nm laser, as pointed out before,[206] since the absorption of water molecules, especially at around 800 nm, is quite weak.

If we fix our attention on the structure of the nanoparticles, besides their colloidal stability and target abilities in biomedical applications, they often exhibit limitations related to the drastic reduction of the luminescence efficiency due to the increase of non-radiative processes caused by the interactions with other molecules at their surfaces.[236] It is also difficult in a simple particle to implement multifunctionality.[237] To overcome these limitations, core@shell or multishell nanoparticles have emerged as a very promising strategy. The core@shell or multishell structure allows for flexible designs, incorporating efficient multifunctionality, and the facile incorporation of dopants with the desired spatial distribution, allowing the manipulation of ET processes among different ions located in different layers.[238,239] Hence, here we will highlight the advantages offered by core@shell nanocrystalline structures when compared with bare nanocrystals in luminescence thermometry.

First, we focus on luminescent nanothermometers based on the Yb^{3+} and Tm^{3+} emissions located in the II-BW, which display higher relative thermal sensitivities than Yb^{3+}/Nd^{3+} thermometers (Table 3). A typical example that explores the differences between the core@shell and the simple particles is the case of Er^{3+},Yb^{3+}:LaF_3@Tm^{3+},Yb^{3+}:LaF_3 nanocrystals with sizes ~32 nm, synthesized *via* wet chemistry methodologies.[223,240] These active core@active shell nanocrystalline structures were compared, in terms of the intensity of the emissions generated after excitation at either 690 nm or 808 nm and in terms of the thermometric performance, with their corresponding simple cores. Upon excitation at 690 nm, the energy is absorbed by Tm^{3+}, promoting its electrons from the ground state to the $^3F_{2,3}$ excited state. From this state, a

Table 3 Ln^{3+}-doped luminescent thermometers operating in the II-BW. The table includes activators (A) and sensitizers (S). The excitation (λ_{exc}) and emission (λ_{em}) wavelengths are indicated in nanometers (nm), together with the corresponding electronic transition with which the emissions are associated. ΔT stands for the temperature range where the temperature reading was investigated. The thermometric parameter (Δ) indicates the luminescent nanothermometry class used in each case: FIR for band-shape, I for intensity ratio, and Δ for bandwidth thermometry, respectively. VPR stands for valley-to-peak ratio. The maximum relative thermal sensitivity (S_{rel}) is given at the temperature at which this value was obtained. The minimum temperature resolution (δT) is given at the same temperature. We indicate with an asterisk S_{rel} or δT values calculated by us using the parameters published in the corresponding references. The double line separation between rows stands for different types (single or dual emitting centers) of lanthanide-doped nanothermometers, as discussed in the corresponding subsections

A	S	Host	λ_{exc} (nm)	λ_{em} (nm)	Transitions	ΔT (K)	Δ	S_{rel}/T (% K^{-1})/K	δT (K)	Ref.
Yb^{3+}	Yb^{3+}	ZrO_2	980	1023, 1036	$^2F_{5/2} \rightarrow {}^2F_{7/2}$	293–493	$VPR_{1023/1036}$	1.1/293	0.45*	193
Yb^{3+}	Yb^{3+}	dppz-ePMO@Yb(tta)$_3$	350	986, 1015	$^2F_{5/2} \rightarrow {}^2F_{7/2}$	110–310	$FIR_{986/1015}$	0.17/110	2.9*	234
Yb^{3+}	Yb^{3+}	dppz-vSilica@Yb(tta)$_3$	350	990, 1025	$^2F_{5/2} \rightarrow {}^2F_{7/2}$	110–310	$FIR_{990/1025}$	0.13/110	3.8*	234
Yb^{3+}, Tm^{3+}	Tm^{3+}	Er,Yb:LaF_3@Tm,Yb:LaF_3	690	1000 (Yb^{3+}), 1230 (Tm^{3+})	$^2F_{5/2} \rightarrow {}^2F_{7/2}$ (Yb^{3+}), $^3H_5 \rightarrow {}^3H_6$ (Tm^{3+})	293–323	I_{1000}/I_{1230}	3.9/293	0.3	240
Yb^{3+}, Tm^{3+}	Tm^{3+}	LaF_3	690	1000 (Yb^{3+}), 1230 (Tm^{3+})	$^2F_{5/2} \rightarrow {}^2F_{7/2}$ (Yb^{3+}), $^3H_5 \rightarrow {}^3H_6$ (Tm^{3+})	293–323	I_{1000}/I_{1230}	1.3/293	0.38*	240
Nd^{3+}, Yb^{3+}	Nd^{3+}	Er,Yb:$NaYF_4$@Yb,Nd:$NaYF_4$	808	980 (Yb^{3+}), 1060 (Nd^{3+})	$^2F_{5/2} \rightarrow {}^2F_{7/2}$ (Yb^{3+}), $^4F_{3/2} \rightarrow {}^4I_{9/2}$ (Nd^{3+})	103–443	I_{1060}/I_{980}	2.1/370	0.24*	241
Nd^{3+}, Yb^{3+}	Nd^{3+}	Tm,Yb:SrF_2@Y:SrF_2@, Er:SrF_2@Nd:SrF_2	806	980 (Yb^{3+}), 1060 (Nd^{3+})	$^2F_{5/2} \rightarrow {}^2F_{7/2}$ (Yb^{3+}), $^4F_{3/2} \rightarrow {}^4I_{11/2}$ (Nd^{3+})	293–323	I_{980}/I_{1060}	1.62/323	1.7	242
Nd^{3+}, Yb^{3+}	Nd^{3+}	PDC	808	1005 (Yb^{3+}), 1065 (Nd^{3+})	$^2F_{5/2} \rightarrow {}^2F_{7/2}$ (Yb^{3+}), $^4F_{3/2} \rightarrow {}^4I_{11/2}$ (Nd^{3+})	298–368	I_{1065}/I_{1005}	0.53/368	1.09	243
Nd^{3+}, Yb^{3+}	Nd^{3+}	PDC	808	1005 (Yb^{3+}), 1052 (Nd^{3+})	$^2F_{5/2} \rightarrow {}^2F_{7/2}$ (Yb^{3+}), $^4F_{3/2} \rightarrow {}^4I_{11/2}$ (Nd^{3+})	298–368	I_{1052}/I_{1005}	0.48/298	0.08	243
Nd^{3+}, Yb^{3+}	Nd^{3+}	Nd:LaF_3@Yb:LaF_3	790	1000 (Yb^{3+}), 1300 (Nd^{3+})	$^2F_{5/2} \rightarrow {}^2F_{7/2}$ (Yb^{3+}), $^4F_{3/2} \rightarrow {}^4I_{13/2}$ (Nd^{3+})	283–323	I_{1300}/I_{1000}	0.41/283	1.61	223
Nd^{3+}, Yb^{3+}	Nd^{3+}	Nd:LaF_3@Yb:LaF_3	790	1000 (Yb^{3+}), 1060 (Nd^{3+})	$^2F_{5/2} \rightarrow {}^2F_{7/2}$ (Yb^{3+}), $^4F_{3/2} \rightarrow {}^4I_{11/2}$ (Nd^{3+})	283–323	I_{1060}/I_{1000}	0.41/283	1.61	223
Nd^{3+}, Yb^{3+}	Nd^{3+}	Nd:LaF_3@Yb:LaF_3	790	1000 (Yb^{3+}), 890 (Nd^{3+})	$^2F_{5/2} \rightarrow {}^2F_{7/2}$ (Yb^{3+}), $^4F_{3/2} \rightarrow {}^4I_{9/2}$ (Nd^{3+})	283–323	I_{890}/I_{1000}	0.41/283	1.61	223
Nd^{3+}, Yb^{3+}	Nd^{3+}	Yb:LaF_3@Nd:LaF_3	790	1000 (Yb^{3+}), 1300 (Nd^{3+})	$^2F_{5/2} \rightarrow {}^2F_{7/2}$ (Yb^{3+}), $^4F_{3/2} \rightarrow {}^4I_{13/2}$ (Nd^{3+})	283–323	I_{1300}/I_{1000}	0.36/283	1.61	223
Nd^{3+}, Yb^{3+}	Nd^{3+}	Yb:LaF_3@Nd:LaF_3	790	1000 (Yb^{3+}), 1060 (Nd^{3+})	$^2F_{5/2} \rightarrow {}^2F_{7/2}$ (Yb^{3+}), $^4F_{3/2} \rightarrow {}^4I_{11/2}$ (Nd^{3+})	283–323	I_{1060}/I_{1000}	0.36/283	1.61	223
Nd^{3+}, Yb^{3+}	Nd^{3+}	Yb:LaF_3@Nd:LaF_3	790	1000 (Yb^{3+}), 890 (Nd^{3+})	$^2F_{5/2} \rightarrow {}^2F_{7/2}$ (Yb^{3+}), $^4F_{3/2} \rightarrow {}^4I_{9/2}$ (Nd^{3+}),	283–323	I_{890}/I_{1000}	0.36/283	1.61	223
Nd^{3+}, Yb^{3+}	Nd^{3+}	Yb,Nd:LaF_3	790	1000 (Yb^{3+}), 890 (Nd^{3+})	$^2F_{5/2} \rightarrow {}^2F_{7/2}$ (Yb^{3+}), $^4F_{3/2} \rightarrow {}^4I_{9/2}$ (Nd^{3+})	283–323	I_{890}/I_{1000}	0.1/283	1.61	223
Nd^{3+}, Yb^{3+}	Nd^{3+}	Yb,Nd:LaF_3	790	1000 (Yb^{3+}), 1060 (Nd^{3+})	$^2F_{5/2} \rightarrow {}^2F_{7/2}$ (Yb^{3+}), $^4F_{3/2} \rightarrow {}^4I_{11/2}$ (Nd^{3+})	283–323	I_{1300}/I_{1000}	0.1/283	1.61	223
Nd^{3+}, Yb^{3+}	Nd^{3+}	Yb,Nd:LaF_3	790	1000 (Yb^{3+}), 1300 (Nd^{3+})	$^2F_{5/2} \rightarrow {}^2F_{7/2}$ (Yb^{3+}), $^4F_{3/2} \rightarrow {}^4I_{13/2}$ (Nd^{3+})	283–323	I_{1300}/I_{1000}	0.1/283	1.61	223
Nd^{3+}	Nd^{3+}	YAP	532	1348	$^4F_{3/2} \rightarrow {}^4I_{13/2}$	293–370	Δ_{1348}	3.3/293	0.37	157
Nd^{3+}	Nd^{3+}	$LiLuF_4$@$LiLuF_4$	793	1316, 1328	$^4F_{3/2} \rightarrow {}^4I_{13/2}$	293–318	$FIR_{1316/1328}$	0.49/293	1.02	164
Nd^{3+}	Nd^{3+}	$LiLuF_4$@$LiLuF_4$	793	1045, 1055	$^4F_{3/2} \rightarrow {}^4I_{11/2}$	293–318	$FIR_{1045/1055}$	0.48/293	1.05	164
Nd^{3+}	Nd^{3+}	YVO_4@SiO_2	808	1064, 1066	$^4F_{3/2} \rightarrow {}^4I_{11/2}$	297–331	$FIR_{1064/1066}$	0.45/331	0.50	244
Nd^{3+}	Nd^{3+}	PDC	808	1054, 1065	$^4F_{3/2} \rightarrow {}^4I_{11/2}$	298–368	$FIR_{1054/1065}$	0.44/368	0.3	243
Nd^{3+}	Nd^{3+}	Y_2O_3	532	1053, 1075	$^4F_{3/2} \rightarrow {}^4I_{11/2}$	298–333	$FIR_{1053/1075}$	0.43/298	0.2	166
Nd^{3+}	Nd^{3+}	YVO_4	808	1064, 1066	$^4F_{3/2} \rightarrow {}^4I_{11/2}$	297–331	$FIR_{1064/1066}$	0.35/331	0.44	244
Nd^{3+}	Nd^{3+}	Y^{3+}:CaF_2	808	1053, 1062	$^4F_{3/2} \rightarrow {}^4I_{11/2}$	300–333	$FIR_{1053/1062}$	0.18/300	2.7*	245
Nd^{3+}	Nd^{3+}	$KGd(WO_4)_2$	808	1067, 1075	$^4F_{3/2} \rightarrow {}^4I_{11/2}$	298–333	$FIR_{1067/1075}$	0.16/298	3*	174
Nd^{3+}, QDs	Nd^{3+}, QDs	Nd:$NaGdF_4$@QD@PGLA	808	1060 (Nd^{3+}), 1300 (QDs)	$^4F_{3/2} \rightarrow {}^4I_{11/2}$ (Nd^{3+}), first exciton (QDs)	283–323	I_{1060}/I_{1300}	2.5/303	0.2	63
Nd^{3+}, Ho^{3+}	Nd^{3+}	Er,Ho,Yb:$NaGdF_4$@Yb:$NaGdF_4$@Nd,Yb:$NaGdF_4$@$NaGdF_4$	806	1180 (Ho^{3+}), 1340 (Nd^{3+})	$^5I_6 \rightarrow {}^5I_8$ (Ho^{3+}), $^4F_{3/2} \rightarrow {}^4I_{13/2}$ (Nd^{3+})	293–323	I_{1180}/I_{1340}	1.17/293	1.2	246

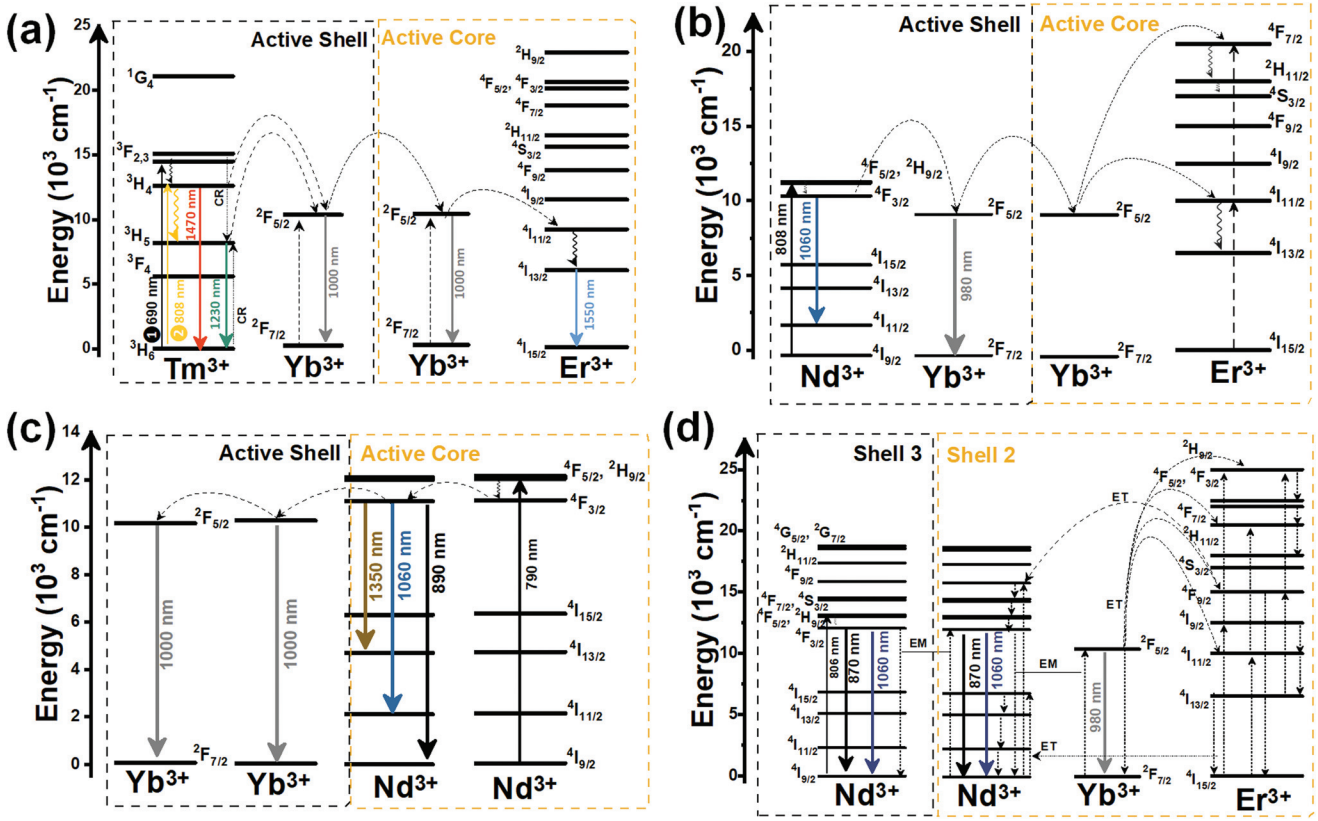

Fig. 27 (a) Mechanisms of generation of the emission lines of core@shell nanostructures:(a) Er^{3+},Yb^{3+}:LaF_3@Tm^{3+},Yb^{3+}:LaF_3 nanocrystals excited either at 690 nm or 808 nm, (b) Er^{3+},Yb^{3+}:$NaYF_4$@Nd^{3+},Yb^{3+}:$NaYF_4$ nanoparticles excited at 808 nm, (c) Nd^{3+}:LaF_3@Yb^{3+}:LaF_3 nanoparticles excited at 790 nm, and (d) Tm^{3+},Yb^{3+}:SrF_2@Y^{3+}:SrF_2@Er^{3+},Nd^{3+},Yb^{3+}:SrF_2@Nd^{3+}:SrF_2 nanocrystals excited at 806 nm.

cross relaxation process $^3F_{2,3}$; $^3H_6 \rightarrow {}^3F_4$; $^3H_5$ (Fig. 27(a)) takes place leading to the population of the $^3H_5$ energy level, from which a radiative decay to the ground state generates the 1230 nm emission of Tm^{3+}. From the $^3H_5$ energy level and from the $^3H_4$ energy level (populated by a non-radiative decay from the $^3F_{2,3}$ state), ET processes to the energy-resonant $^2F_{5/2}$ state of Yb^{3+} takes place, followed by a radiative relaxation to the ground state, which leads to the 1000 nm emission of Yb^{3+}. Further ET processes between the active shell and the active core, as presented in Fig. 27(a), lead to the population of the $^2F_{5/2}$ and $^4I_{11/2}$ energy levels of Yb^{3+} and Er^{3+}, respectively, present in the active core. The electrons in the $^4I_{11/2}$ state of Er^{3+} can non-radiatively decay to the $^4I_{13/2}$ state, prior to relaxing back radiatively to the ground state, leading to the generation of the 1550 nm emission. The intensity of the 1000 nm, 1230 nm and 1550 nm emissions of Yb^{3+}, Tm^{3+} and Er^{3+} ions in this core–shell structure were compared with the ones obtained in the Tm^{3+}, Er^{3+}, Yb^{3+} nanocrystals in which the three ions are located in the same layer.

Under excitation at 690 nm, brighter emissions are obtained in the core@shell structures (Fig. 28(a)). This big difference between the intensity of the emissions is a direct effect of the core@shell architecture, according to the authors, leading to a spatial separation between Er^{3+} and Tm^{3+} ions in such a way that the $Er^{3+} \rightarrow Tm^{3+}$ ET process, involving the $^4I_{13/2}$ and $^3F_4$ energy levels of Er^{3+} and Tm^{3+}, respectively, is avoided or reduced, as confirmed also from the fluorescence lifetime measurements performed.[240] As can be observed also in Fig. 28(a), a significant effect on the signal of the emissions (and in the thermometric performance as well, as we will analyze in section 5) was produced by excitation at 808 nm in the core@shell structures, although in that case the emission of Tm^{3+} is almost non detected. A possible explanation for this might be that upon 808 nm excitation, the mechanism of generation of the Tm^{3+} emission is mainly governed by the de-excitation of the $^3H_4$ state and not through the cross relaxation process. Hence, as presented in Fig. 27(a), upon 808 nm excitation, the electrons of Tm^{3+} will be excited to the $^3H_4$ state, from where through a direct radiative decay to the ground state, the 1470 nm emission will be generated.

Since the $^3H_5$ energy level is not populated any more *via* cross relaxation processes, but through a simple non-radiative decay from the $^3H_4$ energy level (Fig. 27(a)), the emission at 1230 nm is almost inexistent. Here, the thermometric parameter was defined by the three intensity ratios that can be calculated combining the emissions of Yb^{3+}, Tm^{3+} and Er^{3+}: (i) the 1000 nm emission of Yb^{3+} combined with the 1230 nm emission of Tm^{3+}, both located in the II-BW; (ii) the 1000 nm

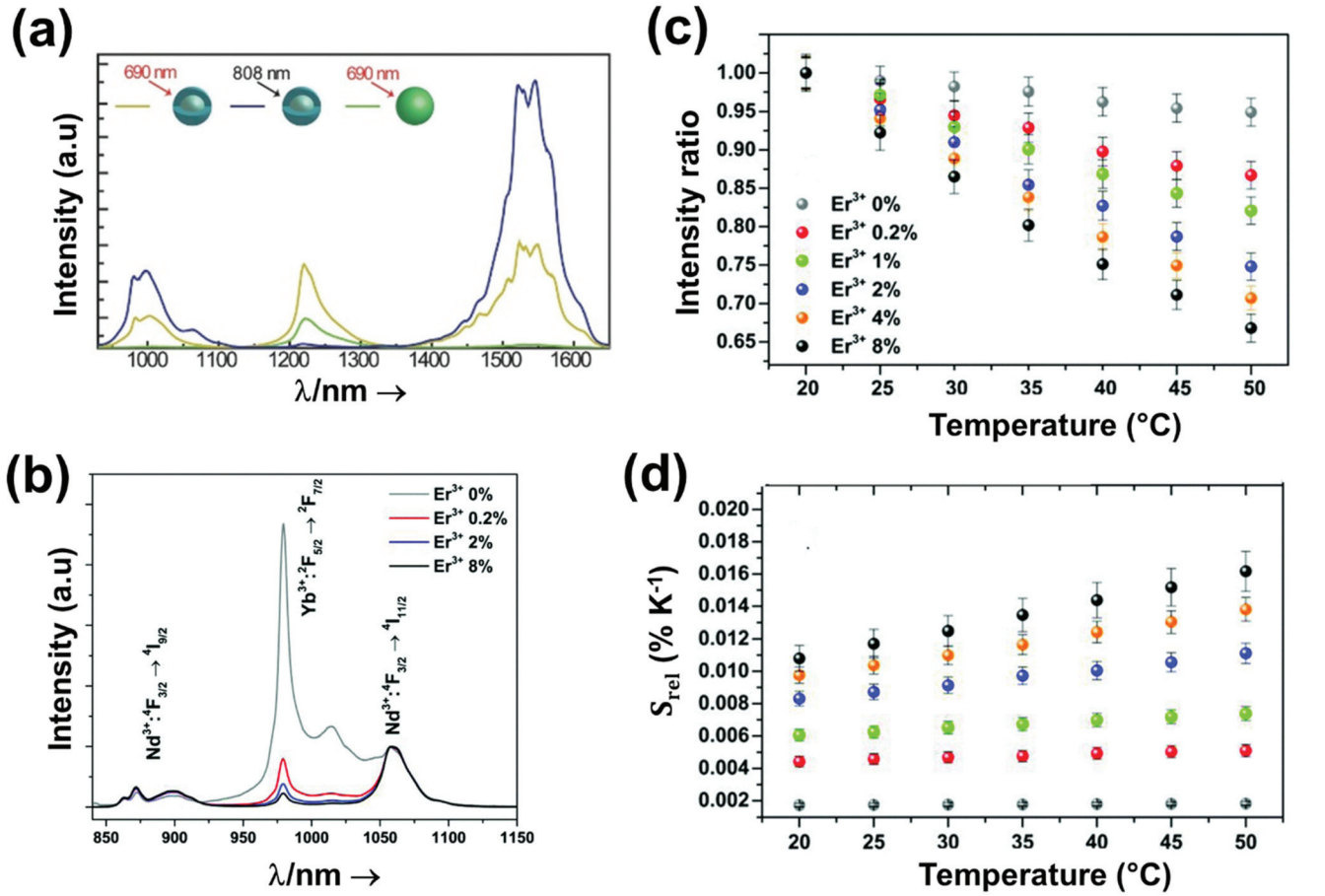

Fig. 28 (a) Room temperature emission spectra of simple core Er^{3+},Tm^{3+}, Yb^{3+}:LaF_3 under 690 nm excitation (green) and of active core@active shell Er^{3+},Yb^{3+}:LaF_3@Yb^{3+},Tm^{3+}:LaF_3 (concentrations of lanthanide ions Tm^{3+},Yb^{3+} and Er^{3+} are 10 mol%, 10 mol% and 2 mol%, respectively) under 690 (yellow) and 808 nm (blue) laser excitation. The green sphere and the grey core covered with a blue sphere represent the simple core and the active core@active shell, respectively. Reprinted with permission from ref. 240. Copyright 2017, Wiley-VCH Verlag GmbH & Co. KGaA. Effect of the Er^{3+} concentration on: (b) the intensity of the emissions, (c) the intensity ratio, and (d) S_{rel} on Tm^{3+},Yb^{3+}:SrF_2@Y^{3+}:SrF_2@Er^{3+},Nd^{3+},Yb^{3+}:SrF_2@Nd^{3+}:SrF_2 nanocrystals. (b)–(d) Adapted with permission from ref. 242. Copyright 2018, The Royal Society of Chemistry.

emission of Yb^{3+} combined with the 1550 nm emission of Er^{3+}, located within the II- and III-BWs, that will be described in section 5; and (iii) the 1230 nm emission of Tm^{3+} combined with the 1550 nm emission of Er^{3+}, located within the II- and III-BWs, that will be also described in section 5. For the luminescent thermometer operating exclusively in the II-BW, a maximum S_{rel} of 3.9% K^{-1} was obtained at room temperature,[240] three times higher than that corresponding to the nanoparticles in which the three Ln^{3+} were located in the same layer (Table 3). This improvement was assigned to the efficient ET and quenching rates in the core@shell structures.[240]

Returning to the case of Yb^{3+} and Nd^{3+} emissions located in the II-BW, a hexagonal Er^{3+},Yb^{3+}:$NaYF_4$@Nd^{3+},Yb^{3+}:$NaYF_4$ core@shell structure was analyzed as a luminescent temperature sensor. Here, to determine the temperature, the authors used the emissions generated by Yb^{3+} and Nd^{3+} located in the outer shell (the emissions generated by the ions in the inner core were used for sensing in the visible range, which is out of the scope of this review).[241] By exciting the nanocrystals at 808 nm, the electrons are excited from the Nd^{3+} ground state to the $^4F_{5/2}$ excited state, followed by a fast non-radiative decay to populate the $^4F_{3/2}$ metastable state. At this stage, different radiative and non-radiative processes can take place (Fig. 27(b)), starting from the generation of the Nd^{3+} emission at 1060 nm, corresponding to the $^4F_{3/2} \rightarrow {}^4I_{11/2}$ electronic transition, and the ET between the Nd^{3+} and Yb^{3+} ions present in the shell, ruled by the Miyakawa–Dexter model.[231] From here, the emission of Yb^{3+} located at 980 nm, assigned to the $^2F_{5/2} \rightarrow {}^2F_{7/2}$ transition, is generated. Also, the energy migration from the Yb^{3+} ions in the shell to the Yb^{3+} ions in the core, followed by an ET between Yb^{3+} and Er^{3+}, can take place, leading finally to the green emission of Er^{3+} in the visible range.[241] The mechanisms for the generation of the green emissions of Er^{3+} are out of the scope of this review; thus, they are not discussed here. The intensity ratio, fitted to the model described by eqn (42) between the 1060 nm emission of Nd^{3+} and the 980 nm emission of Yb^{3+}, was analyzed as a function of temperature, in the 103–443 K range, and the concentration of Nd^{3+}

in the outer shell, tuned from 1 to 15 at% with respect to the concentration of Yb^{3+}.[241] The results show that a maximum S_{rel} of 2.1% K^{-1} at 370 K could be obtained.[241] In addition, this S_{rel} is proportional to the content of Nd^{3+} in the outer shell. This effect is related to the shortening of the average Nd^{3+}–Yb^{3+} distance, hence facilitating the Nd^{3+} to Yb^{3+} ET.[241]

In simple Nd^{3+},Yb^{3+}-doped LaF_3 nanoparticles and two different active core@active shell nanostructures, one having the core doped with Nd^{3+} ions and the shell with Yb^{3+} ions (Nd^{3+}:LaF_3@Yb^{3+}:LaF_3) and the other constituted by a Yb^{3+}-doped core and a Nd^{3+}-doped shell (Yb^{3+}:LaF_3@Nd^{3+}:LaF_3),[223] Nd^{3+} displayed two additional emission bands at 890 nm (located in the I-BW) and 1350 nm (located in the II-BW), corresponding to the $^4F_{3/2} \rightarrow {}^4I_{9/2}$ and $^4F_{3/2} \rightarrow {}^4I_{13/2}$ transitions, respectively, when excited at 790 nm. The energy of this excitation source is absorbed by Nd^{3+} ions, promoting their electrons to the $^4F_{5/2}$ excited state. Then, a rapid phonon-assisted relaxation to the metastable $^4F_{3/2}$ state takes place, from which three radiative decays to the $^4I_{9/2}$, $^4I_{11/2}$ and $^4I_{13/2}$ levels produce the emissions located at 890 nm, 1060 nm and 1350 nm, respectively (Fig. 27(c)). A further ET process to Yb^{3+} can lead to the excitation of the electrons of these ions from their ground state up to the $^2F_{5/2}$ state, from which the 1000 nm emission is produced.

Here, all the possible intensity ratios considering the emissions of Nd^{3+} *versus* the emission of Yb^{3+}, which obey a linear function when plotted against temperature, were explored for temperature sensing by luminescence means. The same S_{rel} was found for all the three intensity ratios, either in the simple nanoparticles or in the core@shell structures (Table 3). Comparing the performance of the simple nanoparticles with that of the core@shell structures, a four-fold improvement in their S_{rel} was observed. Nevertheless, the S_{rel} values are relatively low, with a maximum of ~0.41% K^{-1} in the physiological range of temperatures.[223]

The thermal sensitivity of these Nd^{3+},Yb^{3+}-doped LaF_3 nanoparticles is comparable to that of Nd^{3+} and Yb^{3+}-codoped lanthanide complex with pyridine-3,5-dicarboxylate (hereafter PDC).[243] Here, Nd^{3+} emission peaks at 1054 nm and 1065 nm are generated from the transitions between the different Stark sublevels in the $^4F_{3/2} \rightarrow {}^4I_{11/2}$ electronic transition, whereas the Yb^{3+} emission at 1005 nm corresponds to the $^2F_{5/2} \rightarrow {}^2F_{7/2}$ transition, after excitation at 808 nm. The intensity ratios among the three combinations (the combination of Nd^{3+} emissions is presented in section 4.2.1) of these emissions were analyzed for temperature-sensing purposes. The temperature dependence of the 1065 nm/1005 nm intensity ratio was fitted to eqn (14), while the 1054 nm/1005 nm intensity ratio was fitted to a linear equation. The highest S_{rel} was obtained for the 1054 nm/1005 nm ratio with a value of 0.48% K^{-1} and a δT of 0.08 K.[243] It should be underlined here that the uncertainty in the determination of the intensity ratio here was taken as 0.033%,[243] which of course, will imply a lower δT.

Cortelletti *et al.* reported the thermometric performance of a complex system in the form of a core@multishell nanostructure composed of Tm^{3+},Yb^{3+}:SrF_2@Y^{3+}:SrF_2@Er^{3+},Nd^{3+}, Yb^{3+}:SrF_2@Nd^{3+}:SrF_2,[242] based on the intensity ratio between the emissions of Yb^{3+} at 980 nm and of Nd^{3+} located at 1060 nm (another emission of Nd^{3+} is generated at 870 nm, but the authors used only the one located at 1060 nm for temperature-sensing purposes due to its higher emission intensity). The performance of this luminescence nanothermometer was closely related to the amount of Er^{3+} ions in shell 2. In this structure, the energy of the 806 nm excitation source is absorbed by the Nd^{3+} ions present in the most external shell. This energy allows the promotion of the Nd^{3+} electrons to the $^4F_{5/2}$ excited state, from which a non-radiative decay will populate the lower $^4F_{3/2}$ excited state. From here, radiative decays to $^4I_{9/2}$ and $^4I_{11/2}$ states generate the emissions located at 870 nm and 1060 nm, respectively. From the $^4F_{5/2}$ excited state of Nd^{3+}, an ET process can lead to the population of the Nd^{3+} ions located in shell 2 (Fig. 27(d)). Then, an ET process to Yb^{3+} can lead to the population of its excited state prior to a radiative decay to its ground state, generating the 980 nm emission.[242] Hence, between Nd^{3+} ions and Yb^{3+} ions, ET and BET processes may exist. However, this is true only when no Er^{3+} ions in shell 2 are found. With the addition of Er^{3+} ions, several ET processes between Yb^{3+} and Er^{3+} ions may occur, influencing in this way not only the intensity of the emissions generated, but also the thermometric performance of the system. With the increase of Er^{3+} concentration, the emission intensity of Yb^{3+} clearly decreases (Fig. 28(b)), due to the increase of the probability of the $Yb^{3+} \rightarrow Er^{3+}$ ET process. This ET process quenches the emission of Yb^{3+}, which works in favor of the luminescence nanothermometry means. When considering the evolution of the intensity ratio between the emissions of Yb^{3+} and Nd^{3+} with temperature, its slope increases as the concentration of Er^{3+} increases (Fig. 28(c)), and so does S_{rel} (Fig. 28(d)), generating better luminescent thermometers. From these figures it can be concluded that the S_{rel} of the luminescent thermometer with the highest Er^{3+} concentration is approximately 5 times better compared with the material without this ion. Thus, efficient $Yb^{3+} \rightarrow Er^{3+}$ ET processes are beneficial for thermometric performance, although it is difficult to predict the effect of these processes in complex systems. Nevertheless, the maximum S_{rel} achieved (1.62% K^{-1} in the physiological range of temperatures) is still lower when compared with the one achieved in Er^{3+},Yb^{3+}:LaF_3@Tm^{3+},Yb^{3+}:LaF_3,[240] and Er^{3+},Yb^{3+}:$NaYF_4$@Nd^{3+},Yb^{3+}:$NaYF_4$ nanostructures.[241]

To conclude this subsection, it is clear that core@shell and core@multishell nanoarchitectures offer a boost in the brightness of the emissions generated and in addition, a significant enhancement of their temperature-sensing performance. However, it should be admitted that these structures constitute very complex systems either from the synthetic or the spectroscopic point of view. Additionally, most of them are hydrophobic because they are coated with organic surfactants; hence, for biomedical applications further modifications of their surfaces are needed to make them water dispersible.

4.2. Nd^{3+}-doped luminescent nanothermometers operating in the II-BW

4.2.1. Single Nd^{3+}-doped luminescent thermometers operating in the II-BW. Luminescent thermometers based on single Nd^{3+}-doped nanoparticles operating in the II-BW are mainly based on the emissions generated by the Stark sublevels of the $^4F_{3/2} \rightarrow {}^4I_{11/2}$ electronic transition located at ~1064 nm. Hence, to determine the performance of these thermometers, the fitting model based on FIR was applied, using eqn (9). Another option for temperature sensing with this ion relies on the use of the emission at the limit of the II-BW spectral region located at ~1350 nm. When the 1064 nm emission band is used, S_{rel} is quite low, ranging from 0.16% K^{-1} to 0.45% K^{-1} (Table 3). Despite this, from these 1064 nm emission-based luminescent thermometers, some useful strategies can be extracted. For instance, the incorporation of an amorphous silica coating can tailor the performance of the luminescent nanothermometers, as explored in Nd^{3+}:YVO_4@SiO_2 nanoparticles.[244] The luminescent thermometric performance of this material was tested as a function of the thickness of the silica layer and compared with that of the uncoated material. The results show that there exists a proportional relationship between S_{rel} and the thickness of the silica shell (Fig. 29(a)).

In Nd^{3+}:YAP nanoparticles, the 1350 nm emission band was used for temperature-sensing purposes by analyzing the full width at half maximum ($\Delta\nu$) of the emission located at 1348 nm as a function of the temperature, from room temperature to 370 K.[157] Upon green light excitation, Nd^{3+} promotes its electrons from the $^4I_{9/2}$ ground state to the $^4G_{9/2}$ or $^4G_{7/2}$ excited states, followed by a non-radiative decay process to the $^4F_{5/2}$ and $^4F_{7/2}$ states. The $^4F_{3/2}$ level can also be populated by a non-radiative decay from the $^4F_{5/2}$ level. From this state, a radiative decay to the $^4I_{13/2}$ level generates the emission located at 1348 nm (Fig. 30(a)). As the temperature increased, $\Delta\nu$ became broader and its dependence on temperature could be fitted to a second-order polynomial function of the form:[157]

$$\Delta\nu = a + bT + cT^2 \quad (43)$$

where a, b and c are constants to be determined from the fitting of the experimental data. The maximum S_{rel} for this

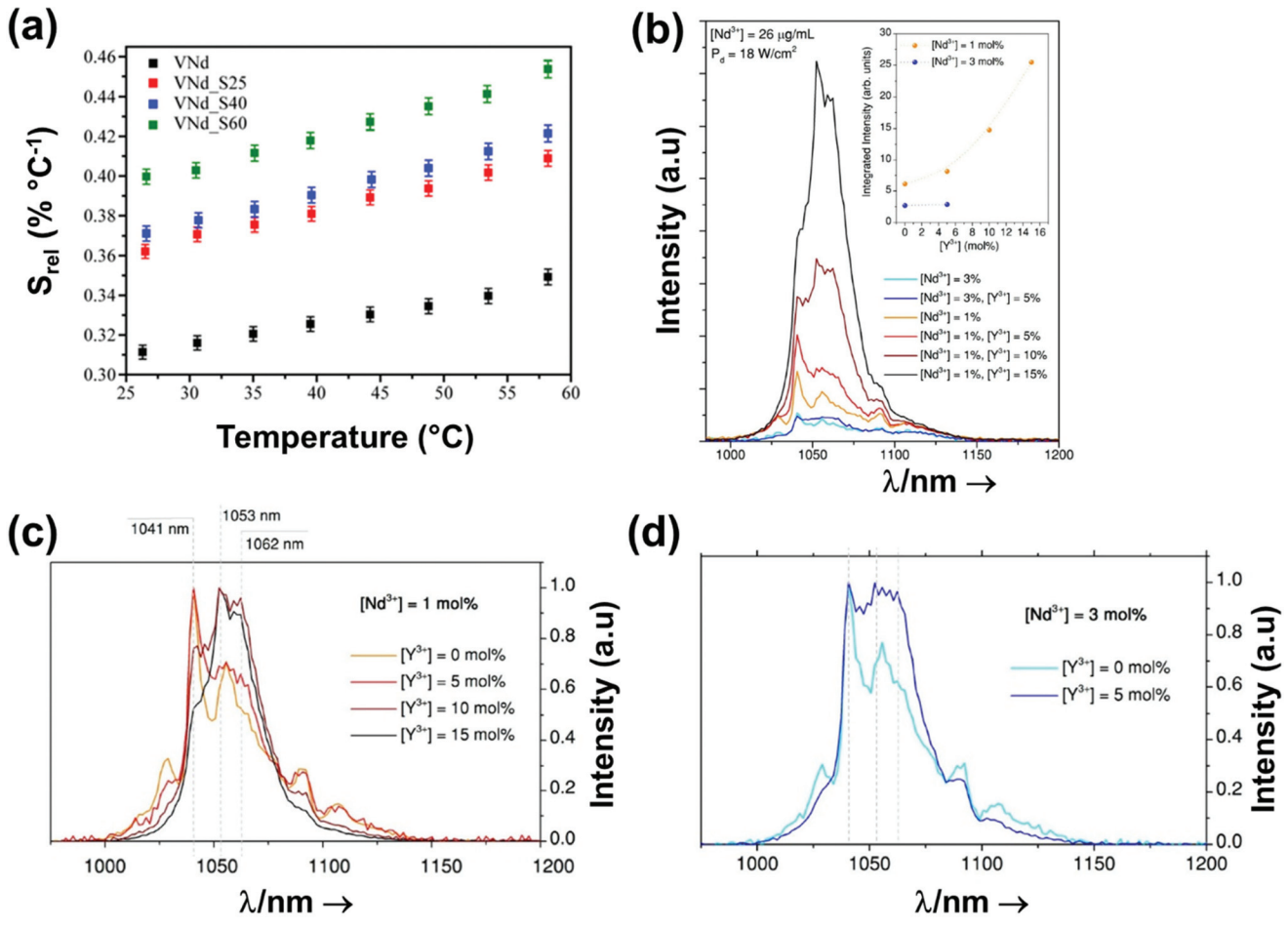

Fig. 29 (a) Effect of the thickness of the silica shell on the thermal performance of Nd^{3+}-doped YVO_4@SiO_2, where S25, S40, S60 stand for the thickness of the silica in nm. Reprinted with permission from ref. 244, Copyright 2016, Elsevier. Effect of Y^{3+} impurities in Nd^{3+}-doped CaF_2 on: (b) the intensity, and (c) and (d) the spectral line shape of the $^4F_{3/2} \rightarrow {}^4I_{11/2}$ emission band. Reprinted with permission from ref. 245. Copyright 2018, American Chemical Society.

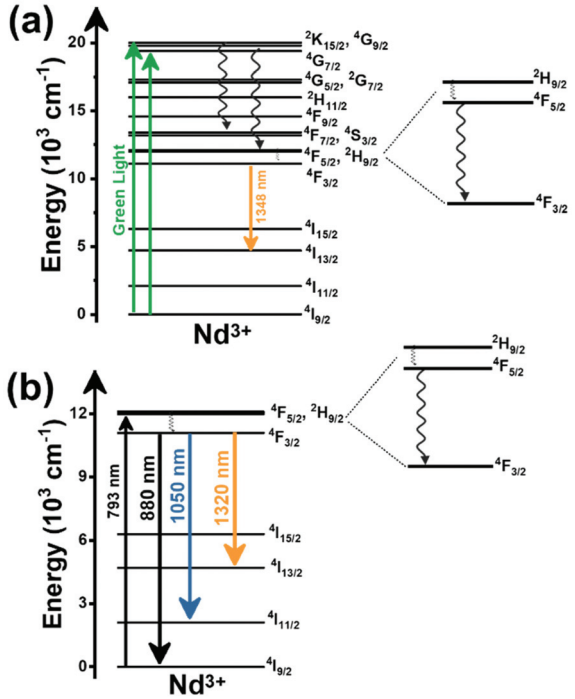

Fig. 30 Mechanisms of generation of the: (a) 1348 nm emission band in Nd^{3+}:YAP nanoparticles under green light excitation, and (b) 1050 nm and 1320 nm emission bands in Nd^{3+}:$LiLuF_4$@$LiLuF_4$ nanoparticles under 793 nm excitation.

luminescence thermometer is 3.3% K^{-1} and the minimum δT = 0.37 K at room temperature.[157]

An additional strategy towards tuning the performance of these luminescent thermometers is the introduction of impurities in the host, such as the incorporation of Y^{3+} ions in Nd^{3+}:CaF_2 cubic nanoparticles.[245] The presence of Y^{3+} avoids the formation of clusters of Nd^{3+} ions in these nanoparticles, and thus it prevents the quenching of their emissions, leading to a brighter luminescence upon using the proper doping ratio (Fig. 29(b)).[245] A brighter emission lead to a more accurate and reliable performance of the luminescent thermometer.[13] Nevertheless, the S_{rel} of these nanocrystals, determined as a function of the amount of Y^{3+} on the structure, is relatively low, since the emissions used in this luminescent thermometers arise from TCLs with a low ΔE between them, in the range of 49–98 cm^{-1}, depending on the Y^{3+} content.[245] Besides the generation of a brighter emission, the introduction of Y^{3+} generated changes in the shape of the emission band (Fig. 29(c) and (d)), due to the modification of the environment surrounding the Nd^{3+} ions and to a different distribution of luminescent centers in the nanoparticles.

Skripka *et al.* demonstrated that upon intermixing and discriminating different factors such as the absolute intensity, the spectral shift and the line broadening of the emissions generated by different Stark sublevels, contributing to the shape of the Nd^{3+} emissions, a better thermometric performance can be obtained that is based only on the thermalization of the Stark sublevels.[164] Hence, upon excitation at 793 nm, the Nd^{3+} ions in Nd^{3+}:$LiLuF_4$@$LiLuF_4$ core–shell nanoparticles can absorb the energy and excite its electrons to the $^4F_{5/2}$ state, from which the $^4F_{3/2}$ state can be populated due to non-radiative decays (Fig. 30(b)). From here, successive radiative decays can lead to the generation of emissions lines located at 880 nm (explained in section 2.2.1), 1050 nm and 1320 nm. The corresponding FIRs between different emission peaks coming from different Stark sublevels of each of these emissions were analyzed to develop luminescent thermometers with these nanomaterials. Hence, the FIR of these emission bands provided S_{rel} values ~0.49% K^{-1} in the physiological range of temperatures. The authors strongly emphasized that if only the thermalization of the Stark sublevels would have been taken into account, S_{rel} would have been ~0.09% K^{-1}, since the ΔE between the different Stark sublevels was around 55 cm^{-1}.[164] Thus, by resolving the fine Stark structure of the Nd^{3+} spectra with the adequate detector systems (InGaAs NIR sensors in this case) and the proper choice and design of the host material, an improvement in the thermal sensitivity based on single Nd^{3+} nanothermometers can be achieved.

Overall, concerning the thermometric performance of single Nd^{3+}-doped luminescent thermometers, the use of the 1350 nm emission band results in a higher S_{rel}. However, if advanced detector systems and proper host materials are chosen, the 1050 nm emission band can stand as a promising alternative. Nevertheless, the luminescent thermometers based on the 1350 nm emission band rely on excitation in the visible range, which will, of course, limit the biomedical applications of these temperature sensors.[13,86,90] On the other hand, normally the 1050 nm emission is obtained after excitation in the I-BW, which despide their low S_{rel}, facilitates their use in biological applications.

4.2.2. Dual emitting doped Nd^{3+} luminescent thermometers operating in the II-BW. Although there are not too many examples of dual emitting luminescent thermometers combining Nd^{3+} with other materials or Ln^{3+} ions apart from Yb^{3+}, the ones reported exhibit a high S_{rel}.

For example, Cerón *et al.*[63] developed a high-resolution temperature sensor consisting of Nd^{3+}:$NaGdF_4$ dielectric nanoparticles and semiconductor PbS/CdS/ZnS quantum dots (QDs) combined in a poly(lactic-*co*-glycolic acid) (PLGA) hybrid nanostructure, excited within the I-BW (808 nm) and emitting in the II-BW. This luminescent thermometer worked on the basis of the different temperature responses of its components. While the intensity of the emission of Nd^{3+}, located at 1060 nm, remained unchanged in the physiological range of temperatures, the intensity of the 1300 nm emission band of the QDs, assigned to their first exciton, decreased linearly due to photon-assisted processes (Fig. 31(a)). Hence, they developed a highly sensitive thermometer based on the change in the emission intensity of the quantum dots and using the emission of the Ln^{3+} ion as a reference probe. The maximum value of S_{rel} and the minimum value of δT, obtained at 303 K, were 2.5% K^{-1} and 0.2 K, respectively.[63]

A water-soluble multishell complex nanostructure based on hexagonal $NaGdF_4$ has been also proposed as a temperature

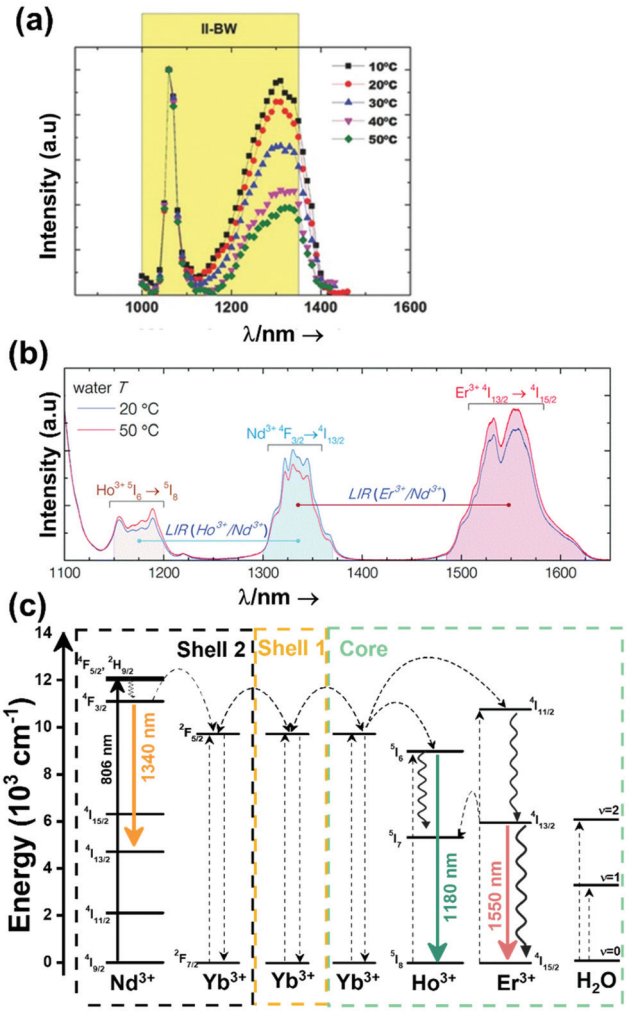

Fig. 31 (a) Evolution of the intensity of the emissions of Nd:$NaGdF_4$ and PbS/CdS/ZnS nanoparticles combined in PGLA hybrid nanostructures. Reprinted with permission from ref. 63. Copyright 2015, Wiley-VCH Verlag GmbH & Co. KGaA. (b) Emissions of Er^{3+},Ho^{3+}, Yb^{3+}@Yb^{3+}@Nd^{3+},Yb^{3+}@$NaGdF_4$ multishell nanostructures (Reprinted with permission from ref. 246. Copyright 2017, The Royal Society of Chemistry), and (c) mechanisms of generation of these emission lines.

probe in the II-BW (and in the II- and III-BW regions, as will be discussed in section 5). This multishell nanostructure, formed by an active core, a Yb^{3+} doped inner shell, a second active shell containing Nd^{3+}, and a final inert shell, Er^{3+},Ho^{3+},Yb^{3+}:$NaGdF_4$@Yb^{3+}:$NaGdF_4$@Nd^{3+},Yb^{3+}:$NaGdF_4$@$NaGdF_4$, was synthesized *via* a thermal decomposition process, leading to oleate-capped nanoparticles.[246] To make these nanostructures water dispersible, they were encapsulated in polyethylene glycol-grafted phospholipid (PEG-DOPE) micelles. After excitation at 806 nm emissions located in the II-BW and III-BW (Fig. 31(b)) were generated. The energy of the excitation source is absorbed by the Nd^{3+} ions located in shell 2 that subsequently generate the emission at 1340 nm, after a non-radiative decay process to the $^4F_{3/2}$ level. Part of this energy is also transferred, *via* several ET processes through Yb^{3+} ions in shell 1, to the core, leading to the population of the $^5I_6$ and $^4I_{11/2}$ levels of Ho^{3+} and Er^{3+}, respectively (Fig. 31(c)). The 1180 nm emission of Ho^{3+} is generated after a radiative decay to the ground state $^5I_8$. From the excited $^4I_{11/2}$ level of Er^{3+}, a non-radiative decay process leads to the population of the lower excited level $^4I_{13/2}$, prior to relaxing to the ground state, where the 1550 nm emission located in the III-BW is produced. Therefore, the role of the inert shell 1 is to suppress the interionic quenching of the Er^{3+} and Ho^{3+} emissions by Nd^{3+} ions, while the presence of Yb^{3+} in the core, shell 1 and shell 2 facilitates the energy migration across these multiple layers.[246] Hence, from this nanostructure, three emissions are generated, two of them located in the II-BW (1180 nm of Ho^{3+} and 1340 nm of Nd^{3+}) and one in the III-BW (1550 nm of Er^{3+}). In this section, we will review only the luminescence thermometric possibilities of the emissions located in the II-BW. The temperature determination from this luminescent thermometer was done by studying the temperature dependence of the intensity ratio between the emission at 1180 nm of Ho^{3+} (located in the core) and the 1340 nm emission of Nd^{3+} (located in shell 2) in the physiological range of temperatures. With the increase of the temperature, the intensity of the emission of Ho^{3+} increased, due to the phonon-assisted Yb^{3+} ($^2F_{5/2}$) → Ho^{3+} ($^5I_6$) process,[247] whereas the emission of Nd^{3+} decreased, due to the phonon-assisted ET Nd^{3+} ($^4F_{3/2}$) → Yb^{3+} ($^2F_{5/2}$) process[201,246] (Fig. 31(b) and (c)). Since these multishell nanocrystals were dispersible in water, additional de-excitation channels associated with the presence of water molecules on the surfaces of these nanocrystals were expected. In order to prevent these de-excitation channels, the third passivating undoped shell was introduced. The maximum S_{rel} obtained for the 1180 nm/1340 nm intensity ratio was 1.17% K^{-1}.

Despite its relatively good temperature-sensing performance, the core@shell and multishell materials presented in this subsection are based on fluoride-doped hosts synthesized (mostly) through the thermal decomposition of trifluoroacetate precursors to control the size and the morphology of the nanoparticles, which is accompanied by highly toxic by-products of the reactions.[248] Nevertheless, in terms of the thermometric performance, clearly complex nanoarchitectures, such as core@shell and multishell materials, exhibit high relative thermal sensing compared with the other forms of materials presented up to now (Fig. 32(a) and (b)) and fulfill the conditions to be used in biomedical applications. They can be excited in the BWs and generated highly temperature-dependent emissions, also located within the BWs spectral regions.

5. Lanthanide-doped luminescent nanothermometers operating in the II and III-BWs simultaneously

Based on the emission at 1550 nm, Er^{3+} ions represent one of the most explored lanthanide luminescent ions for thermome-

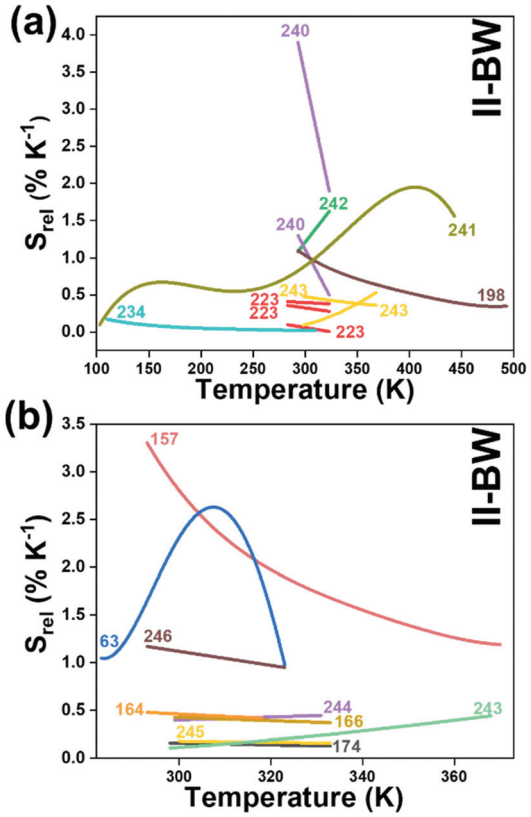

Fig. 32 Temperature dependence of S_{rel} of: (a) Yb^{3+}- and (b) Nd^{3+}-doped luminescent thermometers operating in the II-BW region. The numbers indicate corresponding references for each thermometer.

try operating in the II- and III-BWs simultaneously, by combining them with other emissions located in the II-BW arising either from other Ln^{3+} ions or transition metals. Concerning the combination of Er^{3+} with Ln^{3+} ions, typical examples involve Yb^{3+}, Nd^{3+} and Ho^{3+} emissions. For the combination with transition metals, only one example involves the application of the Er^{3+} emission with the emission of nickel(II), located in the II-BW. A few cases involve also single center emitting Ln^{3+} ions (Nd^{3+} and Tm^{3+}) as potential thermometers operating in this region.

5.1. Er^{3+}-doped luminescent nanothermometers operating in the II- and III-BWs simultaneously

Several luminescent nanothermometers have been reported using the 1550 nm emission of Er^{3+} together with the emission of other Ln^{3+} ions, including Yb^{3+}, Ho^{3+} and Nd^{3+}, operating in this way in the II- and III-BWs simultaneously. Among these combinations, pairing it with the 1000 nm emission of Yb^{3+} stands out as one of the most promising strategies to develop highly sensitive luminescent thermometers, especially when sensitized *via* Tm^{3+} (Table 4). For example, Er^{3+},Yb^{3+}:LaF_3@Tm^{3+},Yb^{3+}:LaF_3 core–shell nanocrystals (also explored in the II-BW) display an outstanding S_{rel} with a value of 5% K^{-1} at room temperature.[240] This high S_{rel} was extracted from the intensity ratio between the 1000 nm emission of Yb^{3+} and the 1550 nm emission of Er^{3+}, generated after the core@shell nanocrystals were excited at 690 nm (the mechanism of generation of the emission lines is presented in Fig. 26(a)). Compared with the performance of the Er^{3+},Tm^{3+},Yb^{3+}:LaF_3 nanoparticles, the core@shell nanocrystals have a 7-fold higher S_{rel} (Table 4).[240] Furthermore, the authors investigated the effect of the excitation laser wavelength applied (690 nm and 808 nm) on the temperature-sensing properties of these nanocrystals. The results suggest that the high S_{rel} obtained when exciting the nanoparticles at 690 nm is due to the contribution of the $^3H_5$ level of Tm^{3+} ions to the overall emission spectrum generated by the nanoparticles and/or when the $^3H_5$ (Tm^{3+}), $^2F_{5/2}$ (Yb^{3+}) → $^3H_5$ (Tm^{3+}), $^2F_{5/2}$ (Yb^{3+}) ET process is involved, implying that excitation at 690 nm, contrary to the excitation at 808 nm, highly favors this ET process.[240] For the case of excitation at 808 nm, the maximum S_{rel} was only ~0.80% K^{-1}. Hence, an important conclusion that can be drawn from this reference is that engineering core@shell nanostructures is not always a key feature for producing highly sensitive luminescent nanothermometers, but one has to properly select the most suitable excitation wavelength.

Er^{3+},Yb^{3+}:$Na_2K(Lu_3Si_6O_{18})$ nanoparticles, with a triclinic crystalline structure, and synthesized by an autoclave-assisted hydrothermal process, were also tested as luminescent nanothermometers over a wide range of temperatures (12–450 K).[249] The emission lines, located at 930–1125 nm corresponding to electronic transitions of Yb^{3+} and 1425–1640 nm corresponding to electronic transitions of Er^{3+}, were generated after excitation at 903 nm. Yb^{3+} acted here also as a sensitizer, by absorbing the energy of the excitation source and promoting its electrons to the $^2F_{5/2}$ level. From this level, radiatively decaying to the ground state can generate the emission of these ions. In addition, from the excited level of Yb^{3+}, an ET process can populate the $^4I_{11/2}$ level of Er^{3+}. From this level, a non-radiative decay can populate the $^4I_{13/2}$ level, prior to a radiative decay to the ground state, generating the emission of Er^{3+}. A typical mechanism for the generation of these emission lines is similar to the ones presented in Fig. 24(a) or Fig. 26(b).

To extract the intensity ratio and eventually S_{rel}, the authors correlated the total transition probabilities to the inverse of the lifetime using the classic Mott–Seitz model.[250,251] Besides this, this lifetime, considered as the sum of the radiative (assumed to be temperature independent) and non-radiative lifetime (expressing an Arrhenius type of temperature dependence), is proportional to the intensity of the emissions, as follows:[250,251]

$$\frac{I\,(T)}{I_0} = \frac{\tau\,(T)}{\tau_0} \tag{44}$$

where $I\,(T)$ and I_0 stand for the intensity at temperature T and 0 K, respectively, whereas $\tau\,(T)$ and τ_0 stand for the lifetime at T and 0 K (the radiative lifetime), respectively. Taking into account two deactivation channels arising from two different

Table 4 Ln^{3+}-doped luminescent thermometers operating simultaneously in the II and III-BWs regions. In the table are shown the activators (A) and sensitizers (S). The excitation (λ_{exc}) and emission (λ_{em}) wavelengths are shown in nanometers (nm), together with the corresponding transitions of the emissions. ΔT stands for the temperature range where the temperature reading was investigated. The thermometric parameter (Δ) indicates the luminescent nanothermometry class used: *I* for intensity ratio thermometry. The maximum relative thermal sensitivity (S_{rel}) and the minimum temperature resolution (δT) are presented at the temperature where these values were obtained. We indicate with an asterisk the values of S_{rel} or δT calculated by us using the parameters published in the corresponding references. The double line separation between rows stands for different types of lanthanide-doped nanothermometers, as discussed in the corresponding subsections

A	S	Host	λ_{exc} (nm)	λ_{em} (nm)	Transitions	ΔT (K)	Δ	S_{rel}/T (% K^{-1})/K	δT (K)	Ref.
Er^{3+}, Yb^{3+}	Tm^{3+}	Er,Yb:LaF_3@Tm,Yb:LaF_3	690	1000 (Yb^{3+}), 1550 (Er^{3+})	$^2F_{5/2} \rightarrow {}^2F_{7/2}$ (Yb^{3+}), $^4I_{13/2} \rightarrow {}^4I_{15/2}$ (Er^{3+})	293–323	I_{1000}/I_{1550}	5/293	0.3	240
Er^{3+}, Yb^{3+}	Yb^{3+}	$Na_2K(Lu_3Si_6O_{18})$	903	1125 (Yb^{3+}), 1640 (Er^{3+})	$^2F_{5/2} \rightarrow {}^2F_{7/2}$ (Yb^{3+}), $^4I_{13/2} \rightarrow {}^4I_{15/2}$ (Er^{3+})	12–450	I_{1125}/I_{1640}	2.6/26.8	0.08	249
Er^{3+}, Yb^{3+}	Tm^{3+}	Er,Yb:LaF_3@Tm,Yb:LaF_3	808	1000 (Yb^{3+}), 1550 (Er^{3+})	$^2F_{5/2} \rightarrow {}^2F_{7/2}$ (Yb^{3+}), $^4I_{13/2} \rightarrow {}^4I_{15/2}$ (Er^{3+})	293–323	I_{1000}/I_{1550}	0.80/293	0.62*	240
Er^{3+}, Yb^{3+}	Tm^{3+}	Er, Tm, Yb:LaF_3	690	1000 (Yb^{3+}), 1550 (Er^{3+})	$^2F_{5/2} \rightarrow {}^2F_{7/2}$ (Yb^{3+}), $^4I_{13/2} \rightarrow {}^4I_{15/2}$ (Er^{3+})	293–323	I_{1000}/I_{1550}	0.7/293	0.71*	240
Er^{3+}, Ho^{3+}	Yb^{3+}	$NaYF_4$	980	1150 (Ho^{3+}), 1550 (Er^{3+})	$^5I_6 \rightarrow {}^5I_8$ (Ho^{3+}), $^4I_{13/2} \rightarrow {}^4I_{15/2}$ (Er^{3+})	299–319	I_{1150}/I_{1550}	2.17/299	0.23*	252
Er^{3+}, Ho^{3+}	Yb^{3+}	$NaYF_4$	980	1150 (Ho^{3+}), 1550 (Er^{3+})	$^5I_6 \rightarrow {}^5I_8$ (Ho^{3+}), $^4I_{13/2} \rightarrow {}^4I_{15/2}$ (Er^{3+})	298–319	I_{1150}/I_{1550}	1.87/298	0.2	253
Er^{3+}, Ho^{3+}	Yb^{3+}	Gd_2O_3	980	1149 (Ho^{3+}), 1545 (Er^{3+})	$^5I_6 \rightarrow {}^5I_8$ (Ho^{3+}), $^4I_{13/2} \rightarrow {}^4I_{15/2}$ (Er^{3+})	313–573	I_{1550}/I_{1149}	0.82/498	0.61*	254
Er^{3+}, Ho^{3+}	Yb^{3+}	Y_2O_3	980	1149 (Ho^{3+}), 1545 (Er^{3+})	$^5I_6 \rightarrow {}^5I_8$ (Ho^{3+}), $^4I_{13/2} \rightarrow {}^4I_{15/2}$ (Er^{3+})	313–573	I_{1550}/I_{1149}	0.80/523	0.62*	254
Er^{3+}, Ho^{3+}	Yb^{3+}	YAG	980	1149 (Ho^{3+}), 1545 (Er^{3+})	$^5I_6 \rightarrow {}^5I_8$ (Ho^{3+}), $^4I_{13/2} \rightarrow {}^4I_{15/2}$ (Er^{3+})	313–573	I_{1550}/I_{1149}	0.48/573	1.05*	254
Er^{3+}, Ho^{3+}	Yb^{3+}	$BaTiO_3$	980	1149 (Ho^{3+}), 1545 (Er^{3+})	$^5I_6 \rightarrow {}^5I_8$ (Ho^{3+}), $^4I_{13/2} \rightarrow {}^4I_{15/2}$ (Er^{3+})	313–573	I_{1550}/I_{1149}	0.40/573	1.25*	254
Er^{3+}, Ho^3	Yb^{3+}	$NaLuF_4$	975	1177 (Ho^{3+}), 1545 (Er^{3+})	$^5I_6 \rightarrow {}^5I_8$ (Ho^{3+}), $^4I_{13/2} \rightarrow {}^4I_{15/2}$ (Er^{3+})	298–568	I_{1177}/I_{1545}	0.21/298	2.38*	191
Er^{3+}, Ho^{3+}	Yb^{3+}	YVO_4	980	1149 (Ho^{3+}), 1545 (Er^{3+})	$^5I_6 \rightarrow {}^5I_8$ (Ho^{3+}), $^4I_{13/2} \rightarrow {}^4I_{15/2}$ (Er^{3+})	313–573	I_{1550}/I_{1149}	0.17/573	2.9*	254
Er^{3+}, Nd^3	Nd^{3+}	Er,Ho,Yb:$NaGdF_4$@Yb:$NaGdF_4$@Nd,Yb:$NaGdF_4$@$NaGdF_4$	806	1340(Nd^{3+}), 1550 (Er^{3+})	$^4F_{3/2} \rightarrow {}^4I_{13/2}$ (Nd^{3+}), $^4I_{13/2} \rightarrow {}^4I_{15/2}$ (Er^{3+})	293–323	I_{1550}/I_{1340}	1.1/293	0.8	246
Er^{3+}, Ni^{2+}	Er^{3+}, Ni^{2+}	$SrTiO_3$	375	1245 (Ni^{2+}), 1540 (Er^{3+})	$^3T_{2g} \rightarrow {}^3A_{2g}$ (Ni^{2+}), $^4I_{13/2} \rightarrow {}^4I_{15/2}$ (Er^{3+})	123–483	I_{1540}/I_{1245}	5.8/483	0.08*	255
Tm^{3+}	Tm^{3+}	LaF_3	690	1230, 1470	$^3H_5 \rightarrow {}^3H_6$ $^3H_4 \rightarrow {}^3F_4$	297–361	I_{1470}/I_{1230}	1.90/297	0.26*	256
Nd^{3+}	Nd^{3+}	Gd_2O_3	808	1315, 1350	$^4F_{3/2} \rightarrow {}^4I_{13/2}$	303–393	I_{1315}/I_{1350}	0.23/303	2.17*	257

emissions, from which one dominates over the other, such as in the case of this thermometer, the thermometric parameter, related to the ratios between two intensities, is expressed as:

$$\Delta = \frac{I_1}{I_2} = \frac{\Delta_0}{1 + \alpha_1 \exp\left(-\frac{\Delta E_1}{k_B T}\right) + \alpha_2 \exp\left(-\frac{\Delta E_2}{k_B T}\right)} \quad (45)$$

where Δ_0 is the thermometric parameter at 0 K, α is the ratio between the radiative and non-radiative rates, and ΔE_1 and ΔE_2 are the activation energies of the two deactivation channels. For the case of Er^{3+},Yb^{3+}:$Na_2K(Lu_3Si_6O_{18})$ nanoparticles these two channels, responsible for thermal sensing due to Er^{3+}-to-Yb^{3+} ET associated with ΔE_1 and ΔE_2, are, respectively, the Er^{3+}-to-Yb^{3+} ET through the resonant excited levels, and the energy migration between two distinct neighboring Yb^{3+} sites.[249] S_{rel} calculated over the temperature range from 12 K to 450 K reached a maximum of 2.6% K^{-1} at 26.8 K.[249] Despite this high value, if we observe the temperature dependence of S_{rel} in the physiological range of temperatures, the value is close to zero (Fig. 33).

A second combination of emissions for luminescent thermometers operating simultaneously in the II- and III-BWs is that formed by the emissions of Er^{3+} and Ho^{3+}, located at ~1550 nm and ~1150 nm, respectively. These emission lines are generated in the presence of Yb^{3+} as a sensitizer; hence special attention should be paid to the overheating problem when pumping at 980 nm.[206]

For Er^{3+},Ho^{3+},Yb^{3+}:$NaYF_4$ luminescent nanothermometers operating within these spectral regions, we would like to stress that by using Yb^{3+} as a sensitizer, which has to be excited at 980 nm, and Er^{3+} as an emitter at 1550 nm,[253,254] an overlap with the water absorption bands is produced, generating heat and hampering their potential biomedical applications.[258,259] For temperature sensing, the intensity ratio between the 1150 nm emission of Ho^{3+} and the 1550 nm emission of Er^{3+} was used. These emissions lines are generated after the absorbance of the energy of the 980 nm excitation source by Yb^{3+}, which promotes its electrons to the $^2F_{5/2}$ excited state. From here, the $^4I_{11/2}$ level of Er^{3+} and the $^5I_6$ level of Ho^{3+} can be populated by ET or photon-assisted ET processes (Fig. 34), respectively. From the $^4I_{11/2}$ level, Er^{3+} can be relaxed non-radiatively to the $^4I_{13/2}$ level, prior to decaying radiatively to the $^4I_{15/2}$ ground state, generating the emission at 1550 nm.[253,254] The 1150 nm emission of Ho^{3+} can be generated by the direct relaxation from the $^5I_6$ level to the $^5I_8$ ground state (Fig. 34). In terms of S_{rel}, Er^{3+},Ho^{3+},Yb^{3+}:$NaYF_4$ nanocrystals[253,254] show a 9-fold higher sensitivity than Er^{3+},Ho^{3+},Yb^{3+}:$NaLuF_4$ nanocrystals,[191] both being based on the intensity ratio between the 1150 nm emission of Ho^{3+} and 1550 nm of Er^{3+} (Fig. 33 for a comparison of the evolution of the S_{rel} of these two materials and Table 4 for the maximum S_{rel} values). We observed that the thermometric parameter of the Er^{3+},Ho^{3+},Yb^{3+}:$NaYF_4$ nanocrystals was fitted to a linear function (as in eqn (22)),[253,254] whereas for $NaLuF_4$, nanocrystals it was fitted to a second-order polynomial function (as in eqn (23)).[191] This would explain the differences observed in S_{rel}.

Similar S_{rel} values for Er^{3+},Ho^{3+},Yb^{3+}:$NaYF_4$ nanocrystals were also achieved by Wortmann *et al.*[252] The authors evaluated the performance of these nanocrystals by tuning their sizes, dispersing agent (distilled water *versus* an apolar organic solvent such as cyclohexane) and concentration of the emitting ions. Three trends were observed: (i) S_{rel} increased as the size of the nanocrystals decreased, attributed to the increase of the number of emitting ions in the surface of the nanoparticles due to the increase of the surface-to-volume ratio as the size decreased; (ii) S_{rel} was higher when the nanocrystals were dispersed in water than in cyclohexane, attributed to the O–H vibrational stretching mode of water molecules which leads to quenching of the luminescence;[260,261] and (iii) S_{rel} depended on the concentration of Ho^{3+} ions, due to the influence of the amount of this ion on the ET and CR rates that might take place between the sensitizer and the activators.[252] These three

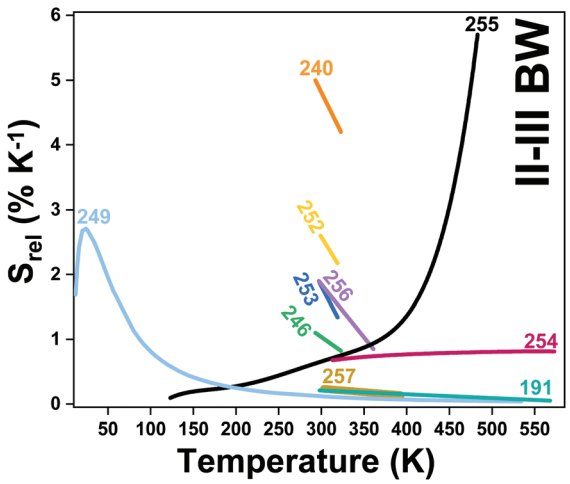

Fig. 33 Temperature dependence of S_{rel} of all nanothermometers operating simultaneously in the II- and III-BW regions. Numbers represent the corresponding literature references for each thermometer.

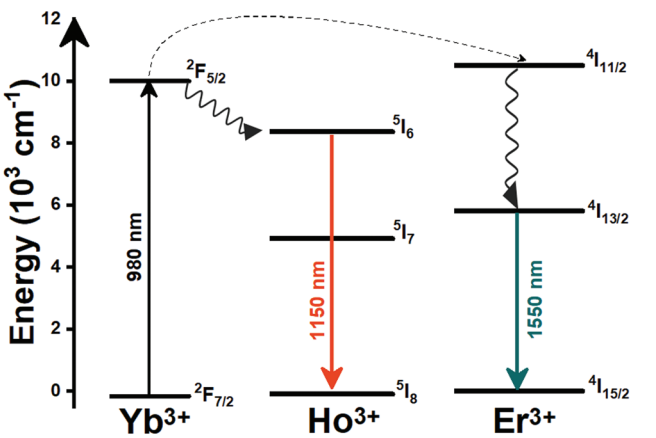

Fig. 34 Mechanism of generation of the emissions lines located in the II- and III-BWs of Er^{3+},Ho^{3+},Yb^{3+}:$NaYF_4$ nanoparticles under 980 nm excitation.

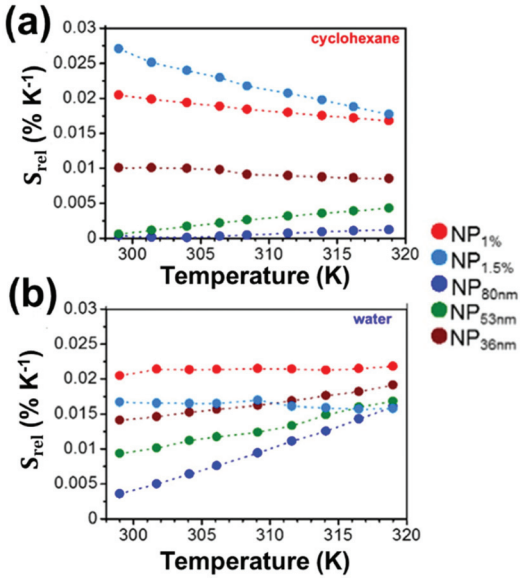

Fig. 35 S_{rel} of Er^{3+},Ho^{3+},Yb^{3+}:$NaYF_4$ nanocrystals as a function of dispersing agents: (a) cyclohexane and (b) distilled water. Also the effect of the Ho^{3+} concentration (1.5 mol% and 3 mol%) and the size of the nanocrystals (36 nm, 53 nm and 83 nm) can be observed. Adapted with permission from ref. 252. Copyright 2016, Elsevier.

tendencies can be seen in Fig. 35. The maximum S_{rel} (2.17% K^{-1}) was obtained for nanoparticles with a size ~48 nm, dispersed in cyclohexane and with a Ho^{3+} concentration of 1.5 mol%.[252]

Continuing the combination between the emissions of Er^{3+} and Ho^{3+}, Jia *et al.*[254] reasoned that phonons can play an essential role in allocation of harvested energy *via* two types of phonon-assisted processes: multi-phonon relaxation (MPR) between the $^4I_{11/2}$ and $^4I_{13/2}$ states of Er^{3+}, and PAET from the $^2F_{5/2}$ state of Yb^{3+} to the $^5I_6$ state of Ho^{3+}, that will govern the electronic population of the energy states of Er^{3+} and Ho^{3+} (Fig. 34). The temperature dependence of the probability rates of these processes happening can be described as:[254,262]

$$WPR_{MPR} = WPR_{MPR}(0)\left[\frac{\exp\left(\frac{h\nu}{k_BT}\right)}{\exp\left(\frac{h\nu}{k_BT}\right)-1}\right]^{\frac{\Delta E_1}{h\nu}} \quad (46)$$

$$WPR_{PAT} = WPR_{PAT}(0)\left[\frac{\exp\left(\frac{h\nu}{k_BT}\right)}{\exp\left(\frac{h\nu}{k_BT}\right)-1}\right]^{\frac{\Delta E_2}{h\nu}} \quad (47)$$

where $WPR_{MPR}(0)$, $WPR_{PAT}(0)$, $h\nu$, $\Delta E_1$and ΔE_2 represent the MPR rate at 0 K, the PAT rate at 0 K, the phonon energy of the host, the energy gap between the $^4I_{11/2}$ and $^4I_{13/2}$ states of Er^{3+}, and the energy gap between the $^2F_{5/2}$ electronic level of Yb^{3+} and the $^5I_6$ electronic state of Ho^{3+}, respectively. The thermometric parameter, defined as the intensity ratio between the emissions of Er^{3+} and Ho^{3+}, and the corresponding S_{rel} can be calculated according to:[254,262]

$$\Delta = \frac{I_{Er}}{I_{Yb}} = \frac{N_{Yb}W_RW_{MPR}A_1}{N_{Yb}W_{PAT}A_2} = a\left[\frac{\exp\left(\frac{h\nu}{k_BT}\right)}{\exp\left(\frac{h\nu}{k_BT}\right)-1}\right]^b \quad (48)$$

$$S_{rel} = \left|\frac{1}{\Delta}\frac{d\Delta}{dT}\right| = \frac{\Delta E_1 - \Delta E_2}{k_BT^2}\,\frac{1}{\exp\left(\frac{h\nu}{k_BT}\right)-1} \quad (49)$$

where $a = \frac{W_RW_{MPR}(0)A_1}{W_{PAT}(0)A_2}$, $b = \frac{\Delta E_1 - \Delta E_2}{h\nu}$, N_{Yb} represents the electronic population of the $^2F_{5/2}$ state of Yb^{3+}, W_R is the probability rate of the ET process, and A_1 and A_2 represent the spontaneous emission rates of the corresponding emission transitions.

For temperature-sensing purposes, the effect of these two mechanisms was tested in different hosts, including $BaTiO_3$, Gd_2O_3, Y_2O_3, YAG and YVO_4.[254] Theoretically, the different phonon modes of the host would contribute differently to the MPR and PAT processes; however one of them should play a major role.[263] In this study, the authors investigated the effect of the dominant and cutoff phonons on the thermometric performance of these luminescent thermometers, and determined that the dominant phonons have a major contribution to the MPR and PAT processes, and as a consequence, also to their temperature-sensing performance. Hence, the term $h\nu$ in eqn (48) and (49) was assigned to the dominant phonons presented in each of the tested hosts.[254] S_{rel} was inversely proportional to the dominant phonon energy (Fig. 36), assuming identical $\Delta E_1 - \Delta E_2$ in the different hosts. The highest S_{rel} was obtained for Er^{3+},Ho^{3+},Yb^{3+}:Gd_2O_3 nanoparticles, which had the lowest dominant phonon energy. It should be noticed that the maximum S_{rel} of these materials was usually obtained at

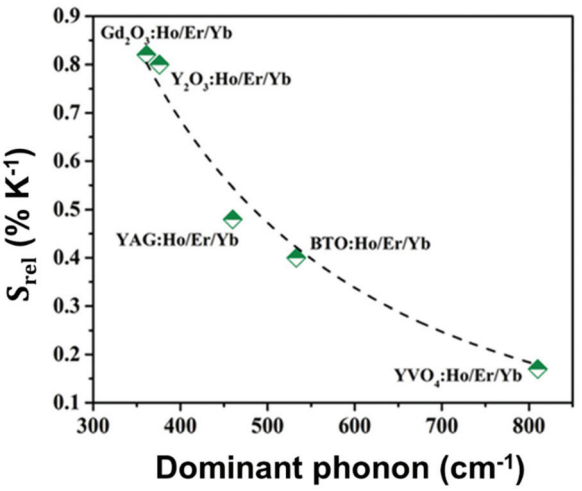

Fig. 36 S_{rel} of Er^{3+},Ho^{3+},Yb^{3+}-co-doped nanoparticles as a function of the dominant phonon energy. Reprinted with permission from ref. 254. Copyright 2020, Wiley-VCH Verlag GmbH & Co. KGaA.

the maximum temperature investigated (Table 4), contrary to the general trend observed in the other luminescence thermometers considered. In Table 4, however, it can be also observed that these phonon-assisted luminescent thermometers do not offer an improvement of thermal sensitivity, when compared with the other thermometers (for example Er^{3+},Ho^{3+},Yb^{3+}:$NaYF_4$ nanoparticles[252,253]).

For the combination of the emissions arising from Er^{3+} and Nd^{3+} ions, located at 1550 nm and 1340 nm, respectively, we recall the water-soluble Er^{3+},Ho^{3+},Yb^{3+}@Yb^{3+}@Nd^{3+}, Yb^{3+}@$NaGdF_4$ core@shell nanoparticles in PEG-DOPE micelles commented on previously in section 4.2.2, as the only example that could be found in the literature.[246] The mechanism of the generation of these emission lines is presented in Fig. 31(c). S_{rel}, calculated from the intensity ratio of the emissions at 1550 nm and 1340 nm, is 1.1% K^{-1} at room temperature.[246] This value is relatively low compared with other types of core@shell nanoparticles, such as is the case for Er^{3+},Yb^{3+}:LaF_3@Tm^{3+},Yb^{3+}:LaF_3 nanocrystals, but still higher than that of most of the luminescent nanothermometers based on the combination of emissions arising from Er^{3+} and Ho^{3+} (Table 4). Despite this, the temperature-sensing properties of this multishell structure are good for biomedical applications since they are water dispersible and are excited within the BW spectral regions.

Combining the emission of Er^{3+} with a transition metal, Ni^{2+} in this case, resulted in a S_{rel} slightly higher than the one obtained with Er^{3+},Yb^{3+}:LaF_3@Tm^{3+},Yb^{3+}:LaF_3 nanocrystals. Er^{3+},Ni^{2+}:$SrTiO_3$ nanocrystals were excited at 375 nm, and two emission bands were generated at 1540 nm, corresponding to Er^{3+}, and 1240 nm, corresponding to Ni^{2+}.[255] Upon excitation at 375 nm, Er^{3+} ions are excited from the ground state to the $^4G_{11/2}$ state. From here, successive non-radiative decay processes can populate the $^4S_{3/2}$ and $^4I_{13/2}$ states, and a radiative relaxation from the latter to the ground state results in the generation of the 1540 nm emission band. Similarly, the 1245 nm emission of Ni^{2+} is generated by the absorption of the energy of the 375 nm excitation source, promoting its electrons to the $^3T_{1g}$ (P) excited state. From here, non-radiative decay processes can populate the $^3T_{1g}$ (F) and $^3T_{2g}$ (F) metastable states, prior to relaxing radiatively to the ground state, which results in the generation of the corresponding emission band of this transition metal ion. In addition, from the $^3T_{1g}$ (F) of Ni^{2+} an ET process to the $^4S_{3/2}$ state of Er^{3+} can take place (Fig. 37), which might contribute to increasing the population of the $^4I_{13/2}$ state, eventually contributing to the generation of the emission band at 1540 nm. The emission located at 1245 nm, as for all the emissions of Ln^{3+} ions in luminescent thermometers combined with transition metal ions, is temperature insensitive, serving as a reference, whereas the emission at 1240 nm drastically changes as the temperature increases.[255]

The maximum S_{rel} for this luminescent thermometer was 5.8% K^{-1}, obtained at the highest temperature under investigation (483 K). This value is comparable to that reported for Er^{3+},Yb^{3+}:LaF_3@Tm^{3+},Yb^{3+}:LaF_3 nanocrystals, despite the significant differences in terms of excitation wavelengths. However, to have a proper comparison with other luminescent thermometers as potential temperature sensors for biomedical applications, S_{rel} should be compared in the physiological range of temperatures. By doing so, the S_{rel} for this luminescent thermometer is reduced to ~0.80% K^{-1} (Fig. 33).[255] In addition, another significant limitation for the luminescent thermometers based on the combination of Er^{3+} and Ni^{2+} is the need for excitation in the UV at 375 nm, which reduces significantly the penetration depth that can be achieved in biological tissues, and more important, this light induces phototoxicity in these kinds of sample.[13,86,90]

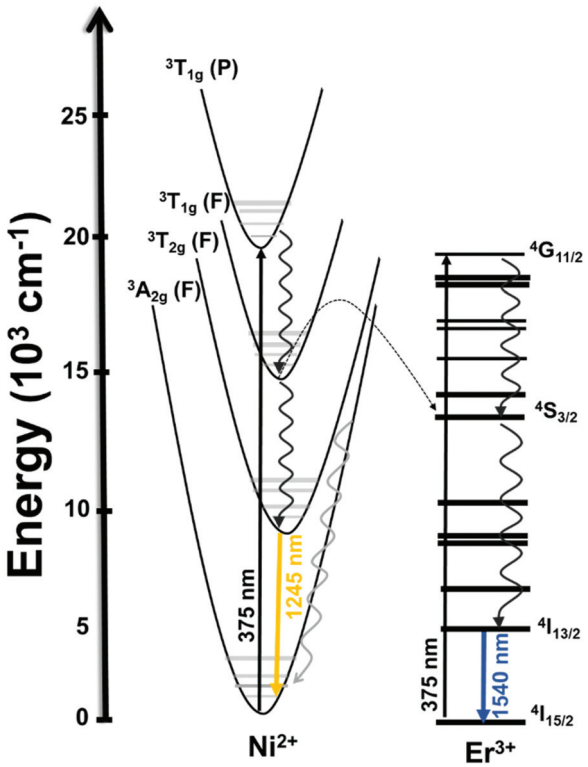

Fig. 37 Mechanism of generation of emission lines in Ni^{2+},Er^{3+}:$SrTiO_3$ nanoparticles under 375 nm excitation.

5.2. Other Ln^{3+}-doped luminescent nanothermometers operating in the II- and III-BWs simultaneously

Single-doped lanthanide materials based on the emission of Tm^{3+} and Nd^{3+} have been also reported as thermometers operating simultaneously in the II- and III-BWs.

For the Tm^{3+}-doped luminescent thermometers, their performance is based on the intensity ratio between the emissions located at 1230 nm and 1470 nm, generated after excitation either at 690 nm or 790 nm, as reported in Tm^{3+}:LaF_3 nanoparticles, arising from the $^3H_4$ and $^3H_5$ levels of Tm^{3+}, respectively.[256] The mechanism of generation of these emission bands is based on cross-relaxation (CR) and multiphonon decay processes (Fig. 38(a)). The population of the $^3H_5$ level is favored by a CR process, whereas the population of the $^3H_4$

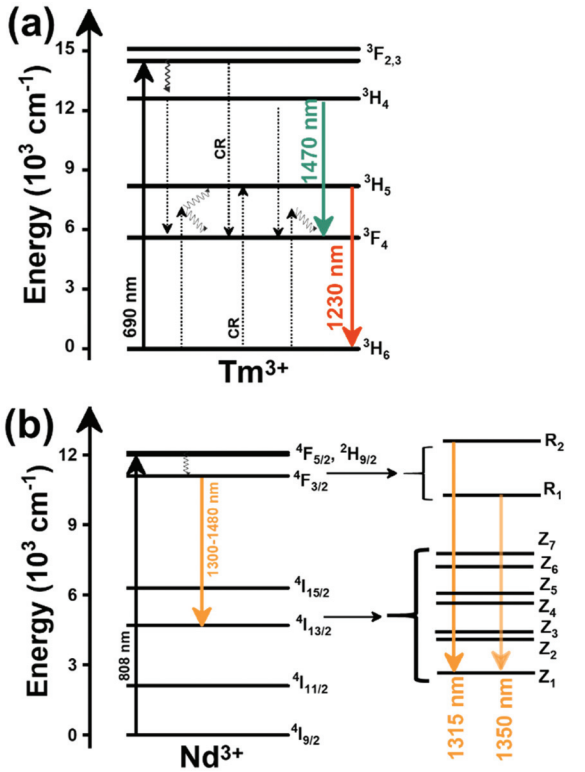

Fig. 38 Mechanism of the generation of the emission lines on: (a) Tm^{3+}-doped LaF_3 nanocrystals, and (b) Nd^{3+}:Gd_2O_3 nanospheres, operating in the II-BW and III-BW regions simultaneously.

level is due to multiphonon decay processes after electrons are excited to the $^3F_{2,3}$ levels by absorption of the energy of the 690 nm excitation source. From the $^3H_5$ level, a radiative decay to the $^3H_6$ ground state generates the emission located at 1230 nm, whereas through the $^3H_4 \rightarrow {}^3F_4$ transition, the emission band located at 1470 nm is generated.[256]

Concerning the temperature-sensing properties of this Tm^{3+} luminescent thermometer, the thermometric parameter was calculated from a linear fitting of the intensity ratio between the 1230 nm and the 1470 nm emission bands of Tm^{3+} with temperature. However, several parameters were analysed before determining the optimal S_{rel}. First, two different excitation wavelengths (690 nm and 790 nm) were tested with the goal of determining which one generated the brightest emissions. Upon 690 nm excitation, both emissions were brighter than when 790 nm excitation was used (Fig. 39(a)), demonstrating a more efficient excitation path. In fact, when excited at 790 nm, the 1230 nm emission band shows a considerably lower intensity compared with the other emission band, mainly due to the inefficient population of the $^3H_5$ level due to the small branching ratio of the $^3H_4 \rightarrow {}^3H_5$ transition and the low phonon energy of the LaF_3 host (<400 cm^{-1}),[264] which hampers multiphonon decay processes in this large ΔE. When excited at 690 nm, this level is populated through a CR process ($^3F_3$; $^3H_6 \rightarrow {}^3F_4$; $^3H_5$) that could be probed by the increase of the intensity of the 1230 nm emission band when the concentration of Tm^{3+} increased. Second, by tuning the concentration of Tm^{3+} from 1 mol% to 5 mol%, the Tm^{3+} concentration that displayed the highest change in the intensity of the emissions as the temperature increased was selected. It can be observed in Fig. 39(b) that the intensity of the 1230 nm

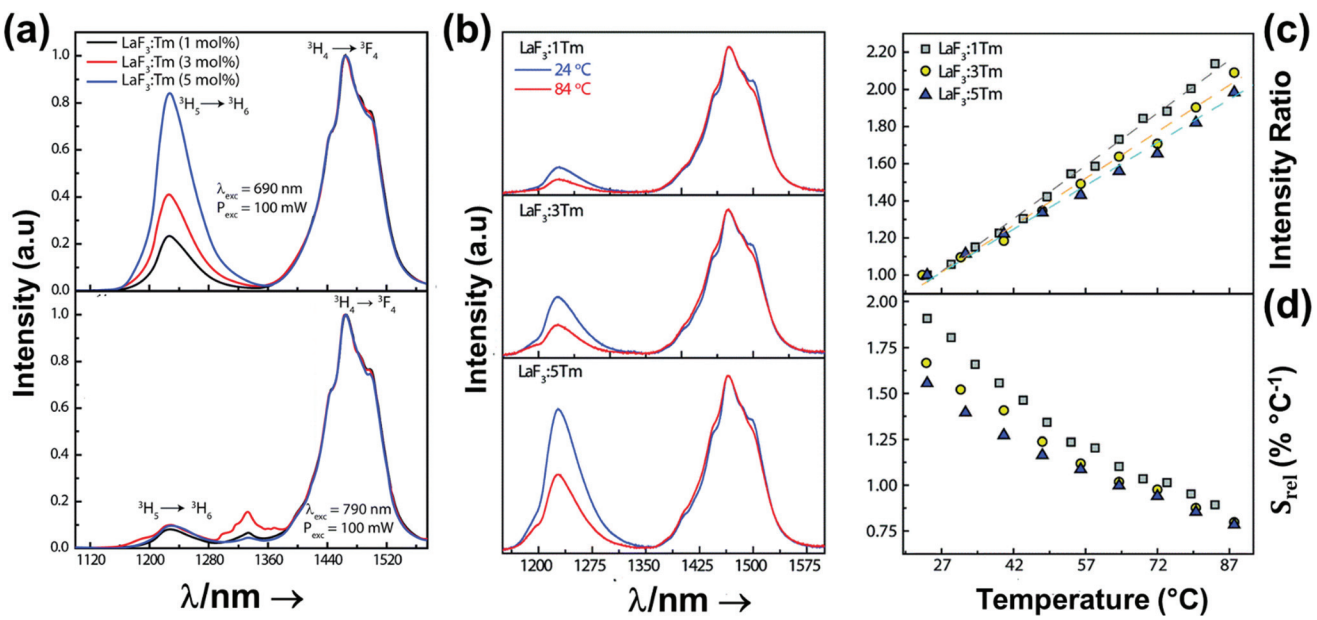

Fig. 39 (a) Emission spectra in Tm^{3+}-doped LaF_3 nanocrystals as a function of the concentration of the Tm^{3+} ions (1, 3, 5 mol%) and the excitation source (690 and 790 nm). (b) Variation of the intensity of the emissions in Tm^{3+}-doped LaF_3 nanocrystals with the change of the temperature. Variation of the: (c) intensity ratio and (d) S_{rel} of Tm^{3+}-doped LaF_3 nanocrystals as a function of the concentration of Tm^{3+} ions and temperature. Reprinted with permission from ref. 256. Copyright 2019, The Royal Society of Chemistry.

emission band changed substantially as a function of the concentration of Tm^{3+}, whereas the band at 1470 nm was almost insensitive, upon increasing the temperature from 297 K to 361 K. The intensity ratio decreased slightly as the Tm^{3+} concentration increased (Fig. 39(c)), and the maximum S_{rel}, 0.90% K^{-1}, was obtained for 1 mol% Tm^{3+} (Fig. 39(d)).[256] This value is quite high and comparable to that of dual emitting center luminescent thermometers operating in these spectral regions (Table 4). These results, combined with a δT of ~0.2 K, clearly underline the potential of this luminescent thermometer for biomedical applications.

For the Nd^{3+} luminescent thermometers operating in these spectral regions, the only example that could be found in the literature is that of Nd^{3+}:Gd_2O_3 nanoparticles, with the shape of nanospheres with a mean diameter of 108 nm ± 21 nm, synthesized *via* a precipitation method.[257] The performance of this material as a temperature sensor is based on the FIR from the emission lines of the Stark sublevels of the $^4F_{3/2} \rightarrow {}^4I_{13/2}$ transition, located in the 1300 nm–1480 nm region, while excited at 808 nm. This excitation source promotes Nd^{3+} electrons from the ground state to the $^4F_{5/2}$ excited state. From there, the $^4F_{3/2}$ level, and its different Stark sublevels, are populated through non-radiative decay processes (Fig. 38(b)). Radiative decays from these Stark sublevels to the lower Stark sublevel of the $^4I_{13/2}$ state generate the two emissions located at 1315 nm and 1350 nm used for temperature sensing in this particular case, with a S_{rel} of 0.23% K^{-1}.[257] According to the authors, this value was independent of the concentration of Nd^{3+} and was exclusively governed by the δT between the Stark sublevels (150 ± 20 cm^{-1}),[257] which is relatively low, providing this low value of S_{rel}.

6. Lanthanide-doped luminescent nanothermometers operating in the III-BW

The third biological window (III-BW), or the short wavelength infrared (SWIR) region as it was originally named,[126] started gaining the attention of researchers when Naczynski *et al.* reported that longer wavelengths than those lying in the I- and II-BWs transmitted up to three times more efficiently through oxygenated blood and melanin-containing tumors, and as a consequence for luminescent thermometry this would allow for deeper thermal readings in biological samples due to the reduction of tissue scattering and absorption, compared with the other BWs.[126] Moreover, up to now, the luminescent thermometers reported operating in the III-BW are all excited at wavelengths lying in the I-BW (Table 5), providing an important advantage for their possible application in biomedicine. Typical Ln^{3+} ions applied for temperature sensing in the III-BW are mainly based on the emissions arising from Tm^{3+} located at ~1450 nm and ~1800 nm, the emission of Er^{3+} located at ~1550 nm, and the emission of Ho^{3+} located at ~1960 nm. For the case of Tm^{3+}-doped luminescent thermometers operating in this spectral region, their performance is determined by the temperature dependence of the intensity ratio of their two emissions, or as more often encountered, combined with the emission of Ho^{3+}, using or not using Yb^{3+} a as sensitizer, and for the case of Er^{3+}-doped thermometers, the intensity ratio of their two emissions, or as more often encountered, combined with the emission of Ho^{3+}, using or not using Yb^{3+} as a sensitizer. For the case of Er^{3+}-doped

Table 5 Ln^{3+}-doped luminescent thermometers operating in the III-BW. In the table are shown the activators (A) and sensitizers (S). The excitation (λ_{exc}) and emission (λ_{em}) wavelengths are shown in nanometers (nm), together with the corresponding electronic transition producing these emissions. ΔT stands for the temperature range where the temperature reading was investigated. The thermometric parameter (Δ) indicates the luminescent nanothermometry class used in each case: FIR for band-shape and *I* for intensity ratio thermometry, respectively. The maximum relative thermal sensitivity (S_{rel}) and the minimum temperature resolution (δT) are presented at the temperature where these values were obtained. Marked by an asterisk are the values of S_{rel} or δT calculated by us, using the parameters published in the corresponding references. The double line separation between rows stands for different types of lanthanide-doped nanothermometers, as discussed in the corresponding subsections

A	S	Host	λ_{exc} (nm)	λ_{em} (nm)	Transitions	ΔT (K)	Δ	S_{rel}/T (% K^{-1})/K	δT (K)	Ref.
Tm^{3+}	Tm^{3+}	$KLu(WO_4)_2$	808	1470, 1740	$^3H_4 \rightarrow {}^3F_4$, $^3F_4 \rightarrow {}^3H_6$	298–333	I_{1470}/I_{1740}	0.08/298	6.2*	265
Tm^{3+}	Yb^{3+}	$NaYF_4$	980	1470, 1740	$^3H_4 \rightarrow {}^3F_4$, $^3F_4 \rightarrow {}^3H_6$	298–333	I_{1470}/I_{1740}	0.6/298	0.8*	265
Tm^{3+}	Yb^{3+}	$KLu(WO_4)_2$	980	1470, 1740	$^3H_4 \rightarrow {}^3F_4$, $^3F_4 \rightarrow {}^3H_6$	298–333	I_{1470}/I_{1960}	0.22/298	2.2*	265
Tm^{3+}	Yb^{3+}	$KLu(WO_4)_2$	808	1470, 1740	$^3H_4 \rightarrow {}^3F_4$, $^3F_4 \rightarrow {}^3H_6$	298–333	I_{1470}/I_{1740}	0.06/298	8.3*	265
Tm^{3+},Ho^{3+}	Tm^{3+}	$KLu(WO_4)_2$	808	1800 (Tm^{3+}), 1960 (Ho^{3+})	$^3H_4 \rightarrow {}^3F_4$ (Tm^{3+}), $^5I_7 \rightarrow {}^5I_8$ (Ho^{3+})	293–333	I_{1800}/I_{1960}	0.90/293	0.7	266
Tm^{3+},Ho^{3+}	Yb^{3+}	$KLu(WO_4)_2$	980	1480 (Tm^{3+}), 1960 (Ho^{3+})	$^3H_4 \rightarrow {}^3F_4$ (Tm^{3+}), $^5I_7 \rightarrow {}^5I_8$ (Ho^{3+})	298–333	I_{1480}/I_{1960}	0.52/298	0.9*	265
Er^{3+}	Yb^{3+}	$LuVO_4$	980	1637, 1660	$^4I_{13/2} \rightarrow {}^4I_{15/2}$	298–523	$FIR_{1637/1660}$	0.54/523	0.92*	267
Er^{3+}	Yb^{3+}	$LuVO_4$@SiO_2	915	1469, 1527	$^4I_{13/2} \rightarrow {}^4I_{15/2}$	298–523	$FIR_{1469/1527}$	0.18/298	2.7*	268
Er^{3+}	Yb^{3+}	NaY_2F_5O	980	1535, 1554	$^4I_{13/2} \rightarrow {}^4I_{15/2}$	298–333	$FIR_{1535/1554}$	0.15/298	3.3*	265
Er^{3+}	Yb^{3+}	$BaMoO_4$	980	1521, 1531	$^4I_{13/2} \rightarrow {}^4I_{15/2}$	293–553	$FIR_{1521/1531}$	0.13/293	3.8*	269
Er^{3+}	Yb^{3+}	$BaMoO_4$	980	1504, 1531	$^4I_{13/2} \rightarrow {}^4I_{15/2}$	293–553	$FIR_{1504/1531}$	0.095/293	5.2*	269
Er^{3+}	Yb^{3+}	$KLu(WO_4)_2$	980	1535, 1554	$^4I_{13/2} \rightarrow {}^4I_{15/2}$	298–333	$FIR_{1535/1554}$	0.095/298	5.2*	265
Er^{3+}	Yb^{3+}	Lu_2O_3	980	1535, 1554	$^4I_{13/2} \rightarrow {}^4I_{15/2}$	298–333	$FIR_{1535/1554}$	0.09/298	5.5*	265
Er^{3+}	Yb^{3+}	$NaYF_4$	980	1535, 1554	$^4I_{13/2} \rightarrow {}^4I_{15/2}$	298–333	$FIR_{1535/1554}$	0.06/298	8.3*	265

thermometers, the performance is entirely based on the temperature dependence of emissions arising from TCLs constituted by the Stark sublevels of the $^4I_{13/2} \rightarrow {}^4I_{15/2}$ transition, using Yb^{3+} as a sensitizer.

6.1. Tm^{3+}-doped luminescent nanothermometers operating in the III-BW

Tm^{3+}-doped luminescent thermometers operating in the III-BW were either excited at 980 nm or 808 nm, depending on whether Yb^{3+} has been used as sensitizer or not. When Yb^{3+} was used as a sensitizer, Tm^{3+}-doped luminescent thermometers were excited at 980 nm (Table 5). These thermometers can be formed by nanoparticles doped with Tm^{3+} or co-doped with Ho^{3+}, using Yb^{3+} as the ion that absorbed the energy of the excitation source. Upon 980 nm excitation, the luminescence spectrum of the Tm^{3+}-doped nanoparticles in the III-BW was composed of two emissions at ~1450 nm and ~1800 nm, whereas when Ho^{3+} was also present, a third emission band at ~1960 nm was observed. Yb^{3+} ions acting as a sensitizer absorb the 980 nm excitation light, promoting their electrons from the $^2F_{7/2}$ ground stated to the $^2F_{5/2}$ excited state. Due to the energy resonance between this level of Yb^{3+} and the $^3H_5$ level of Tm^{3+}, an ET process can take place, populating this level of Tm^{3+}. From the $^3H_5$ level, electrons can relax non-radiatively to the $^3F_4$ level.

From this state, the energy of a second excited electron of Yb^{3+} is transferred to Tm^{3+} while its electrons are in the $^3F_4$ excited state, promoting them to the $^3F_{2,3}$ state. From this state, a second non-radiative process can take place towards the $^3H_4$ energy level, from which the emission band located at 1450 nm is generated through the $^3H_4 \rightarrow {}^3F_4$ electronic transition (Fig. 40(a)). Finally, a radiative relaxation of the electrons from the $^3F_4$ level to the ground state gives rise to the second emission of Tm^{3+} located at 1800 nm.[265]

With the addition of Ho^{3+}, an additional ET process can take place from Yb^{3+} to the $^5I_6$ level of Ho^{3+} that is resonant in energy with the $^2F_{5/2}$ excited state of Yb^{3+}. From it, the $^5I_7$ level of Ho^{3+} can be populated through a non-radiative relaxation process, prior to a radiative transition to the ground state ($^5I_8$), generating the emission at 1960 nm. Another mechanism for the generation of the Ho^{3+} emission band is a direct ET process from the $^3H_5$ level of Tm^{3+} to the resonant $^5I_6$ level of Ho^{3+} (Fig. 40(a)). This mechanism, however, has a lower probability of happening due to the high concentration of Yb^{3+} in the nanoparticles, up to ten times higher than that of Tm^{3+}, which makes more feasible the ET between Yb^{3+} and Ho^{3+}.[265]

The addition of Ho^{3+} provided positive effects not only in the intensity of the luminescence of the whole spectrum, which was improved, but also in the temperature-sensing properties.

Hence, the presence of Ho^{3+} plays an important role in transferring additional energy towards Tm^{3+} ions through the $^5I_6$ and $^3H_5$ levels of Ho^{3+} and Tm^{3+}, respectively (Fig. 40(a)), apart from that already transferred by Yb^{3+}. The intensity ratio between the two emissions of Tm^{3+} ions was considered for luminescence thermometry purposes in Ho^{3+},Tm^{3+},Yb^{3+}:KLu

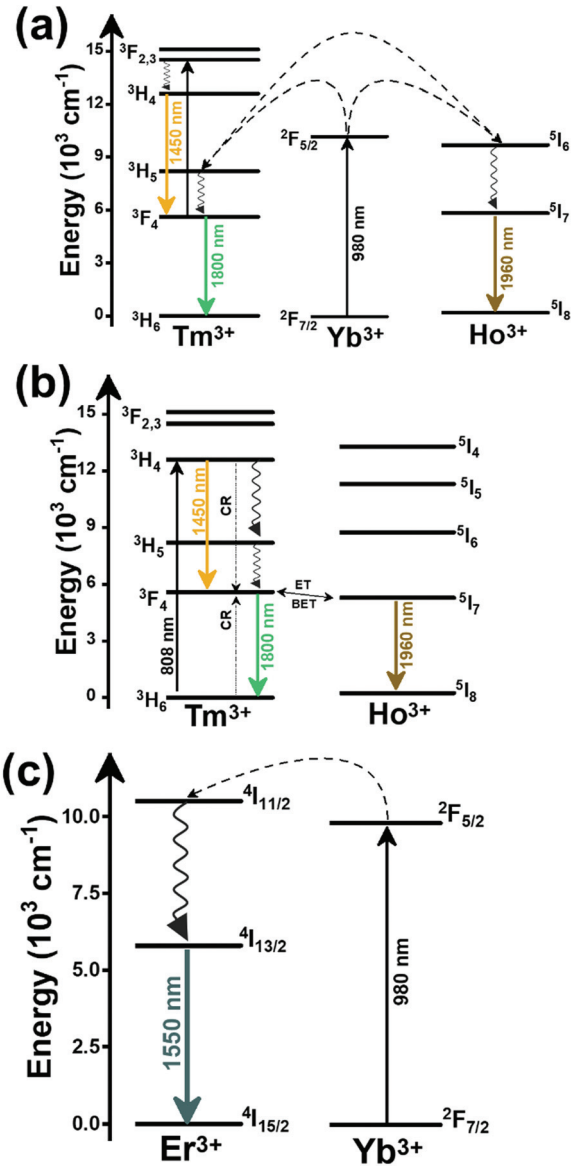

Fig. 40 Mechanism of the generation of the emission lines in: (a) Ho^{3+}, Tm^{3+},Yb^{3+}:$KLu(WO_4)_2$, (b) Ho^{3+},Tm^{3+}:$KLu(WO_4)_2$, and (c) Er^{3+},Yb^{3+}-doped materials operating as luminescent thermometers in the III-BW.

$(WO_4)_2$ nanoparticles, obtaining a two-fold higher S_{rel} in the nanoparticles containing Ho^{3+} when compared with those containing only Tm^{3+} (Table 5).

Besides the benefits demonstrated by this kind of luminescent thermometer, one thing that should be considered is the fact that they were excited at 980 nm, which would hamper their potential biomedical applications due to the absorption of this radiation by water and the subsequent heat generation.[206] To surpass this drawback, the possibility of exciting these materials at 808 nm through the direct absorption of energy by Tm^{3+} was considered as a solution.

Hence, in the absence of Yb^{3+} ions, an illustrative example is Ho^{3+},Tm^{3+}:$KLu(WO_4)_2$ nanocrystals. Upon excitation at 808 nm, Tm^{3+} promotes its electrons from the $^3H_6$ ground

state to the $^3H_4$ excited state. The electrons decay radiatively to the $^3F_4$ manifold, generating the emission line at 1.45 μm. From the $^3F_4$ level, a second radiative relaxation to the $^3H_6$ ground state generates the emission line at 1.8 μm. Tm^{3+} might undergo a CR process $^3H_4$, $^3H_6$ → $^3F_4$, $^3F_4$, which contributes to the higher intensity observed for the emission band at 1.8 μm. Also, due to the energy resonance between the $^3F_4$ level of Tm^{3+} and the $^5I_7$ level of Ho^{3+}, ET and BET processes might take place between these electronic levels, promoting the electrons of Ho^{3+} to this excited state from the ground state. Then, the electrons of Ho^{3+} relax radiatively to the $^5I_8$ ground state, giving rise to the emission band at 1.96 μm (Fig. 40(b)).[270] The temperature-sensing properties of Tm^{3+}:$KLu(WO_4)_2$, Tm^{3+},Yb^{3+}:$KLu(WO_4)_2$ and Ho^{3+},Tm^{3+}:$KLu(WO_4)_2$ nanocrystals were compared upon excitation at 808 nm in the physiological range of temperatures. It was observed that when the temperature increased, the intensity of the 1450 nm band remained unchanged, while the intensity of the 1800 nm band decreased for Tm^{3+} and Tm^{3+},Yb^{3+} particles. Instead, for Tm^{3+},Ho^{3+} nanoparticles, the intensity of both the 1450 nm and 1960 nm bands decreased as the temperature increased, while the intensity of the 1800 nm band increased (Fig. 41(a)), indicating that the BET mechanism (Fig. 40(b)) between these two ions is promoted as the temperature increased.[265]

As a consequence, the S_{rel} of Ho^{3+},Tm^{3+}:$KLu(WO_4)_2$ nanoparticles is approximately 5 times higher than that of Tm^{3+}:$KLu(WO_4)_2$ and Tm^{3+},Yb^{3+}:$KLu(WO_4)_2$ nanoparticles, by considering either the 1450 nm/1800 nm or the 1800 nm/1960 nm intensity ratio, which provided the same S_{rel} since the electronic populations of the two emitting levels of Tm^{3+} from which the emissions at 1450 and 1800 nm are generated are linked through the CR process $^3H_4$, $^3H_6$ → $^3F_4$,$^3F_4$ (Fig. 41(b)).[266] Then, the effects of other parameters like the excitation power, the different lanthanide doping concentrations, and the choice between the 1450 nm/1800 nm, 1450 nm/1960 nm or 1800 nm/1960 nm intensity ratios were analyzed. The 1800 nm/1960 nm intensity ratio changed the most as the excitation power increased (Fig. 41(b)). The linear variation of these intensity ratios with the excitation power represents a very important point when envisaging the application of these luminescent nanothermometers in biomedical fields. During biomedical applications, there is no real control of the excitation power reaching the nanoparticles within the biological sample; hence this might lead to inaccuracy that can be reduced with this linear variation, while always maintaining it at a value low enough to avoid damage to the biological tissues. The optimal doping concentration to maximize the luminescence intensity was found at 3 at% of Ho^{3+} and 5 at% of Tm^{3+}.[266] The doping concentration that allowed obtaining

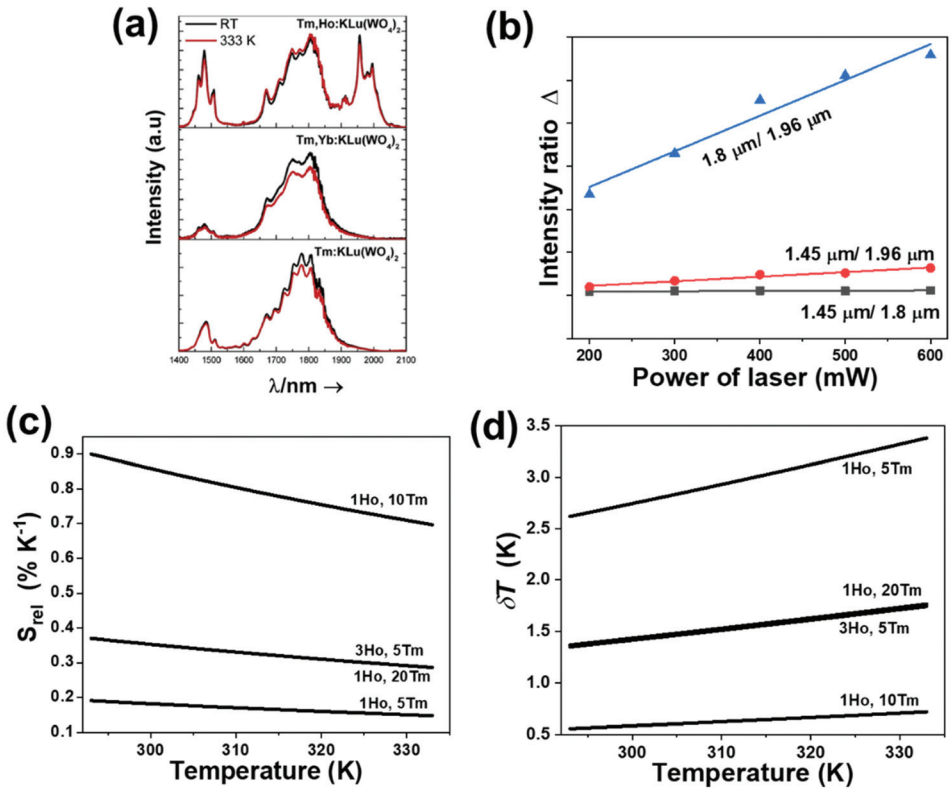

Fig. 41 (a) Effect of temperature in the III-BW emissions for the $KLu(WO_4)_2$ nanoparticles doped with Tm^{3+}; Tm^{3+},Yb^{3+} and Ho^{3+},Tm^{3+} ions after pumping at 808 nm. Reprinted with permission from ref. 265. Copyright 2016, Elsevier. (b) Evolution of the intensity ratios in Ho^{3+},Tm^{3+}:$KLu(WO_4)_2$ nanoparticles as a function of the excitation power. Effect of different lanthanide doping concentrations in Ho^{3+},Tm^{3+}:$KLu(WO_4)_2$ nanoparticles on: (c) S_{rel}, and (d) temperature resolution. (b)–(d) Adapted with permission from ref. 266. Copyright 2020, The Royal Society of Chemistry.

the highest S_{rel} (0.90% K^{-1}), and subsequently the minimum δT (0.55 K at 293 K), was found at 1 at% of Ho^{3+} and 10 at% of Tm^{3+} (Fig. 41(c) and (d) and Table 5). Thus, different doping concentrations of Tm^{3+} and Ho^{3+} imply different efficiencies for the electronic population processes, especially those concerning the ET and BET processes between the $^3F_4$ level of Tm^{3+} and the $^5I_7$ level of Ho^{3+}, and consequently different thermometric performances.[266] We underline as an important conclusion from this section the combination of Tm^{3+} and Ho^{3+} emissions to generate highly sensitive thermometers.

6.2. Er^{3+}-doped luminescent nanothermometers operating in the III-BW

Er^{3+} doped luminescent nanothermometers operating in the III-BW exhibit, in general, a very low S_{rel} (Table 5). Their performance, based entirely on the emissions generated from the different Stark sublevels of the $^4I_{13/2} \rightarrow {}^4I_{15/2}$ transition, has been evaluated through the FIR model (eqn (9)), being strictly related to the ΔE between the Stark sublevels involved in the generation of the emissions in which these luminescent thermometers are based (50–130 cm^{-1}), which in general are very small.

Er^{3+}-doped luminescent thermometers operating in the III-BW used Yb^{3+} as a sensitizer, which implies excitation at 980 nm. The mechanism of generation of this emission band is depicted in Fig. 40(c). After the absorption of a photon at 980 nm by Yb^{3+}, its electrons are promoted to the $^2F_{5/2}$ level. Then, an ET to Er^{3+} occurs, populating its $^4I_{11/2}$ level. After a multiphonon relaxation to the $^4I_{13/2}$ energy level followed by a radiative decay to the ground state through the $^4I_{13/2} \rightarrow {}^4I_{15/2}$ transition, the emission centered at 1550 nm is generated.[265,267,268]

The intensity of the emission generated and the thermometric performance of different Er^{3+}-doped luminescent thermometers operating the III-BW was analyzed by Savchuk *et al.* as a function of different hosts, including oxyfluorides (NaY_2F_5O), fluorides ($NaYF_4$), simple oxides (Lu_2O_3) and complex oxides ($KLu(WO_4)_2$).[265] In terms of intensity, the fluoride host exhibited the highest one, mainly attributed to its low phonon energy (Fig. 42(a)). Comparing their temperature-sensing properties in the physiological range of temperatures, calculated from eqn (9), the oxyfluoride host (NaY_2F_5O) exhibited the highest S_{rel}, with a value of 0.15% K^{-1} at room temperature, almost 3 times higher than that obtained for the other hosts.[265]

In another study, in which $BaMoO_4$ was studied as a host for Er^{3+}, the authors demonstrated that the performance of these Er^{3+}-doped luminescent thermometers is influenced by

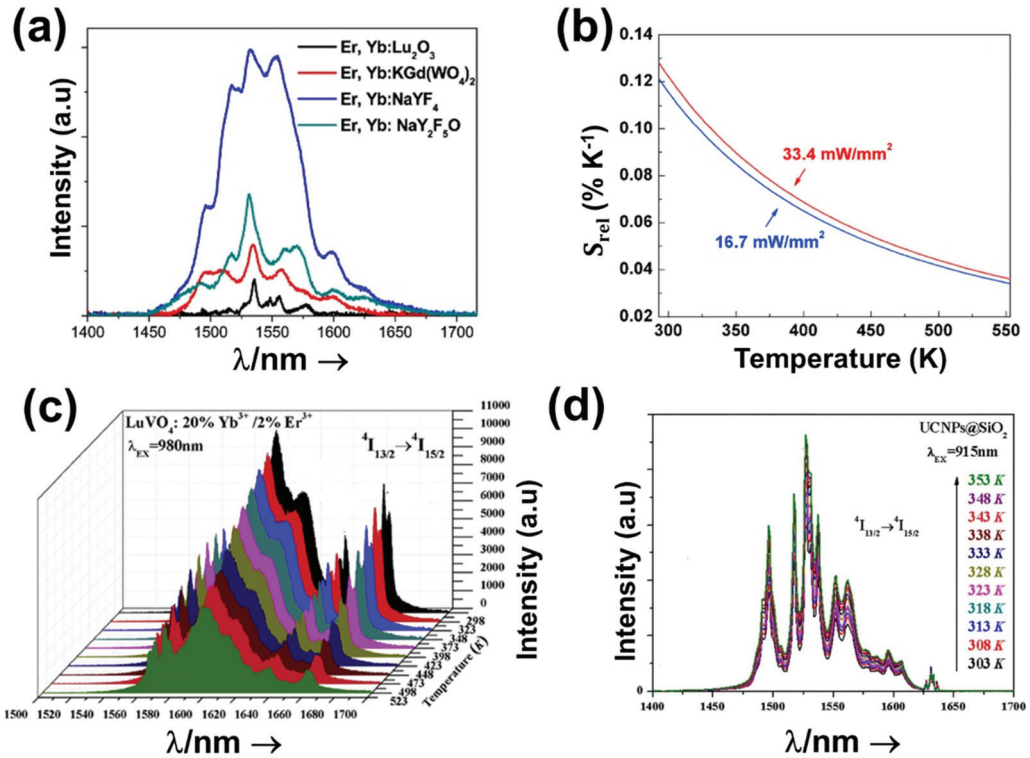

Fig. 42 (a) Intensity of the Er^{3+} 1550 nm emission in different hosts after excitation at 980 nm. Reprinted with permission from ref. 265. Copyright Elsevier. (b) Effect of the excitation power density at 980 nm in S_{rel} of Er^{3+},Yb^{3+}:$BaMoO_4$ nanoparticles. Reprinted with permission from ref. 269. Copyright 2018, Elsevier. (c) Temperature dependence of the intensity of the Er^{3+} 1550 nm emission in Er^{3+},Yb^{3+}:$LuVO_4$ nanoparticles, excited at 980 nm. Reprinted with permission from ref. 267. Copyright 2018, Elsevier. (d) Temperature dependence of the intensity of the Er^{3+} 1550 nm emission in $LuVO_4$@SiO_2 core–shell nanoparticles, excited at 915 nm. Reprinted with permission from ref. 268. Copyright 2019, American Chemical Society.

the excitation power density.[269] The authors tested two different intensity ratios from the Stark sublevels of the $^4I_{13/2} \rightarrow {}^4I_{15/2}$ transition (1504 nm/1531 nm and 1521 nm/1531 nm) under two different excitation power densities (16.7 mW mm^{-2} and 33.4 mW mm^{-2}). The 1504 nm/1531 nm intensity ratio was almost insensitive to the variation of the excitation power density, whereas the 1521 nm/1531 nm intensity ratio allowed a slightly higher S_{rel} to be obtained at higher excitation power densities (Fig. 42(b)).

All the thermometers mentioned above calculated their performance based on the Boltzmann model; however, in some cases another phenomenological fitting model was applied. This is the case for Er^{3+},Yb^{3+}:$LuVO_4$[267] and Er^{3+},Yb^{3+}:$LuVO_4$@SiO_2 nanoparticles,[268] where the thermometric parameter was fitted to the phenomenological equation:

$$\Delta = B \exp(a + b + cT^2) \quad (50)$$

where B, a, b and c are all constants to be determined by the fitting.

According to that, S_{rel} could be calculated as:

$$S_{rel} = |b + cT| \times 100\% \quad (51)$$

The maximum S_{rel} (0.54% K^{-1}) was obtained for the uncoated Er^{3+},Yb^{3+}:$LuVO_4$ nanoparticles, at the highest temperature under study (523 K).[267] For the silica-coated nanoparticles, a lower S_{rel} (~0.18% K^{-1}) was obtained at room temperature, although they were excited at a different wavelength.[268]

An additional difference between these two materials was observed in the evolution of the intensity of the emission as the temperature increased. For the uncoated nanoparticles, excited at 980 nm, the intensity of the emission decreased as the temperature increased (Fig. 42(c)), while for the SiO_2-coated nanoparticles a general increase of the intensity of the emission band as the temperature increased was observed (Fig. 42(d)), assigned, according to the authors, to the improvement of the multiphonon relaxation process from the $^4I_{11/2}$ level to the $^4I_{13/2}$ level as the temperature increased.

A final remark for this subsection should be devoted to the fact that the excitation wavelength used for these luminescent thermometers has the drawback of causing overheating, hampering their use in biomedical applications.[206] Even though in Er^{3+},Yb^{3+}:$LuVO_4$@SiO_2 core–shell nanoparticles excitation at 915 nm was applied to overcome this problem, the absorption cross section of Yb^{3+} at this wavelength is only half of that at 980 nm, which generates weaker emissions and might make their practical use as luminescent thermometers difficult.[271]

In summary, the variation of S_{rel} with the increase of temperature for the luminescent thermometers operating in the III-BW is presented in Fig. 43(a) and (b). In general, for these thermometers a decrease of S_{rel} is observed as the temperature increases, with the exception of the thermometer based on Er^{3+},Yb^{3+}:$LuVO_4$ nanoparticles, due to the different model to which the experimental data were fitted. In addition, the S_{rel} of the Er^{3+}-doped luminescent thermometers operating within the III-BW is relatively low compared with the Tm^{3+}-doped ones. When compared with the luminescent thermometers operating in the other BWs, the relative thermal sensitivities of the thermometers operating in the III-BW are lower, implying that additional strategies to boost their performances need to be developed.

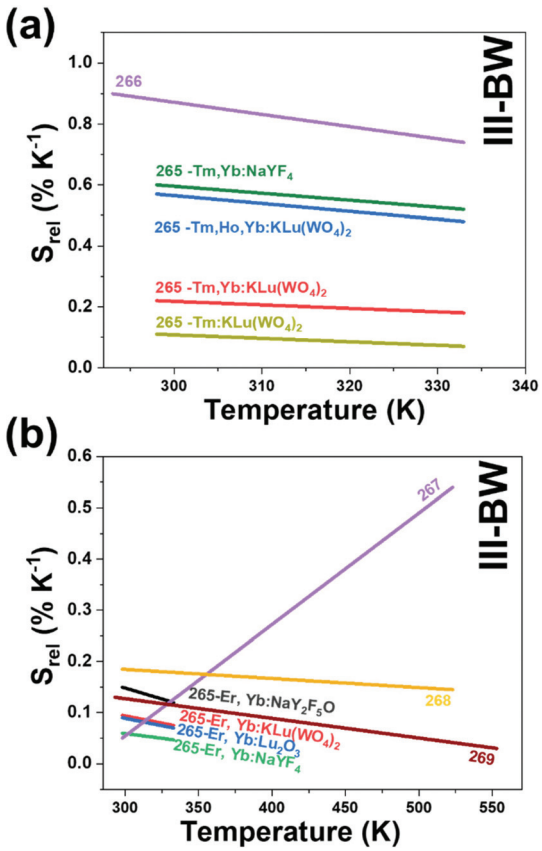

Fig. 43 Temperature dependence of S_{rel} of: (a) Tm^{3+}- and (b) Er^{3+}-doped thermometers operating in the III-BW. The numbers indicate the corresponding references for each thermometer.

7. Applications of lanthanide-doped luminescent nanothermometers operating within the BWs

The development of highly sensitive lanthanide-doped luminescent nanothermometers by means of tunable synthetic strategies and the combination of different emission bands has accelerated their application as potential tools for thermal sensing in *ex vivo*, *in vitro* and *in vivo* trials, including 2D subcutaneous dynamic thermal imaging as well as controlled photothermal therapy experiments. This section covers most of the examples published up to now devoted to the applications of these Ln^{3+}-doped luminescent nanothermometers operating within the different BW spectral ranges. It concludes with some other applications, distinct from those in the bio-

medical/biological fields in which these luminescent thermometers have also been used.

7.1. Biological/biomedical applications of lanthanide-doped luminescent nanothermometers operating within the BWs

7.1.1. *Ex vivo* thermometry using lanthanide-doped luminescent nanothermometers operating in the BWs. Lanthanide-doped luminescent nanothermometers, upon suitable excitation and analysis of their emissions, can sense the temperature within biological tissues. The temperature-dependence properties of the luminescence of the Ln^{3+}-doped materials allows their applicability as nanothermometers, despite the fact that a recalibration is required when they are embedded in a new medium,[13,47,214,259] which in most cases is neglected. Here, we cover the examples published in the literature of Ln^{3+}-doped luminescence nanothermometers acting as thermal sensing agents in *ex vivo* experiments. *Ex vivo* refers to experimentation or measurements done in or on tissue from a biological organism in an external environment with minimal alteration of its natural conditions.[272] The luminescent thermometers most used in biological/biomedical applications are those based on Nd^{3+}. This ion can be excited with cost-effective NIR laser diodes with emissions in the I-BW (790 nm and 808 nm). Among these, 808 nm has been demonstrated to be a risk-free wavelength for biological applications.[199,273] Additionally, all the characteristic emission bands of Nd^{3+}, located at ~890 nm, ~1060 nm and ~1350 nm, lie within the BWs, respectively in the I-, II- and III-BWs. Hence, excitation and emissions within the BWs will allow higher penetration depths and deeper temperature sensing to be achieved.

Benayas *et al.*[171] reported the ability of Nd^{3+}:YAG luminescent nanothermometers for *ex vivo* temperature monitoring, based on their emissions located in the I-BW (Table 1). The temperature-sensing properties of these nanothermometers were based on the emission lines from different Stark sublevels of the $^4F_{3/2} \rightarrow {}^4I_{11/2}$ transition, located at 938 nm and 945 nm, after pumping at 800 nm with a power of 100 mW. 100 μL of a 0.1 wt% water dispersion of Nd^{3+}:YAG nanoparticles were injected into chicken breast tissue at a depth of 5 mm. The biological tissue was externally heated using a hot air flow (343 K) for 90 s, prior to letting it to cool down to room temperature naturally, as illustrated in Fig. 44(a). The luminescence and the intensity ratio of the particles during the heating/cooling cycles was monitored for a period of more than 8 min. The time evolution of the intensity ratio between the two emission lines and the corresponding subtissue temperature determined from it revealed that during the heating process a linear increase of the subtissue temperature with time was produced, reaching a maximum temperature change of about 328 K (Fig. 44(b)).[171]

When the hot air flow was turned off, an exponential decrease of the temperature due to thermal diffusion was observed (Fig. 44(b)).

Based on heating–cooling cycle dynamics, Skripka *et al.* used water-dispersible Nd^{3+}:$LiLuF_4$@$LiLuF_4$ nanocrystals as *ex vivo* luminescent temperature sensors.[164] These nanocrystals, in principle, can work as *ex vivo* thermal sensors in the three BWs (they generate emissions located at 880 nm, 1050 nm and 1320 nm). However, the authors selected the emission band located in the II-BW ($^4F_{3/2} \rightarrow {}^4I_{11/2}$ transition, 1050 nm) due to its higher intensity. The heating–cooling cycles generated in a pork fat tissue sample when a 980 nm laser (power density ~37 W cm^{-2}) was turned on and off were measured with an aqueous dispersion of these Nd^{3+}:$LiLuF_4$@$LiLuF_4$ nanocrystals with a concentration of 5 mg mL^{-1} as a function of the tissue thickness (Fig. 45(a)). To record the emission generated by the nanocrystals they were continuously excited at 793 nm with a power density ~49 W cm^{-2} for a period of 12 min. The recorded photoluminescence and the calculated intensity ratio based on the different emission lines arising from the different Stark sublevels that generate the 1050 nm emission of Nd^{3+} were used to determine the temperature. A temperature increase was induced in the pork fat tissue sample by turning ON the 980 nm laser after 2 min from the beginning of the experiment (2 min after the 793 nm laser was turned ON to excite the luminescent nanoparticles) and heating the sample for 5 min, after which it was switched OFF (Fig. 45(a)). After switching OFF the 980 nm laser, the cooling profile was also monitored through the emission generated by the nanoparticles over the next 5 min with the 793 nm laser still ON. In addition, a thermocouple was used to verify the temperature measurements. Based on these heating–cooling cycles, the heat dissipation time constant of the nanoparticles in the surrounding medium, δT, and the temporal uncertainty of the luminescent nanothermometers were determined at different biological tissue thicknesses. The results revealed that as the biological tissue becomes thicker, the values for the heat dissipation time constant determined from the spectra collected with the nanoparticles began to deviate from those measured with the thermocouple.[164] Also, a signifi-

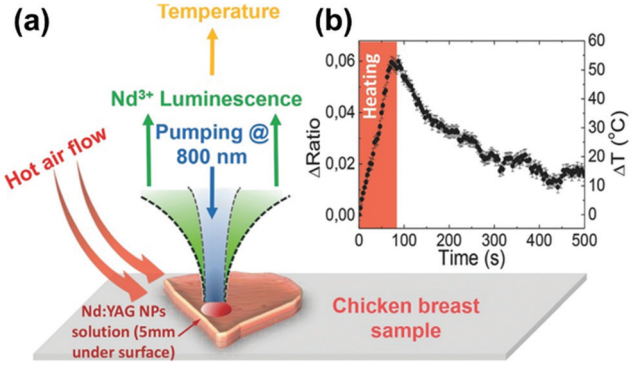

Fig. 44 *Ex vivo* temperature sensing in the I-BW with Nd^{3+}:YAG nanoparticles. (a) Scheme of the experimental procedure used to measure the time evolution of the subtissue temperature of a chicken breast sample in which an aqueous dispersion of the luminescent nanothermometers was injected, externally heated by a flow of hot air. (b) Time evolution of the subtissue temperature determined from the ratio between the intensities of the 938 nm and 945 nm emission bands of Nd^{3+}. Reprinted with permission from ref. 171. Copyright 2015, Wiley-VCH Verlag GmbH & Co. KGaA.

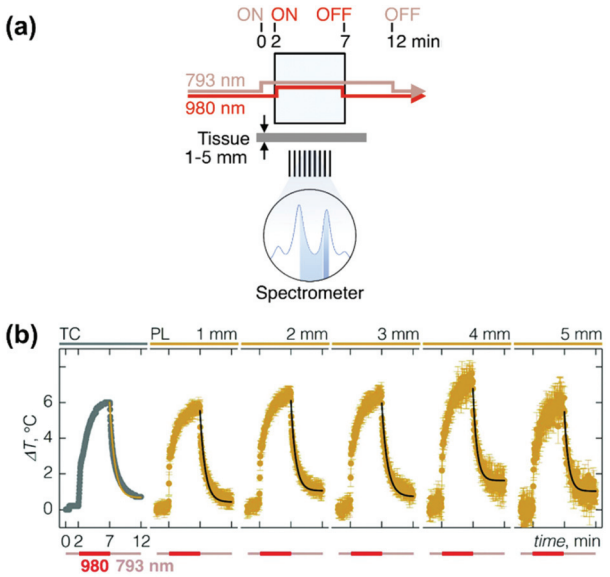

Fig. 45 (a) Scheme of the heating–cooling experiment measurements in pork fat tissue. (b) Heating-cooling cycles measured with an aqueous dispersion of Nd:$LiLuF_4$@$LiLuF_4$ nanocrystals measured with a thermocouple (TC) and *via* the intensity ratio among the emissions generated by the different Stark sublevels of the 1050 nm emission of Nd^{3+}, as a function of the pork fat tissue thickness. Reprinted with permission from ref. 164. Copyright 2019, The Royal Society of Chemistry.

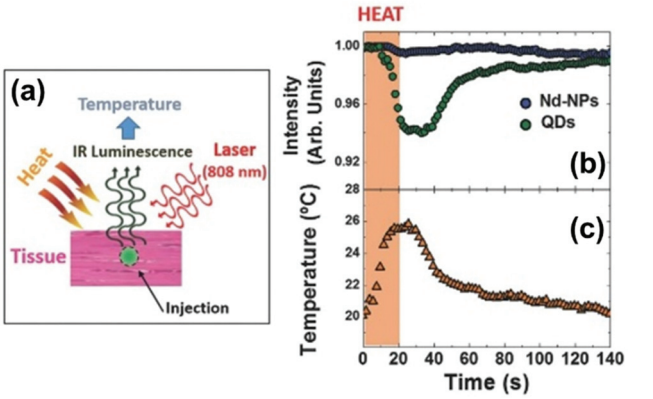

Fig. 46 *Ex vivo* temperature sensing in the II-BW with hybrid Nd^{3+}:$NaGdF_4$ and QDs in PGLA particles. (a) Scheme of the experimental procedure. (b) Evolution of the intensity of the 1060 nm (Nd^{3+}) and 1220 nm (QDs) emissions, normalized to their room temperature values, of the hybrid particles injected into the chicken breast tissue during a heating/cooling cycle. (c) Sub-tissue temperature evolution during the heating/cooling cycle determined from the intensity ratio of the emissions of the hybrid Nd^{3+}:$NaGdF_4$ and QDs in PGLA particles. Reprinted with permission from ref. 63. Copyright 2015, Wiley-VCH Verlag GmbH & Co. KGaA.

cant error was observed in the determination of the temperature difference induced solely by the 980 nm light, and calculated between the OFF point of the 980 nm laser and the end of the cycle, attributed to the photoluminescence extinction of the biological tissue. With the increase of the thickness of the biological tissue from 1 to 5 mm, the δT of the luminescent thermometer changed from 0.19 to 1.23 K, while the temporal uncertainty changed from 0.52 ± 0.37 to 4.26 ± 6.60 s.[164] As a conclusion, and as can be observed in Fig. 45(b), the reliability of these nanothermometers is highly compromised for a tissue thickness above 2 mm.

Another example of a luminescent nanothermometer applied in an *ex vivo* experiment is that of water-dispersible hybrid Nd^{3+}:$NaGdF_4$ nanoparticles and the semiconductor PbS/CdS/ZnS QDs in PGLA, operating in the II-BW using the intensity ratio between the 1060 nm emission of Nd^{3+} and the 1220 nm emission of QDs (Table 3).[63] The ability of these particles to sense the temperature in biological tissues was tested by injecting subcutaneously 100 μL of a 1 mg mL^{-1} dispersion of these particles in distilled water into a chicken breast sample at a depth of ~2 mm. The biological tissue was externally heated using a hot air current at 323 K for 20 s, prior to letting it to cool down to room temperature naturally. The emissions of the Nd^{3+}:$NaGdF_4$ nanoparticles and the QDs, generated within the tissue after excitation at 808 nm with a 1 W cm^{-2} power density, were collected by an optical fiber and spectrally analyzed through a high-resolution spectrometer (Fig. 46(a)). The temperature profile of these emissions displayed a different behavior during heating/cooling cycles (Fig. 46(b)). During the heating cycle (shadowed area), the emission of Nd^{3+} remained unchanged, while the emission of the QDs drastically decreased due to thermal quenching effects.[63] During the cooling process, the emission of the QDs recovered its initial value. The variation of temperature of the tissue during the heating/cooling cycles was determined by calculating the intensity ratio between these two emissions (Fig. 46(c)). The results showed a temperature increase of approximately 6 K at the end of the heating pulse.[63] During the cooling cycle, a pseudo-exponential decreasing profile was observed, monitored for two minutes until the initial room temperature was recovered. From the magnitude of the random fluctuations in the temperature profile (Fig. 46(c)), δT was estimated to be 0.2 K (Table 3).[63]

Ex vivo lanthanide nanothermometers operating in the III-BW have been also reported. Savchuk *et al.* investigated the intensity ratio between the 1470 nm and 1711 nm emissions of Tm^{3+} in Ho,Tm:KLuW nanoparticles to sense the temperature inside a chicken breast sample at a depth of 2 mm, after being excited at 808 nm with a power of 200 mW.[265] For the experiment, the nanoparticles were deposited on a microscope glass slide, on top of which the slice of chicken breast was placed. A heating gun, with a power of 1 W and fixed to a horizontal moving stage to control its movement, was used to induce the heating of the chicken breast sample. The heating gun was moved away from its initial position, close to the chicken breast sample, to generate a decrease of temperature in the biological tissue. The maximum temperature reached in the chicken breast sample was maintained below 318 K to avoid exceeding the denaturalization temperature of biological tissues. The excitation beam was focused on the nanoparticles by using a 40× microscope objective with a numerical aperture

(hereafter N.A.) of 0.6. The photoluminescence generated by the Ho,Tm:KLuW nanoparticles was collected with a Yokogawa AQ6375 optical spectrum analyzer and the temperature was determined through the intensity ratio indicated above. In addition, close to the nanoparticles, and inside the chicken breast sample, a small Pt-100 thermocouple was placed to verify the changes of temperature (the schematic representation of the experimental setup is in Fig. 47(a)). The temperature profile resulting from moving the heating gun away from the chicken breast sample is shown in Fig. 47(b), showing a temperature drop of 1.5 K cm^{-1}. The temperature determined by the nanoparticles displayed a difference of 0.8 K with respect to the one determined by the Pt-100 thermocouple.[265] This difference was assigned to the different thermal conductivity of the two materials (nanoparticles and thermocouple) or also to the different location of the thermal probes within the chicken breast sample.[265]

7.1.2. *Ex vivo* photothermal experiments combined with luminescence thermometry using lanthanide-doped luminescent nanothermometers operating in the BWs. Lanthanide-doped luminescent nanothermometers, upon laser irradiation, not only can sense temperature, but they can also generate heat under special conditions. These two processes are generated due to the peculiar electronic configuration of the Ln^{3+} ions, which gives rise to radiative and non-radiative processes, upon the proper selection of the excitation source. These two processes are the main ones responsible for the production of luminescence and heat in Ln^{3+}-doped materials, respectively. Thus, Ln^{3+}-doped materials have the potential of being implemented as photothermal agents within biological/biomedical media.

Photothermal therapy, which employs light-absorbing agents to convert photoenergy into heat to achieve local hyperthermia, is regarded as a minimally invasive and highly efficient method for targeted cancer treatment.[4,49,274] Typical conditions that have to be fulfilled by a material to act as a potential photothermal agent include high light-to-heat conversion efficiency, nanometric sizes, excitation and emission within the BW spectral ranges, and real-time temperature feedback.[275] Here, we cover the examples published in the literature which involve the application of Ln^{3+}-doped luminescence as nanothermometers combined with materials that can generate heat, and the so-called self-assessed Ln^{3+}-doped nanothermometers, which can simultaneously sense the temperature but also generate heat within the medium where they are embedded.

Nd^{3+},Y^{3+}:CaF_2 nanoparticles, combined with Au nanorods, have been used in *ex vivo* photothermal experiments.[245] The nanoparticles that could sense the temperature (Nd^{3+},Y^{3+}:CaF_2) were combined with nanoparticles that could generate heat (Au nanorods). It must be emphasized that the Nd^{3+}-doped particles alone would have also the ability to generate heat upon NIR excitation due to their ladder-like electronic configuration.[15,199,204] In fact, the heat generated by the Nd^{3+}-doped nanoparticles is a consequence of both the increase of the absorbed pump power when irradiated at 808 nm (since the absorption coefficient of these nanoparticles is proportional to the Nd^{3+} concentration), and the decrease of the fluorescence quantum yield due to Nd^{3+}–Nd^{3+} interactions (such as cross relaxations and energy migrations when the distance among these ions is short enough). Therefore, it would be possible to tailor the balance between light and heat generation through an appropriate choice of the Nd^{3+} concentration inside the nanoparticles. Nevertheless, the authors chose Au nanorods as photothermal agents because the use of Nd^{3+}-doped nanoparticles would require higher illumination doses to reach the targeted temperature.[245,276] Au nanorods, upon excitation on their longitudinal plasmon mode, can efficiently generate heat.[4,277] Hence, nanorods with a local surface plasmon resonance maximum at ~810 nm were used. Concerning the Nd^{3+},Y^{3+}:CaF_2 luminescence temperature sensors, they operated in the II-BW using different emission lines of the band located at 1050 nm through the FIR model (Table 3). For the *ex vivo* experiment, 1 mol% Nd^{3+} and 10 mol% Y^{3+} co-doped CaF_2 nanoparticles were chosen due to their S_{rel} and good emission intensity. A solution of these nanoparticles with a concentration of 1.6 mg mL^{-1} was combined with a solution of the Au nanorods with a concentration of 1.3 × 10^{-3} mM.[245] A TEM image of the combined nanoparticle dispersion is in Fig. 48(a). Chicken breast samples with different thicknesses were placed on the top of the cuvette containing the nanoparticle suspension. On the

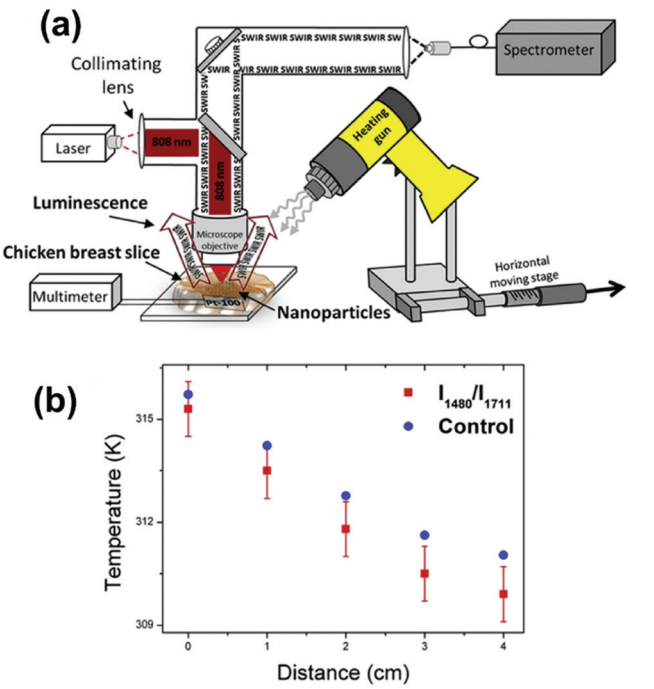

Fig. 47 *Ex vivo* temperature sensing in the III-BW with Ho, Tm:KLu$(WO_4)_2$ nanoparticles. (a) Schematic representation of the experimental setup. (b) Temperature profile determined from the intensity ratio of the 1480 nm and 1711 nm emission bands of Tm^{3+} in Ho,Tm:KLu$(WO_4)_2$ particles (red squares) and by a Pt-100 thermocouple (blue spheres). Reprinted with permission from ref. 265. Copyright 2018, Elsevier.

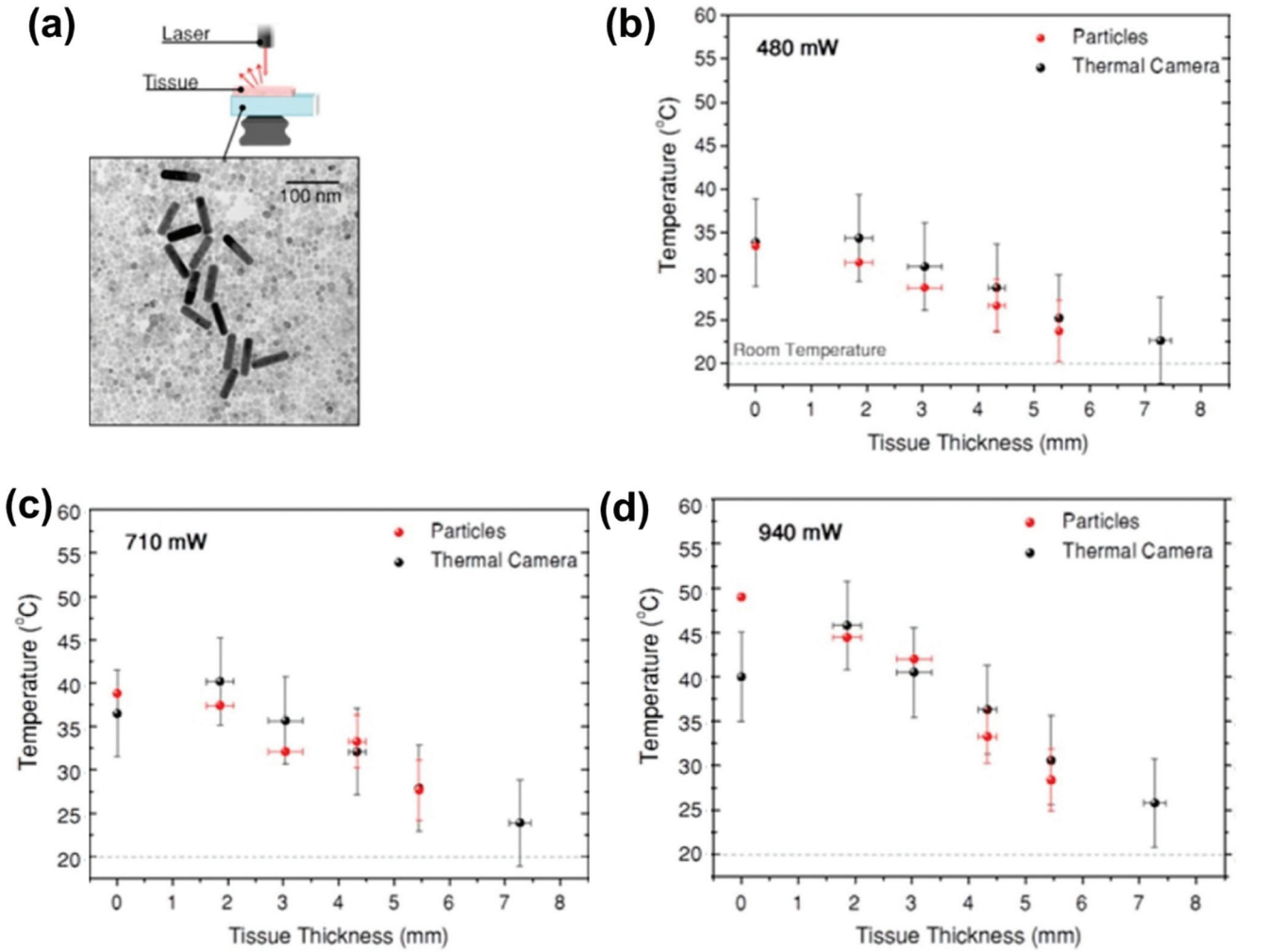

Fig. 48 (a) *Ex vivo* photothermal experiment in chicken breast using a colloidal solution containing gold nanorods as photothermal agents and Nd^{3+},Y^{3+}:CaF_2 nanoparticles as luminescent thermometers (a TEM image of the mixed colloid is presented as well). Temperature determined by using the intensity ratio of the Stark sublevels of the 1050 nm emission of Nd^{3+} (in red) in the Nd^{3+},Y^{3+}:CaF_2 nanoparticles, and by a thermal camera (in black) as a function of the power of the 808 nm laser applied: (b) 480 mW, (c) 710 mW and (d) 940 mW. Adapted with permission from ref. 245. Copyright 2018, American Chemical Society.

bottom of the cuvette, a thermal camera was used to monitor also the generation of heat (Fig. 48(a)). The luminescence generated by the Nd^{3+},Y^{3+}:CaF_2 nanoparticles, after 808 nm excitation, was recorded by an InGaAs spectrometer, and then the temperature was determined by calculating the corresponding intensity ratio. For the experiment, the power of the excitation laser was maintained below 0.94 W to avoid any overheating in the biological tissue. Also, a low concentration of Nd^{3+} in the nanoparticles was used to avoid the generation of heat by them; thus, the generated heat could be only attributed to the Au nanorods.[245] Under these conditions, the temperature read by the thermal camera and the temperature determined by the intensity ratio between the emission lines coming from different Stark sublevels of the emitting state in the 1050 nm emission ($^4F_{3/2} \rightarrow {}^4I_{11/2}$ transition) of the Nd^{3+},Y^{3+}:CaF_2 nanoparticles were compared as a function of the power of the laser applied (Fig. 48(b)–(d)), showing a good agreement for thicknesses of the chicken breast below 5.5 mm.[245] For a thickness of 2 mm, a δT of 0.2 K was obtained, fulfilling the requirements for a nanothermometer to be operative in biomedical applications.[13] This δT was determined using eqn (3) after recalibrating the luminescent nanothermometer in the new aqueous dispersion medium of the mixture of the Nd^{3+},Y^{3+}:CaF_2 and Au nanoparticles.[245] Above this thickness, δT increased, reaching a value of 3.5 K for a thickness of 5.5 mm, clearly jeopardizing the reliability of this luminescent thermometer, and indicating that a new recalibration of the luminescence thermometer is required, probably inside the chicken breast.

Another reported *ex vivo* photothermal experiment is the one in which so-called self-assessed photothermal agents were used.[266] These self-assessed photothermal agents are materials that can simultaneously generate heat and sense the temperature. Here, these self-assessed photothermal agents were com-

posed of only Ln^{3+}-doped nanoparticles, which were the responsible for sensing the temperature and generating heat at the same time. As an example, we can mention Ho^{3+},Tm^{3+}:KLu$(WO_4)_2$ nanoparticles,[266] operating as luminescent nanothermometers in the III-BW, based on the intensity ratio between the 1800 nm emission of Tm^{3+} and the 1960 nm emission of Ho^{3+}, that generated heat simultaneously due to the existence of non-radiative processes within the relaxations between the different electronic levels and non-resonant ET processes between Ln^{3+} ions (Fig. 49(a)). In the *ex vivo* experiment, the nanoparticles were placed in between two pieces of chicken breast, ensuring a complete medium homogeneity, with a maximum thickness of 2 mm. Close to the nanoparticles, a thermocouple was also located to verify the temperature determined. Upon excitation at 808 nm, a fast increase of temperature during the first 100 s was observed by monitoring the temperature with a thermocouple, prior to reaching a plateau, produced only by the Ho^{3+},Tm^{3+}:KLu$(WO_4)_2$ (Fig. 49(b)). At this point, the temperature was determined through the intensity ratio of the emissions generated also by the luminescent nanoparticles (inset of Fig. 49(b)) and compared with the temperature measured with the thermocouple. The results showed a difference of up to 0.8 K between these two temperatures, probably due to the different thermal conductivities of the nanoparticles (a dielectric material) and the thermocouple (a metal), and the different medium in which the nanoparticles were embedded during the calibration procedure (air) and during the experiment (chicken breast). Hence, this *ex vivo* experiment demonstrated that Ho^{3+},Tm^{3+}:KLuW nanoparticles could be used as self-assessed photothermal conversion agents.

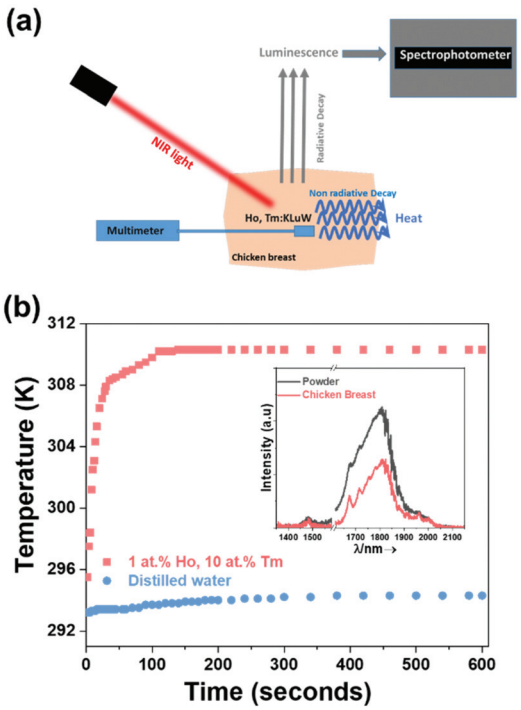

Fig. 49 (a) Schematic representation of the experimental procedure for *ex vivo* temperature determination in chicken breast using self-assessed 1 at% Ho, 10 at% Tm:KLuW photothermal agents that allow the generation of heat and the measurement of temperature at the same time, with the luminescent thermometer operating in the III-BW. (b) Time-dependent temperature profiles of distilled water and aqueous dispersion of 1 at% Ho, 10 at% Tm:KLuW nanocrystals when illuminated with the 808 nm laser. The inset stands for the emissions in the III-BW of 1 at% Ho, 10 at% Tm:KLuW nanocrystals as powder in air and covered by a 2 mm thick chicken breast piece of meat. Adapted with permission from ref. 266. Copyright 2020, The Royal Society of Chemistry.

7.1.3. *In vitro* thermometry using lanthanide-doped luminescent nanothermometers operating in the BWs. Lanthanide-doped luminescent nanothermometers have also been used in *in vitro* media. *In vitro* stands for investigation performed with microorganisms, cells, or biological molecules outside their normal biological context.[278] *In vitro* nanothermometry (also known as cellular nanothermometry[3,16,55,279]) has been explored principally in the visible spectral region because of the sufficient penetration depth achieved with VIS light in *in vitro* cell culture to analyze the whole thickness of the sample, and also because this light can be easily visualized using conventional optical microscopes, which produces an easier location of the nanoparticles and recording of their luminescence spectra within the cell culture. Typical examples of lanthanide-doped *in vitro* luminescent nanothermometers operating within the VIS involve Er^{3+},Yb^{3+}-co-doped nanoparticles particles pumped in the NIR region,[22,280] and Eu^{3+} complexes with organic molecules excited with UV light.[62,281,282] Clearly, these examples are out of the scope of this review. For a more comprehensive understanding of *in vitro* luminescent nanothermometry operating in the VIS region, the reader is referred to other references.[279]

By working with luminescent thermometers operating within the BW spectral regions, higher thermal sensitivities can be achieved when compared with those operating in the VIS, and thermal maps with higher spatial resolution can be recorded, due to the lower scattering at these wavelengths.[279] Nevertheless, the number of Ln^{3+}-doped nanoparticles operating within the BWs used as *in vitro* luminescent nanothermometers is very limited. In fact, we could identify only one *in vitro* luminescent nanothermometer based on a hybrid nanostructure that combines plasmonic Au nanoparticles as an efficient optical heater with Nd^{3+},Y^{3+}:CaF_2 nanoparticles acting as luminescent thermometers.[276] These materials can both be excited with the same wavelength, 808 nm, located in the I-BW, while the emissions of the lanthanide nanoparticles used to determine the temperature are located within the II-BW. Hence, both functionalities (heating and temperature sensing) can be triggered by using a single excitation source. The luminescent thermometer constituted by the Nd^{3+},Y^{3+}:CaF_2 nanoparticles was based on the FIR of different emission lines generated by different Stark sublevels of the $^4F_{3/2} \rightarrow {}^4I_{11/2}$ transition of Nd^{3+}, located at ~1050 nm. Y^{3+} ions were intentionally added to break the energy migration paths between Nd^{3+} ions, which would otherwise quench the emission intensity. Concerning the nanoheater, the authors chose Au nano-

stars, which exhibited a higher light-to-heat conversion capacity when compared with the Au nanorods used previously in *ex vivo* thermometry (section 7.1.1).[277] To properly prepare the combination of these nanoparticles for *in vitro* luminescence nanothermometry, the Nd^{3+},Y^{3+}:CaF_2 nanoparticles and Au nanostars were co-assembled into hybrid structures by using polysterene beads with diameters ~500 nm as the colloidal support that were finally coated with a silica shell (~7 nm thick) to prevent their dissociation when used in biological environments.[276] TEM images of the hybrid structures can be seen in Fig. 50(a) and (b). Finally, these hybrids were internalized into a 3D spheroid tumor cell model prepared using a U-87MG human glioblastoma cell line. The hybrids, dispersed in water with a concentration of 100 μg mL^{-1}, were added to the cell culture medium and incubated for 48 hours at room temperature to allow internalization. The location of the hybrid particles inside the 3D tumor cells could be monitored through the observation of the Nd^{3+} luminescence, using a modified Lightsheet microscope to properly record the emission band at 1050 nm. The emission of Nd^{3+} (presented in a red color) was observed surrounding the DAPI (4,6-diamidino-2-phenylindole, used to label cell nuclei) emission, indicating that the hybrid beads were located in the cell cytoplasm (Fig. 50(c)).

The ability of these hybrids to emit light and generate heat was monitored in the cell medium, applying the experimental procedure schematically shown in Fig. 50(d) with an aqueous dispersion of 0.02 wt% of these hybrids. The hybrid particles were illuminated at 808 nm with a fiber-coupled laser diode using different powers and the beam was collimated to a 3 mm diameter spot. The emissions were collected with a lens, filtered with a longpass filter cut-off at 850 nm to remove the laser signal, and finally recorded by an InGaAs spectrometer. The generated heat was monitored also by a thermal camera. In the *in vitro* experiment, the local temperature inside the 3D spheroids tumor cells was investigated as a function of the different concentrations of the hybrids and different excitation power densities, during a period of time of 10 min to maintain the spheroids alive.[276] The recorded temperature data, after transforming each of the intensity ratios of the emissions of the Nd^{3+},Y^{3+}:CaF_2 nanoparticles into temperatures, are shown in Fig. 50(e). The temperature increased fast initially until thermal equilibrium was reached at around 100 s. Then, it remained stable for all the samples, with the only exception of the hybrid nanoparticles excited at 31 W cm^{-2} and loaded with a concentration of 70 μg mL^{-1}, for which, according to the authors, the boiling point of water was likely reached prior to cooling due to the expansion and death of the 3D spheroids. δT was found to be between 3 K and 4 K, although it could reach up to 9 K for the sample with the lowest concentration of the hybrids, excited at the lowest power density.[276]

The average temperature at equilibrium increased proportionally to the increase in the concentration of the hybrids and the laser power density (Fig. 50(f)). It was also observed that the temperature measured by the hybrid particles was higher than that recorded by the thermal camera, in agreement with the fact that the particles measure the temperature in the local proximity of the Au nanostars, while the thermal camera monitors the temperature at the surface of the cell medium. A final cell viability test (Fig. 50(g)) revealed that when the local temperature surpassed 328 K, the cells were almost completely dead, with a viability below 1% for a treatment reaching 334 K, and 0.3% above this temperature.[276]

It is important to note here that this luminescent thermometer was based on the FIR model. According to this model, and eqn (9) that is used to fit the experimental data, ΔE, *i.e.* the energy gap between the electronic energy levels from which the emissions are generated (in this case the different Stark sublevels of the $^4F_{3/2}$ and $^4I_{11/2}$ levels of Nd^{3+}), is independent of the external environment due to shielding of the 4f orbitals by the more external 5s orbitals of the Ln^{3+} ions.

Nevertheless, the pre-exponential factor B can be understood as a correction parameter related to detected differences in the intensity of the emissions when embedded in different media. According to that, the intensity of the emission of the Nd^{3+},Y^{3+}:CaF_2 nanoparticles, combined in the hybrid structures, can change when located in air or immersed in the tumor cell culture. To correct the value of the B parameter in eqn (9), fortunately a full re-calibration was not needed. Instead it was sufficient to record several spectra at different excitation powers inside the cells.[214] By doing so, a linear fit to the data allowed a calculation of the intensity ratio at zero power, which can be assumed to be the value of FIR at room temperature.[214,276] By introducing this correction, the results obtained were in agreement with the temperature measured by the thermal camera (differences below 1.5 K).[276] Despite the positive results obtained in this *in vitro* experiment, there are, however, some aspects to be improved. One would be the size of the hybrid particles used, with a diameter of 830 ± 30 nm, clearly above the desired dimensions of nanometers in the biomedical field.[13] Additionally, the number of the lanthanide-doped temperature sensors per Au nanoparticle should be increased, to favor a higher intensity of the emission of Nd^{3+} in order to improve the signal-to-noise ratio and to reduce the time required to record the spectra. Also the distance between the Au nanoparticles and the Ln^{3+} ions should be larger than 5 nm, in order to avoid quenching of the Nd^{3+} emissions. Another issue to take into consideration is the low S_{rel} of these luminescent thermometers, 0.18% K^{-1} at room temperature (Table 3).

7.1.4. *In vivo* thermometry using lanthanide-doped luminescent nanothermometers operating in the BWs. Lanthanide-doped luminescent nanothermometers can be used also in *in vivo* media. *In vivo* stands for investigations performed on whole living organisms,[283] basically mice in this review.

Nd^{3+}:LaF_3 nanoparticles have been used as a luminescent nanothermometer for *in vivo* applications operating in the I-BW. In addition, these nanoparticles can release heat under excitation at 808 nm at a power density of 4 W cm^{-2} when the doping level inside the nanoparticles is high enough, such as 5.6 at%.[168] As described in section 7.1.1, it is possible to tailor the balance between light and heat generation through an

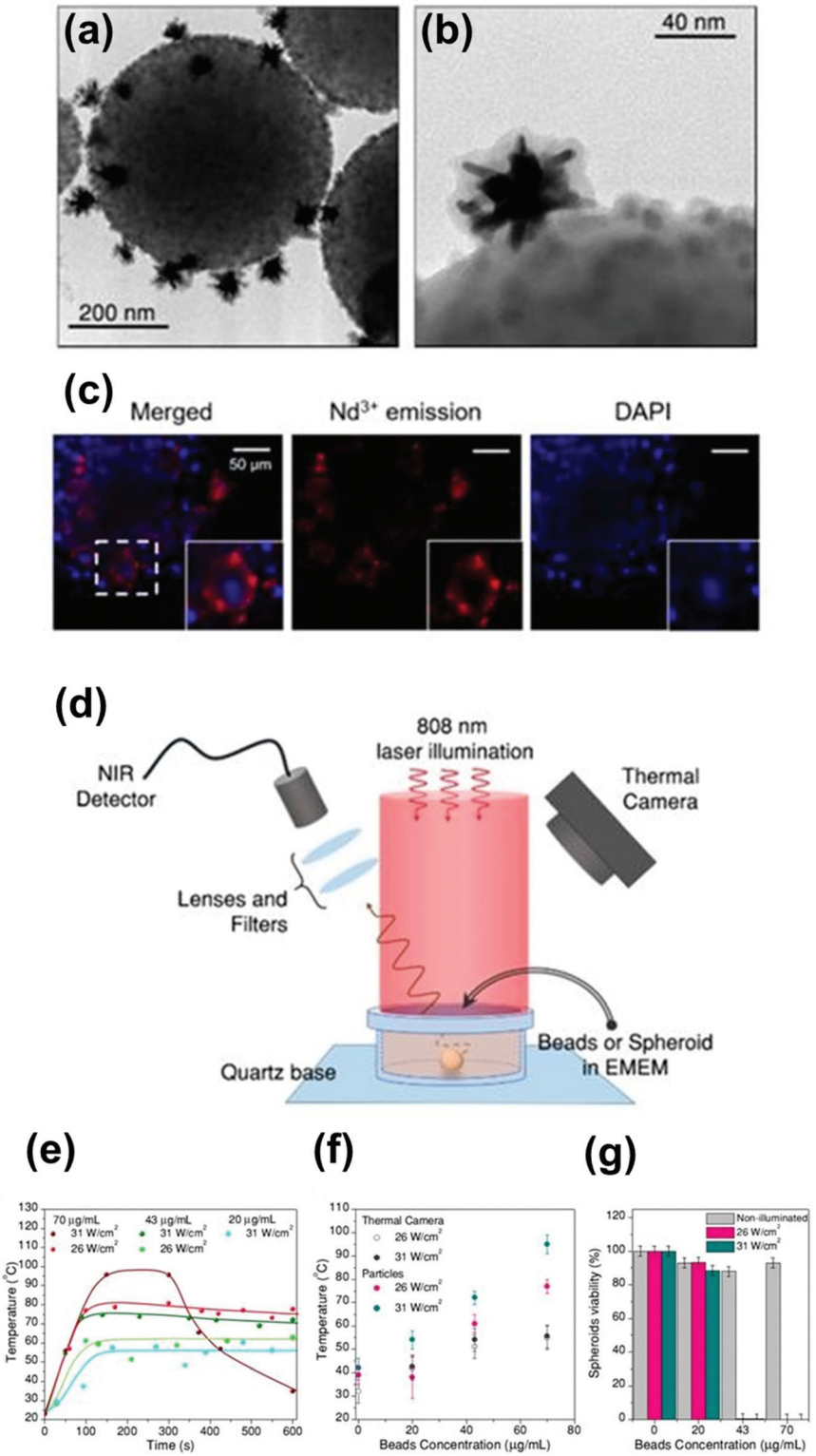

Fig. 50 *In vitro* temperature sensing using Nd^{3+},Y^{3+}:CaF_2 nanoparticles and Au nanostars, combined in polysterene beads, and coated with a silica shell, forming a hybrid structure. (a) and (b) TEM images of the hybrid nanostructures. (c) Images of treated 3D spheroid tumor cells, showing the Nd^{3+} emission apparently located in the cytoplasm. (d) Schematic representation of the experimental procedure used to determine the temperature inside the 3D spheroid tumor cells. (e) Temperature measurements inside the spheroids during photothermal treatment as a function of time, using different excitation powers and different concentrations of the hybrid beads. (f) Average temperature at thermal equilibrium compared with the temperature determined by the thermal camera. (g) Viability of the 3D spheroid tumor cells 24 h after photothermal treatment. Adapted with permission from ref. 276. Copyright 2019, IvySpring International Publisher.

appropriate choice of the Nd^{3+} content inside the nanoparticles. Carrasco *et al.* used these Nd^{3+}:LaF_3 nanoparticles for *in vivo* photothermal treatment with continuous temperature monitoring in a mouse model.[168] The authors chose the intensity ratio between the emission lines at 865 and 885 nm, assigned to two Stark sublevels of the $^4F_{3/2} \rightarrow {}^4I_{9/2}$ transition of Nd^{3+} (Table 1). Fig. 51(a) shows a schematic representation of the experimental procedure used in this investigation. Tumor-bearing mice, with one tumor per flank, were injected with a dispersion of Nd^{3+}:LaF_3 nanoparticles in phosphate-buffered saline (PBS) at a concentration of 10% in mass into one of the tumors, while the other one was used as a control (Fig. 51(b)). The injected volume was equal to $\frac{1}{2}$ of the estimated tumor volume, from which it was estimated that around 7×10^{13} nanoparticles were injected. Intratumor injection was chosen to avoid the preferential take up of the nanoparticles by the liver and spleen observed in intravenous injection. Only the tumor containing the nanoparticles exhibited luminescence within the I-BW (Fig. 51(c)), and heating capability (Fig. 51(d)) recorded with a thermographic camera. During the photothermal therapy experiment, the intratumoral temperature was monitored (Fig. 51(e)), together with the temperature determined at the surface of the skin of the mouse (being obtained by infrared thermographic imaging) in the treated tumor and the control tumor (injected only with the equivalent amount of pure PBS and illuminated also with the 808 nm laser). The photothermal treatment lasted for 4 min. Fig. 51(e) shows the discrepancy between the intratumoral temperature, determined with the luminescent nanothermometers internalized in the tumor, and the surface temperature, determined by thermographic imaging, indicating the importance of an accurate temperature control at the injection site to minimize collateral damage due to overheating. The photothermal therapy treatment had a successful result, with a decrease of the size

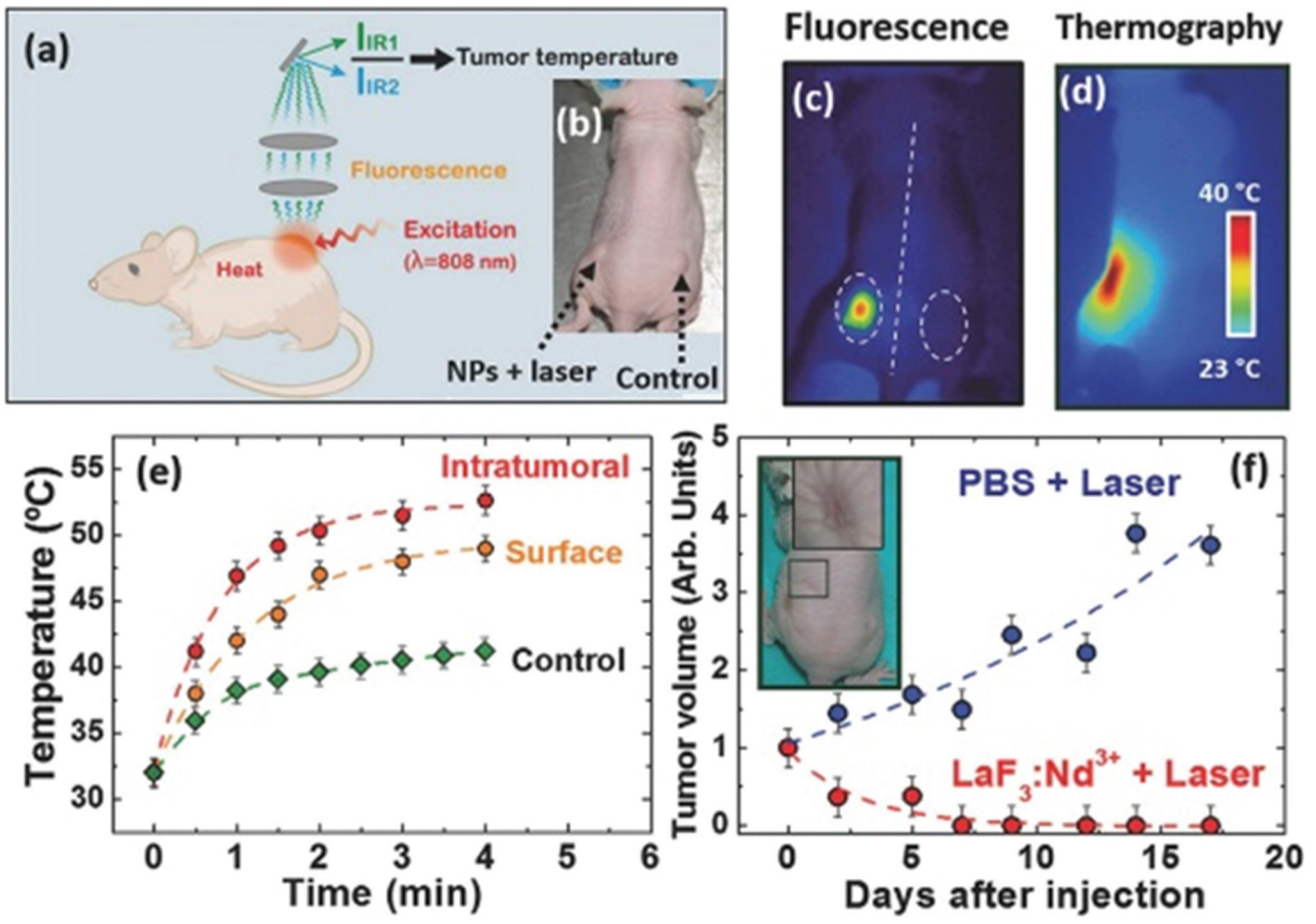

Fig. 51 Temperature-controlled photothermal therapy in living mice with Nd^{3+}:LaF_3 nanoparticles operating in the I-BW. (a) Schematic representation of the experimental procedure for the dynamic controlled photothermal treatment of tumors in mice by using Nd^{3+}:LaF_3 nanoparticles. (b) Optical image of a tumor-bearing mouse. The left tumor was treated with Nd^{3+}:LaF_3 nanoparticles and laser, while the one on the right was used as a control. (c) Luminescent and (d) thermal images collected after a 4 min long irradiation treatment. (e) Time evolution of the intratumoral temperature determined from the analysis of the luminescence of the Nd^{3+}:LaF_3 nanoparticles, and tumor surface temperature (both treated and control tumor) as measured by infrared thermal imaging. (f) Post-treatment size evolution of both treated and control tumors. The inset shows the optical image of the surface scar left at the tumor site 15 days after the therapy. Reprinted with permission from ref. 168. Copyright 2015, Wiley-VCH Verlag GmbH & Co. KGaA.

of the tumor after treatment to finally leave only a surface scar behind (Fig. 51(f)). Meanwhile, the growth of the control tumor did not stop.

Real-time subcutaneous thermal sensing has been proposed as a powerful tool for the study of the thermal dynamics of biological tissues during *in vivo* experiments. Such studies would, in turn, provide access to the basic properties of biological tissues from which possible alterations related to incipient diseases could be detected.[284] Ximendes *et al.* used Nd^{3+}:LaF_3@Yb^{3+}:LaF_3 core@shell nanoparticles to measure subcutaneous thermal transients as a potential theranostics tool.[223] The core@shell nanoparticles were excited at 790 nm, and by using the intensity ratio between the emissions of Nd^{3+} at 1.3 μm ($^4F_{3/2} \rightarrow {}^4I_{13/2}$) and Yb^{3+} at around 1 μm ($^2F_{5/2} \rightarrow {}^2F_{7/2}$), the temperature could be determined (Table 2). The authors used these luminescent nanothermometers to measure subcutaneous thermal transients, since the cooling dynamics strongly depend on the biological tissue properties. By measuring these cooling relaxation profiles it was possible to determine the characteristic thermal relaxation time that is unequivocally related to the fundamental properties of a particular biological tissue, and that additionally can provide information about the tissue status. The detection of small variations in the subcutaneous tissue relaxation times would allow for the identification of possible alterations of its thermal diffusivity, specific heat, thermal conductivity and density associated with diseases and, hence, could be used to detect anomalies caused by incipient diseases, such as dehydration, inflammation, ischemia or, even, tumor growth. To do that, the authors injected subcutaneously 200 μL of Nd^{3+}:LaF_3@Yb^{3+}:LaF_3 core@shell nanoparticles dispersed in PBS with a concentration of 1% in mass over the right flank of a CD1 mouse at a depth of 2 mm approximately. The mouse was anesthetized by isoflurane inhalation, and placed in a small animal imaging chamber equipped with a body temperature controller so that the mouse's temperature was maintained at 307 K ± 1 K. A moderate temperature increment was induced at the injection site by illuminating the mouse with a 808 nm laser beam with a power density of 0.7 W cm^{-2} for 4 min that activated the release of heat by the nanoparticles. After that, a low-power 790 nm laser diode at a power of 30 mW was also focused on the nanoparticles through an infrared long working distance microscope objective to generate the luminescence of the nanoparticles from which temperature could be determined. After 4 min of irradiation, the 808 nm laser was turned off and the mouse tissues gradually recovered their initial temperature. Fig. 52(a) shows a schematic representation of the experimental procedure used for this experiment. The luminescence of the nanoparticles was used to monitor the dynamics of the subcutaneous thermal relaxation. Just after the end of the heating cycle, the subcutaneous temperature was determined to be 312 K ± 1 K. The authors were able to reveal clear differences between the thermal relaxation curves corresponding to the subcutaneous and skin temperatures (Fig. 52(b)). According to the authors, those differences arise mainly due to the different physical mechanisms responsible for heat dissipation: whereas for the skin the dissipation may be essentially convective, for the subcutaneous tissues it could be assumed to be mainly conductive, due to the lack of any physical contact with air. Another reason for these different thermal relaxation curves is the minimum blood flow in the hypodermis, several orders of magnitude lower than in internal organs.

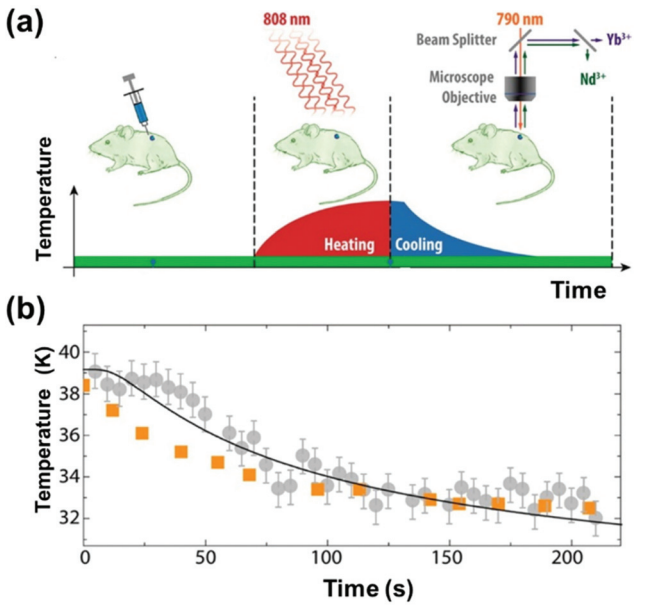

Fig. 52 Measurement of *in vivo* subcutaneous thermal transients in biological tissues using luminescence thermometry within the BWs. (a) Schematic representation of the experimental procedure used to measure subcutaneous thermal relaxation. (b) Time evolution of the temperature measured by the subcutaneous luminescent thermometers (grey and orange) and the IR camera (blue). Dots correspond to experimental subcutaneous (circles) and skin (squares) temperatures. Reprinted with permission from ref. 223. Copyright 2016, American Chemical Society.

Through the analysis of the subcutaneous thermal relaxation dynamics, which allowed access to the characteristic thermal relaxation time of a given subcutaneous tissue, it was possible to compute the thermal diffusivity of the mouse tissue, resulting in a value of 0.13 ± 0.04 mm^2 s^{-1}, which was similar to that reported for chicken breast tissue determined by frequency-domain photon migration.[285] Additionally, the subcutaneous thermal monitoring allowed the quantification of the local thermal dose administrated in a hyperthermia treatment which in that case was 54 ± 8 J. This parameter is considered nowadays to be one of the most important factors which influences the efficiency of hyperthermia treatments. Since the total energy given by the 808 nm laser in the tissue was 560 ± 63 J, the biological tissue absorbed only 10% of this energy. Thus, the absorption coefficient of the biological tissue was 0.23 ± 0.05 cm^{-1}, also in agreement with previous reported data in the literature.[285]

Despite this big advance, accurate thermal-based diagnosis would require, at least, the dynamic acquisition of 2D sub-

cutaneous thermal images. To do that it is necessary to acquire low-noise luminescence thermal images with commercially available shortwave infrared cameras, and therefore to reconstruct accurate bidimensional thermal images. For this purpose, Ximendes *et al.* designed and synthesized Er^{3+},Yb^{3+}:LaF_3@Yb^{3+},Tm^{3+}:LaF_3 core@shell nanoparticles capable of producing 2D subcutaneous dynamic thermal imaging when excited at 690 nm (in the I-BW), emitting in the II- and III-BWs.[240] In these Ln^{3+}-doped nanoparticles, Tm^{3+} and Er^{3+} ions were spatially separated, with Tm^{3+} acting as the sensitizer, while Er^{3+} and Yb^{3+} were used as activators. The emissions used for the luminescent thermometer in this case were those of Er^{3+} at 1550 nm (III-BW), and Yb^{3+} at 1000 nm (II-BW) (Table 4). The authors used these core@shell nanoparticles for the acquisition of 2D thermal videos unveiling heat diffusion at the subcutaneous level. These videos allowed the acquisition of 2D patterns of tissue thermal properties that, in turn, could be used to identify and localize damaged (or non-healthy) biological tissues *in vivo*. Moreover, this analysis made possible the quantification of the thermal dose administered in the whole area of injection during a hyperthermia treatment. For that, the authors subcutaneously injected 200 μL of a dispersion of the Er^{3+},Yb^{3+}:LaF_3@Yb^{3+},Tm^{3+}:LaF_3 core@shell nanoparticles in PBS in a CD1 mouse model. Then, the temperature at the injection site was increased by illuminating at 808 nm with an excitation density of 0.7 W cm^{-2}, and the temperature was measured through the luminescence of the nanoparticles excited at 690 nm with a power density of 0.1 W cm^{-2}, low enough to avoid additional heating.[240] A schematic representation of the experimental procedure used can be seen in Fig. 53(a). From the videos recorded, the authors extracted thermal images at different time delays during the heating and cooling cycles (Fig. 53(b)–(c)), providing detailed 2D images of the subcutaneous spatial distribution of temperature with a time resolution better than 1 s. From these data the authors computed the time evolution of the subcutaneous temperature during both heating and cooling cycles (Fig. 53(d)). The thermal diffusivity of the tissue was determined to be 0.15 ± 0.02 mm^2 s^{-1} for the heating process, and 0.12 ± 0.02 mm^2 s^{-1} for the cooling one.

7.2. Other applications of lanthanide-doped luminescent nanothermometers operating within the BWs

Lanthanide-doped luminescent materials can be used as nanothermometers also outside the biological/biomedical fields. An example involves the application of lanthanide-doped luminescent materials as thermal probes on the surface of a copper microwire to visualize the Joule induced heating effect.[171] Nd^{3+}:YAG luminescent nanothermometers, operating in the I-BW based on the thermally coupled Stark sublevels of the $^4F_{3/2} \rightarrow {}^4I_{9/2}$ electronic transition of Nd^{3+}, located at ~940–950 nm (Table 1), have been used for this purpose. A drop of an aqueous dispersion of these nanoparticles (1 wt%) was deposited onto a 100 μm thick copper wire fixed on a glass

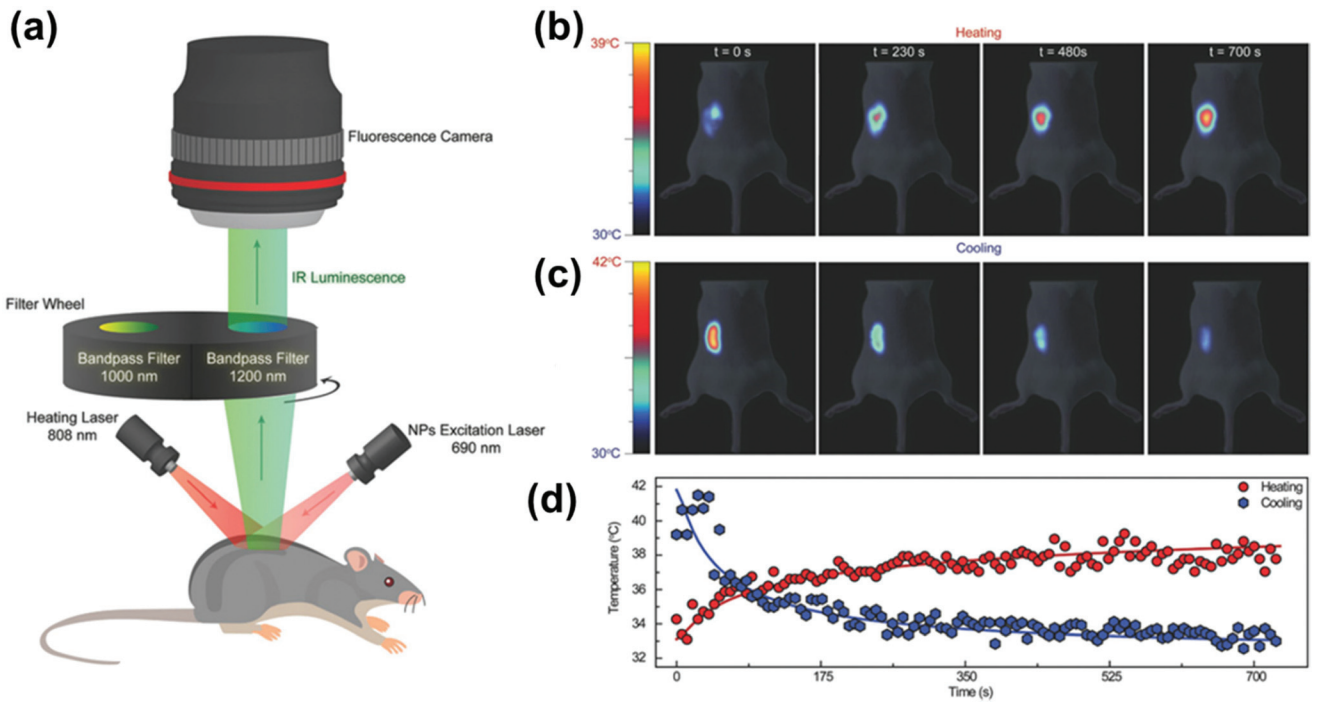

Fig. 53 *In vivo* acquisition of 2D subcutaneous thermal images. (a) Schematic representation of the experimental procedure used in the *in vivo* experiment. (b) Thermal images obtained during the heating and relaxation (cooling) cycles. (c) Time evolution of the average temperature in the injection area as measured by the subcutaneous lanthanide nanothermometers during heating and thermal relaxation cycles. Reprinted with permission from ref. 240. Copyright 2017, Wiley-VCH Verlag GmbH & Co. KGaA. (d) Time evolution of the average temperature of the injection area as measured by subcutaneous luminescence nanothermometry during heating and thermal relaxation processes.

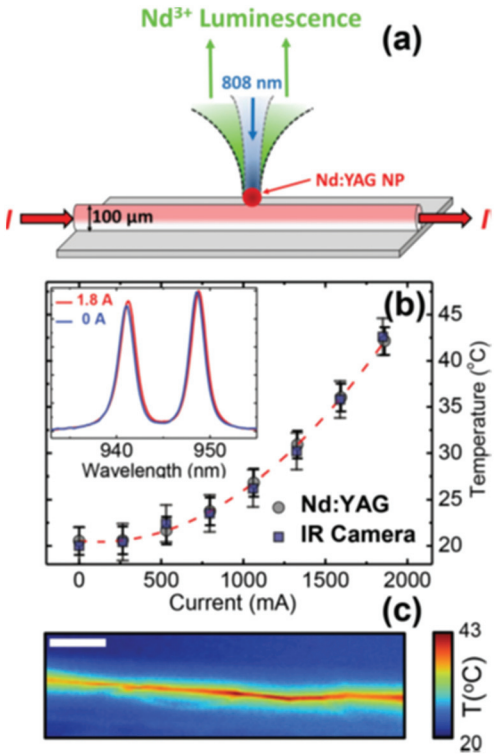

Fig. 54 Temperature sensing in metallic microwires heated by the Joule effect using lanthanide-doped luminescent nanothermometers operating in the I-BW. (a) Scheme of the experimental procedure used. (b) Temperature of the microwire as a function of the applied current, obtained from the intensity ratio of the emissions generated by the nanoparticles and from an infrared thermographic camera. The emission spectra generated by the nanoparticles placed on the wire obtained at the two extreme values of the electrical current (0 and 1.8 A) can be seen in the inset. (c) Thermal image of the microwire when conducting the maximum electrical current applied (1.8 A), as obtained with the thermographic camera (scale bar is 2 cm long). Adapted with permission from ref. 171. Copyright 2015, Wiley-VCH Verlag GmbH & Co. KGaA.

plate. After the evaporation of water, an 808 nm laser diode was focused onto the wire using a 10× magnification microscope objective with a N.A. = 0.55, which produced a laser spot of approximately 1.8 µm in diameter on the wire. Using the same microscope objective, the luminescence arising from the Nd^{3+}:YAG nanoparticles was collected (Fig. 54(a) for the schematic representation of the experimental procedure used). The increase of the temperature caused by the ohmic heating of the microwire was monitored by an infrared thermographic camera and by the emissions of the luminescent particles. The temperature calculated from the intensity ratio of the emission generated by the nanoparticles presented a parabolic dependence on the different electrical currents applied (Fig. 54(b)), as expected since the Joule heating effect is directly proportional to the square of the intensity of the electrical current applied.[171] These results were validated with those recorded with the infrared thermographic camera (Fig. 54(b) and (c)).

Nd^{3+}:YAG nanoparticles with the same emissions as in the previous example have also been used as thermal probes in microfluidics.[171] Taking advantage of the water dispersibility of these Nd^{3+}:YAG nanoparticles, thermal imaging of a simple optofluidic device consisting of a 100 µm thick microchannel was recorded. In this microchannel, a single-mode fiber-coupled 1480 nm diode laser with a maximum power of 200 mW was used as a heating source. This laser was focused on the channel containing the dispersion of the nanoparticles in water through a 10× microscope objective with a N.A. = 0.25. To extract the temperature distribution pattern generated by the 1480 nm laser irradiation, strongly absorbed by water, the microfluidic channel was filled with a 0.1 wt% aqueous dispersion of the nanoparticles, while being monitored with a thermal camera (Fig. 55(a) for the schematic representation of the experimental procedure used). Nd^{3+}:YAG nanoparticles were excited with a 808 nm laser, which was focused onto the optofluidic device using a 10× microscope objective with NA = 0.55, that produced a laser spot of approximately 1.8 µm in diameter on the channel.

The luminescence generated by the nanoparticles was collected using the same microscope objective. Fig. 55(b) shows the temperature increment at the focus of the 1480 nm heating laser spot as a function of its power. The measurements of temperature were performed by overlapping both the focused heating and probe (808 nm) laser beams. It can be seen that for laser powers below 60 mW, the "on-focus" temperature increased linearly, whereas above this value the relationship did not obey a linear function any more.[171] The authors considered that at high laser powers additional

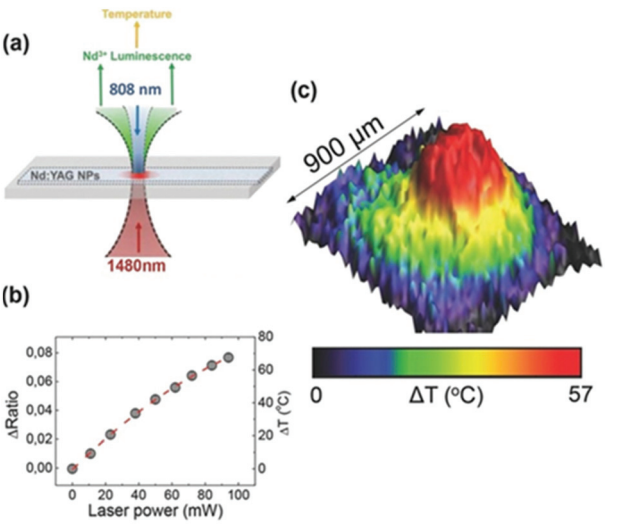

Fig. 55 Temperature sensing in optofluidics using luminescent nanothermometers operating in the I-BW. (a) Scheme of the experimental procedure used to record the temperature distribution within an optical trap created by a 1480 nm focalized laser beam on a microchannel filled with an aqueous dispersion of Nd^{3+}:YAG nanoparticles. (b) Temperature increment as a function of the power of the 1480 nm laser. (c) All-optical thermal imaging (2D temperature distribution map) of the area where the optical trap was created under pumping with the 1480 nm laser. Adapted with permission from ref. 171. Copyright 2015, Wiley-VCH Verlag GmbH & Co. KGaA.

heating was produced, which could lead to the creation of relevant convection currents and the formation of bubbles. By applying a power of 60 mW, a 2D thermal image of the microchannel in the surroundings of the 1480 nm laser spot was recorded by scanning the 808 nm laser along a 900 × 900 μm^2 area around the heating laser spot. It was observed that the laser-induced heating caused an increase of the temperature in a large area surrounding the laser spot (Fig. 54(c)), far from the microchannel itself, due to thermal diffusion.[171]

Luminescence nanothermometers operating in the I-BW can be also used as a tool for unveiling the thermal properties of the nanoparticles themselves, such as the determination of their thermal resistance. Thermal resistance is a key parameter to model the heat transfer at the nanoscale.[150] In order to achieve this, Savchuk *et al.*[150] applied Ho^{3+},Tm^{3+}:$KLu(WO_4)_2$ nanoparticles, excited with an 808 nm laser, as upconversion luminescent nanothermometers based on the 696 nm emission of Tm^{3+} and the 755 nm emission of Ho^{3+}, both located in the I-BW (Table 1).

The 808 nm laser was focused on the surface of the nanoparticles, generating, simultaneously, upconversion luminescent emissions and heat, due to radiative and non-radiative processes, respectively. A beam splitter was used to redirect a part of the emitted signal to a portable spectrophotometer that recorded the upconversion emission generated by the nanoparticles (Fig. 56(a) for the schematic representation of the experimental procedure used). The intensities of these emissions were recorded as a function of time and were converted into temperature by calculating the intensity ratio between the emissions of Ho^{3+} and Tm^{3+}, following eqn (19). The temperature increment ($\Delta T(t)$) generated in the nanoparticles by the excitation laser was measured as a function of the concentration of the emitting ions within the host (1 at% Ho^{3+}, 5 at% Tm^{3+} (black squares) and 1 at% Ho^{3+}, 15 at% Tm^{3+} (green circles) in Fig. 56(b)). The results showed that $\Delta T(t)$ generated was smaller for the nanoparticles with a smaller amount of Tm^{3+} ions, suggesting a positive correlation between the heat generated due to non-radiative Tm^{3+}-to-Ho^{3+} ET and Ho^{3+}-to-Tm^{3+} BET (Fig. 9(a)) and the Tm^{3+} concentration.

In addition, the temperature plateau observed at high power densities above 300 × 10^6 W m^{-2} and not observed in the sample with a higher Tm^{3+} concentration seemed to be related to a saturation effect on the Tm^{3+} absorption at 808 nm.

The heat dissipation could be modelled following the classical Fourier law, resulting in a temperature increase given by:[286,287]

$$\Delta T(t) = \Delta T_m \left[1 - \exp\left(-\frac{hA}{mc}t\right)\right] = \Delta T_m \left[1 - \exp\left(-\frac{t}{RC}\right)\right] = \Delta T_m \left[1 - \exp\left(-\frac{t}{\tau}\right)\right] \quad (52)$$

where ΔT_m is the temperature increase in the steady-state regime (Fig. 56(c)), h is the convective heat transfer coefficient, A is the thermal contact area, $R = 1/hA$ is the convective thermal resistance and $\tau = RC$ stands for the system's thermal time constant.

By fitting this equation to the heating curve of the 1 at% Ho^{3+}, 5 at% Tm^{3+}:$KLu(WO_4)_2$ particles in contact with air, presented in Fig. 56(c), a temperature increase ΔT_m = 18.3 ± 0.2 K and a thermal time constant τ = 0.223 ± 0.004 s were obtained, corresponding to a thermal resistance of $R = (9.50 \pm 0.17) \times 10^7$ K W^{-1}.[150] In addition, the extraction of τ allowed for the determination of the temporal resolution of the luminescent nanothermometers, δT = 0.0033 ± 0.0007 s, calculated using eqn (5), (2)–(4), orders of magnitude faster than the thermometers based on scanning thermal microscopy (0.1 s,[288] and 1.5 s),[289,290] and Raman spectroscopy (90 s).[291]

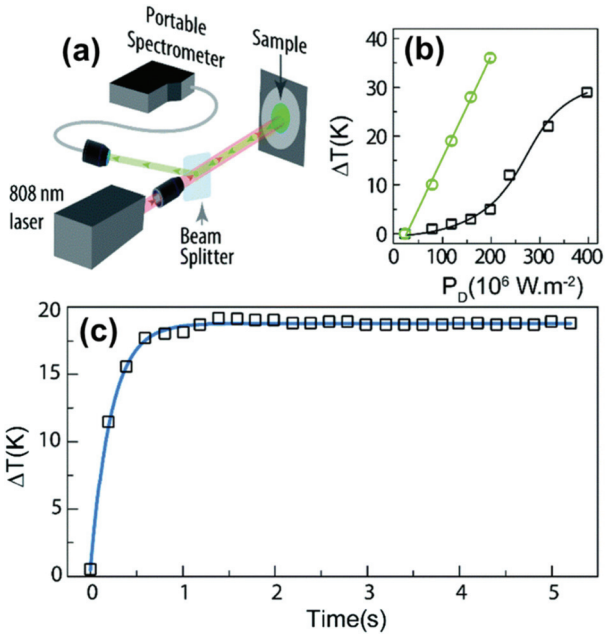

Fig. 56 Determination of the thermal resistance of nanoparticles by lanthanide-doped luminescent nanothermometers operating in the I-BW. (a) Scheme of the experimental procedure used. (b) Temperature increase induced as a function of the different laser powers applied, and as a function of the concentration of the two emitting ions in the nanoparticles: 1 at% Ho^{3+}, 5 at% Tm^{3+} (black squares) and 1 at% Ho^{3+}, 15 at% Tm^{3+} (green circles) in $KLu(WO_4)_2$. (c) Heating curve obtained for the 1 at% Ho^{3+}, 5 at% Tm^{3+}-doped $KLu(WO_4)_2$ nanoparticles excited with the 808 nm laser operating with a power density of 318 × 10^6 W m^{-2}. The blue line corresponds to the best fit of experimental data following the Fourier law. Reprinted with permission from ref. 150. Copyright 2018, The Royal Society of Chemistry.

8. Concluding remarks

Lanthanide-doped luminescent materials have triggered the development of highly sensitive luminescent thermometers, particularly if the operating regime of their emissions is located within the BWs. In this review, several strategies towards obtaining better temperature-sensing performances within the BWs have been analyzed.

Hence, for the choice of the excitation wavelength, the selection of a NIR source is highly recommended, allowing for

deeper penetration depths and better temperature readings, implying no phototoxicity or photobleaching effects, enhancing significantly the interest in these luminescent thermometers in biological/biomedical applications. Related to the choice of hosts for the Ln^{3+} ions, a strategy that results in highly sensitive thermometers is the use of active core@active shell nanostructures. Another choice is the combination of the emissions of Ln^{3+} ions with those arising from transition metal ions or quantum dots, acting as a reference and as highly thermally quenched probes, respectively. Also, coating Ln^{3+}-doped nanothermometers with an inert shell (including silica) can result in higher intensities and better temperature-sensing performances due to the reduced thermal quenching resulting from the influence of surface defects and ligands. Related to the choice of the Ln^{3+} ions, a proper selection of the concentration of the ion to be used and the operating biological window in which one wants to work is required. The intentional introduction of impurities inside the hosts (such as in the case of Y^{3+} in Nd^{3+}:CaF_2,[245,276] or Gd^{3+} in Nd^{3+}:SrF_2)[163] might lead to reduced thermal quenching effects, and upon a proper selection of the concentration of these impurities, to a better thermometric performance. In terms of Ln^{3+} ions included as emitters, Nd^{3+} and Tm^{3+} are the ones that attracted most of the attention (Table 1 for example). Nevertheless, a better choice for efficient luminescent nanothermometers is that constituted by dual emitting centers, since they provide better thermal sensitivity and allow the incorporation of multifunctionalities in these nanoparticles.

Despite the big number of works devoted to the development of luminescent thermometers operating in the BW spectral ranges, and the demonstration of amazing applications for them, there are still challenges that remain unsolved. From the synthetic point of view, a vast amount of research is devoted to the synthesis of fluoride-doped hosts, either in the form of bare, core@shell or multishell nanostructures, through the thermal decomposition of trifluoroacetate precursors to achieve control over their sizes and shapes. This synthetic approach suffers from the toxicity of the by-products and final products generated in the reactions,[103] and an additional surface functionalization of the obtained nanoparticles is required for their potential use in biomedical applications.[103] Therefore, new synthetic routes towards biocompatible nanomaterials are highly desirable. Furthermore, new choices for hosts for the Ln^{3+} ions should also be proposed.

Concerning the thermometric performance of the Ln^{3+}-doped luminescent nanothermometers, clearly some discrepancies in the evaluation of their performances (calculation of the thermometric parameter or S_{rel}) appear. In this way, it would be recommended that all authors follow the same procedures in order to be able to compare properly the performance of the different luminescent thermometers proposed. Additional strategies to boost the thermal sensitivity of the Ln^{3+}-doped nanothermometers, such as the use of induced structural stress by lattice self-adaptation in heterojunctions producing a lattice distortion at the interface between two materials,[292] dopant-induced local site symmetry distortions,[293] and the effect of anisotropic interfacial strain in mismatched core–shell nanoparticles,[294] which are sensitive to temperature changes, are really interesting. Up to now, these strategies have only been applied for luminescence thermometry in the visible range, and thus attempts to implement these strategies within the biological window spectral regions should be considered.

In addition, besides S_{rel} and δT, a very low number of publications reported about their resolution (either spatial or temporal), reproducibility and repeatability. These parameters are also important to facilitate the implementation of the Ln^{3+}-doped luminescent thermometers in real biological/biomedical applications outside of laboratories. Another very important parameter that should be taken into account when developing a novel luminescent thermometer is the quantum yield, both absolute and relative. A good quantum yield would allow for an easier detection scheme for the emissions generated by the luminescent thermometers by using cheaper detectors and lower laser excitation powers, simplifying also the protocols of use of these luminescent nanoparticles, and facilitating their use by non-experts in these subjects. As can be seen in this review, the absolute quantum yield has not been yet reported for any Ln^{3+}-doped luminescent thermometer. Thus, an additional effort is required to take this parameter into account.

From Tables 1–5 presented in this review, it can be noted that an important number of the luminescent thermometers presented are based on using Yb^{3+} ion as a sensitizer. Lanthanide ions such as Er^{3+} or Tm^{3+} are typically encountered in materials co-doped with Yb^{3+} in order to enhance the intensity of their photoluminescence since Yb^{3+} presents a strong absorption band at around 980 nm, with an absorption cross section higher than that of these ions. However, the use of this excitation source is not suitable for biological/biomedical applications due to the self-heating effects generated by the absorption of the energy of the excitation source by water present in the biological tissues through the absorption band of this molecule at the same wavelength.[148] Different strategies have been developed to substitute this excitation source in order to make lanthanide-doped nanomaterials more biological tissue-friendly. It is worth mentioning the replacement of Yb^{3+} by Nd^{3+} or Tm^{3+} ions acting as sensitizers. The absorption cross section of Nd^{3+} at 800 nm ($\approx 10^{-19}$ cm^2) is one order of magnitude higher than that of Yb^{3+} at 980 nm ($\approx 10^{-20}$ cm^2).[204] Furthermore, at this wavelength the absorption coefficient of water is around 20 times smaller than that at 980 nm.[206] In this way, the overheating effect in biological tissues can be highly reduced. Concerning the choice of Tm^{3+} as a sensitizer, a successful strategy has been successfully developed by co-doping these systems with Ho^{3+}.[150,266] Tm^{3+} has a strong absorption band at 808 nm that can be directly pumped by diode lasers, and the energy transfer processes between Tm^{3+} and Ho^{3+} allow use of the emissions of these two ions for luminescence thermometry purposes.[295] Hence, these combinations of Ln^{3+} ions are highly attractive for biomedical applications.

From the biological/biomedical applications point of view, the studies published up to now are mostly focused on the II-BW spectral region because of the deeper penetration depths that can be achieved. However, according to Naczynski *et al.*[126] and other recent publications, this parameter should be even better at longer wavelengths,[296] in the III- and IV-BW spectral ranges. Therefore, these spectral regions should be further explored in the future.

In this context, luminescence thermometers fully operative within the BWs, especially those excited within the II, III and IV BWs, and generating emissions in the same spectral regions, would be very important to advance towards their real application in the biomedical field, because they will allow for a deeper penetration depth in biological tissues[105,123,124] that would allow for a full diagnosis and treatment of diseases. Nevertheless, the research work done in this area is very scarce, and the number of lanthanide ions that can be used for this purpose is limited. In fact, the Ln^{3+} ions which can fulfill these conditions are mainly Tm^{3+} and Er^{3+} due to their ability to absorb energy within these BW regions (Tm^{3+} at 1210 nm,[297] 1319 nm,[128] and 1640 nm,[297] and Er^{3+} at 1500–1550 nm).[298] This strategy has been successfully applied in *in vivo* biosensing applications by combining Er^{3+} with other lanthanide ions, such as Ho^{3+} and Nd^{3+}, in $NaErF_4@NaYF_4$:Ho@$NaYF_4$ or $NaErF_4@NaYF_4$:Nd@$NaYF_4$ core–shell nanoarchitectures, and taking advantage of their emissions located in the II-BW (1180 nm of Ho^{3+}, 1060 nm of Nd^{3+}, and 980 nm of Er^{3+}) after the energy of the 1530 nm excitation source was absorbed by Er^{3+}.[298] Furthermore, it has been confirmed that the penetration depth in biological tissues (in chicken pectoral muscle in that particular case) is two times higher when using an excitation source at 1319 nm than when using a 800 nm excitation source in Tm^{3+}-doped nanoparticles.[128]

In addition, for the biological/biomedical applications, the biological tissues in which these luminescent thermometers have been applied are different (chicken breast,[63,166,171,174,245,266,299] pork fat,[164,300] phantom tissue,[157,163,301] or mice[126,223,302]), leading to different and non-comparable penetration depths (Fig. 57) due to the different responses to the interaction with the light of their biological components. Thus, extensive research should be developed to understand the similarities and differences in the interaction of light with the different biological tissues to extract reliable conclusions in this area. Nevertheless, and regardless of the nature of the biological tissue, when operating at longer wavelengths, in general, the penetration depth increased, considering only those examples in which chicken breast was used as a subject of study, as can be seen in Fig. 57. Also from this figure, it can be seen that the majority of the luminescent nanothermometers developed up to now operat-

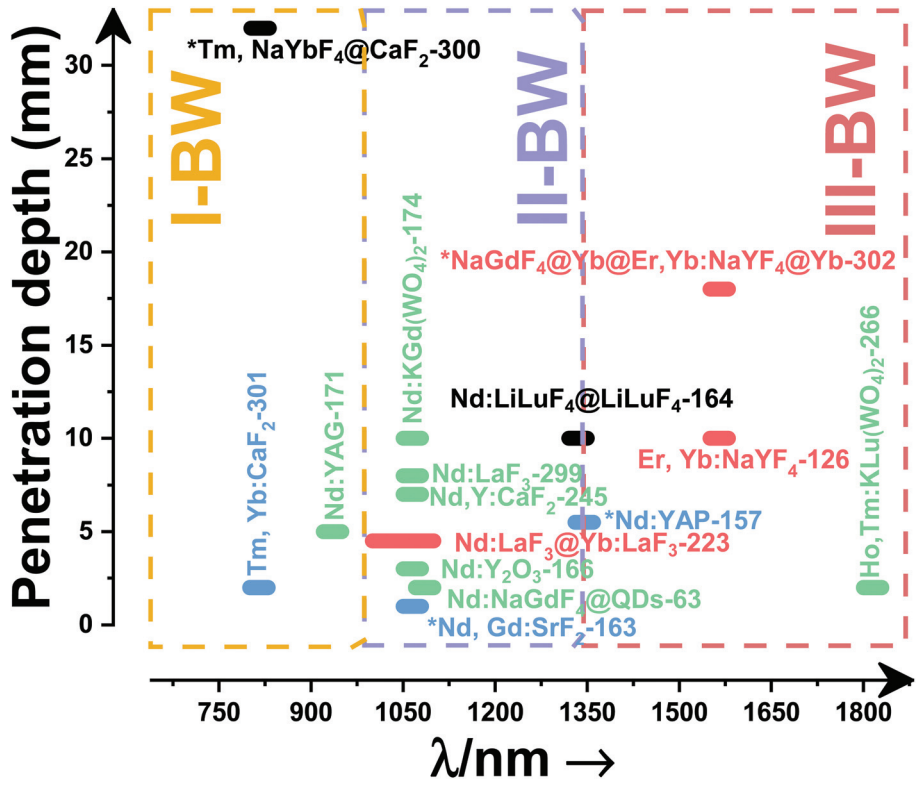

Fig. 57 Penetration depth in the BWs spectral regions reported for Ln^{3+}-doped luminescent nanomaterials. The intervals represent the operating wavelength regimes for the corresponding nanothermometer, whereas the asterisk indicates only one reported wavelength. The black, blue, red and green colors stand for the different types of biological medium: black = pork tissue, blue = phantom tissue, red = mice and green = chicken tissue. The numbers are the corresponding references.

ing within the BW spectral ranges, including also these materials used only to determine the penetration depth in biological tissues, were based on Nd^{3+}-doped materials, when other choices are also possible, like the combination of Ho^{3+} and Tm^{3+} ions, for instance, to develop multifunctional nanoparticles such as self-assessed photothermal agents.

Nevertheless, there are some current challenges for luminescent nanothermometers when used inside biological tissues that should be addressed for future biomedical applications, such as the distortion of the shape of the spectra recorded for these luminescent nanothermometers produced when they are recorded through the biological tissues.[303] Possible solutions for this drawback could be the calibration of the luminescent nanothermometers when already embedded in the biological medium, as proposed recently by Shen *et al.*[303] or the use of lifetime luminescence nanothermometry, which is not affected by changes in the optical properties of the surrounding medium, including biological tissues, by the concentration of the luminescent nanothermometers or by the excitation power density used.[227]

Furthermore, in *in vitro* applications, concepts related to the temperature flocculation at the nanoscale, the disagreement between the calculated and the experimental temperature, and the understanding of the thermal conductivity in a cell,[304] should be addressed. In fact, the discrepancies in *in vitro* applications could also affect the *in vivo* applications.[304]

Finally, another research direction that should be further taken into account would be exploring the application of these luminescent thermometers outside the biological/biomedical fields, since their reported applicability in this direction is scarce.

As a final note, we would like to highlight, according to all the data analyzed in this review, which strategies would provide a better performance for the luminescent nanothermometers operating in the BWs. It is clear that to maximize the relative thermal sensitivity of the luminescent thermometer, and consequently minimize the temperature resolution, the most effective strategy consists of maximizing the separation between the emission lines used in the thermometer when the band-shape luminescent thermometry method is used. If this is done by using emissions arising from two non-thermally coupled electronic levels that are apart a distance higher than the upper limit defining the thermally coupled range of energies, the performance of the thermometer would be even better. In fact, by combining two different emission centers, and especially if emissions arising from transition metals are involved, the highest thermal sensitivities reported up to now are achieved, although these systems are quite complex, and we still have a low understanding of the factors that govern the temperature-sensing properties. Nevertheless, there are other aspects that have to be taken into account to develop efficient and practical luminescent nanothermometers, such as the use of emission lines with similar intensities in the thermometer, that would facilitate their recording and analysis with enough guarantees. Another important aspect to consider, especially when developing these luminescent thermometers for biological/biomedical applications, is that the maximum of their relative thermal sensitivity should be in the range of 350–400 K, and not at room temperature, as happens with the majority of the luminescent thermometers developed up to now. All these aspects are important to analyze when considering developing luminescent thermometers operating in the III- and IV-BW, where the S_{rel} achieved up to now is still low, although the number of publications devoted to developing luminescence thermometers in this spectral range is still very low, or null in the case of the IV-BW.

After this analysis, we believe that working with Nd^{3+} and Ho^{3+},Tm^{3+}-doped and codoped materials is a promising approach to not only promote the thermometric performance of the luminescent nanothermometers, but also to develop multifunctional platforms that can combine thermal sensing and photothermal therapy, for instance. Furthermore, using lifetime thermometry in these systems would allow current challenges on the biomedical application of these materials to be addressed, such as the spectral distortion. Finally, novel strategies towards the challenge of increasing the low brightness of Ln^{3+}-doped materials should also be addressed. Up to now core–shell and core–multishell nanoarchitectures offered a boost in the brightness of the emissions generated by lanthanide ions and a significant enhancement of their temperature-sensing performance. However, other strategies that can improve this brightness, such as pairing them with plasmonic structures, use of organic-dye sensitization, and/or coupling them with semiconductors,[107,108] might be explored.

Conflicts of interest

There are no conflicts to declare.

Acknowledgements

This work was supported by the Spanish Government under projects MAT2016-75716-C2-1-R (AEI/FEDER, UE) and by the Generalitat de Catalunya under project 2017SGR755. A. N. acknowledges financial support from the Generalitat de Catalunya under grant 2017FI_B00620, 2018FI_B100161 and 2019 FI_B2 00154.

References

1 S. W. Allison and G. T. Gillies, *Rev. Sci. Instrum.*, 1997, **68**, 2615–2650.
2 A. H. Khalid and K. Kontis, *Sensors*, 2008, **8**, 5673–5744.
3 S. Uchiyama, C. Gota, T. Tsuji and N. Inada, *Chem. Commun.*, 2017, **53**, 10976–10992.
4 D. Jaque, L. Martínez-Maestro, B. del Rosal, P. Haro-Gonzalez, A. Benayas, J. L. Plaza, E. Martín-Rodríguez and J. García-Solé, *Nanoscale*, 2014, **6**, 9494–9530.

5 K. M. McCabe and M. Hernandez, *Pediatr. Res.*, 2010, **67**, 469–475.
6 O. S. Wolfbeis, *Adv. Mater.*, 2008, **20**, 3759–3763.
7 P. R. Childs, J. Greenwood and C. Long, *Rev. Sci. Instrum.*, 2000, **71**, 2959–2978.
8 Grand View Research Inc., https://www.marketsandmarkets.com/Market-Reports/temperature-sensor-market-522.html (accessed on 10 July 2020).
9 Y. Yue and X. Wang, *Nano Rev.*, 2012, **3**, 11586–11597.
10 D. Jaque and F. Vetrone, *Nanoscale*, 2012, **4**, 4301–4326.
11 S. S. Laha, A. R. Naik, E. R. Kuhn, M. Alvarez, A. Sujkowski, R. J. Wessells and B. P. Jena, *Nano Lett.*, 2017, **17**, 1262–1268.
12 X. Wang, O. S. Wolfbeis and R. J. Meier, *Chem. Soc. Rev.*, 2013, **42**, 7834–7869.
13 M. Quintanilla and L. M. Liz-Marzan, *Nano Today*, 2018, **19**, 126–145.
14 A. E. Albers, E. M. Chan, P. M. McBride, C. M. Ajo-Franklin, B. E. Cohen and B. A. Helms, *J. Am. Chem. Soc.*, 2012, **134**, 9565–9568.
15 U. Rocha, C. Jancito, W. F. Silva, I. Guedes, A. Benayas, L. Martínez-Maestro, M. Acosta-Elias, E. Bovero, F. C. J. M. van Veggel, J. García-Solé and D. Jaque, *ACS Nano*, 2013, **7**, 1188–1199.
16 K. Okabe, N. Inada, C. Gota, Y. Harada, T. Funatsu and S. Uchiyama, *Nat. Commun.*, 2012, **3**, 705.
17 P. R. N. Childs, in *Thermometry at the Nanoscale: Techniques and Selected Applications*, ed. L. D. Carlos and F. Palacio, The Royal Society of Chemistry, Cambridge, 2016, ch. 1, vol. 38, pp. 1–22.
18 R. J. DeBerardinis, J. J. Lum, G. Hatzivassiliou and C. B. Thompson, *Cell Metab.*, 2008, **7**, 11–20.
19 M. Karnebogen, D. Singer, M. Kallerhoff and R. H. Ringert, *Thermochim. Acta*, 1993, **229**, 147–155.
20 G. A. Sotiriou, F. Starsich, A. Dasargyri, M. C. Wurnig, F. Krumeich, A. Boss, J. C. Leroux and S. E. Pratsinis, *Adv. Funct. Mater.*, 2014, **24**, 2818–2827.
21 C. D. S. Brites, A. Millán and L. D. Carlos, in *Handbook on the Physics and Chemistry of Rare Earths*, ed. B. Jean-Claude and P. K. Vitalij, Elsevier, 2016, vol. 49, pp. 339–427.
22 F. Vetrone, R. Naccache, A. Zamarrón, A. J. de la Fuente, F. Sanz-Rodríguez, L. Martínez-Maestro, E. Martín-Rodríguez, D. Jaque, J. García-Solé and J. A. Capobianco, *ACS Nano*, 2010, **4**, 3254–3258.
23 R. Sakaguchi, S. Kiyonaka and Y. Mori, *Curr. Opin. Biotechnol.*, 2015, **31**, 57–64.
24 D. G. Cahill, *Rev. Sci. Instrum.*, 2004, **75**, 5119–5122.
25 P. Löw, B. Kim, N. Takama and C. Bergaud, *Small*, 2008, **4**, 908–914.
26 S. H. Kim, J. Noh, M. K. Jeon, K. W. Kim, L. P. Lee and S. I. Woo, *J. Micromech. Microeng.*, 2006, **16**, 526–530.
27 M. Corke, A. D. Kersey, D. A. Jackson and J. D. C. Jones, *Electron. Lett.*, 1983, **19**, 471–473.
28 K. Kim, W. Jeong, W. Lee and P. Reddy, *ACS Nano*, 2012, **6**, 4248–4257.
29 J. R. Greenwood, P. R. N. Childs and P. Chaloner, *Gold Bull.*, 1999, **32**, 85–89.
30 Y. Gao and Y. Bando, *Nature*, 2002, **415**, 599–599.
31 B. Klinkert and F. Narberhaus, *Cell. Mol. Life Sci.*, 2009, **66**, 2661–2676.
32 G. Mills, H. Zhou, A. Midha, L. Donaldson and J. M. R. Weaver, *Appl. Phys. Lett.*, 1998, **72**, 2900–2902.
33 A. Hammiche, M. Reading, H. M. Pollock, M. Song and D. J. Hourston, *Rev. Sci. Instrum.*, 1996, **67**, 4268–4274.
34 P. D. Tovee, M. E. Pumarol, M. C. Rosamond, R. Jones, M. C. Petty, D. A. Zeze and O. V. Kolosov, *Phys. Chem. Chem. Phys.*, 2014, **16**, 1174–1181.
35 J. Kortmann, S. Sczodrok, J. Rinnenthal, H. Schwalbe and F. Narberhaus, *Nucleic Acids Res.*, 2011, **39**, 2855–2868.
36 F. Narberhaus, T. Waldminghaus and S. Chowdhury, *FEMS Microbiol. Rev.*, 2006, **30**, 3–16.
37 S. Chowdhury, C. Maris, F. H. T. Allain and F. Narberhaus, *EMBO J.*, 2006, **25**, 2487–2497.
38 C. D. S. Brites, P. P. Lima, N. J. O. Silva, A. Millán, V. S. Amaral, F. Palacio and L. D. Carlos, *Nanoscale*, 2012, **4**, 4799–4829.
39 D. Ananias, C. D. S. Brites, L. D. Carlos and J. Rocha, *Eur. J. Inorg. Chem.*, 2016, **2016**, 1967–1971.
40 M. A. Omary and H. H. Patterson, in *Encyclopedia of Spectroscopy and Spectrometry*, ed. J. C. Lindon, G. E. Tranter and D. W. Koppenaal, Academic Press, Oxford, 3rd edn, 2017, pp. 636–653.
41 J. A. DeLuca, *J. Chem. Educ.*, 1980, **57**, 541–545.
42 S. A. Wade, S. F. Collins and G. W. Baxter, *J. Appl. Phys.*, 2003, **94**, 4743–4756.
43 B. Dong, B. Cao, Y. He, Z. Liu, Z. Li and Z. Feng, *Adv. Mater.*, 2012, **24**, 1987–1993.
44 F. Hu, J. Cao, X. Wei, X. Li, J. Cai, H. Guo, Y. Chen, C. K. Duan and M. Yin, *J. Mater. Chem. C*, 2016, **4**, 9976–9985.
45 M. Leroux, N. Grandjean, B. Beaumont, G. Nataf, F. Semond, J. Massies and P. Gibart, *J. Appl. Phys.*, 1999, **86**, 3721–3728.
46 N. Ishiwada, S. Fujioka, T. Ueda and T. Yokomori, *Opt. Lett.*, 2011, **36**, 760–762.
47 M. Quintanilla, A. Benayas, R. Naccache and F. Vetrone, in *Thermometry at the Nanoscale: Techniques and Selected Applications*, ed. L. D. Carlos and F. Palacio, The Royal Society of Chemistry, Cambridge, 2016, ch. 5, vol. 38, pp. 124–166.
48 C. D. S. Brites, S. Balabhadra and L. D. Carlos, *Adv. Opt. Mater.*, 2019, **7**, 1801239–1801269.
49 X. He, J. Gao, S. S. Gambhir and Z. Cheng, *Trends Mol. Med.*, 2010, **16**, 574–583.
50 J. S. Donner, S. A. Thompson, M. P. Kreuzer, G. Baffou and R. Quidant, *Nano Lett.*, 2012, **12**, 2107–2111.
51 V. V. Nazarenko, A. Remeeva, A. Yudenko, K. Kovalev, A. Dubenko, I. M. Goncharov, P. Kuzmichev, A. V. Rogachev, P. Buslaev, V. Borshchevskiy, A. Mishin, G. V. Dhoke, U. Schwaneberg, M. D. Davari, K. E. Jaeger,

U. Krauss, V. Gordeliy and I. Gushchin, *Photochem. Photobiol. Sci.*, 2019, **18**, 1793–1805.
52 O. A. Savchuk, O. F. Silvestre, R. M. R. Adão and J. B. Nieder, *Sci. Rep.*, 2019, **9**, 7535–7546.
53 S. Kiyonaka, T. Kajimoto, R. Sakaguchi, D. Shinmi, M. Omatsu-Kanbe, H. Matsuura, H. Imamura, T. Yoshizaki, I. Hamachi, T. Morii and Y. Mori, *Nat. Methods*, 2013, **10**, 1232–1238.
54 M. Nakano, Y. Arai, I. Kotera, K. Okabe, Y. Kamei and T. Nagai, *PLoS One*, 2017, **12**, 172344–172358.
55 C. Gota, K. Okabe, T. Funatsu, Y. Harada and S. Uchiyama, *J. Am. Chem. Soc.*, 2009, **131**, 2766–2767.
56 T. Hayashi, K. Kawamoto, N. Inada and S. Uchiyama, *Polymers*, 2019, **11**, 1305–1317.
57 S. Uchiyama, T. Tsuji, K. Kawamoto, K. Okano, E. Fukatsu, T. Noro, K. Ikado, S. Yamada, Y. Shibata, T. Hayashi, N. Inada, M. Kato, H. Koizumi and H. Tokuyama, *Angew. Chem., Int. Ed.*, 2018, **57**, 5413–5417.
58 S. M. Borisov and O. S. Wolfbeis, *Anal. Chem.*, 2006, **78**, 5094–5101.
59 C. Tan and Q. Wang, *Inorg. Chem. Commun.*, 2011, **14**, 515–518.
60 H. Peng, M. I. J. Stich, J. Yu, L. Sun, L. H. Fischer and O. S. Wolfbeis, *Adv. Mater.*, 2010, **22**, 716–719.
61 X. Zhu, W. Feng, J. Chang, Y. W. Tan, J. Li, M. Chen, Y. Sun and F. Li, *Nat. Commun.*, 2016, **7**, 10437–10447.
62 Y. Takei, S. Arai, A. Murata, M. Takabayashi, K. Oyama, S. Ishiwata, S. Takeoka and M. Suzuki, *ACS Nano*, 2014, **8**, 198–206.
63 E. N. Cerón, D. H. Ortgies, B. del Rosal, F. Ren, A. Benayas, F. Vetrone, D. Ma, F. Sanz-Rodríguez, J. G. Solé, D. Jaque and E. M. Rodríguez, *Adv. Mater.*, 2015, **27**, 4781–4787.
64 C. D. S. Brites, P. P. Lima, N. J. O. Silva, A. Millán, V. S. Amaral, F. Palacio and L. D. Carlos, *Adv. Mater.*, 2010, **22**, 4499–4504.
65 T. Sekiguchi, S. Sotoma and Y. Harada, *Biophys. Physicobiol.*, 2018, **15**, 229–234.
66 Y. K. Tzeng, P. C. Tsai, H. Y. Liu, O. Y. Chen, H. Hsu, F. G. Yee, M. S. Chang and H. C. Chang, *Nano Lett.*, 2015, **15**, 3945–3952.
67 G. Kucsko, P. C. Maurer, N. Y. Yao, M. Kubo, H. J. Noh, P. K. Lo, H. Park and M. D. Lukin, *Nature*, 2013, **500**, 54–58.
68 Z. Wang, D. Ananias, A. Carné-Sánchez, C. D. S. Brites, I. Imaz, D. Maspoch, J. Rocha and L. D. Carlos, *Adv. Funct. Mater.*, 2015, **25**, 2824–2830.
69 D. Zhao, X. Rao, J. Yu, Y. Cui, Y. Yang and G. Qian, *Inorg. Chem.*, 2015, **54**, 11193–11199.
70 J. Rocha, C. D. S. Brites and L. D. Carlos, *Chem. – Eur. J.*, 2016, **22**, 14782–14795.
71 Y. Cui, F. Zhu, B. Chen and G. Qian, *Chem. Commun.*, 2015, **51**, 7420–7431.
72 N. Chandrasekharan and L. A. Kelly, *J. Am. Chem. Soc.*, 2001, **123**, 9898–9899.
73 J. Feng, K. Tian, D. Hu, S. Wang, S. Li, Y. Zeng, Y. Li and G. Yang, *Angew. Chem., Int. Ed.*, 2011, **50**, 8072–8076.
74 R. Samy, T. Glawdel and C. L. Ren, *Anal. Chem.*, 2008, **80**, 369–375.
75 R. Victor, P. Woisel and R. Hoogenboom, *Mater. Today*, 2016, **19**, 44–55.
76 C. Pietsch, U. S. Schubert and R. Hoogenboom, *Chem. Commun.*, 2011, **47**, 8750–8765.
77 V. A. Vlaskin, N. Janssen, J. van Rijssel, R. Beaulac and D. R. Gamelin, *Nano Lett.*, 2010, **10**, 3670–3674.
78 L. M. Maestro, E. M. Rodríguez, F. S. Rodríguez, M. C. I. la Cruz, A. Juarranz, R. Naccache, F. Vetrone, D. Jaque, J. A. Capobianco and J. G. Solé, *Nano Lett.*, 2010, **10**, 5109–5115.
79 L. M. Maestro, C. Jacinto, U. R. Silva, F. Vetrone, J. A. Capobianco, D. Jaque and J. G. Solé, *Small*, 2011, **7**, 1774–1778.
80 P. Haro-González, W. T. Ramsay, L. Martínez-Maestro, B. del Rosal, K. Santacruz-Gomez, M. C. I. de la Cruz, F. Sanz-Rodríguez, J. Y. Chooi, P. R. Sevilla and M. Bettinelli, *Small*, 2013, **9**, 2162–2170.
81 S. Li, K. Zhang, J. M. Yang, L. Lin and H. Yang, *Nano Lett.*, 2007, **7**, 3102–3105.
82 X. Wang, Q. Liu, Y. Bu, C. S. Liu, T. Liu and X. Yan, *RSC Adv.*, 2015, **5**, 86219–86236.
83 S. Kiyonaka, R. Sakaguchi, I. Hamachi, T. Morii, T. Yoshizaki and Y. Mori, *Nat. Methods*, 2015, **12**, 801–802.
84 G. Baffou, H. Rigneault, D. Marguet and L. Jullien, *Nat. Methods*, 2014, **11**, 899–901.
85 K. S. Soni, S. S. Desale and T. K. Bronich, *J. Controlled Release*, 2016, **240**, 109–126.
86 E. Hemmer, A. Benayas, F. Légaré and F. Vetrone, *Nanoscale Horiz.*, 2016, **1**, 168–184.
87 A. Rassamesard, Y. F. Huang, H. Y. Lee, T. S. Lim, M. C. Li, J. D. White, J. H. Hodak, T. Osotchan, K. Y. Peng, S. A. Chen, J. H. Hsu, M. Hayashi and W. Fann, *J. Phys. Chem. C*, 2009, **113**, 18681–18688.
88 R. A. Bohara, in *Hybrid Nanostructures for Cancer Theranostics*, ed. R. Ashok Bohara and N. Thorat, Elsevier, 2019, ch. 1, pp. 1–16.
89 D. Jaque, B. del Rosal, E. Martín-Rodríguez, L. Martinez Maestro, P. Haro-González and J. García-Solé, *Nanomedicine*, 2014, **9**, 1047–1062.
90 B. del Rosal, E. Ximendes, U. Rocha and D. Jaque, *Adv. Opt. Mater.*, 2017, **5**, 1600508–1600522.
91 M. H. Alkahtani, F. Alghannam, L. Jiang, A. Almethen, A. A. Rampersaud, R. Brick, C. L. Gomes, M. O. Scully and P. R. Hemmer, *Nanophotonics*, 2018, **7**, 1423–1454.
92 C. Bradac, S. F. Lim, H. C. Chang and I. Aharonovich, *Adv. Opt. Mater.*, 2020, **8**, 2000183–2000212.
93 E. Petryayeva, W. R. Algar and I. L. Medintz, *Appl. Spectrosc.*, 2013, **67**, 215–252.
94 H. Zhao, A. Vomiero and F. Rosei, *Small*, 2020, **16**, 2000804–2000822.
95 K. M. Tsoi, Q. Dai, B. A. Alman and W. C. W. Chan, *Acc. Chem. Res.*, 2013, **46**, 662–671.

96 X. Qiu, X. Zhu, X. Su, M. Xu, W. Yuan, Q. Liu, M. Xue, Y. Liu, W. Feng and F. Li, *Adv. Sci.*, 2019, **6**, 1801834–1801842.
97 A. Teitelboim and D. Oron, *ACS Nano*, 2016, **10**, 446–452.
98 D. Jaque and J. G. Solé, in *Thermometry at the Nanoscale: Techniques and Selected Applications*, ed. L. D. Carlos and F. Palacio, The Royal Society of Chemistry, Cambridge, 2016, ch. 4, vol. 38, pp. 83–123.
99 J. C. G. Buenzli and S. V. Eliseeva, *Chem. Sci.*, 2013, **4**, 1939–1949.
100 L. D. Carlos, R. A. Ferreira, V. d. Z. Bermudez and S. J. Ribeiro, *Adv. Mater.*, 2009, **21**, 509–534.
101 J. Zhou, J. L. Leano Jr., Z. Liu, D. Jin, K. L. Wong, R. S. Liu and J. C. G. Bünzli, *Small*, 2018, **14**, 1801882–1801911.
102 G. Chen, C. Yang and P. N. Prasad, *Acc. Chem. Res.*, 2013, **46**, 1474–1486.
103 A. Gnach, T. Lipinski, A. Bednarkiewicz, J. Rybka and J. A. Capobianco, *Chem. Soc. Rev.*, 2015, **44**, 1561–1584.
104 R. R. Anderson and J. A. Parrish, *J. Invest. Dermatol.*, 1981, **77**, 13–19.
105 A. M. Smith, M. C. Mancini and S. Nie, *Nat. Nanotechnol.*, 2009, **4**, 710–711.
106 J. C. G. Bünzli, *Acc. Chem. Res.*, 2006, **39**, 53–61.
107 R. Marin, D. Jaque and A. Benayas, *Nanoscale Horiz.*, 2021, **6**, 209–230.
108 R. Marin and D. Jaque, *Chem. Rev.*, 2021, **121**, 1425–1462.
109 P. V. d. Santos, M. T. d. Araujo, A. S. Gouveia-Neto, J. A. M. Neto and A. S. B. Sombra, *Appl. Phys. Lett.*, 1998, **73**, 578–580.
110 S. Collins, G. Baxter, S. Wade, T. Sun, K. Grattan, Z. Zhang and A. W. Palmer, *J. Appl. Phys.*, 1998, **84**, 4649–4654.
111 S. N. Baker, T. M. McCleskey and G. A. Baker, in *Ionic Liquids IIIB: Fundamentals, Progress, Challenges, and Opportunities*, American Chemical Society, 2005, ch. 14, vol. 902, pp. 171–181.
112 O. A. Savchuk, J. J. Carvajal, C. Cascales, M. Aguiló and F. Díaz, *ACS Appl. Mater. Interfaces*, 2016, **8**, 7266–7273.
113 J. W. Bartlett and C. Frost, *Ultrasound Obstet. Gynecol*, 2008, **31**, 466–475.
114 B. N. Taylor and C. E. Kuyatt, *Guidelines for evaluation and expressing the uncertainty of NIST Measurement Results (NIST Technical Note 1297)*, 1994.
115 J. J. Carvajal, O. Savchuk, A. Nexha, M. C. Pujol, M. Aguiló and F. Díaz, Expanding luminescence thermometry detection range to the SWIR for biomedical applications, *Optical Sensing and Detection V*, SPIE, Strasbourg, France, 2018, p. 34.
116 Y. T. Lim, S. Kim, A. Nakayama, N. E. Stott, M. G. Bawendi and J. V. Frangioni, *Mol. Imaging*, 2003, **2**, 50–64.
117 G. Zonios, J. Bykowski and N. Kollias, *J. Invest. Dermatol.*, 2001, **117**, 1452–1457.
118 G. M. Hale and M. R. Querry, *Appl. Opt.*, 1973, **12**, 555–563.
119 S. Prahl, Optical absorption of hemoglobin, http://omlc.ogi.edu/spectra/hemoglobin, (accessed on 14 October 2020).
120 S. L. Jacques and D. J. McAuliffe, *Photochem. Photobiol.*, 1991, **53**, 769–775.
121 L. V. Wang and H. Wu, *Biomedical optics: principles and imaging*, John Wiley & Sons, 2012.
122 S. Jacques, *Phys. Med. Biol.*, 2013, **58**, 37–61.
123 M. Chaplin, Water Structure and Science, 2016. Available online: http://www.1.lsbu.ac.uk/water/water_vibrational_spectrum.html (accessed on 14 October 2020).
124 L. Shi, L. A. Sordillo, A. Rodríguez-Contreras and R. Alfano, *J. Biophotonics*, 2016, **9**, 38–43.
125 B. del Rosal, I. Villa, D. Jaque and F. Sanz-Rodríguez, *J. Biophotonics*, 2016, **9**, 1059–1067.
126 D. J. Naczynski, M. C. Tan, M. Zevon, B. Wall, J. Kohl, A. Kulesa, S. Chen, C. M. Roth, R. E. Riman and P. V. Moghe, *Nat. Commun.*, 2013, **4**, 2199–2209.
127 M. A. Hernandez-Rodriguez, A. D. Lozano-Gorrin, V. Lavin, U. R. Rodriguez-Mendoza and I. R. Martin, *Opt. Express*, 2017, **25**, 27845–27856.
128 A. F. Pereira, J. Ferreira, A. S. Gouveia-Neto and C. Jacinto, *Sens. Actuators, B*, 2017, **238**, 525–531.
129 F. Auzel, *Chem. Rev.*, 2004, **104**, 139–174.
130 Y. Chen, G. Chen, X. Liu, J. Xu, X. Zhou, T. Yang, C. Yuan and C. Zhou, *Opt. Mater.*, 2018, **81**, 78–83.
131 O. Savchuk, J. J. Carvajal, C. Cascales, P. Haro-Gonzalez, F. Sanz-Rodríguez, M. Aguilo and F. Diaz, *Nanomaterials*, 2020, **10**, 993–1010.
132 M. Runowski, A. Shyichuk, A. Tymiński, T. Grzyb, V. Lavín and S. Lis, *ACS Appl. Mater. Interfaces*, 2018, **10**, 17269–17279.
133 L. Xing, W. Yang, D. Ma and R. Wang, *Sens. Actuators, B*, 2015, **221**, 458–462.
134 L. Li, F. Qin, Y. Zhou, Y. Zheng, H. Zhao and Z. Zhang, *J. Lumin.*, 2018, **202**, 301–308.
135 Y. Bu and X. H. Yan, *Appl. Phys. B*, 2017, **123**, 59–69.
136 W. Ge, M. Xu, J. Shi, J. Zhu and Y. Li, *Chem. Eng. J.*, 2019, **391**, 123546–123553.
137 J. Zhang and C. Jin, *Ind. Eng. Chem. Res.*, 2019, **58**, 3490–3498.
138 J. Zhang, G. Chen, Z. Zhai, H. Chen and Y. Zhang, *J. Alloys Compd.*, 2019, **771**, 838–846.
139 L. Yu, L. Ye, R. Bao, X. Zhang and L. G. Wang, *Opt. Commun.*, 2018, **410**, 632–636.
140 N. Wang, Z. Fu, Y. Wei and T. Sheng, *J. Alloys Compd.*, 2019, **772**, 371–380.
141 E. Casagrande, M. Back, D. Cristofori, J. Ueda, S. Tanabe, S. Palazzolo, F. Rizzolio, V. Canzonieri, E. Trave and P. Riello, *J. Mater. Chem. C*, 2020, **8**, 7828–7836.
142 W. Chen, J. Cao, F. Hu, R. Wei, L. Chen and H. Guo, *J. Alloys Compd.*, 2018, **735**, 2544–2550.
143 Q. Min, W. Bian, Y. Qi, W. Lu, X. Yu, X. Xu, D. Zhou and J. Qiu, *J. Alloys Compd.*, 2017, **728**, 1037–1042.
144 H. Lu, J. Yang, D. Huang, Q. Zhou, M. Yang, X. Zhang, Y. Wang and H. Zhu, *J. Lumin.*, 2018, **206**, 613–617.
145 Y. Fu, L. Zhao, Y. Guo and H. Yu, *New J. Chem.*, 2019, **43**, 16664–16669.

146 P. Du, L. Luo and J. Yu, *J. Alloys Compd.*, 2018, **739**, 926–933.
147 A. Zhou, F. Song, F. Song, M. Feng, K. Adnan, D. Ju and X. Wang, *Opt. Mater.*, 2018, **78**, 438–444.
148 R. Wu, J. Zhou, L. Lei, S. Zhang, Z. Xiao, J. Zhang and S. Xu, *Chem. Phys. Lett.*, 2017, **667**, 206–210.
149 M. Ding, M. Zhang and C. Lu, *Mater. Lett.*, 2017, **209**, 52–55.
150 O. A. Savchuk, J. J. Carvajal, C. D. S. Brites, L. D. Carlos, M. Aguilo and F. Diaz, *Nanoscale*, 2018, **10**, 6602–6610.
151 H. Lu, H. Haoyue, Y. Gao, D. Li, G. Shi, Y. Song, Y. Wang and X. Zhang, *Microchim. Acta*, 2017, **184**, 641–646.
152 H. Lu, H. Hao, G. Shi, Y. Gao, R. Wang, Y. Song, Y. Wang and X. Zhang, *RSC Adv.*, 2016, **6**, 55307–55311.
153 D. Chen, S. Liu, X. Li, S. Yuan and P. Huang, *J. Eur. Ceram. Soc.*, 2017, **37**, 4939–4945.
154 M. Ding, D. Chen, C. Lu, J. Xi, Z. Ji and Z. Xu, *Mater. Lett.*, 2017, **189**, 5–8.
155 L. Marciniak, A. Bednarkiewicz, J. Drabik, K. Trejgis and W. Strek, *Phys. Chem. Chem. Phys.*, 2017, **19**, 7343–7351.
156 G. Jiang, X. Wei, S. Zhou, Y. Chen, C. Duan and M. Yin, *J. Lumin.*, 2014, **152**, 156–159.
157 M. A. Hernández-Rodríguez, A. D. Lozano-Gorrín, I. R. Martín, U. R. Rodríguez-Mendoza and V. Lavín, *Sens. Actuators, B*, 2018, **255**, 970–976.
158 S. Balabhadra, M. L. Debasu, C. D. S. Brites, L. A. O. Nunes, O. L. Malta, J. Rocha, M. Bettinelli and L. D. Carlos, *Nanoscale*, 2015, **7**, 17261–17267.
159 M. Suta, Ž. Antić, V. Đorđević, S. Kuzman, M. D. Dramićanin and A. Meijerink, *Nanomaterials*, 2020, **10**, 543–563.
160 E. A. Lalla, S. F. León-Luis, V. Monteseguro, C. Pérez-Rodríguez, J. M. Cáceres, V. Lavín and U. R. Rodríguez-Mendoza, *J. Lumin.*, 2015, **166**, 209–214.
161 P. Haro-González, I. R. Martín, L. L. Martín, S. F. León-Luis, C. Pérez-Rodríguez and V. Lavín, *Opt. Mater.*, 2011, **33**, 742–745.
162 P. Huang, W. Zheng, D. Tu, X. Shang, M. Zhang, R. Li, J. Xu, Y. Liu and X. Chen, *Adv. Sci.*, 2019, **6**, 1802282–1802289.
163 M. Pedroni, P. Cortelletti, I. X. Cantarelli, N. Pinna, P. Canton, M. Quintanilla, F. Vetrone and A. Speghini, *Sens. Actuators, B*, 2017, **250**, 147–155.
164 A. Skripka, A. Morinvil, M. Matulionyte, T. Cheng and F. Vetrone, *Nanoscale*, 2019, **11**, 11322–11330.
165 L. Marciniak, A. Bednarkiewicz, D. Hreniak and W. Strek, *J. Mater. Chem. C*, 2016, **4**, 11284–11290.
166 I. E. Kolesnikov, A. A. Kalinichev, M. A. Kurochkin, D. V. Mamonova, E. Y. Kolesnikov, A. V. Kurochkin, E. Lähderanta and M. D. Mikhailov, *J. Lumin.*, 2018, **204**, 506–512.
167 L. Đačanin-Far, S. R. Lukić-Petrović, V. Đorđević, K. Vuković, E. Glais, B. Viana and M. D. Dramićanin, *Sens. Actuators, A*, 2018, **270**, 89–96.
168 E. Carrasco, B. del Rosal, F. Sanz-Rodríguez, Á. J. de la Fuente, P. H. Gonzalez, U. Rocha, K. U. Kumar, C. Jacinto, J. G. Solé and D. Jaque, *Adv. Funct. Mater.*, 2015, **25**, 615–626.
169 I. E. Kolesnikov, E. V. Golyeva, M. A. Kurochkin, E. Lähderanta and M. D. Mikhailov, *Sens. Actuators, B*, 2016, **235**, 287–293.
170 G. Dantelle, M. Matulionyte, D. Testemale, A. Cantarano, A. Ibanez and F. Vetrone, *Phys. Chem. Chem. Phys.*, 2019, **21**, 11132–11141.
171 A. Benayas, B. del Rosal, A. Pérez-Delgado, K. Santacruz-Gómez, D. Jaque, G. A. Hirata and F. Vetrone, *Adv. Opt. Mater.*, 2015, **3**, 687–694.
172 P. M. Gschwend, F. H. L. Starsich, R. C. Keitel and S. E. Pratsinis, *Chem. Commun.*, 2019, **55**, 7147–7150.
173 D. Wawrzynczyk, A. Bednarkiewicz, M. Nyk, W. Strek and M. Samoc, *Nanoscale*, 2012, **4**, 6959–6961.
174 O. Savchuk, J. J. Carvajal, L. G. De la Cruz, P. Haro-González, M. Aguiló and F. Díaz, *J. Mater. Chem. C*, 2016, **4**, 7397–7405.
175 L. Marciniak, A. Pilch, S. Arabasz, D. Jin and A. Bednarkiewicz, *Nanoscale*, 2017, 9, 8288–8297.
176 W. Xu, H. Zhao, Z. Zhang and W. Cao, *Sens. Actuators, B*, 2013, **178**, 520–524.
177 H. Song, Q. Han, X. Tang, X. Zhao, K. Ren and T. Liu, *Opt. Mater.*, 2018, **84**, 263–267.
178 W. Xu, Q. Song, L. Zheng, Z. Zhang and W. Cao, *Opt. Lett.*, 2014, **39**, 4635–4638.
179 A. F. Silva, F. Elan, E. L. Falcão-Filho, L. J. Q. Maia and C. B. de Araújo, *J. Mater. Chem. C*, 2017, **5**, 1240–1246.
180 W. Xu, H. Qi, L. Zheng, Z. Zhang and W. Cao, *Opt. Lett.*, 2015, **40**, 5678–5681.
181 G. Gao, D. Busko, S. Kauffmann-Weiss, A. Turshatov, I. A. Howard and B. S. Richards, *J. Mater. Chem. C*, 2018, **6**, 4163–4170.
182 Z. Zhao, F. Hu, Z. Cao, F. Chi, X. Wei, Y. Chen, C. Duan and M. Yin, *Ceram. Int.*, 2017, **43**, 14951–14955.
183 I. Kolesnikov, D. Mamonova, A. Kalinichev, M. Kurochkin, V. Medvedev, E. Kolesnikov, E. Lahderanta and A. Manshina, *Nanoscale*, 2020, **12**, 5953–5960.
184 J. Drabik, B. Cichy and L. Marciniak, *J. Phys. Chem. C*, 2018, **122**, 14928–14936.
185 K. Trejgis and L. Marciniak, *Phys. Chem. Chem. Phys.*, 2018, **20**, 9574–9581.
186 A. S. Souza, L. A. O. Nunes, I. G. N. Silva, F. A. M. Oliveira, L. L. da Luz, H. F. Brito, M. C. F. C. Felinto, R. A. S. Ferreira, S. A. Júnior, L. D. Carlos and O. L. Malta, *Nanoscale*, 2016, **8**, 5327–5333.
187 K. Lu, Y. Yi, L. Xu, X. Sun, L. Liu and H. Li, *Nanomaterials*, 2020, **10**, 24–36.
188 K. Lu, X. Sun, L. Xu, B. Jiang, J. Ren, J. J. Carvajal, E. Zhao, L. Liu and J. Zhang, *J. Alloys Compd.*, 2020, **842**, 155602–155610.
189 A. C. Brandão-Silva, M. A. Gomes, Z. S. Macedo, J. F. M. Avila, J. J. Rodrigues and M. A. R. C. Alencar, *J. Phys. Chem. C*, 2018, **122**, 20459–20468.
190 D. Chen, W. Xu, S. Yuan, X. Li and J. Zhong, *J. Mater. Chem. C*, 2017, **5**, 9619–9628.

191 M. Runowski, A. Bartkowiak, M. Majewska, I. R. Martín and S. Lis, *J. Lumin.*, 2018, **201**, 104–109.
192 A. Ćirić, J. Aleksić, T. Barudžija, Ž. Antić, V. Đorđević, M. Medić, J. Periša, I. Zeković, M. Mitrić and M. D. Dramićanin, *Nanomaterials*, 2020, **10**, 627–637.
193 J. Zhou, R. Lei, H. Wang, C. Chen, B. Chen, E. Pan, S. Zhao and S. Xu, *ACS Appl. Nano Mater.*, 2020, **3**, 186–194.
194 O. A. Savchuk, J. J. Carvajal, M. C. Pujol, E. W. Barrera, J. Massons, M. Aguilo and F. Diaz, *J. Phys. Chem. C*, 2015, **119**, 18546–18558.
195 Z. Wang, H. Jiao and Z. Fu, *Inorg. Chem.*, 2018, **57**, 8841–8849.
196 G. Boulon, *J. Alloys Compd.*, 2008, **451**, 1–11.
197 J. Xu, A. Gulzar, P. Yang, H. Bi, D. Yang, S. Gai, F. He, J. Lin, B. Xing and D. Jin, *Coord. Chem. Rev.*, 2019, **381**, 104–134.
198 L. Xing, Y. Xu, R. Wang, W. Xu and Z. Zhang, *Opt. Lett.*, 2014, **39**, 454–457.
199 U. Rocha, C. Jacinto, K. U. Kumar, F. J. López, D. Bravo, J. G. Solé and D. Jaque, *J. Lumin.*, 2016, **175**, 149–157.
200 I. E. Kolesnikov, A. A. Kalinichev, M. A. Kurochkin, E. V. Golyeva, E. Y. Kolesnikov, A. V. Kurochkin, E. Lähderanta and M. D. Mikhailov, *Sci. Rep.*, 2017, **7**, 18002.
201 L. Marciniak, A. Bednarkiewicz, M. Stefanski, R. Tomala, D. Hreniak and W. Strek, *Phys. Chem. Chem. Phys.*, 2015, **17**, 24315–24321.
202 S. Zheng, W. Chen, D. Tan, J. Zhou, Q. Guo, W. Jiang, C. Xu, X. Liu and J. Qiu, *Nanoscale*, 2014, **6**, 5675–5679.
203 B. d. Rosal, A. Pérez-Delgado, M. Misiak, A. Bednarkiewicz, A. S. Vanetsev, Y. Orlovskii, D. J. Jovanović, M. D. Dramićanin, U. Rocha, K. U. Kumar, C. Jacinto, E. Navarro, E. M. Rodríguez, M. Pedroni, A. Speghini, G. A. Hirata, I. R. Martín and D. Jaque, *J. Appl. Phys.*, 2015, **118**, 143104–143115.
204 Z. Yu, W. K. Chan and T. T. Y. Tan, *Small*, 2020, **16**, 1905265–1905286.
205 Y. Chen, X. Lin, Z. Luo and Y. Huang, *Chem. Phys. Lett.*, 2003, **381**, 598–604.
206 Y. F. Wang, G. Y. Liu, L. D. Sun, J. W. Xiao, J. C. Zhou and C. H. Yan, *ACS Nano*, 2013, **7**, 7200–7206.
207 Y. Fan, P. Wang, Y. Lu, R. Wang, L. Zhou, X. Zheng, X. Li, J. A. Piper and F. Zhang, *Nat. Nanotechnol.*, 2018, **13**, 941–946.
208 W. Shao, G. Chen, A. Kuzmin, H. L. Kutscher, A. Pliss, T. Y. Ohulchanskyy and P. N. Prasad, *J. Am. Chem. Soc.*, 2016, **138**, 16192–16195.
209 D. K. Sardar and R. M. Yow, *Phys. Status Solidi A*, 1999, **173**, 521–534.
210 D. K. Sardar and R. M. Yow, *Opt. Mater.*, 1998, **10**, 191–199.
211 J. G. Solé, L. L. Bausá and D. Jaque, in *An Introduction to the Optical Spectroscopy of Inorganic Solids*, Wiley, 2005, ch. 1, pp. 1–38.
212 Y. Cheng, Y. Gao, H. Lin, F. Huang and Y. Wang, *J. Mater. Chem. C*, 2018, **6**, 7462–7478.
213 J. F. Suijver, in *Luminescence: From Theory to Applications*, ed. C. Ronda, Wiley, 2007, ch. 6, pp. 133–177.
214 S. Balabhadra, M. L. Debasu, C. D. S. Brites, R. A. S. Ferreira and L. D. Carlos, *J. Phys. Chem. C*, 2017, **121**, 13962–13968.
215 Y. Zhou, F. Qin, Y. Zheng, Z. Zhang and W. Cao, *Opt. Lett.*, 2015, **40**, 4544–4547.
216 M. Peng, X. Yin, P. A. Tanner, M. G. Brik and P. Li, *Chem. Mater.*, 2015, **27**, 2938–2945.
217 B. Wang, H. Lin, F. Huang, J. Xu, H. Chen, Z. Lin and Y. Wang, *Chem. Mater.*, 2016, **28**, 3515–3524.
218 M. G. Brik, S. J. Camardello and A. M. Srivastava, *ECS J. Solid State Sci. Technol.*, 2014, **4**, 39–43.
219 D. Chen, Y. Zhou and J. Zhong, *RSC Adv.*, 2016, **6**, 86285–86296.
220 P. Cortelletti, C. Facciotti, I. X. Cantarelli, P. Canton, M. Quintanilla, F. Vetrone, A. Speghini and M. Pedroni, *Opt. Mater.*, 2017, **68**, 29–34.
221 G. Chen, H. Qiu, P. N. Prasad and X. Chen, *Chem. Rev.*, 2014, **114**, 5161–5214.
222 M. Pedroni, F. Piccinelli, T. Passuello, S. Polizzi, J. Ueda, P. Haro-González, L. Martínez-Maestro, D. Jaque, J. García-Solé, M. Bettinelli and A. Speghini, *Cryst. Growth Des.*, 2013, **13**, 4906–4913.
223 E. C. Ximendes, W. Q. Santos, U. Rocha, U. K. Kagola, F. Sanz-Rodríguez, N. Fernández, A. d. S. Gouveia-Neto, D. Bravo, A. M. Domingo, B. del Rosal, C. D. S. Brites, L. D. Carlos, D. Jaque and C. Jacinto, *Nano Lett.*, 2016, **16**, 1695–1703.
224 L. Marciniak, A. Bednarkiewicz, D. Kowalska and W. Strek, *J. Mater. Chem. C*, 2016, **4**, 5559–5563.
225 M. Runowski, N. Stopikowska, D. Szeremeta, S. Goderski, M. Skwierczyńska and S. Lis, *ACS Appl. Mater. Interfaces*, 2019, **11**, 13389–13396.
226 Z. Ji, Y. Cheng, X. Cui, H. Lin, J. Xu and Y. Wang, *Inorg. Chem. Front.*, 2019, **6**, 110–116.
227 M. Tan, F. Li, N. Cao, H. Li, X. Wang, C. Zhang, D. Jaque and G. Chen, *Small*, 2020, **16**, 2004118–2004128.
228 T. Wang, T. Xiao, Y. Fan, F. He, Y. Li, Y. Peng, Q. Wang, Z. Yin, Z. Yang, J. Qiu and Z. Song, *J. Mater. Chem. C*, 2019, **7**, 13811–13817.
229 L. Marciniak and A. Bednarkiewicz, *Sens. Actuators, B*, 2017, **243**, 388–393.
230 I. Richman, *J. Chem. Phys.*, 1964, **41**, 2836–2837.
231 T. Miyakawa and D. L. Dexter, *Phys. Rev. B: Solid State*, 1970, **1**, 70–80.
232 L. Marciniak, A. Bednarkiewicz and W. Strek, *Sens. Actuators, B*, 2017, **238**, 381–386.
233 E. Hemmer, N. Venkatachalam, H. Hyodo, A. Hattori, Y. Ebina, H. Kishimoto and K. Soga, *Nanoscale*, 2013, **5**, 11339–11361.
234 A. M. Kaczmarek, D. Esquivel, J. Ouwehand, P. Van Der Voort, F. J. Romero-Salguero and R. Van Deun, *Dalton Trans.*, 2017, **46**, 7878–7887.

235 S. Han, R. Deng, X. Xie and X. Liu, *Angew. Chem., Int. Ed.*, 2014, **53**, 11702–11715.
236 F. Wang and X. Liu, *Chem. Soc. Rev.*, 2009, **38**, 976–989.
237 V. Mahalingam, F. Vetrone, R. Naccache, A. Speghini and J. A. Capobianco, *Adv. Mater.*, 2009, **21**, 4025–4028.
238 H. Wen, H. Zhu, X. Chen, T. F. Hung, B. Wang, G. Zhu, S. F. Yu and F. Wang, *Angew. Chem., Int. Ed.*, 2013, **52**, 13419–13423.
239 X. Xie, N. Gao, R. Deng, Q. Sun, Q. H. Xu and X. Liu, *J. Am. Chem. Soc.*, 2013, **135**, 12608–12611.
240 E. C. Ximendes, U. Rocha, T. O. Sales, N. Fernández, F. Sanz-Rodríguez, I. R. Martín, C. Jacinto and D. Jaque, *Adv. Funct. Mater.*, 2017, **27**, 1702249.
241 L. Marciniak, K. Prorok, L. Francés-Soriano, J. Pérez-Prieto and A. Bednarkiewicz, *Nanoscale*, 2016, **8**, 5037–5042.
242 P. Cortelletti, A. Skripka, C. Facciotti, M. Pedroni, G. Caputo, N. Pinna, M. Quintanilla, A. Benayas, F. Vetrone and A. Speghini, *Nanoscale*, 2018, **10**, 2568–2576.
243 X. Zhou, Y. Wang, H. Wang, L. Xiang, Y. Yan, L. Li, G. Xiang, Y. Li, S. Jiang, X. Tang and X. Zhou, *Sens. Biosensing Res.*, 2020, **29**, 100345–100354.
244 I. E. Kolesnikov, M. A. Kurochkin, A. A. Kalinichev, D. V. Mamonova, E. Y. Kolesnikov, A. V. Kurochkin, E. Lähderanta and M. D. Mikhailov, *J. Alloys Compd.*, 2018, **734**, 136–143.
245 M. Quintanilla, Y. Zhang and L. M. Liz-Marzán, *Chem. Mater.*, 2018, **30**, 2819–2828.
246 A. Skripka, A. Benayas, R. Marin, P. Canton, E. Hemmer and F. Vetrone, *Nanoscale*, 2017, **9**, 3079–3085.
247 R. Martín-Rodríguez and A. Meijerink, *J. Lumin.*, 2014, **147**, 147–154.
248 R. Naccache, Q. Yu and J. A. Capobianco, *Adv. Opt. Mater.*, 2015, **3**, 482–509.
249 D. Ananias, F. A. Almeida-Paz, L. D. Carlos and J. Rocha, *Chem. – Eur. J.*, 2018, **24**, 11926–11935.
250 F. Seitz, *J. Chem. Soc., Faraday Trans.*, 1939, **35**, 74–85.
251 N. F. Mott, *Proc. R. Soc. A*, 1938, **167**, 384–391.
252 L. Wortmann, S. Suyari, T. Ube, M. Kamimura and K. Soga, *J. Lumin.*, 2018, **198**, 236–242.
253 S. Sekiyama, M. Umezawa, S. Kuraoka, T. Ube, M. Kamimura and K. Soga, *Sci. Rep.*, 2018, **8**, 16979–16991.
254 M. Jia, Z. Fu, G. Liu, Z. Sun, P. Li, A. Zhang, F. Lin, B. Hou and G. Chen, *Adv. Opt. Mater.*, 2020, **8**, 1901173–1901180.
255 C. Matuszewska, K. Elzbieciak-Piecka and L. Marciniak, *J. Phys. Chem. C*, 2019, **123**, 18646–18653.
256 E. C. Ximendes, A. F. Pereira, U. Rocha, W. F. Silva, D. Jaque and C. Jacinto, *Nanoscale*, 2019, **11**, 8864–8869.
257 S. Balabhadra, M. L. Debasu, C. D. S. Brites, J. Rocha and L. D. Carlos, *J. Lumin.*, 2016, **180**, 25–30.
258 E. Thimsen, B. Sadtler and M. Y. Berezin, *Nanophotonics*, 2017, **6**, 1043–1054.
259 L. Labrador-Páez, M. Pedroni, A. Speghini, J. García-Solé, P. Haro-González and D. Jaque, *Nanoscale*, 2018, **10**, 22319–22328.
260 S. V. Eliseeva and J. C. G. Bünzli, *Chem. Soc. Rev.*, 2010, **39**, 189–227.
261 R. Arppe, I. Hyppänen, N. Perälä, R. Peltomaa, M. Kaiser, C. Würth, S. Christ, U. Resch-Genger, M. Schäferling and T. Soukka, *Nanoscale*, 2015, **7**, 11746–11757.
262 H. Suo, C. Guo, W. Wang, T. Li, C. Duan and M. Yin, *Dalton Trans.*, 2016, **45**, 2629–2636.
263 N. Yamada, S. Shionoya and T. Kushida, *J. Phys. Soc. Jpn.*, 1972, **32**, 1577–1586.
264 Z. Xiaoting, T. Hayakawa, Y. Ishikawa, Y. Liushuan and M. Nogami, *J. Alloys Compd.*, 2015, **644**, 77–81.
265 O. A. Savchuk, J. J. Carvajal, P. Haro-Gonzalez, M. Aguiló and F. Díaz, *J. Alloys Compd.*, 2018, **746**, 710–719.
266 A. Nexha, J. J. Carvajal, M. C. Pujol, F. Díaz and M. Aguiló, *J. Mater. Chem. C*, 2020, **8**, 180–191.
267 Y. Ma, G. Xiang, J. Zhang, Z. Liu, P. Zhou, W. Liu, X. Tang, S. Jiang, X. Zhou, L. Li, Y. Luo and Y. Jin, *J. Alloys Compd.*, 2018, **769**, 325–331.
268 G. Xiang, X. Liu, J. Zhang, Z. Liu, W. Liu, Y. Ma, S. Jiang, X. Tang, X. Zhou, L. Li and Y. Jin, *Inorg. Chem.*, 2019, **58**, 8245–8252.
269 R. Lei, X. Liu, F. Huang, D. Deng, S. Zhao, H. Xu and S. Xu, *Opt. Mater.*, 2018, **86**, 278–285.
270 V. Jambunathan, A. Schmidt, X. Mateos, M. C. Pujol, U. Griebner, V. Petrov, C. Zaldo, M. Aguiló and F. Díaz, *J. Opt. Soc. Am. B*, 2014, **31**, 1415–1421.
271 Q. Zhan, J. Qian, H. Liang, G. Somesfalean, D. Wang, S. He, Z. Zhang and S. Andersson-Engels, *ACS Nano*, 2011, **5**, 3744–3757.
272 Wikipedia Contributors, *Ex vivo*, https://en.wikipedia.org/w/index.php?title=Ex_vivo&oldid=876353685 (accessed on 24 November 2020).
273 K. Koenig, H. Liang, M. W. Berns and B. J. Tromberg, *Opt. Lett.*, 1996, **21**, 1090–1092.
274 L. Cheng, C. Wang, L. Feng, K. Yang and Z. Liu, *Chem. Rev.*, 2014, **114**, 10869–10939.
275 A. Benayas, E. Hemmer, G. Hong and D. Jaque, *Near Infrared-Emitting Nanoparticles for Biomedical Applications*, Springer, 2020.
276 M. Quintanilla, I. García, I. de Lázaro, R. García-Alvarez, M. Henriksen-Lacey, S. Vranic, K. Kostarelos and L. M. Liz-Marzán, *Theranostics*, 2019, **9**, 7298–7312.
277 L. M. Maestro, P. Haro-González, A. Sánchez-Iglesias, L. M. Liz-Marzán, J. García-Solé and D. Jaque, *Langmuir*, 2014, **30**, 1650–1658.
278 Wikipedia Contributors, *In Vitro*, https://en.wikipedia.org/wiki/In_vitro (accessed on 26 November 2020).
279 S. Uchiyama and N. Inada, in *Thermometry at the Nanoscale: Techniques and Selected Applications*, ed. L. D. Carlos and F. Palacio, The Royal Society of Chemistry, 2016, ch. 12, pp. 353–382.
280 L. H. Fischer, G. S. Harms and O. S. Wolfbeis, *Angew. Chem., Int. Ed.*, 2011, **50**, 4546–4551.
281 O. Zohar, M. Ikeda, H. Shinagawa, H. Inoue, H. Nakamura, D. Elbaum, D. L. Alkon and T. Yoshioka, *Biophys. J.*, 1998, **74**, 82–89.

282 K. Oyama, M. Takabayashi, Y. Takei, S. Arai, S. Takeoka, S. i. Ishiwata and M. Suzuki, *Lab Chip*, 2012, **12**, 1591–1593.
283 Wikipedia Contributors, *In Vivo*, https://en.wikipedia.org/wiki/In_vivo (accessed 30 November 2020).
284 U. Ozerdem and A. R. Hargens, *Microvasc. Res.*, 2005, **70**, 116–120.
285 B. J. Tromberg, O. Coquoz, J. B. Fishkin, T. Pham, E. R. Anderson, J. Butler, M. Cahn, J. D. Gross, V. Venugopalan and D. Pham, *Philos. Trans. R. Soc. London, Ser. B*, 1997, **352**, 661–668.
286 J. H. Lienhard, *A heat transfer textbook*, Courier Corporation, 2013.
287 F. P. Incropera, T. L. Bergman and A. S. Lavine, *Introduction to Heat Transfer*, Wiley, New York, 5th edn, 2006.
288 E. Saïdi, N. Babinet, L. Lalouat, J. Lesueur, L. Aigouy, S. Volz, J. Labéguerie-Egéa and M. Mortier, *Small*, 2011, **7**, 259–264.
289 J.-P. Tetienne, A. Lombard, D. A. Simpson, C. Ritchie, J. Lu, P. Mulvaney and L. C. L. Hollenberg, *Nano Lett.*, 2016, **16**, 326–333.
290 I. Sedmak, I. Urbančič, J. Štrancar, M. Mortier and I. Golobič, *Sens. Actuators, A*, 2015, **230**, 102–110.
291 V. V. Deshpande, S. Hsieh, A. W. Bushmaker, M. Bockrath and S. B. Cronin, *Phys. Rev. Lett.*, 2009, **102**, 105501–105505.
292 X. Wu, S. Zhan, J. Han and Y. Liu, *Nano Lett.*, 2021, **21**, 272–278.
293 H. Suo, X. Zhao, Z. Zhang, R. Shi, Y. Wu, J. Xiang and C. Guo, *Nanoscale*, 2018, **10**, 9245–9251.
294 J. Zhao, X. Chen, B. Chen, X. Luo, T. Sun, W. Zhang, C. Wang, J. Lin, D. Su, X. Qiao and F. Wang, *Adv. Funct. Mater.*, 2019, **29**, 1903295–1903302.
295 M. Wang, L. Yi, G. Wang, L. Hu and J. Zhang, *Solid State Commun.*, 2009, **149**, 1216–1220.
296 L. Sordillo, Y. Pu, S. Pratavieira, Y. Budansky and R. Alfano, *J. Biomed. Opt.*, 2014, **19**, 56004–56010.
297 H. Rodríguez-Rodríguez, S. Imanieh, F. Lahoza and I. Martin, *Sol. Energy Mater. Sol. Cells*, 2016, **144**, 29–32.
298 L. Liu, S. Wang, B. Zhao, P. Pei, Y. Fan, X. Li and F. Zhang, *Angew. Chem., Int. Ed.*, 2018, **57**, 7518–7522.
299 U. Rocha, K. U. Kumar, C. Jacinto, I. Villa, F. Sanz-Rodríguez, M. C. I. de la Cruz, A. Juarranz, E. Carrasco, F. C. J. M. van Veggel, E. Bovero, J. G. Solé and D. Jaque, *Small*, 2014, **10**, 1141–1154.
300 G. Chen, J. Shen, T. Y. Ohulchanskyy, N. J. Patel, A. Kutikov, Z. Li, J. Song, R. K. Pandey, H. Ågren, P. N. Prasad and G. Han, *ACS Nano*, 2012, **6**, 8280–8287.
301 N. N. Dong, M. Pedroni, F. Piccinelli, G. Conti, A. Sbarbati, J. Ramirez, L. Martínez-Maestro, M. C. I. de la Cruz, F. Sanz-Rodriguez, A. Juarranz, F. Chen, F. Vetrone, J. Capobianco, J. Solé, M. Bettinelli, D. Jaque and A. Speghini, *ACS Nano*, 2011, **5**, 8665–8671.
302 R. Wang, X. Li, L. Zhou and F. Zhang, *Angew. Chem., Int. Ed.*, 2014, **53**, 12086–12090.
303 Y. Shen, J. Lifante, N. Fernández, D. Jaque and E. Ximendes, *ACS Nano*, 2020, **14**, 4122–4133.
304 M. Suzuki and T. Plakhotnik, *Biophys. Rev.*, 2020, **12**, 593–600.